

## DTIC FILE COPY REPORT DOCUMENTATION PAGE

1a. REP <b>AD-A229 979</b>			1b. RESTRICTIVE MARKINGS		
2a. SECURITY CLASSIFICATION AUTHORITY <b>UNCLASSIFIED</b>			3. DISTRIBUTION/AVAILABILITY OF REPORT Approved for public release, distribution unlimited.		
2b. DECLASSIFICATION/DOWNGRADING SCHEDULE <b>DEC 26 1990</b>			5. MONITORING ORGANIZATION REPORT NUMBER(S) <b>AFOSR-TR- 86-11</b>		
4. PERFORMING ORGANIZATION REPORT NUMBER(S) <b>60 D</b>			7a. NAME OF MONITORING ORGANIZATION <b>Air Force Office of Scientific Research</b>		
6a. NAME OF PERFORMING ORGANIZATION <b>Mech. &amp; Nuc. Engr. Dept. Mississippi State University</b>		6b. OFFICE SYMBOL (If applicable)	7b. ADDRESS (City, State, and ZIP Code) <b>Bolling Air Force Base Washington, DC 20332</b>		
6c. ADDRESS (City, State, and ZIP Code) <b>P. O. Drawer ME Mississippi State, MS 39762</b>		9. PROCUREMENT INSTRUMENT IDENTIFICATION NUMBER <b>AFOSR-86-0178</b>			
8a. NAME OF FUNDING/SPONSORING ORGANIZATION		8b. OFFICE SYMBOL (If applicable) <b>AFOSR/NA</b>	10. SOURCE OF FUNDING NUMBERS		
8c. ADDRESS (City, State, and ZIP Code) <b>Bolling Air Force Base Washington, DC 20332</b>		PROGRAM ELEMENT NO. <b>61102 F</b>	PROJECT NO. <b>2307</b>	TASK NO. <b>A4</b>	WORK UNIT ACCESSION NO.
11. TITLE (Include Security Classification) <b>Investigations of Surface Roughness Effects on Turbulent Flow and Heat Transfer</b>					
12. PERSONAL AUTHOR(S) <b>Coleman, Hugh W.; Taylor, Robert P.; Hosni, M. H.</b>					
13a. TYPE OF REPORT <b>Final</b>		13b. TIME COVERED <b>FROM May 86 TO Sep 90</b>		14. DATE OF REPORT (Year, Month, Day) <b>1990, October</b>	
15. PAGE COUNT <b>263</b>					
16. SUPPLEMENTARY NOTATION					
17. COSATI CODES			18. SUBJECT TERMS (Continue on reverse if necessary and identify by block number)		
FIELD	GROUP	SUB-GROUP	Heat Transfer, Turbulent Boundary Layer, Surface Roughness Effects, <b>15-71-1</b>		
19. ABSTRACT (Continue on reverse if necessary and identify by block number) <p>The primary objective of this research program was to investigate the effects of surface roughness on turbulent boundary layer heat transfer by obtaining accurate, comprehensive, quality heat transfer data for zero pressure gradient incompressible air flow over constant temperature test surfaces with well-defined surface roughness geometries. Knowledge gained from the experimental investigation was used to improve and extend the roughness energy transport model used in the discrete element prediction method, thus enhancing and expanding the capability to predict the effects of surface roughness on turbulent flow and heat transfer.</p> <p>Fluid dynamics and heat transfer data for turbulent boundary layer flow over a smooth and five rough surfaces were taken in the Turbulent Heat Transfer Test Facility (THTF) for x-Reynolds numbers ranging up to 10,000,000. The smooth wall data was used for qualification of the THTF and provided base line data for comparison with the data from rough surfaces. <i>Per...</i></p>					
20. DISTRIBUTION/AVAILABILITY OF ABSTRACT <input checked="" type="checkbox"/> UNCLASSIFIED/UNLIMITED <input type="checkbox"/> SAME AS RPT. <input type="checkbox"/> DTIC USERS			21. ABSTRACT SECURITY CLASSIFICATION <b>Unclass</b>		
22a. NAME OF RESPONSIBLE INDIVIDUAL <b>Dr. James McMichael</b>			22b. TELEPHONE (Include Area Code) <b>(202) 767-4987</b>		22c. OFFICE SYMBOL <b>AFOSR/NA</b>

## 19. ABSTRACT (Continued)

The THTF fluid dynamics and heat transfer data taken in aerodynamically smooth, transitionally rough, and fully rough flow regimes over the three well-defined hemispherically roughened surfaces (with element spacing to base diameter ratios of  $L/d_0 = 2, 4$ , and  $10$ , respectively) were compared with previously published data on a single well-defined rough surface comprised of spherical elements packed in the most dense array. It was observed that the Stanton numbers for a given surface collapse together in  $St$  versus  $Re_x$  coordinates as the freestream velocity increases, with the Stanton number level being larger for rougher surfaces. This behavior had not been recognized previously. It was also observed that the behavior of the  $St$  versus  $Re_x$  data does not correspond to the flow regime characterizations of transitionally rough and fully rough based on fluid mechanics behavior. That is, the Stanton number data collapsed together for the  $L/d_0 = 10$  surface at freestream velocities for which the turbulent boundary layers were clearly in the transitionally rough state, while the same Stanton number behavior was observed for the  $L/d_0 = 2$  surface for freestream velocities corresponding to the fully rough state.

Fluid dynamics and heat transfer data were also collected for flows over two surfaces with truncated cone roughness elements spaced  $2$  and  $4$  base diameters apart, respectively, in staggered arrays to investigate surface roughness shape effects on rough-wall turbulent boundary layer flow and heat transfer. No dependence of skin friction coefficients on roughness element shape could be concluded considering the uncertainty of the hot-wire anemometry technique used to determine  $C_f$ . The Stanton number data (which have uncertainties of about  $2-4\%$ ) exhibit slightly distinguishable differences for the two  $L/d_0 = 4$  surfaces and definitive differences for the two  $L/d_0 = 2$  surfaces. In  $St$  versus  $Re_x$  coordinates, for  $L/d_0 = 4$  the Stanton numbers are consistently about  $2-4\%$  larger for the surface with hemispherical roughness than for the surface with conical roughness. For  $L/d_0 = 2$ , this difference is increased to about  $10\%$ .

The heat transfer data from the hemispherically roughened surfaces was used to modify the roughness energy transport model in the discrete element prediction method. This new model was used in calculation of the fluid dynamics and heat transfer for all of the THTF surfaces, and the predictions were generally in excellent agreement with the data.

Investigations of Surface Roughness  
Effects on Turbulent Flow and  
Heat Transfer

Hugh W. Coleman  
Robert P. Taylor  
M. H. Hosni

Thermal & Fluid Dynamics Laboratory  
Mechanical and Nuclear Engineering Department  
Mississippi State University  
Mississippi State, MS 39762

October 1990

Final Report for Period 15 May 1986 - 14 September 1990

Approved for public release; distribution unlimited

AIR FORCE OFFICE OF SCIENTIFIC RESEARCH  
AIR FORCE SYSTEMS COMMAND  
BOLLING AIR FORCE BASE, DC 20332-6448

## PREFACE

This program was conducted by the Mechanical and Nuclear Engineering Department, Mississippi State University, P. O. Drawer ME, Mississippi State, MS 39762 under Grant AFOSR-86-0178 from the Air Force Office of Scientific Research, Bolling Air Force Base, Washington, DC 20332. Dr. James Wilson, Capt. Henry Helin and Dr. James McMichael managed the program for the Air Force Office of Scientific Research. The part of the program with which this report is concerned was conducted from May 1986 through September 1990.

The experimental apparatus used in this research program was acquired under Grant AFOSR-85-0075.

The authors wish to thank Dr. Jim Wilson, Capt. Hank Helin and Dr. Jim McMichael for their support and encouragement. The authors also wish to acknowledge the efforts of P. V. Suryanarayana, G. B. Brown, P. H. Love, and J. B. Garner, who participated in this research during their respective M.S. graduate programs.



Account No.

RHS

DID

DATE

SIGNATURE

J

6-10-71

A-1

## ABSTRACT

The primary objective of this research program was to investigate the effects of surface roughness on turbulent boundary layer heat transfer by obtaining accurate, comprehensive, quality heat transfer data for zero pressure gradient incompressible air flow over constant temperature test surfaces with well-defined surface roughness geometries. Knowledge gained from the experimental investigation was used to improve and extend the roughness energy transport model used in the discrete element prediction method, thus enhancing and expanding the capability to predict the effects of surface roughness on turbulent flow and heat transfer.

Fluid dynamics and heat transfer data for turbulent boundary layer flow over a smooth and five rough surfaces were taken in the Turbulent Heat Transfer Test Facility (THTTF) for  $x$ -Reynolds numbers ranging up to 10,000,000. The smooth wall data was used for qualification of the THTTF and provided base line data for comparison with the data from rough surfaces.

The THTTF fluid dynamics and heat transfer data taken in aerodynamically smooth, transitionally rough, and fully rough flow regimes over the three well-defined hemispherically roughened surfaces (with element spacing to base diameter ratios of  $L/d_0 = 2, 4, \text{ and } 10$ , respectively) were compared with previously published data on a single well-defined rough surface comprised of spherical elements packed in the most dense array. It was observed that the Stanton numbers for a given surface collapse together in  $St$  versus  $Re_x$  coordinates as the

freestream velocity increases, with the Stanton number level being larger for rougher surfaces. This behavior had not been recognized previously. It was also observed that the behavior of the  $St$  versus  $Re_x$  data does not correspond to the flow regime characterizations of transitionally rough and fully rough based on fluid mechanics behavior. That is, the Stanton number data collapsed together for the  $L/d_0 = 10$  surface at freestream velocities for which the turbulent boundary layers were clearly in the transitionally rough state, while the same Stanton number behavior was observed for the  $L/d_0 = 2$  surface for freestream velocities corresponding to the fully rough state.

Fluid dynamics and heat transfer data were also collected for flows over two surfaces with truncated cone roughness elements spaced 2 and 4 base diameters apart, respectively, in staggered arrays to investigate surface roughness shape effects on rough-wall turbulent boundary layer flow and heat transfer. No dependence of skin friction coefficients on roughness element shape could be concluded considering the uncertainty of the hot-wire anemometry technique used to determine  $C_f$ . The Stanton number data (which have uncertainties of about 2-4%) exhibit slightly distinguishable differences for the two  $L/d_0 = 4$  surfaces and definitive differences for the two  $L/d_0 = 2$  surfaces. In  $St$  versus  $Re_x$  coordinates, for  $L/d_0 = 4$  the Stanton numbers are consistently about 2-4% larger for the surface with hemispherical roughness than for the surface with conical roughness. For  $L/d_0 = 2$ , this difference is increased to about 10%.

The heat transfer data from the hemispherically roughened surfaces was used to modify the roughness energy transport model in the discrete element prediction method. This new model was used in calculation of the fluid dynamics and heat transfer for all of the THTF surfaces, and the predictions were generally in excellent agreement with the data.

## CHAPTER 1

### INTRODUCTION

Knowledge of flow resistance and heat transfer characteristics between fluids and solid surfaces is essential in engineering applications. Both the fluid dynamics and thermal characteristics of a flow field are affected by the shape and surface condition of a solid wall. The surface condition becomes particularly important in applications where roughness is an inherent feature. Many surfaces of engineering interest are rough in the aerodynamic sense. Turbine blades, missiles, reentry vehicles, ship hulls, heat exchangers, and piping networks are examples of systems in which surface roughness can play an important role in heat transfer and skin friction. Both heat transfer and skin friction can be significantly larger for a turbulent flow over a rough surface compared with an equivalent turbulent flow over a smooth surface. In light of the importance of the effects of surface roughness and the broad applicability, there is significant engineering interest in the development of accurate predictive models for heat transfer and fluid mechanics in turbulent flow over rough surfaces.

The most logical and direct calculation method for turbulent flows over rough surfaces would be to solve the complete unsteady Navier-Stokes equations in a grid system fine enough to resolve the details of both the turbulence and the geometry of the rough sur-



face. Such an effort would be beyond the state of the art since the computer storage and computational time required would be astronomical.

An alternative approach would be to solve the time-averaged Navier-Stokes equations in a grid system fine enough to resolve the geometry of the rough surface. This scheme too is not feasible for "real" surfaces, since the grid for such a scheme would still be beyond the present computer storage capabilities. Since this scheme, which is used extensively for smooth wall flow conditions, does not attempt to temporally resolve the turbulent fluctuations, turbulent closure models are required as the time averaging process introduces new variables (the so-called Reynolds stresses) but no new equations. Therefore, empirical inputs are required to "close" the system of equations.

A scheme that circumvents some of the difficulties mentioned above is to solve the time-averaged Navier-Stokes equations in a coarse grid system which does not resolve the roughness geometry, allowing the problem to be placed on current computers to the same extent as for smooth wall flows. Here, as in the second scheme, turbulent closure models are required. Also, since the details of the roughness geometry are not resolved, some empirically based roughness model must be introduced into the governing equations to account for the physics of the interaction of the roughness and the flow field.

Since many flows of engineering interest meet the boundary layer assumptions, further simplifications of the equations are possible to obtain the so-called boundary layer equations. For subsonic flows, these equations are parabolic as opposed to the elliptic Navier-Stokes equations and offer comparative computational efficiency. Nevertheless, turbulent closure models and roughness models are still required.

From this discussion it is apparent that accurate computational schemes for calculations of turbulent flows require turbulent closure models to close the system of equations since the time averaging process introduces new variables. Likewise, if the flows over rough surfaces are to be computed, some efficient, accurate roughness models must be supplied to the calculation scheme to incorporate the physics of the process. To develop such roughness models, accurate, precise, well-documented experimental data sets over well-defined rough surfaces are required.

### 1.1 OVERVIEW OF RESEARCH PROGRAM

In the past, most of the research effort in predicting turbulent flows was to develop computational methods for various geometries with smooth surfaces, and the roughness problem received relatively little attention. However, many systems of engineering interest have surfaces which are aerodynamically rough. In order to predict the heat transfer and fluid dynamics of turbulent flow over

rough surfaces, computational procedures to model the effects of rough surfaces must be developed and proven with well-documented data sets.

Most of the roughness-influenced turbulence data taken over the years has been on ill-defined rough surfaces. A research program at Stanford University [Healzer (1974), Pimenta (1975), Coleman (1976), Ligrani (1979)] produced the only data sets which have been reported for a well-defined rough surface that contain heat transfer and skin friction distributions and velocity, temperature and Reynolds stress profiles. However, these data sets are for a single rough surface comprised of spheres of a single size packed in the most dense array. Holden (1983) reported heat transfer and skin friction distribution measurements on well-defined surface roughness on cones for hypersonic flow conditions.

Considering the limited range of previously reported rough surface data, it became apparent that there existed a critical need for accurate, precise, comprehensive data sets on both the heat transfer and the fluid dynamics in turbulent flow over well-defined rough surfaces. It was concluded that if a reasonable predictive capability were to be developed, then the additional experimental information (particularly for heat transfer) must be obtained. Recognition of this need led to the development of a water tunnel facility and the Turbulent Heat Transfer Test Facility (THTTF) in the Thermal & Fluid Dynamics Laboratory at Mississippi State University. A comprehensive investigation of the effects of surface roughness element size, spacing and shape on skin friction in fully

developed pipe flow over a wide range of Reynolds numbers was recently completed using the water tunnel facility in this laboratory [Scaggs et al. (1988a, 1988b, 1988c), Taylor et al. (1988)]. The major part of the experimental facility is the Turbulent Heat Transfer Test Facility (THTTF) described in Chapter 3.

## 1.2 OBJECTIVES AND THE EXPERIMENTAL PLAN

This research program was designed to provide accurate, comprehensive sets of measurements of Stanton number distributions, skin friction coefficient distributions, and profiles of velocity, temperature and Reynolds stresses in turbulent boundary layer flows over surfaces roughened with well-defined roughness elements. These data are used in a parallel effort to improve and extend the roughness models in a discrete element prediction method discussed later, thus expanding our capability to predict the effects of surface roughness on turbulent flow and heat transfer.

The phase of the research program discussed herein used six different test surfaces in the THTTF--one smooth and five rough. The smooth surface tests served as a qualification check on the test facility and experimental procedures. Three of the rough test surfaces consist of smooth plates roughened with hemispherical roughness elements of 1.27 mm diameter spaced 2, 4, and 10 base diameters apart, respectively. The other two rough test surfaces consist of smooth plates roughened with elements that are truncated right circular cones of 1.27 mm base diameter with spacings of 2 and 4 base diameters, respectively.

The experimental plan was to test each set of surfaces with basic boundary conditions of zero pressure gradient and constant wall temperature over a number of freestream velocities between about 6 and 67 m/s such that the total set of data thoroughly cover behavior in the aerodynamically smooth, transitionally rough, and fully rough regimes. The heat transfer data are the most critical, since the only prior data available on a well-described rough surface are those from the previously discussed Stanford experiments, which used a single rough surface composed of 1.27 mm diameter spheres packed in the most dense array.

The THTTF was designed so that the 24 test plates, which make up its test surface, can be replaced with a new set without completely tearing down the test section. Some re-instrumentation, calibration and qualification are necessary for each new set of test plates, however, to maintain the high accuracy and precision which are inherent parts of the overall objective of this test program.

### 1.3 CONTENTS AND GENERAL ORGANIZATION

This report presents experimental results and prediction method development for the smooth test surface and the 5 rough surfaces. The first tests were the calibration, qualification and general "shake-down" of the facility using the smooth wall test surface. The ability to reproduce accepted smooth wall results for non-isothermal turbulent boundary layer flow in the THTTF was deemed necessary before proceeding with rough wall investigations using the facility. In addition, the smooth wall data provide an appropriate

baseline with which to compare the data obtained for rough walls using the same test apparatus.

The general organization of the work presented in the following chapters is described below. In Chapter 2, the background on study of surface roughness effects is reviewed, previous experimental work is discussed, and the discrete element prediction approach is introduced. The experimental apparatus and measurement techniques and a summary of smooth wall qualification results for the THTF are discussed in Chapter 3. Chapter 4 contains fluid dynamics data, including skin friction coefficient distributions and boundary layer profiles of mean velocity and Reynolds stresses, for the three rough test surfaces with hemispherical elements spaced 2, 4, and 10 base diameters apart, respectively. In Chapter 5, experimental heat transfer data, which include Stanton number distributions and boundary layer temperature profiles for the same 3 rough surfaces, are presented, and the heat transfer characteristics of these surfaces are compared. In Chapter 6, predictions from the discrete element method are presented and compared with the previously published Stanford rough surface data and the THTF results for the 3 surfaces roughened with hemispherical elements. The effects of roughness element shape are discussed in Chapter 7, with fluid mechanics and heat transfer data from the 2 surfaces roughened with truncated cones being compared with data from the equivalent hemisphere roughened surfaces and with results from the prediction method. The summary and conclusions of the work are given in Chapter 8.

## CHAPTER 2

### BACKGROUND

Given the geometry of an object immersed in a flow field, a specification of the freestream flow conditions, and a geometrical description of the roughness of the system surfaces, an analyst or designer would like at least to be able to predict the surface shear distribution, the heat transfer distribution, and the total drag. In the past, most of the research efforts concerning turbulent flows, either experimental or computational, were devoted to flows over smooth surfaces of various geometries, and the roughness problem has received relatively little attention. Thus, the vast majority of the available data sets and computational models for turbulent flows deal with smooth wall cases. However, many systems of engineering interest have surfaces which are aerodynamically rough, and engineering applications of such systems require reliable prediction models and practical computational schemes for heat transfer coefficient and skin friction coefficient distributions.

Previous work on the effects of surface roughness can be broadly classified as either experimental or computational (prediction modeling, numerical calculation methods, etc.). The types of surface roughnesses, categorized based on their distinct characteristics by previous workers in the literature, are (1) the so-called

"rib-type" roughnesses (transverse ribs, for example) and (2) the so-called "distributed-type" roughnesses (sandgrain roughness, uniform roughness elements distributed in a staggered array, etc.).

The background on roughness studies presented herein deals only with the distributed type roughnesses, since this is the type considered in the current research effort covered in this report. Both the experimental and computational aspects of previous studies on the effects of distributed surface roughness on turbulent flows are reviewed below.

## 2.1 EXPERIMENTAL

The experimental study of surface roughness effects on fluid flow has its origin with the classic work of Nikuradse (1933). He concentrated his experimental efforts on the overall fluid dynamics behavior of rough wall flows by measurements of pressure drop and velocity profile in pipes roughened with tightly sized sandgrains. He made an extensive number of experimental runs covering 6 sandgrain sizes and pipe Reynolds numbers ranging from 500 to 1,000,000. Based on his experimental results on skin friction coefficient distributions from sand roughened fully developed pipe flows, Nikuradse identified three regimes of fully developed flow: aerodynamically smooth, transitionally rough, and fully rough flow. Aerodynamically smooth flow is flow over a surface that has the same resistance as flow over an ideal smooth surface at the same Reynolds number. The aerodynamically smooth regime, thus, is characterized by the skin friction coefficient depending on the Reynolds number of



the gross flow only and being independent of roughness shape, size, density, etc. In contrast, for a fully rough flow the skin friction coefficient depends solely on the character of the roughness and is entirely independent of the Reynolds number of the gross flow. The regime of flow between aerodynamically smooth and fully rough is known as transitionally rough. It is characterized by the dependence of the skin friction coefficient on both flow Reynolds number and roughness character.

The flow regime delimiter Nikuradse chose to measure the state of the flow with respect to the three regimes was the roughness Reynolds number,

$$Re_{k_s} = u^* k_s / \nu \quad (2.1)$$

where  $u^*$  is the friction velocity and  $k_s$  is the size of the sand-grains. His reported limits for the three regimes of fully developed rough surface flow were

aerodynamically smooth	$Re_{k_s} < 5$
transitionally rough	$5 < Re_{k_s} < 55-70$
fully rough	$Re_{k_s} > 55-70$

These three regimes have sometimes been explained in terms of the relationship between the roughness height and the viscous sublayer. It is said that in the aerodynamically smooth regime the roughness elements are all within the sublayer; therefore, viscous effects dominate and the surface appears smooth to the flow. In the transitionally rough regime the roughness elements begin to protrude through the sublayer and both viscous and roughness effects are

significant. Finally, in the fully rough regime the sublayer is said to be fully destroyed and viscous effects become insignificant--hence the Reynolds number is no longer a factor.

The sublayer explanation, while enlightening, depends almost completely on the height of the roughness and ignores the important factors of shape and spacing density of the roughness elements. An otherwise smooth surface with very sparsely spaced large (relative to the sublayer) elements may appear smooth to the flow.

Following Nikuradse's work, Schlichting (1936) conducted experiments in a rectangular channel with the upper surface rough and the remaining sides smooth. He studied the effects of roughness size, shape and density on the flow resistance using well-defined roughness elements and sandgrains. He investigated seven different shapes: large spheres, small spheres, spherical segments, cones, short angles, long angles and a "Hamburg" sand. Each shape was studied over a range of spacings and a limited range of Reynolds numbers. His experiments with different sandgrain sizes were also performed over a limited range of Reynolds numbers. He related his skin friction results on these well-described rough surfaces to the results obtained by Nikuradse for sand-roughened pipes through definition of an equivalent sandgrain roughness. The equivalent sandgrain roughness,  $k_s$ , of a surface was defined as the sandgrain size in Nikuradse's experiment that gave the same flow resistance as the surface of interest at the same Reynolds number based on hydraulic radius. He proposed the use of the equivalent sandgrain roughness as a measure of the flow resistance character of a rough

surface. It was Schlichting's stated purpose to use this parameter as a means of extrapolating a set of experimental resistance data to other Reynolds numbers based on Nikuradse's extensive data set.

During the mid-thirties to early seventies, experimental works on the effects of distributed surface roughness were piecemeal. The reported works were limited to specific cases, and no systematic general studies are found in the literature. A few representative works are discussed here. Hama (1954) looked at air flowing over surfaces roughened by screens attached to them. He obtained velocity profiles of various boundary layers from which he deduced a skin friction drag formula, but no direct measurement of skin friction drag was made. The experiments by Grass (1971) were carried out in a water tunnel using gravel and sandgrain roughness to study the details of turbulent structure near the rough wall. He measured instantaneous velocity distributions using the hydrogen bubble technique. Townes et al. (1972, 1973) studied the structure of turbulent air flows in smooth and rough pipes roughened by sandgrains of various sizes. Wu (1973) used a floating element balance to measure the skin friction of a sandgrain roughened surface in an air tunnel.

In the past, most of the studies on the effects of surface roughness were concentrated on the fluid dynamics behavior of flows over rough surfaces. Much less work has been done in the field of heat transfer. The work of Nunner (1956) is one of the first reported experimental studies on the heat transfer behavior of a rough surface. He used his experimental results for air flow through

rough pipes to establish a single empirical relationship between the increase in Nusselt number due to roughness and the increase in the friction coefficient. Dipprey and Sabersky (1963) studied heat and momentum transfer in smooth and rough tubes at various Prandtl numbers. They investigated the flow of four fluids of different Prandtl numbers through one smooth and three rough pipes with three-dimensional roughness elements and concluded that the heat transfer rate of fully developed rough wall pipe flow varied with Prandtl number. The other early rough wall heat transfer studies for internal flows are summarized by Sood and Johnson (1969) and by Norris (1971). Some sources of early rough wall heat transfer data are referenced by Yaglom and Kader (1974).

The roughness Reynolds number as the delimiter of flow regimes and Schlichting's equivalent sandgrain roughness concept have been extensively used by many workers [Perry and Joubert (1963), Nestler (1970), Cebeci and Chang (1978), for example]]. Many workers have in fact related their experimental data to that of Schlichting by implicitly introducing the equivalent sandgrain roughness into their data reduction. Recently Coleman, Hodge and Taylor (1983, 1984) showed that Schlichting had made erroneous assumptions during his data reduction which had significant effects on the results which he reported. They showed that his skin friction results were too large by amounts ranging up to 73% and that his reported values of equivalent sandgrain roughness,  $k_s$ , were too high by amounts ranging from 26% to 555%. These findings caused some consternation, since prac-

tically all work since the 1930's on surface roughness effects relied significantly on either the skin friction or equivalent sandgrain roughness results as originally reported by Schlichting.

A previously mentioned series of experimental studies at Stanford University [Healzer (1974), Pimenta (1975), Coleman (1976), Ligrani (1979)] has remained as the only source of reported data for a well-defined rough surface that contains detailed fluid dynamics and heat transfer information for boundary layer flows. However, these data sets are for a single rough surface which was comprised of spheres of a single size packed in the most dense array.

Healzer (1974) studied the heat transfer characteristics and the overall aerodynamic performance of this rough surface over a wide range of freestream velocities. He presented experimentally determined Stanton number data and velocity profiles (from Pitot probes) for flow fields with and without transpiration.

Pimenta (1975) investigated the structural features of turbulent boundary layer flows and their interactions with a rough wall with and without transpiration. He documented Stanton number data, friction coefficient distributions, velocity and temperature profiles and profiles of turbulence quantities (components of the Reynolds stress tensor) at various freestream velocities. Moreover, he studied and identified the fully rough state of a turbulent boundary layer with heat transfer and transpiration. Based on his profiles of turbulence quantities, he stated that the near-wall

behavior of the turbulent fluctuations was markedly different from smooth wall flows and may be used as a measure to distinguish between transitionally rough and fully rough regimes.

Coleman (1976) reported the results of his experimental investigation on the behavior of the fully rough turbulent boundary layer subjected to favorable pressure gradients. He presented measurements of profiles of mean velocity, mean temperature and the components of the Reynolds stress tensor for both unblown and blown layers. In addition, he documented Stanton and skin friction coefficients for both unblown and blown boundary layers for various freestream velocities.

Ligrani (1979) investigated the differences between fully rough and transitionally rough behavior using artificially thickened turbulent boundary layers in transitionally rough and fully rough states. He presented measurements of Stanton numbers, skin friction coefficients, mean temperature and velocity profiles, Reynolds stress tensor component profiles, and spectra of the longitudinal velocity fluctuations.

The most recent rough surface study was done by Scaggs et al. (1988a). They investigated the effects of surface roughness on turbulent fully developed pipe flow friction factors using eleven different rough surfaces, nine of which had uniform roughness elements and two of which were roughened nonuniformly. These surfaces covered a range of roughness element sizes, spacings and shapes. Friction factor data from these eleven rough surfaces were acquired over a pipe Reynolds number range from 10,000 to 600,000.

## 2.2 COMPUTATIONAL METHODS

The two basic categories in which calculation efforts have fallen are (1) an entirely empirical method known as the equivalent sandgrain approach, and (2) a semi-empirical method known as the discrete element approach. While both methods require experimental input, the equivalent sandgrain approach may require experimental data on the particular surface under consideration. On the other hand, the discrete element approach incorporates more basic physics of the process and uses a more generalized empirical input. It is therefore applicable to a broader spectrum of rough surfaces without requiring specific experimental data.

### 2.2.1 Equivalent Sandgrain Approach

The equivalent sandgrain roughness,  $k_s$ , has usually been determined by measuring the skin friction and velocity profiles for a particular surface and then comparing these results with the results of Nikuradse (1933). This method is not as straightforward as it first appears. The appropriate origin for the distance from the wall which is needed in comparing the logarithmic velocity profiles is not clearly defined and is subject to the researcher's judgement and various approximations [see Taylor et al. (1984)]. If the equivalent sandgrain roughness approach is to be a useful predictive tool, some method must exist to specify  $k_s$  for different surfaces.

The equivalent sandgrain roughness has been used in predictive modeling through algebraic correlations, integral methods and differential (finite difference) methods. Many correlations for skin friction coefficient and Stanton number have been presented. Examples are Schlichting (1936), Dipprey and Sabersky (1963), Nestler (1970), and Seidman (1978). Dvorak (1969) presented an integral method to predict skin friction and heat transfer.

In the current state of boundary layer computation, the differential methods are by far the most important. These methods solve the partial differential equations of the boundary layer using numerical approximation techniques (finite difference, finite element, etc.). Representative of such approaches is the one reported by Cebeci and Chang (1978), who presented a method that relied heavily on the equivalent sandgrain roughness. They solved the usual incompressible boundary layer continuity and momentum equations for the flow field, and accounted for the roughness via a virtual origin  $\Delta y$  for the Prandtl mixing length, where  $\Delta y$  was taken as a function of  $k_s$ . One of the major problems with differential methods that use the equivalent sandgrain roughness is the ill-defined wall boundary condition. Cebeci and Chang attempted to overcome this by defining "wall" conditions at some distance  $y_0$  above the crest of the roughness. They determined the velocity boundary conditions  $(u_0, v_0)$  at this point from empirical velocity profile "laws."



Lin and Bywater (1980) and Adams and Hodge (1977) presented differential methods that were basically discrete element approaches (discussed below) but which relied on equivalent sandgrain roughness to some degree in the turbulence models.

Note that the above discussion of equivalent sandgrain roughness is almost totally concerned with momentum transport. In fact the equivalent sandgrain roughness,  $k_s$ , is defined only on the basis of the skin friction and velocity profile data. In general, attempts to use equivalent sandgrain roughness to correlate heat transfer data have not been successful. This is most likely because the mechanisms for momentum and energy transport to a roughness element are different. The apparent shear stress at the wall (total tangential force on the wall divided by wall area) is composed of viscous shear forces plus form drag on the elements. For heat transfer there is no transport mechanism which is analogous to the form drag on the element. In fact, there is no physical reason for two surfaces with the same skin friction coefficient to have the same Stanton number.

In spite of problems with the sandgrain roughness approach, one should not conclude that it is a complete failure. Its dominance in the subject of flow over rough surfaces for years is testimony to its value in filling some of the gaps in the science of fluid mechanics. However, many gaps remain.

### 2.2.2 Discrete Element Method

Schlichting, in the same paper in which he introduced the equivalent sandgrain roughness, briefly discussed an alternative approach that has come to be known as the discrete element approach. He proposed that the flow resistance of a rough surface be divided into two components--that due to the form drag on the element and that due to the viscous shear on the smooth surface area between the roughness elements. The discrete element method does not use the equivalent sandgrain roughness concept. It in effect abandons the concept of sandgrain roughness and thereby abandons the roughness Reynolds number as the delimiter for aerodynamically smooth, transitionally rough and fully rough conditions. It considers the momentum and energy transport processes on the collection of individual roughness elements and the smooth surface between the elements. The basic idea is to formulate a system of partial differential equations that describes the mass, momentum and energy transport for the flow over, around and between the roughness elements. In this method the roughness effects are taken as an integral part of the flow problem and not (as with the equivalent sandgrain approach) as some ill-defined boundary condition.

Following Schlichting's idea, Liepmann and Goddard (1957) (as did Lewis (1975)) attempted the formulation of the discrete element method with some degrees of success. In recent years, several serious attempts to use the discrete element method as a basis for calculation methods have been presented. Calculation methods for skin friction and heat transfer on rough surfaces using the discrete

element approach have been reported by several groups of researchers [Finson (1975), Adams and Hodge (1977), Finson and Wu (1979), Finson and Clark (1980), Lin and Bywater (1980), Finson (1982), Christoph (1982), Christoph and Pletcher (1983)]. In these papers, researchers either introduced the equivalent sandgrain roughness in their prediction models implicitly or added terms to the equations in an ad hoc manner to satisfy physical reasoning. No attempts had been made to systematically derive the equations from first principles.

Taylor et al. (1984), following the basic idea of Schlichting and the preceding works listed above, derived from first principles the discrete element approach for two dimensional boundary layer flow that included the physical effects of roughness in the equations which govern the flow. Their scheme accounts for all three of the major physical interactions of the roughness and the flow-blockage, form drag and local element/fluid heat transfer. They documented roughness models for their discrete element method for both fluid dynamics and heat transfer and presented predictions compared with a wide range of experimental data.

The discrete element method used in this work is formulated for roughness elements with three dimensional shapes (as opposed to transverse ribs) for which the element cross section can be approximated as circular at every height,  $y$ . This scheme includes the physical effects of roughness on the flow field by considering the blockage effects of roughness elements, the drag forces which the roughness elements exert on the field and the heat transfer between roughness elements and the flow. The steady (Reynolds-averaged),

two-dimensional turbulent boundary layer equations as derived by Taylor et al. (1984) and presented here are for flow over a rough surface with roughness elements of uniform shape and spacing as shown in Figure 2.1.

The discrete element boundary layer equations and boundary conditions are:

$$\frac{\partial}{\partial x} (\rho \beta_x u) + \frac{\partial}{\partial y} (\rho \beta_y v) = 0 \quad (2.2)$$

and

$$\begin{aligned} \beta_x \rho u \frac{\partial u}{\partial x} + \beta_y \rho v \frac{\partial u}{\partial y} = & - \frac{\partial}{\partial x} (\beta_x P) \\ & + \frac{\partial}{\partial y} \left[ \beta_y \left( \mu \frac{\partial u}{\partial y} - \overline{\rho u' v'} \right) \right] \\ & - \frac{1}{2} \rho C_D d(y) \frac{u^2}{L^2} \end{aligned} \quad (2.3)$$

and

$$\begin{aligned} \beta_x \rho u \frac{\partial H}{\partial x} + \beta_y \rho v \frac{\partial H}{\partial y} = & \frac{\partial}{\partial y} \left[ \beta_y \left( \frac{K}{C_p} \frac{\partial H}{\partial y} - \overline{\rho v' h'} \right) \right] \\ & + u \frac{\partial}{\partial x} (\beta_x P) + \beta_y \frac{\partial u}{\partial y} \left[ \mu \frac{\partial u}{\partial y} - \overline{\rho u' v'} \right] \\ & + \frac{1}{2} \rho C_D \frac{d(y)}{L^2} u^3 \\ & + \pi \frac{K N u_d}{L^2} (T_R - T) \end{aligned} \quad (2.4)$$

Examination of Eqs. (2.3) and (2.4) shows that empirical models for  $\overline{\rho u' v'}$ ,  $\overline{\rho v' h'}$ , the roughness element drag coefficient  $C_D(y)$ , and the roughness element Nusselt number  $Nu_d(y)$  are necessary for closure.

The blockage parameters  $\beta_x$  and  $\beta_y$  and the element shape descriptor  $d(y)$  require no empirical fluid mechanics input as they are determined solely from the geometry of the rough surface. Taylor et al. have shown for uniform three-dimensional roughness elements with circular cross-section that

$$\beta_x = \beta_y = 1 - \frac{\pi d^2}{4L^2} \quad (2.5)$$

The boundary conditions for the discrete element approach for rough wall flows are identical to those for smooth wall flows. The wall location ( $y = 0$ ) is the smooth surface on which the roughness elements occur. At  $y = 0$ ,  $u = v = 0$  and  $H = H_w$ . As  $y \rightarrow \infty$ ,  $u \rightarrow U_\infty$  and  $H \rightarrow H_\infty$ .

The "wall shear stress" is defined as the sum of the shear and drag forces on the wall in the mean flow direction divided by the plan area of the wall. The corresponding skin friction coefficient is then

$$C_f = \frac{(\beta_y)_w \mu \left. \frac{\partial u}{\partial y} \right|_w + \frac{1}{2} \frac{1}{L^2} \int_0^\infty (\rho d C_D u^2) dy}{\frac{1}{2} \rho_\infty U_\infty^2} \quad (2.6)$$

and the Stanton Number is

$$St = \frac{-(\beta_y)_w \frac{K}{C_p} \left. \frac{\partial H}{\partial y} \right|_w + \frac{\pi}{L^2} \int_0^\infty [K N u_d (T_R - T)] dy}{\rho_\infty U_\infty (H_w - H_{0,\infty})} \quad (2.7)$$

These definitions for  $C_f$  and  $St$  can be formulated from physical reasoning. However, they also arise naturally from Eqs. (2.2) - (2.4) in the formulation of the integral boundary layer equations using the discrete element model.

In order to solve Eqs. (2.2), (2.3) and (2.4), turbulence models for  $-\overline{\rho u'v'}$  and  $-\overline{\rho v'h'}$  and roughness models for  $C_D$  and  $Nu_d$  are required. Because of its wide acceptance and proven predictive capability for boundary layer flows over smooth surfaces, the Prandtl mixing length model with van Driest damping and a constant turbulent Prandtl number is used for turbulence closure. Thus

$$-\overline{\rho u'v'} = \rho \ell_m^2 \left[ \frac{\partial u}{\partial y} \right] \left| \frac{\partial u}{\partial y} \right| \quad (2.8)$$

where

$$\ell_m = 0.40y[1 - \exp(-y^+/26)] ; \ell_m < 0.09\delta \quad (2.9)$$

$$\ell_m = 0.09\delta; \text{ otherwise,} \quad (2.10)$$

and

$$-\overline{\rho v'h'} = \frac{\mu_t}{Pr_t} \frac{\partial H}{\partial y} \quad (2.11)$$

where

$$Pr_t = 0.9 \quad (2.12)$$

Taylor et al. (1984), as did Lin and Bywater (1980), chose to formulate the roughness element  $C_D$  and  $Nu_d$  models as functions of the local element Reynolds number

$$Re_d = u(y)d(y)/\nu \quad (2.13)$$

which includes roughness element size and shape information through  $d(y)$ . The general shape of the drag coefficient and Nusselt number versus Reynolds number curves of Zukauskas (1972) were used as

starting points to determine expressions for  $C_D$  and  $Nu_D$  through comparison with calibration data sets from well-defined rough surfaces. As discussed in Taylor et al. (1984), the  $C_D$  model which gave the best overall agreement was

$$\log C_D = -0.125 \log (Re_D) + 0.375 \quad (2.14)$$

This model has been tested for values of  $Re_D$  up to about 25,000 [Taylor et al. (1984), Scaggs et al. (1988a)] using several data sets, and used unchanged for the predictions discussed here.

As discussed previously, Schlichting investigated several different roughness shapes over a range of spacings and Reynolds numbers. Since this work is concerned with three dimensional roughness elements, only the surfaces roughened with spheres, spherical segments and cones were used in the calibration of the  $C_D$  model. The calculated skin friction coefficients,  $C_f$ , from the discrete element method were compared with the data and were for the most part within 10% of the measured results for 11 of the 14 surfaces. The details of comparisons are given by Taylor et al. (1984).

Chen (1971) reported detailed turbulence and skin friction measurements for air flow through a 0.19 meter diameter pipe roughened with hemispheres. He investigated three roughness densities-- $L/k = 18.5$ ,  $10.7$ , and  $6.4$ . Chen stated that the first two cases ( $L/k = 18.5$  and  $10.7$ ) were in the transitionally rough regime and the third ( $L/k = 6.4$ ) was "nearly" in the fully rough regime. The results of predictions from the discrete element method solved in the appropriate internal circular coordinates were compared with Chen's data. The agreement for  $C_f$  for the first two cases ( $L/k =$

18.5 and 10.7) were very good. For the third case ( $L/k = 6.4$ ) fair agreement was obtained--the maximum disagreement was 15%. As Taylor et al. (1984) explained, the greatest part of this 15% disagreement comes from a disagreement in average velocity and not from the calculated shear stress. For further explanation and comparisons see Taylor et al. (1984).

The discrete element energy transport model requires empirical input in the form of a Nusselt number,  $Nu_d$ . Taylor et al. (1984) developed a  $Nu_d = f(Re_d, Pr)$  model, as with the momentum transport model, using the correlation reported by Zukauskas (1972) for banks of tubes as the starting point. Lin and Bywater (1980) used the same correlations in their works; however, they used the correlations directly rather than as a starting point in a calibration procedure.

Taylor et al. formulated the energy transport model using the correlations of Zukauskas as a starting point, conducted numerical experiments using modified correlations, and then compared the results of these experiments with a calibration data set. They chose the 27 m/s experimental run of Pimenta (1975) on the Stanford surface to calibrate their model. The Stanford data were all taken on a rough surface consisting of spheres in the densest array; therefore, the effective wall location determined for Schlichting's most densely packed spheres was used. This effective wall location was 0.2 sphere diameter below the crests of the spheres. After the numerical experiments, the roughness Nusselt number model that was selected is



$$\begin{aligned} \text{Nu}_d &= 2.475 \text{Re}_d^{0.4} \text{Pr}^{0.36} , & \text{Re}_d < 100 \\ \text{Nu}_d &= 1.403 \text{Re}_d^{0.5} \text{Pr}^{0.37} , & 100 < \text{Re}_d < 1000 \quad ** \\ \text{Nu}_d &= 0.963 \text{Re}_d^{0.6} \text{Pr}^{0.36} , & 1000 < \text{Re}_d \end{aligned}$$

This model was tested only for roughness element Reynolds numbers up to  $\text{Re}_d = 1000$ , using heat transfer data from the single Stanford rough surface.

At this point some remarks are in order. Recall that previously the three regimes of flow over a rough surface were discussed. No mention of these regimes has been made in the discussions concerning the development of either drag coefficient or Nusselt number roughness models used in the discrete element approach. All calculation methods that use the sandgrain roughness approach must take care to distinguish between these regimes, because different models are required for smooth, transitionally rough and fully rough flows. This brings forth the added burden of predetermination of the state of the flow. The discrete element approach does not need to make these distinctions a priori, since such information is implicitly included in the roughness element  $C_D$  and  $\text{Re}_d$  models. Therefore, the discrete element method applies to smooth, transitionally rough and fully rough flows without prior determination of the flow regime.

Since the equivalent sandgrain concept is abandoned in the discrete element approach, the use of roughness Reynolds number for classifications of the flow regimes is no longer useful. Taylor et al. (1984) suggested that the ratio of the apparent shear stress due

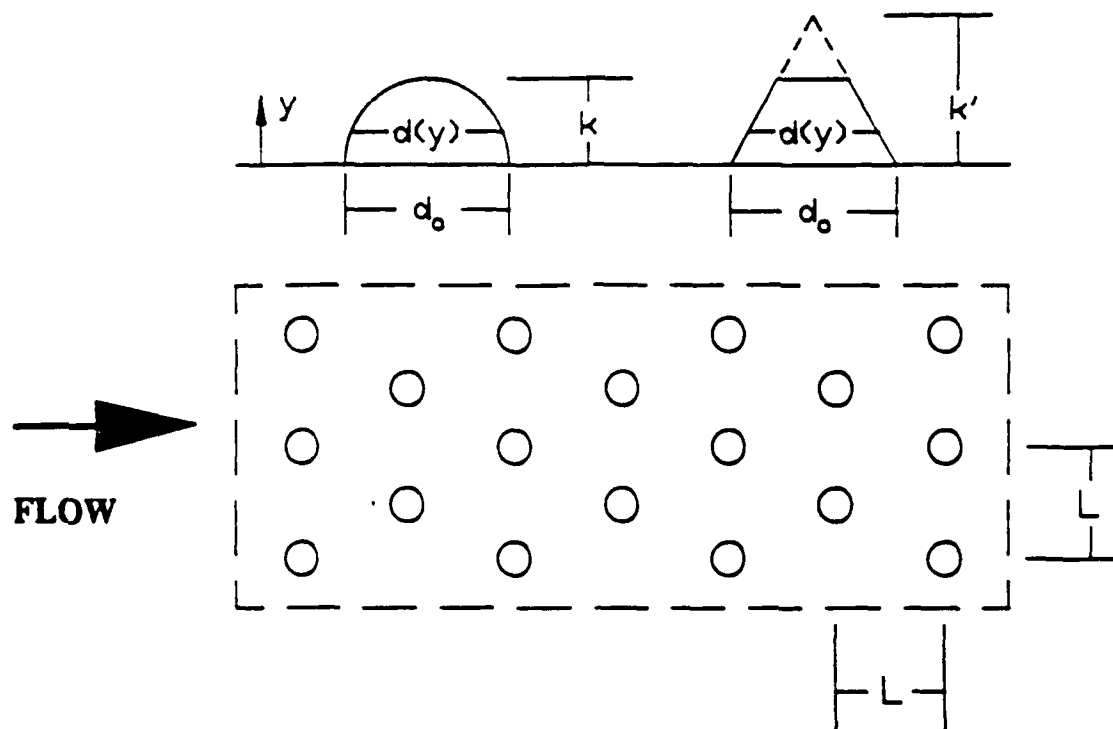
---

\*\* The constant 1.403 has previously been reported incorrectly as 1.043 due to typographical error.

to the roughness elements to the total apparent shear stress ( $R_\tau = \tau_R/\tau_T$ ) as calculated using the discrete element method be used to distinguish aerodynamically smooth, transitionally rough and fully rough regimes. They proposed, based on data available at the time, that

aerodynamically smooth	$R_\tau < 0.05-0.1$
transitionally rough	$0.05-0.1 < R_\tau < 0.80-0.90$
fully rough	$R_\tau > 0.80-0.90$

As discussed previously, Scaggs et al. (1988a) investigated the effects of surface roughness on turbulent pipe flow friction factors using eleven different rough surfaces, nine of which had uniform roughness elements and two of which were roughened nonuniformly. Based on their data, they proposed that a value of  $R_\tau$  about 0.6 might be considered as an appropriate boundary between the transitionally rough and fully rough regimes.



$$d_0 = 1.27 \text{ mm}$$

$$d(k) = 0.21 \text{ mm (for the truncated cone)}$$

$$k = 0.635 \text{ mm}$$

$$k' = 0.76 \text{ mm}$$

## CHAPTER 3

### EXPERIMENTAL APPARATUS AND TECHNIQUES

#### 3.1 OVERVIEW

The Turbulent Heat Transfer Test Facility (THTTF) was constructed for the experimental investigation of heat transfer and fluid dynamics behavior in turbulent boundary layers over rough surfaces. The design of the THTTF was based on the preliminary analysis and design work of Norton (1983). The THTTF is geometrically similar to the test apparatus used in the Stanford University program that investigated turbulent boundary layer flow and heat transfer in flow over a single, porous rough surface with transpiration [Healzer (1974), Pimenta (1975), Coleman (1976), Ligrani (1979)].

The THTTF, shown schematically in Figure 3.1, is a closed loop subsonic wind tunnel designed to deliver a uniform air flow over a set of 24 individually heated flat test plates which are abutted together to form a continuous flat surface. Each plate can be maintained at a constant uniform temperature, and each set of rough plates has a well defined surface roughness. The Stanton number distribution along the test surface is obtained by applying an energy balance to each test plate. Distribution of the local skin friction coefficient along the test surface and boundary layer velocity and turbulence profiles are determined with hot-wire

anemometry. Thermal boundary layer parameters are determined from temperature profiles measured with a thermocouple probe and the appropriate hot-wire data.

Measurement of individual variables such as air velocity and plate temperature, the calibration of the instruments used to measure these variables, the determination of experimental Stanton numbers from these measured variables, and an analysis of the uncertainty associated with these Stanton numbers are presented in Appendix I. The boundary layer probe measurement techniques are described in Appendix II, and the methods of determining local skin friction coefficients are discussed in Appendix III.

### 3.2 DESCRIPTION OF EXPERIMENTAL APPARATUS

Four primary systems comprise the THTTF: (1) the air flow system, (2) the test plate system, (3) the cooling water system, and (4) the Automated Data Acquisition and Control System (ADACS). These are discussed in detail below.

#### 3.2.1 Air Flow System

The air flow system is a closed loop system designed to deliver a uniform velocity (6 to 67 m/s), low turbulence intensity, controlled temperature air flow at the 10.2 by 50.8 cm inlet of the 2.4 m long test section which contains the test surface. These air velocities correspond to an x-Reynolds number range of about one million to ten million at the downstream end of the test section. A Buffalo Forge size 45AW industrial blower is the prime mover for the

air flow system. The blower has a rating of 198 cubic meters of air per minute at 38 cm of water static pressure. An 18.6 kilowatt Dynamatic Model ACM-280 electric motor with an Eaton variable speed eddy current clutch drive system drives the blower with a belt and pulley system. Air velocity in the test section is set using the Eaton eddy clutch controller to control the rotation speed of the blower. The controller can be adjusted and set using a manually adjusted potentiometer or a dc-voltage signal from the ADACS.

Air exiting the blower enters a 1.2 m wide by 0.6 m tall wooden overhead duct which is connected to the blower and header by flexible couplings. The air then turns through the header and passes through a linen cloth filter in the filter box. Next the air passes through an air/water heat exchanger with a 4 row cooling coil. Upon leaving the heat exchanger, the air passes through a 3.8 cm thick aluminum honeycomb with a cell length-to diameter ratio of 6 and then through a series of 4 woven stainless steel screens with an open area-ratio of 0.598 and a wire diameter of 0.136 mm.

Following the screens, the air enters a three-dimensional, 19.8 to 1 contraction ratio fiberglass nozzle with a 84 cm by 122 cm inlet and a 10 cm by 51 cm outlet. The nozzle was designed [Healzer (1974)] to smoothly accelerate the flow without separation at the nozzle inlet or outlet. Uniform velocity air is delivered from the nozzle to the test section inlet. Measurements at freestream air velocities of 12 and 58 m/s indicated the axial velocity at the nozzle exit is uniform within about 0.5%. Freestream turbulence

intensities measured 4 cm downstream of the nozzle exit were less than 0.3% for freestream velocities from 61 m/s down to 6 m/s and less than 0.4% at 3 m/s.

The test section has clear cast acrylic (plexiglass) sidewalls of 1.3 cm thickness and an adjustable, flexible, clear acrylic top of 1.3 cm thickness. The bottom wall is made up of the test plates. Static pressure taps, spaced every 10.2 cm even with the center of each plate in the test surface, are located in one of the sidewalls approximately 2.5 cm above the plates. Access holes for test probes are located along the center of the top wall, centered over each plate, and transversely at strategic locations. The holes are plugged with precision machined acrylic stoppers when probe access is not required.

The flexible upper surface of the test section can be adjusted to maintain the prescribed zero pressure gradient along the flow direction. A Dwyer inclined water manometer with a resolution of 0.06 mm of water was connected to the static pressure taps along the sidewall of the test section to measure the pressure gradient in the flow direction. The difference in static pressure in the test section between all pressure tap locations and that tap located at the second plate was maintained at less than 0.19 mm of water for a velocity of 12 m/s and to less than 0.32 mm of water for a velocity of 43 m/s.

As it exits the test section, the air passes through an adjustable plexiglass diffuser which links the test section to a vaned wooden diffuser. Easily removed screen inserts, which are used to

produce a pressure drop and thus used as a coarse adjustment of the absolute static pressure level in the test section, are located at the entrance of the wooden diffuser. Following the vaned diffuser, the air enters the blower plenum from which it passes through a flexible coupling into the blower intake.

Suction and ejection of air to and from the test section through any small air gaps in the test section were minimized by equalization of the test section static pressure with the ambient pressure. Filtered make-up air to replace the inevitable air leakage from the overhead ducting, filter boxes, and heat exchanger was ducted through a box of adjustable orifices to the blower plenum. Very fine balancing of the test section air static pressure and the ambient pressure, typically to within  $\pm 0.13$  mm of water, was accomplished by adjusting the orifices in the make-up air box.

In order to minimize vibrations, the blower and blower motor, which are the primary sources of mechanical vibrations, are mounted on a massive concrete pad with vibration damping feet. Transfer of mechanical vibrations throughout the THTF has been minimized by the use of non-rigid joints at key locations in the flow path to effectively isolate the test section from vibration sources. Noise from air flowing in the overhead duct, plenum, and header has been reduced by lining these air passages with batt insulation covered by rigid fiberglass insulation board. Blower and blower motor noise have been reduced by housing the blower and motor in vented, insulation-lined boxes.



### 3.2.2 Plate System

A cross sectional view of the test section is shown in Figure 3.2. The test plates are supported on precision straight edges which are thermally isolated from the steel side rails which provide the primary structural support. These side rails are heated and act as guard heaters that help to minimize the conduction heat losses from the plates. A removable, insulated, wooden enclosure around the base of the test section reduces heat loss from the metal support rails to the laboratory environment.

The 24 plates which comprise the test surface are 10.2 cm in the flow direction by 45.7 cm in the transverse direction by 0.95 cm thick. The precision machined test plates are made of electroless nickel plated aluminum. The test plates were manufactured by Hye Precision Products Corp. of Perry, Georgia. The smooth test surfaces were manufactured easily compared with the production of the rough test surfaces, which was complicated, time consuming and costly. Initially, the manufacturer planned to cold form the plates with roughnesses on the surface, but this technique was unsuccessful. After a lengthy development process, efforts at forming plates using heated aluminum blanks and using powdered aluminum were likewise unsuccessful. The next option was to machine the rough plates using a numerically-controlled machine. This procedure required development of a machining scheme and design of a cutter so that a satisfactory surface finish was achieved. After an extensive devel-

opment program, machining of the rough plates was successfully accomplished. Needless to say, the machining of a single rough plate took hours of machining time.

The smooth surface plates used in the baseline tests have a surface finish with centerline average roughness,  $R_a$ , measured as less than 0.5 micrometers. The rough plates with roughness elements 4 base diameters apart have a centerline average roughness measured as less than 1.6 micrometers on the "smooth" wall portion of the plates. The "smooth" portion of the rough plates with roughnesses 10 base diameters apart have a centerline average roughness measured as less than 4.3 micrometers. The surface roughness of the  $L/d_0 = 2$  plates could not be measured because of the physical size of the profilometer; however, visually they appeared to be equal to or better than the  $L/d_0 = 4$  plates. The plates are assembled using dowels to form a continuous and smooth test surface as shown in Figure 3.3. The allowable step (or mismatch) at the joint between two plates is 0.013 mm.

Each plate is instrumented with two thermistors for temperature measurement, and each has its own motor-driven variable voltage transformer/plate heater circuit which is controlled by the ADACS. A flexible resistance heating pad (plate heater) affixed to the bottom of each plate provides a uniform heat flux to the lower plate surface. The plate heaters, which were custom manufactured by Watlow Electric Manufacturing Co., are about one mm thick and are made of resistance wire spiraled around a glass cord sandwiched between two pieces of glass fabric coated with silicone rubber.

All heater circuits are supplied electrical power through the same Powermark-75110 A.C. voltage regulator which is connected to the building service (110 volt) as shown in Figure 3.4. Fine adjustment of the plate heater power is accomplished with a Powerstat-15M21 motor driven variable transformer in each heater circuit. These motor driven transformers are grouped in banks of 8, which are supplied power through 1 of 3 manually set Variac-W10 variable transformers used for gross step-down of the regulated power. Experience in acquiring the heat transfer data has shown that plate temperatures can be held within  $\pm 0.1$  C of a prescribed constant temperature boundary condition along the entire test section.

### 3.2.3 Cooling Water System

The cooling water system maintains the test air at a constant temperature by extracting energy added by the heated plates and blower. Cool water from a 568 liter water storage tank is moved by a 186 watt Bell & Gossett Model 1522 pump through 5 cm PVC piping to a Trane air/water heat exchanger. The heat exchanger has 4 rows (in the flow direction) of finned cooling coils with a 84 cm by 112 cm area normal to the flow direction. Heat from the test air is transferred to the cooling water via the cooling coils before the air enters the nozzle and then the test section. Proportional amounts of warmer water returning from the cooling coils to the storage tank can be dumped into a floor drain through a 1.9 cm motorized ballvalve, GF-Type 105. This ballvalve may be adjusted and con-

trolled manually or by the ADACS. Water level in the storage tank is maintained at a desired level with make-up cooling water dispensed through adjustable depth sensing valves fed by the building supply.

#### 3.2.4 Data Acquisition System

A Hewlett-Packard Series 9000 Model-220 microcomputer and a Hewlett-Packard 3054A Automatic Data Acquisition and Control System are used to monitor and control the THTTF. The ADACS includes an HP-3437A high speed system voltmeter, an HP-3456A high resolution digital voltmeter, an HP-3497A data acquisition/control unit and a number of special function plug-in assemblies. A detailed discussion of the ADACS and its use in the THTTF is given by Suryanarayana (1986).

Transducers that monitor the THTTF are wired into the ADACS, which relays the information to the microcomputer. The microcomputer digests the operating condition information, decides on the proper response based on programming, and sends commands for the proper controller response to the ADACS. The ADACS can control the rail heaters, plate heaters, cooling system dump valve, and blower motor in response to instructions from the microcomputer. When the THTTF has been brought to the desired equilibrium conditions, the computer directs the ADACS to perform the necessary data collection.

### 3.3 MEASUREMENT TECHNIQUES

The measurement techniques for determination of Stanton number and skin friction coefficient distributions and profiles of velocity, turbulence quantities, and temperatures are discussed below.

#### 3.3.1 Stanton Number Determination

The data reduction expression for the Stanton number is obtained by applying an energy balance to each test plate. The expression is

$$St = \frac{W - q_r - q_c}{A\rho C_p U_\infty (T_w - T_o)} \quad (3.1)$$

The plate heater power,  $W$ , is measured with a precision wattmeter. The radiation heat loss rate,  $q_r$ , is estimated by using a gray body enclosure model. In this model, the emissivity,  $\epsilon$ , of the plates is estimated at 0.11. The conductive heat loss rate,  $q_c$ , is calculated using an experimentally determined overall conductance,  $(UA)_{eff}$ , between the test plates and the side rails which support them. These conduction losses are minimized by insulating underneath the test plates and by heating the side support rails. The density and specific heat of the freestream air are determined from moist air property data using measurements of barometric pressure and wet and dry bulb temperatures in the THTTF test section. The freestream velocity is determined with a Pitot probe, and specially calibrated thermistors are used to measure the temperatures. The freestream total temperature  $T_o$ , is calculated using a recovery factor of  $r = 0.86$  for the freestream thermistor probe. The derivation of the

Stanton number data reduction expression from an energy balance on a test plate and the details on determination of each of the variables used are presented in Appendix I.

The uncertainty analysis of the Stanton number is based on the ANSI/ASME Standard on Measurement Uncertainty (1986), following the procedures of Coleman and Steele (1989). The bias limits for all thirteen variables involved in the calculations of Stanton numbers were estimated and are presented in the Appendix I. Because all thermistors used in the experimental Stanton number determination were calibrated against the same standard, some elemental contributions to the bias limits were correlated. The effects of correlated biases were to reduce the overall uncertainty in the Stanton number. The correlated biases were also accounted for in the uncertainty analysis.

As discussed in Appendix I, a detailed uncertainty analysis of the determination of Stanton numbers using the THTTF was made during the design and construction phase of the test facility. This analysis showed that the precision limits corresponding to the measured variables were negligible relative to the bias limits. This meant that replications of Stanton number at a given experimental set point ( $U_\infty$ ) should show negligible scatter, since any significant errors were estimated to be bias errors that would be the same in all replications. The Stanton numbers for smooth wall runs at  $U_\infty = 12$  m/s and the rough wall runs at 6 m/s showed a small but noticeable scatter and the estimate of zero precision limit (no scatter) for these runs was not valid. Investigation showed that at low

freestream velocities-- $U_{\infty} \leq 12$  m/s for the smooth wall tests and  $U_{\infty} \leq 6$  m/s for the rough wall tests--the heat transfer coefficients are relatively low and the time constant of the THTF is thus increased. At these conditions the time constant of the THTF is large enough so that the relatively long period variations in facility line voltage to the test plate heater circuits and the temperature of the incoming make-up water for the heat exchanger loop affect the ability to hold a tight steady state condition. These unexpected annoyances were not accounted for in the uncertainty analysis during the design phase. Observations of the Stanton number results for eight smooth wall runs and three rough wall runs produced a 95 percent confidence estimate of a precision limit in Stanton numbers of 3 percent for these conditions. The 3 percent precision limit contribution was combined by root-sum-square with the estimated bias limit to obtain the overall uncertainty in Stanton numbers.

The Stanton number data reduction program which incorporates the numerical uncertainty calculation scheme suggested by Coleman and Steele (1989) is described in Coleman et al. (1988).

### 3.3.2 Skin Friction Coefficient Determination

All friction coefficient determinations for rough walls were performed using hot-wire anemometry. Distributions of the local skin friction coefficient along the smooth wall test surface were determined with both hot-wire anemometry and the Preston tube method.

For the hot-wire anemometry technique, both a horizontal hot-wire and slant hot-wire were used. The horizontal hot-wire was used to measure the profiles of mean velocity and the fluctuating longitudinal velocity component ( $\overline{u'^2}$ ). The slant hot-wire was used to determine the Reynolds shear stress ( $\overline{u'v'}$ ). The local skin friction coefficient was determined using the measured quantities and continuity and momentum equations integrated from the plate surface to a position  $Y_1$  in the boundary layer as discussed in detail in Appendix III.

The method of Preston (1954) for determining the local skin friction coefficient in turbulent boundary layer flows depends upon the assumption of a universal inner law (law of the wall) common to smooth wall boundary layers. A simple Pitot tube (Preston tube) resting on the surface was used to measure the local total pressure. The difference between the total pressure at the Preston tube and the static pressure at a pressure tap in the test section sidewall at the same x-location was measured and used in conjunction with the calibration equations as given by Patel (1965) to solve for the local skin friction. The details of this technique are given in Appendix III.

### 3.3.3 Profile Measurements

The measurement procedures for profiles of mean velocity, turbulence quantities, and mean temperature are:



A) Mean Velocity:

The profiles of mean velocity were taken with the horizontal hot-wire. The horizontal wire was aligned with the flow in the freestream using the probe holder etched marks. Once the freestream velocity was measured, the probe was lowered to a known height above the test plate surface very close to the wall which was used as a starting point for traversing of the boundary layer velocity profile. The position of the starting point was dictated by the height of the keel (wall stop) which was used to prevent the horizontal hot-wire from hitting the wall. Traversing of the boundary layer velocity profile began with the probe starting just above the wall and moving upward. At each measurement position, 1000 instantaneous anemometer output voltage readings 0.01 seconds apart were taken and were converted into velocities using a fourth order least squares calibration equation. The mean of the 1000 computed velocities was used as the mean velocity at that location. Measurements were typically taken at every 1-2% of the normalized velocity ( $u/U_\infty$ ) in the inner region of the boundary layer and every 2-4% of the normalized velocity in the outer region.

B) Turbulence Quantities:

Measurements of the fluctuating longitudinal velocity component ( $\overline{u'^2}$ ) were made with the horizontal hot-wire in parallel with the mean velocity measurement described above. The longitudinal velocity fluctuation ( $\overline{u'^2}$ ) was taken as the square of the standard deviation (the variance) of the 1000 computed velocities.

The slant wire was used to determine the Reynolds shear stress factor ( $\overline{u'v'}$ ), the normal velocity fluctuation ( $\overline{v'^2}$ ), and the transverse velocity fluctuation ( $\overline{w'^2}$ ). The slant wire was mounted on the rotatable spindle of the probe holder with its prongs parallel to the mean flow direction at any angle of rotation. The spindle was rotated by a cable drive, which could be operated with the probe in the tunnel.

To determine  $\overline{v'^2}$ ,  $\overline{w'^2}$ , and  $\overline{u'v'}$ , the slant wire was positioned approximately 3.3 mm above the surface of the smooth plate (or 4 mm above the smooth surface of the rough plate) and measurements were made at three probe rotation angles  $\theta=45, 90$ , and  $135$ . At each probe rotation angle 4000 instantaneous anemometer output voltage readings 0.025 seconds apart were taken and used to compute 4000 corresponding effective velocities ( $u_{eff}$ ). A fourth order least squares calibration correlation was used to convert anemometer voltages into effective velocities. The fluctuating component of the effective velocity ( $\overline{u'_{eff}^2}$ ) at each rotation angle was taken as the square of the standard deviation (the variance) of the 4000 computed effective velocities. Experience showed that this many readings taken over the 100 second time period provided stable averages.

The values of  $\overline{u'_{eff}^2}$  at the three slant wire orientations were used in conjunction with the value of  $\overline{u'^2}$  from the horizontal wire measurements at the same y-position to solve a system of three linear equations for  $\overline{v'^2}$ ,  $\overline{w'^2}$  and  $\overline{u'v'}$ .

C) Mean Temperature:

The profiles of time mean temperature in the boundary layer were taken using a type E (chromel-constantan) thermocouple probe. The output of the thermocouple in millivolts was measured by the ADACS and was converted to temperature at each probe location using the HP system software package. The probe alignment with the flow and the probe traversing procedure were analogous to the methods used for the hot-wire probe discussed previously. The details of calibrations and boundary layer probe measurements are given in Appendix II.

### 3.4 SUMMARY OF SMOOTH WALL THTTF QUALIFICATION

The Turbulent Heat Transfer Test Facility (THTTF) was designed to provide quality heat transfer data primarily for zero pressure gradient, constant wall temperature, incompressible flow over flat plates with various surface roughnesses. To produce quality convective heat transfer data, the THTTF must produce flows with properties within acceptable fluid dynamics and heat transfer bounds, and the techniques used in collection of the data must be proven. The discussion in this section is intended to briefly show that the THTTF is operating within acceptable fluid dynamics and heat transfer bounds and to document the validity of the instrumentation, data collection and data reduction procedures. This objective is met by comparing the smooth wall fluid dynamics and heat transfer data obtained in the THTTF with previously published, well accepted

smooth wall results of others. The comparisons summarized in this section are for zero pressure gradient, incompressible turbulent boundary flow over a smooth surface.

The momentum thickness ( $\delta_2$ ) of a boundary layer accounts for the upstream history of the flow to a considerable degree. Thus, skin friction data from the THTF are compared with an accepted skin friction correlation based on the momentum thickness Reynolds number ( $Re_{\delta_2}$ ). For zero pressure gradient, incompressible flow over smooth flat plates, Kays and Crawford (1980) recommend

$$C_f/2 = 0.0125 (Re_{\delta_2})^{-0.25} \quad (3.2)$$

Figure 3.5 shows the skin friction coefficient distributions determined by both the hot-wire anemometry and Preston tube methods versus the Reynolds number based on the momentum thickness computed from the measured momentum thickness at each profile station and also Eq. (3.2) with a  $\pm 10\%$  range indicated. The comparison shows that essentially all of the data agrees with Eq. (3.2) within the  $\pm 10\%$  band.

Based on this comparison, it was concluded that the local skin friction coefficient data from the THTF is in substantial agreement with the smooth wall skin friction correlation and that the facility and measurement techniques are performing correctly for skin friction measurements. In particular, the scatter in the skin friction coefficient data determined with hot-wire anemometry fall essentially within the  $\pm 10\%$  bands about the accepted correlation. This is especially encouraging, since this is the sole technique used in

this research program to determine skin friction coefficients in rough surface flows. It also serves as a verification check on the estimated 10 to 12% uncertainty in  $C_f$  from the hot-wire method.

Stanton numbers were determined from energy balances on each test plate, as described in detail in Appendix I. The THTF data are presented using a definition of the Stanton number which is based on the difference between the wall temperature and the free-stream total temperature. Other data with which comparisons are made are based on a definition of the Stanton number which uses the difference between the wall temperature and the freestream recovery temperature. This difference in Stanton number definitions is negligible in the comparisons made because the differences in the total and recovery temperatures are numerically insignificant for the range of air velocities considered by the previous experimenters.

The definitive data sets for zero pressure gradient, constant wall temperature, incompressible turbulent boundary layer flow over smooth flat plates are those of Reynolds, Kays and Kline (1958). In fact, these are the only widely referenced data for all heat transfer correlations for these conditions. They are the only data quoted, for example, by Kays and Crawford (1980) and Rohsenow and Hartnett (1973).

Figure 3.6 shows a plot of these data (with no variable property corrections) along with the correlation

$$St = 0.185 (\log_{10} Re_x)^{-2.584} Pr^{-0.4} \quad (3.3)$$

and  $\pm 5\%$  bands. A Prandtl number of 0.713 was used in the correlation, which is based on the analogy  $StPr^{0.4} = C_f/2$  and uses the Schultz-Grunow expression

$$C_f/2 = 0.185 (\log_{10} Re_x)^{-2.584} \quad (3.4)$$

for  $C_f/2$ . Most of the data scatter within the  $\pm 5\%$  range. These data represent 8 individual runs with freestream velocities ranging from 14 m/s to 39 m/s and with  $Re_x$  up to 3.5 million. The comparison demonstrates that Eq. (3.3) is a reasonable representation of the existing smooth wall, constant temperature, zero pressure gradient Stanton number data and the data scatter within approximately  $\pm 5\%$  of this correlation. Therefore, if the THTTF data with their associated uncertainties of about 2 to 5% are within the  $\pm 5\%$  interval about Eq. (3.3), it can be concluded that a successful comparison has been achieved at the Nth order replication level [Moffat (1988), Coleman and Steele (1989)] and that the qualification has been proven.

Shown in Figure 3.7 are the Stanton data at freestream velocities of 12, 27, 43, 58 and 67 m/s plotted along with the 95% confidence uncertainty interval for representative data points. These data are compared with Eq. (3.3) and its  $\pm 5\%$  interval, and the comparison shows the excellent agreement which is obtained. This comparison validates the qualification of the THTTF for Stanton number measurements.

The present data sets extend to a larger Reynolds number than the previous data ( $Re_x = 1 \times 10^7$  versus  $3.5 \times 10^6$ ). An extensive survey of the literature revealed no flat plate Stanton number data

for  $x$ -Reynolds numbers above 3.5 million for incompressible flows. In the present work the experimental Stanton number range has been essentially tripled up to  $x$ -Reynolds numbers of 10 million. It can be seen that Eq. (3.3) represents the data well over the entire range.

Additional THTTF fluid dynamics and heat transfer qualification tests were performed to insure that the other flow properties were within acceptable bounds. Fluid dynamics variables including profiles of mean velocity and Reynolds stresses were determined, temperature profiles were taken, and these were compared with accepted correlations and data obtained on other test facilities which have generated definitive, accepted data. Profiles of mean temperature and velocity were in good agreement with the usual "laws-of-the-wall". All other comparisons were favorable and provided additional confidence in the qualification of the THTTF. The extensive results of smooth wall THTTF qualifications are presented in detail by Coleman et al. (1988).

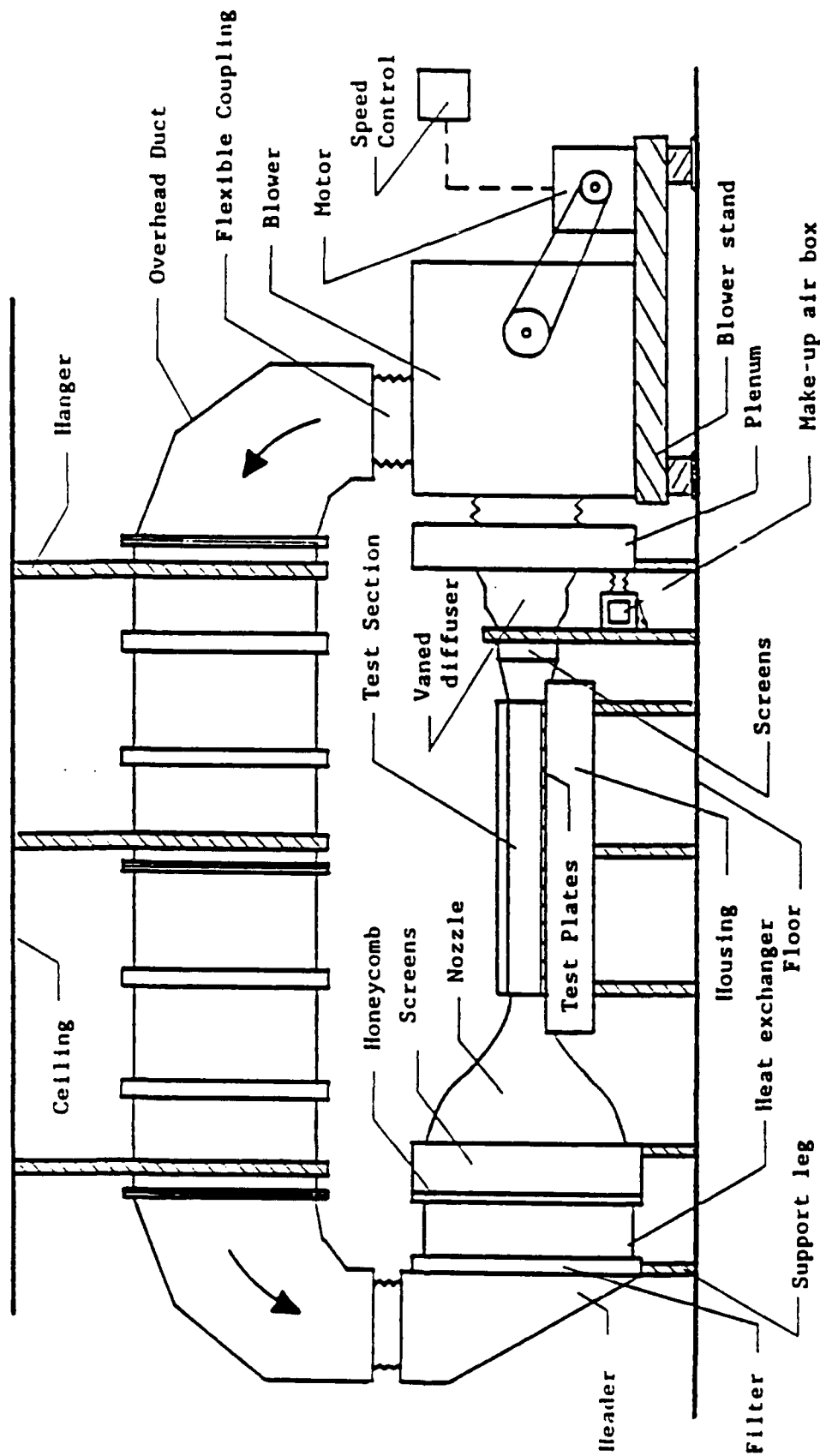


Figure 3.1 Schematic of the Turbulent Heat Transfer Test Facility (THETF).



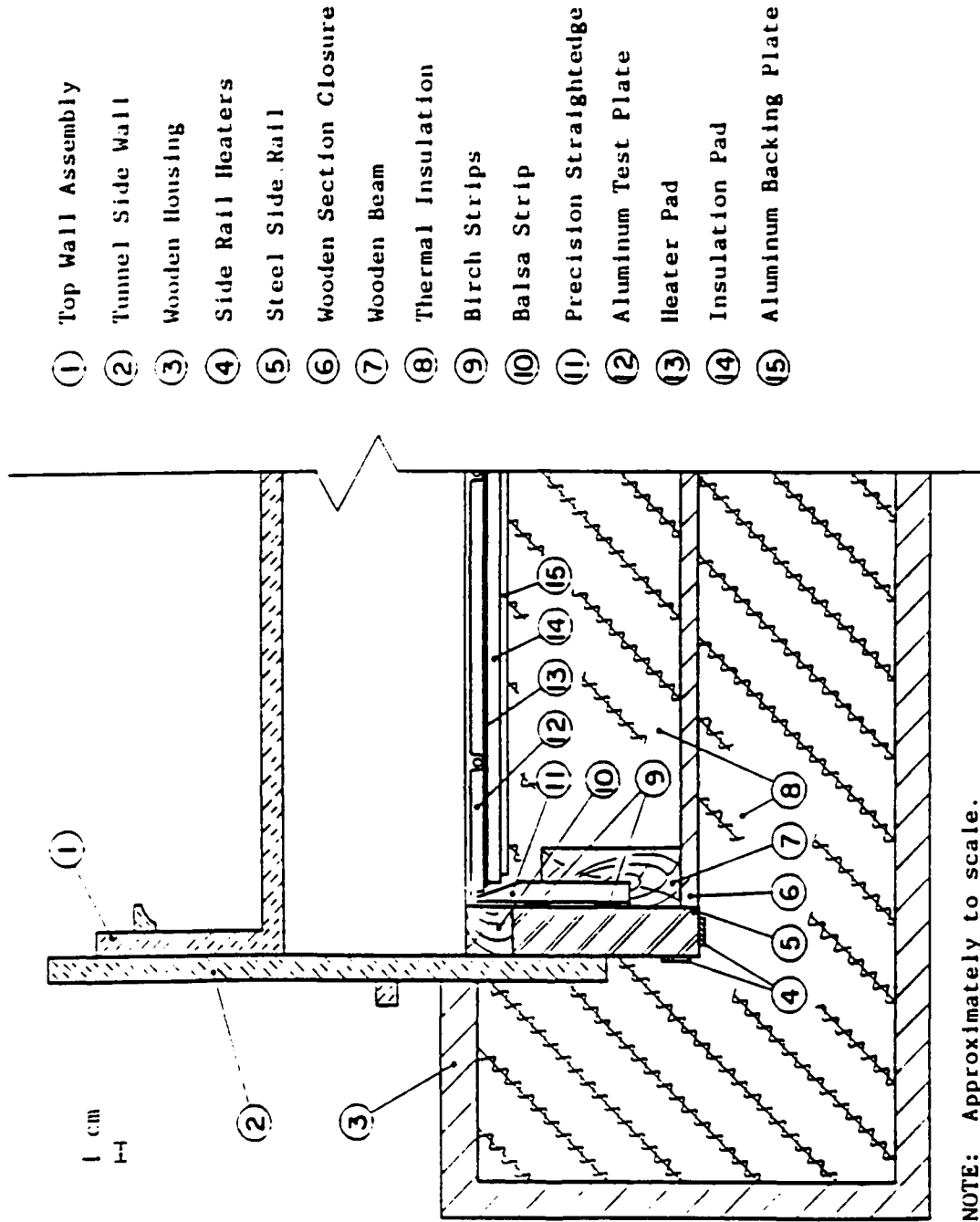


Figure 3.2 Cross section of the THTF test section.

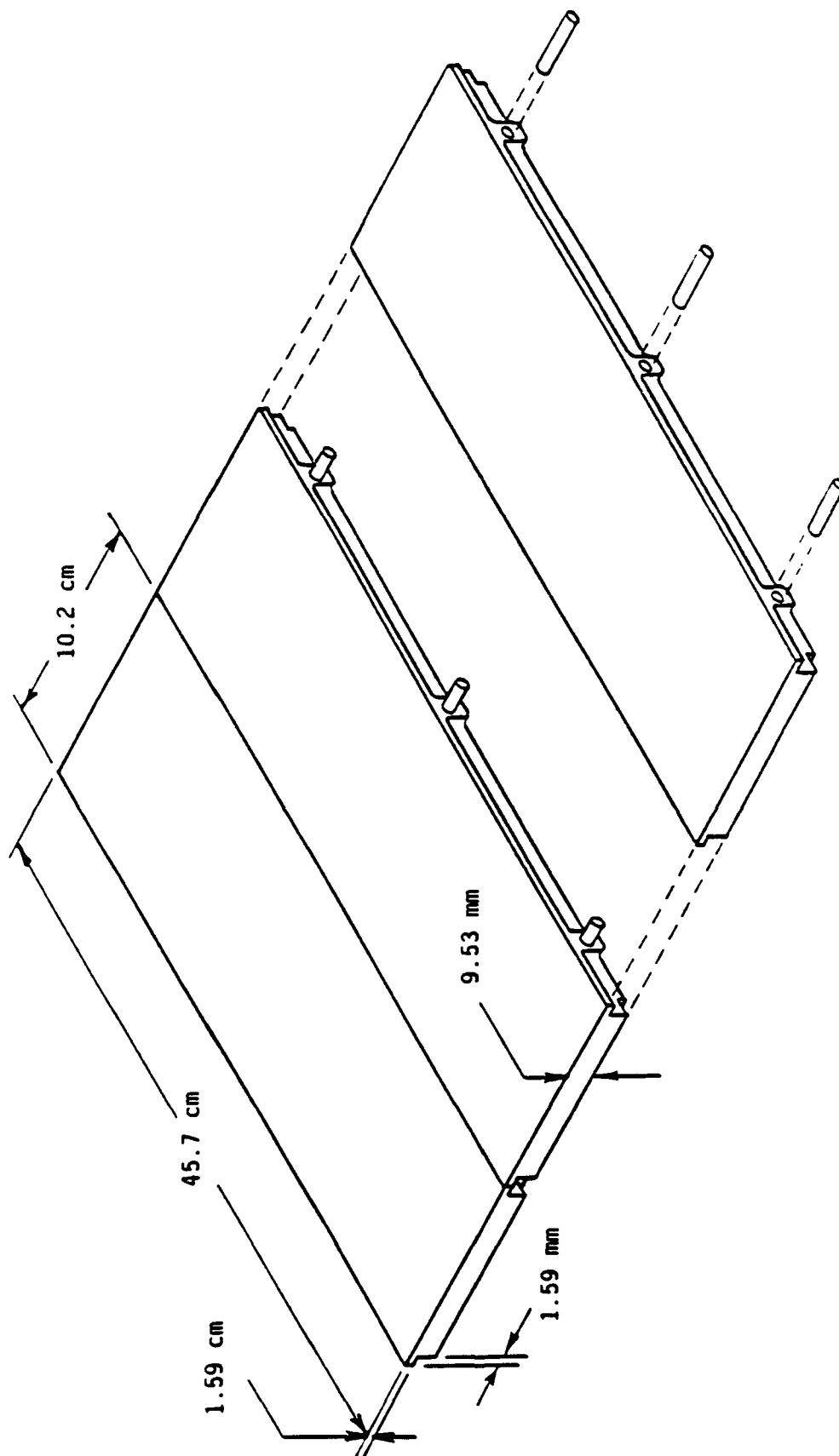


Figure 3.3 Test surface assembly.

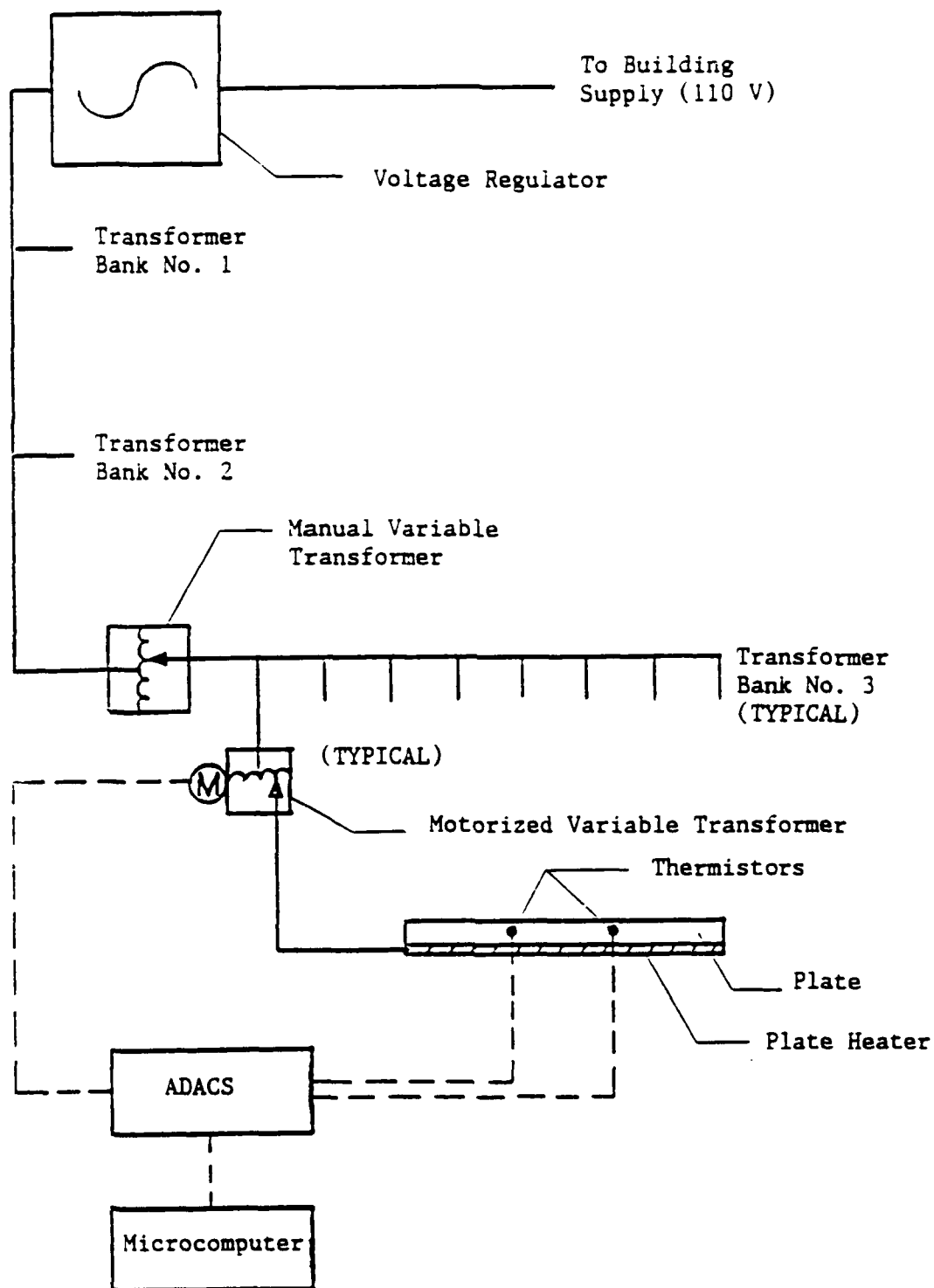


Figure 3.4 Schematic of the plate heater power circuit and control loop.

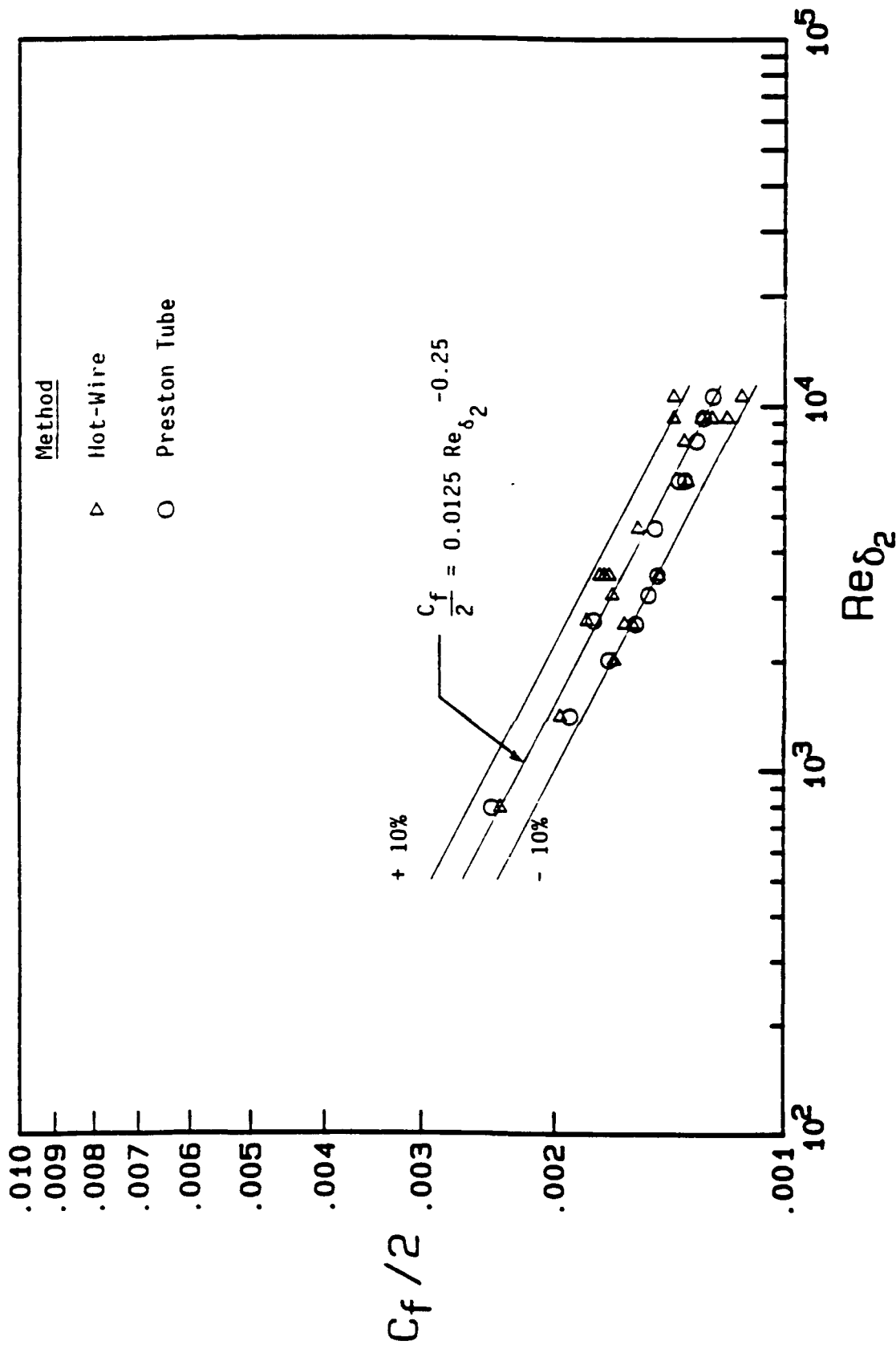


Figure 3.5 Composite plot of the smooth wall skin friction coefficient distributions compared with the  $Re_{\delta_2}$  correlation (Eq. 3.2).

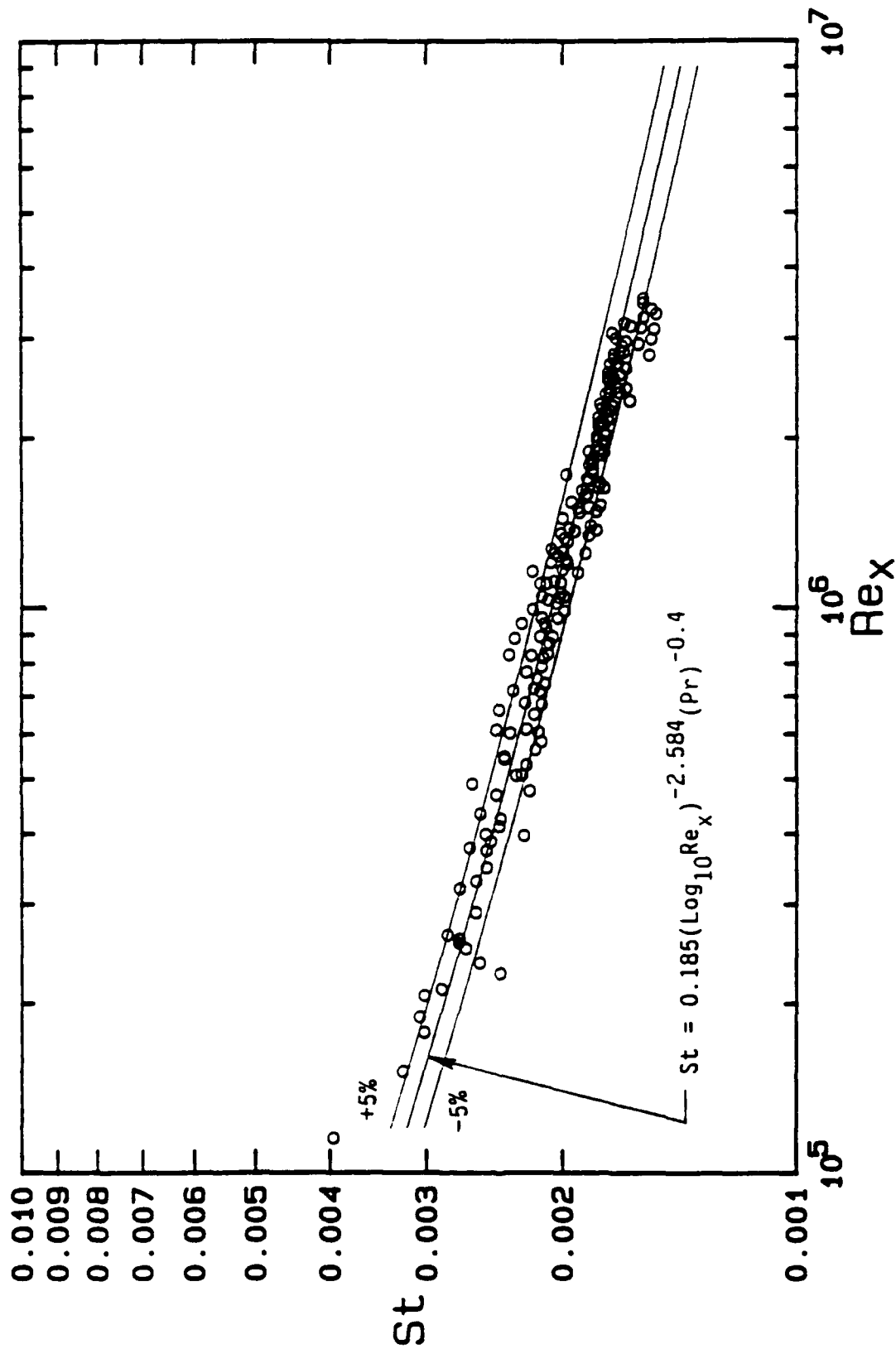


Figure 3.6 Stanton number data of Reynolds, Kays and Kline (1958) compared with the  $Re_x$  correlation (Eq. 3.3).

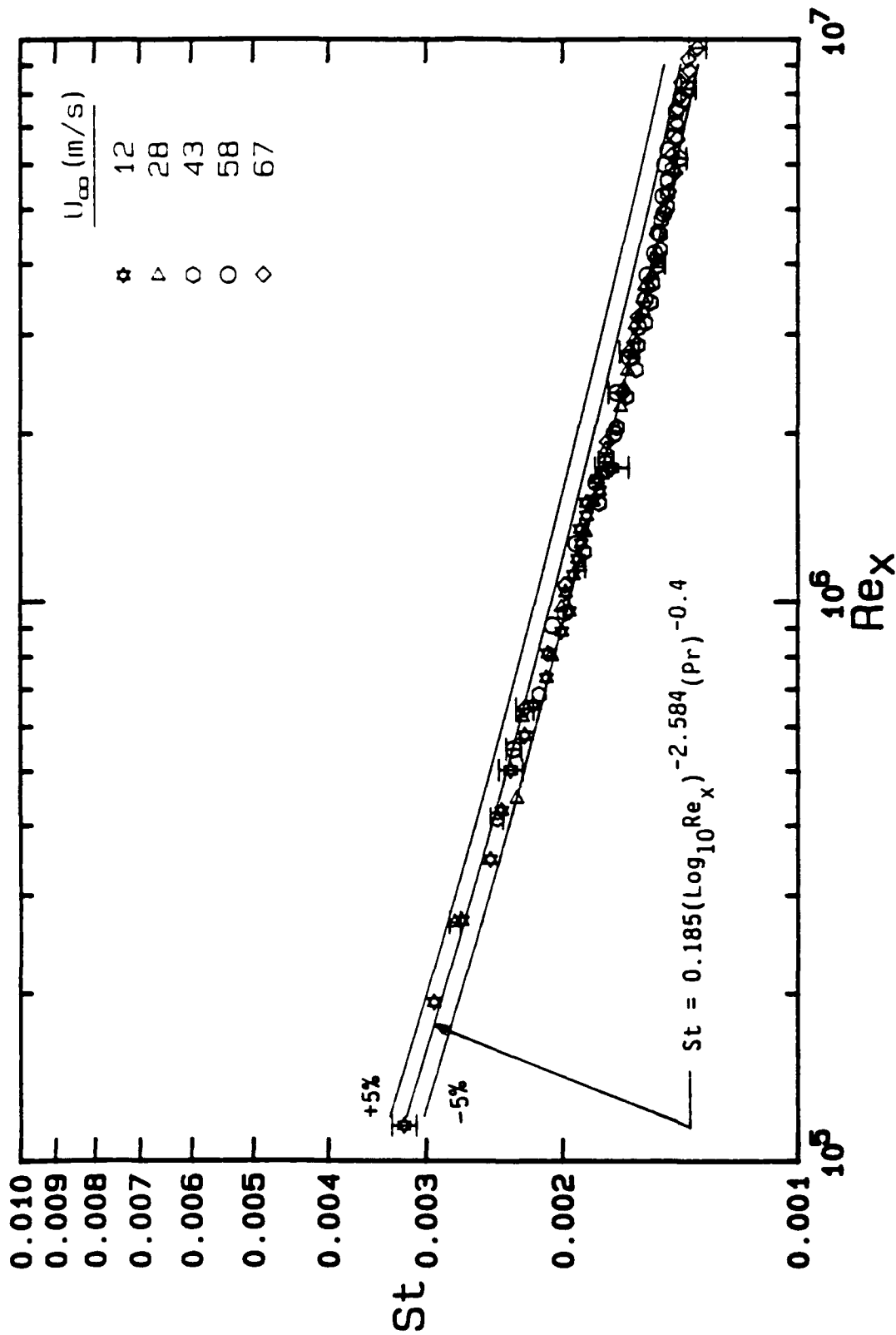


Figure 3.7 Comparison of the THTF smooth wall Stanton number data with the  $Re_x$  correlation (Eq. 3.3).

## CHAPTER 4

### FLUID DYNAMICS RESULTS (Hemispherical Elements)

The primary purpose of the Turbulent Heat Transfer Test Facility (THTTF) is to provide quality heat transfer data for zero pressure gradient, constant wall temperature, incompressible flow of air over flat test plates without transpiration. To produce quality convective heat transfer data on the THTTF, the THTTF must produce flows with properties within acceptable fluid dynamics bounds, and the techniques used in the collection of the fluid dynamics data must be proven correct. In Chapter 3, it was shown that the THTTF is operating within acceptable fluid dynamics bounds, and the correctness of the instrumentation, data collection and data reduction procedures were established using the smooth wall data obtained from the THTTF.

The smooth wall results form the baseline data for comparisons and discussions on the characteristics of rough wall turbulent boundary layer flows. Since the absolute levels of turbulence quantities from different experimental facilities and measurement systems may not be the same, a unique feature of the THTTF is that the freestream conditions, the operational procedures, the data collection and data reduction techniques, and the other parameters inherent to the equipment are preserved. Thus, the turbulent boundary layers over five well-defined rough surfaces and a smooth surface are investigated using the same instrumentation, data col-

lection and data reduction procedures. This is particularly important since the performance and structural features of turbulent boundary layers over deterministic rough surfaces can be contrasted to those for the smooth surface under otherwise equivalent conditions.

This chapter presents the experimental fluid dynamics results obtained in the boundary layer over the three surfaces roughened with hemispheres. Some of the more important rough wall profiles are contrasted with the THTF smooth wall cases. In addition, the transitionally rough and fully rough flow regimes are discussed. The rough surfaces were manufactured as discussed previously by machining arrays of hemispheres on otherwise smooth aluminum plates. The rough surfaces were composed of 1.27 mm diameter hemispheres spaced 2 diameters ( $L/d_0 = 2$ ), 4 diameters ( $L/d_0 = 4$ ) and 10 diameters ( $L/d_0 = 10$ ) apart, respectively, in staggered arrays as in Figure 2.1. All experimental fluid dynamics results presented are for zero pressure gradient, isothermal, incompressible boundary layer flow of air.

Profiles of mean velocity and the Reynolds stress quantities  $\overline{u'^2}$ ,  $\overline{v'^2}$ ,  $\overline{w'^2}$ , and  $\overline{u'v'}$  were measured with a horizontal hot-wire and a slanted hot-wire using the techniques discussed in Appendices II and III. The boundary layer thickness, the momentum thickness, and the skin friction coefficient distribution along each rough surface were also obtained.



#### 4.1 BOUNDARY LAYER MEAN VELOCITY DATA

Boundary layer velocity profiles and boundary layer integral parameters such as the boundary layer thickness ( $\delta$ ), the displacement thickness ( $\delta_1$ ), and the momentum thickness ( $\delta_2$ ) were obtained for the three rough surfaces at nominal freestream velocities of 6, 12, 28, 43, and 58 m/s. The characteristics of a flow close to a rough surface are expected to be affected by the roughness shape, size and spacing.

Boundary layer mean profiles taken with the horizontal hot-wire at a nominal freestream velocity of 12 m/s for the rough surfaces and the smooth surface are shown in Figure 4.1 plotted in  $u/U_\infty$  vs.  $y/\delta$  coordinates. This figure shows that the normalized velocity profiles for the rough surface with roughness elements distributed 10 base diameters apart ( $L/d_0 = 10$ ) and the smooth surface are equivalent. However, the near-wall velocity defect increases for each rough wall as the surface becomes rougher. The smooth wall case has the steepest near-wall velocity gradient compared with the rough walls, as expected. The corresponding inner variable ( $u^+$  vs.  $y^+$ ) velocity profile plot is shown in Figure 4.2. The friction velocity used in  $u^+$  and  $y^+$  for each profile was that determined by the hot-wire method for corresponding surfaces. This figure shows the distinct velocity shift between the smooth and the rough surfaces. A similar plot of data for 58 m/s runs showed that the trend of the velocity shifts were the same as for the 12 m/s runs shown in Figure 4.2.

Some comments concerning the use of the inner coordinates ( $u^+$  vs.  $y^+$ ) for velocity profiles over rough surfaces are in order at this point. We know that for turbulent flow over a smooth surface, the outer region length and velocity scales are  $\delta$  and  $u^*$  and viscosity effects are small. However, in the near-wall region viscosity becomes important and scales such as  $u^+$  and  $y^+$  are used for presenting smooth wall profiles. Although inner variables are mostly used for presentation of smooth wall profiles, their use for presenting rough wall data in Figure 4.2 was considered a logical choice in contrasting the velocity profiles for rough walls to the smooth wall case. This point was brought up here since the use of  $y^+$  for presentation of rough wall profiles sometimes is questioned. Pimenta (1975) has argued that the use of the  $y^+$  coordinate in presenting rough wall profiles implies a dependence of the profiles on the kinematic viscosity and that the fully rough cases do not depend on the viscosity. It should be emphasized that viscosity is a property of a flowing fluid and does play an important role in the aerodynamically smooth and transitionally rough flow regimes. However, despite its lessened significance in fully rough regimes, it is used in this work.

Pimenta (1975) concluded for his surface that the rough wall skin friction coefficients for fully rough regimes were dependent only on the momentum thickness and suggested that the  $y/\delta_2$  coordinate is more appropriate than  $y^+$  for presentation of fully rough velocity profiles. The  $u/U_\infty$  vs.  $y/\delta_2$  coordinates are used in Figure 4.3 to show the behaviors of different rough surfaces as compared

with the smooth wall case for the freestream velocity of 12 m/s. This figure shows that scaling on the momentum thickness alone is not sufficient to produce similar mean velocity profiles for different rough surfaces. These coordinates were also used to plot the profile data taken on the above surfaces at a nominal freestream velocity of 43 m/s. The behavior of the velocity profiles for 43 m/s were identical to 12 m/s runs with no distinguishable differences in these coordinates indicative of the differences between the fully rough and transitionally rough flow regimes.

Figures 4.4, 4.5, and 4.6 show the velocity profiles at nominal freestream velocities of 6, 12, 28, 43, and 58 m/s plotted in  $u/U_\infty$  versus  $y/\delta_2$  coordinates for the rough surfaces. These figures show that in these coordinates the velocity profiles for the same rough surface are essentially independent of freestream velocity and, consequently, of roughness flow regimes.

## 4.2 BOUNDARY LAYER INTEGRAL PARAMETERS

The boundary layer thickness,  $\delta$ , was taken as the distance above the plate at which the boundary layer velocity was within 1 percent of the freestream velocity. A fourth order interpolation polynomial was applied to the velocity profile data obtained with the horizontal hot-wire to determine the boundary layer thickness at each profile station.

Figure 4.7 contrasts the behavior of boundary layer thickness with increasing velocity for the smooth surface to the rough surfaces. For zero pressure gradient boundary layer flow over a smooth

surface, the boundary layer thickness, at a fixed distance  $x$  from the origin, decreases as the freestream velocity increases. However, the boundary layer over a rough surface is influenced by additional factors such as the size, shape and density of the roughness elements. As the freestream velocity is increased, the flow regime may move from aerodynamically smooth to transitionally rough or even to fully rough. In such a case, the boundary layer thickness is initially mostly controlled by the viscosity, then viscosity and roughness, and then roughness, respectively. For the fully rough flow regime, the viscous sublayer is totally destroyed and the dependence on the viscosity is insignificant. In contrast to smooth surface behavior, the rough wall boundary layer thickness, at a fixed distance  $x$  from the origin, increases as the freestream velocity is increased until the flow regime is fully rough. For the fully rough state, the change in boundary layer thickness with increases in velocity becomes insignificant.

Figure 4.7 also contrasts the increase in the boundary layer thickness for the smooth surface to the rough surfaces. As shown, the boundary layer thickness for the smooth surface at plate 17 ( $x = 1.68$  m) for the freestream velocity of 43 m/s is about 2.72 cm. The thickness of the boundary layer at the same location and velocity for the  $L/d_0 = 2$  rough surface is about 4.67 cm. This is an increase of 73% in the thickness of the boundary layer between the rough ( $L/d_0 = 2$ ) and smooth wall cases.

The boundary layer displacement thickness at each profile station was determined from numerical integration of the incompressible flow displacement thickness definition using mean velocity profile data obtained with the horizontal hot-wire,

$$\delta_1 = \int_0^{\infty} \left[ 1 - \frac{u}{U_{\infty}} \right] dy \quad (4.1)$$

Similarly, boundary layer momentum thickness was determined by numerical integration of the definition for the incompressible flow momentum thickness using mean velocity profile data

$$\delta_2 = \int_0^{\infty} \frac{u}{U_{\infty}} \left[ 1 - \frac{u}{U_{\infty}} \right] dy \quad (4.2)$$

The trend in the boundary layer momentum thickness as the freestream velocity is increased, at a fixed distance  $x$  from the origin, is similar to that of boundary layer thickness, as expected. Figure 4.8 contrasts the behavior of momentum thickness with increasing velocity for the smooth surface to the rough surfaces. As shown, the smooth wall momentum thickness at a fixed  $x$  position decreases as the freestream velocity is increased. However, the momentum thickness for rough walls at a fixed  $x$  location increases as the freestream velocity is increased until the fully rough flow regime is obtained and remains mostly unchanged thereafter.

#### 4.3 BOUNDARY LAYER TURBULENCE QUANTITIES

##### 4.3.1 Profiles of Axial Turbulence Intensity

Profiles of the axial turbulence intensity through the boundary layer were determined with a horizontal hot-wire at various stations along the length of the test section as discussed in Appendix II.

Axial turbulence intensity profiles for the smooth surface were taken at various locations for different freestream velocities during the THTTF qualifications. These data were compared with the axial turbulence data of Klebanoff (1955) and Laufer (1954), and the accuracy of smooth wall data taken in the THTTF was established by Coleman et al. (1988). The smooth wall profiles of the axial turbulence through the boundary layer over plates 15, 19, and 23 plotted versus  $y/\delta$  are shown in Figure 4.9 for a nominal freestream velocity of 12 m/s. The three profiles collapse together and show a sharp peak near the wall, which is typical behavior of smooth wall profiles.

Figures 4.10, 4.11, and 4.12 show axial turbulence profiles normalized by  $u^*$  for the three rough plates at a nominal freestream velocity of 12 m/s contrasted to the smooth wall distribution. As shown in Figure 4.10, the axial turbulence intensity for the smooth and the rough wall with roughness elements distributed 10 base diameters apart ( $L/d_0 = 10$ ) follow the same trend, with this rough wall profile exhibiting a sharp near-wall peak similar to the smooth wall profile. However, as the surface becomes rougher, the near-wall peak diminishes as seen in Figures 4.11 and 4.12 for the  $L/d_0 = 4$  and  $L/d_0 = 2$  surfaces, respectively.

A plot of  $\overline{u'^2}$  normalized by  $U_\infty$  versus  $y/\delta$  is presented in Figure 4.13 for the smooth and three rough surfaces at a freestream velocity of 12 m/s. This figure shows clearly that for the same freestream conditions and at the same x-position, the turbulence intensities for the two roughest surfaces are higher than the smooth surface except directly at the wall. In addition, one can conclude

that the effects of the surface roughness are felt (in the form of increased turbulence) throughout the boundary layer. Similar conclusions were reached by both Pimenta (1975) and Ligrani (1979) based on the data taken on the Stanford rough surface.

Pimenta investigated the Reynolds stress tensor components in fully rough and transitionally rough boundary layers. He observed that in the transitionally rough regime,  $\overline{u'^2}$  profiles showed qualitative characteristics similar to the smooth wall state, with a near-wall peak present. In the fully rough regime, the peak in  $\overline{u'^2}$  was lowered, moved away from the wall, and spread over a larger portion of the boundary layer. He pointed out that the distinctive difference in the near-wall profiles of  $\overline{u'^2}$  may be used to distinguish between transitionally rough and fully rough regimes.

In experiments using the same surface, Ligrani used an artificially thickened boundary layer to achieve larger momentum thicknesses, and he also observed the distinct difference in the near-wall peak from  $\overline{u'^2}$  profiles taken at transitionally rough and fully rough conditions as was reported by Pimenta.

The difference in the near wall region depends not only on the rough surface, but also on the freestream velocity. As the freestream velocity (and thus Reynolds number) is increased, the state of flow changes and the near-wall behavior of the longitudinal turbulence intensity differs for the transitionally rough and fully rough regimes. For the transitionally rough regime, the peak in  $\overline{u'^2}$  is similar to the peak for the smooth wall, but in the fully rough regime no near-wall sharp peak in  $\overline{u'^2}$  is present and a broad peak

spreads farther from the wall and continues into the outer region of the boundary layer. This phenomenon is shown in Figure 4.14 using the data from the  $L/d_0 = 4$  rough surface for freestream velocities of 6 and 58 m/s.

Figures 4.15, 4.16, and 4.17 present the profiles of axial turbulence for nominal freestream velocities of 6, 12, 28, 43, and 58 m/s for the  $L/d_0 = 10$ , 4, and 2 rough surfaces, respectively. These are presented to illustrate the qualitative behavior of the near wall peak in the axial turbulence profiles as the freestream velocity increases as well as the level of turbulence for different rough surfaces.

As shown in Figure 4.15, the axial turbulence intensity profiles for freestream velocities of 6 and 12 m/s exhibit a sharp near-wall peak similar to the smooth wall profiles, and the flows at both freestream velocities (6 and 12 m/s) are clearly classified as transitionally rough. The profiles for freestream velocities of 28, 43, and 58 m/s show that the near-wall data points have collapsed together and neither a sharp peak nor a broad peak could be identified. This behavior is not indicative of a different flow regime. The horizontal hot-wire length was greater than 100 wall units ( $\nu/u^*$ ) at these higher freestream velocities. Thus, as discussed by Ligriani and Bradshaw (1987), the hot-wire used was unable to accurately resolve the turbulence very near the surface at the higher freestream velocities. As far as the classification of flow regimes at freestream velocities of 28, 43, and 58 m/s is concerned, all are considered as transitionally rough flow regimes. Thus, from the



observations of the  $\overline{u'^2}$  behavior for the  $L/d_0 = 10$  rough surface, flows at all freestream velocities (6, 12, 28, 43, and 58 m/s) are classified as transitionally rough.

For the  $L/d_0 = 4$  rough surface, the flows at freestream velocities of 6 and 12 m/s appear to be transitionally rough and for 28, 43, and 58 m/s are fully rough, as shown in Figure 4.16.

Figure 4.17 shows that the axial turbulence intensity profile for a freestream velocity of 6 m/s on the  $L/d_0 = 2$  rough surface has a sharp peak, and the flow regime is identified as transitionally rough. The profiles for the freestream velocities of 28, 43, and 58 m/s do exhibit broad peaks and the flows are classified as fully rough. The turbulence intensity profile for the freestream velocity of 12 m/s corresponds to the "fuzzy" region where the transitionally rough and fully rough flow regimes meet.

#### 4.3.2 Profiles of Reynolds Stress Quantities

Measurements of profiles of the Reynolds stress quantities  $\overline{u'^2}$ ,  $\overline{v'^2}$ ,  $\overline{w'^2}$ , and  $\overline{u'v'}$  were made by traversing the boundary layer with a horizontal hot-wire probe and a 45° slant hot-wire probe as described in Appendix II. The axial turbulence intensities ( $\overline{u'^2}$ ) were measured by the horizontal hot-wire. The other normal stresses ( $\overline{v'^2}$  and  $\overline{w'^2}$ ) and the turbulent shear stress ( $\overline{u'v'}$ ) were obtained using the slant hot-wire. In order to protect the sensing wire of each probe from hitting the roughness elements when the probe was lowered to its lowest position near the rough surface, a small pin was installed on the keel of each hot-wire probe. This pin set the

distance limitation between the sensing wire of each probe and the smooth portion of the rough wall. The smallest distance between the wire and the smooth portion of the rough wall for the horizontal hot-wire was about 1.19 mm. Due to requirements for axial rotation of the sensing wire of the slant hot-wire, the smallest distance for it was 3.76 mm. Therefore, the starting point for measurements of the axial turbulence component ( $\overline{u'^2}$ ) was at 1.19 mm and for the other Reynolds stress components ( $\overline{v'^2}$ ,  $\overline{w'^2}$ , and  $-\overline{u'v'}$ ) at 3.76 mm.

The profiles of all three Reynolds normal stresses ( $\overline{u'^2}$ ,  $\overline{v'^2}$ , and  $\overline{w'^2}$ ) were measured at plate 19 for a freestream velocity of 12 m/s during the THTTF smooth wall qualifications and are presented in Figure 4.18. These profiles are compared with solid curves representing the data of Klebanoff (1955). The corresponding profile of the Reynolds shear stress at the same position and conditions is shown in Figure 4.19 and compared with a solid curve which represents the Reynolds shear stress data of Klebanoff. The Reynolds shear stress data taken on the THTTF are in general agreement with the curve representing Klebanoff's data. The uncertainties associated with the hot-wire measurements for  $\overline{u'^2}$ ,  $\overline{v'^2}$ ,  $\overline{w'^2}$ , and  $\overline{u'v'}$  were about  $\pm 5\%$ ,  $\pm 15\%$ ,  $\pm 10\%$ , and  $\pm 10\%$ , respectively. It should be noted that the freestream turbulence intensity influences the turbulence field and, thus, it was expected that the smooth wall turbulence data from THTTF and Klebanoff's data differ somewhat in the outer portion of the boundary layer due to the differences in the freestream turbulence level. The freestream axial turbulence in the

THTTF was about 0.3%, while Klebanoff's apparatus had freestream turbulence intensities of 0.02% for  $U_\infty = 9.1$  m/s and 0.04% for  $U_\infty = 30.5$  m/s.

The rough wall profiles of the Reynolds stress quantities  $\overline{u'^2}$ ,  $\overline{v'^2}$ ,  $\overline{w'^2}$ , and  $\overline{u'v'}$  were measured for freestream velocities of 12 and 58 m/s following the measurement techniques developed and qualified for the smooth surface. In Figures 4.20-4.25, plots of the profiles of the three Reynolds normal stresses and of the Reynolds shear stress for a nominal freestream velocity of 12 m/s are presented for the  $L/d_0 = 10$ , 4, and 2 rough surfaces, respectively. The flow regime at a freestream velocity of 12 m/s for the  $L/d_0 = 2$  rough surface is fully rough, while for the  $L/d_0 = 10$  it is transitionally rough. For the  $L/d_0 = 4$  rough surface, the flow regime at a freestream velocity of 12 m/s corresponds to the upper region of the transitionally rough regime. Considering the data uncertainties, the profiles for each of the Reynolds stress components for the smooth and rough walls at this freestream velocity are similar.

The influence of increasing freestream velocity on the rough wall Reynolds normal stresses is shown in Figures 4.26 and 4.27. In Figure 4.26 the Reynolds normal stress components normalized by the freestream velocity are shown for the  $L/d_0 = 4$  rough surface for freestream velocities of 12 and 58 m/s. A similar plot for the  $L/d_0 = 2$  rough surface is presented in Figure 4.27. The corresponding plots with Reynolds normal stress components normalized by the friction velocity are given in Figures 4.28 and 4.29. For the  $L/d_0 = 4$  rough surface, the flow at a freestream velocity of 12 m/s

corresponds to the transitionally rough regime and, at 58 m/s, the fully rough regime. The flows at both freestream velocities (12 and 58 m/s) on the  $L/d_0 = 2$  rough surface are classified as fully rough.

For a given freestream condition, the near-wall turbulent kinetic energy level in the boundary layer is expected to increase as the surface becomes rougher. This is shown in Figure 4.30, in which the data from the smooth and the three rough surfaces are presented for freestream velocities of 12 and 58 m/s. The turbulent kinetic energy profile for the  $L/d_0 = 10$  rough surface and the smooth surface have similar trends through most of the boundary layer; however, the rough surface exhibits a tendency toward a higher level of turbulent kinetic energy in the region close to the wall ( $y/\delta < 0.2$ ). The turbulent kinetic energy profiles for the  $L/d_0 = 4$  and  $L/d_0 = 2$  rough surfaces exhibit not only higher levels of turbulent kinetic energy near the rough walls, but also show that the influence of roughness extends through most of the boundary layer up to  $y/\delta < 0.7$ .

This observation is important because early workers who investigated the characteristics of rough wall flows postulated that the effect of the roughness was restricted to the region very close to the surface. Perry et al. (1969), based on observations of mean velocity profiles and skin friction distributions, concluded that if proper outer scale factors are used, the profiles of mean velocity and turbulent fluctuations in the outer flow are independent of the detailed nature of the rough surface. Hinze (1959), based on his analysis of the Corrsin et al. (1954) data, proposed  $u^*$  as the

normalizing parameter for the smooth and rough wall data so that beyond  $y/\delta = 0.2$  or so, the data would collapse together. The friction velocity,  $u^*$ , was used as the normalizing parameter for the individual turbulent quantities shown previously and is also used in Figure 4.31 to normalize the turbulent kinetic energy. This figure shows again that the effects of roughness are felt much farther than  $y/\delta = 0.2$  and the smooth and rough profiles do not collapse in these coordinates as suggested by Hinze. These observations agree with those of Pimenta (1975), Coleman (1976) and Ligrani (1979) for the Stanford rough surface.

Figure 4.32 presents the measured correlation coefficients  $R_{q^2}$  and  $R_{uv}$  where

$$R_{q^2} = \overline{-u'v'}/q^2 \quad (4.3)$$

and

$$R_{uv} = \overline{-u'v'}/\overline{u'^2} \overline{v'^2} \quad (4.4)$$

The measured values of the turbulent shear stress normalized by the turbulent kinetic energy ( $R_{q^2}$ ) for the smooth and the three rough surfaces collapse together at an approximately constant value of 0.13 over most of the layer,  $0.1 < y/\delta < 0.95$ , as shown in the figure. The other correlation coefficient ( $R_{uv}$ ) exhibits more scatter but for  $0.2 < y/\delta < 0.8$ , the approximately constant value is about 0.44. These values compare favorably with those reported by Coleman (1976) of 0.145 and 0.46 for the Stanford surface for both zero pressure gradient and accelerated flows.

All reported profiles of Reynolds stress quantities were measured in the region  $x = 1.7 - 1.9$  m.

#### 4.4 SKIN FRICTION COEFFICIENTS

Skin friction coefficient data were determined from Reynolds shear stress and boundary layer mean velocity profiles measured using hot-wire anemometry as described in Appendix III. Since the hot-wire technique is the only method used in determining the skin friction coefficient distributions for rough surfaces, the correctness of the instrumentation, data collection and data reduction procedures were verified by performing qualification tests using smooth test plates. The THTTF smooth wall skin friction data obtained by the hot-wire method was compared with both the local skin friction data determined with the Preston tube method and an accepted smooth wall skin friction correlation, as discussed previously in Chapter 3. The smooth wall skin friction data obtained with the hot-wire method showed excellent agreement with both Preston tube data and the accepted smooth wall skin friction correlation.

The skin friction coefficients along the three rough test surfaces ( $L/d_0 = 2$ ,  $L/d_0 = 4$  and  $L/d_0 = 10$ ) in the THTTF were determined with hot-wire anemometry. Skin friction coefficients for the smooth surface were obtained for nominal freestream velocities of 12 and 43 m/s, and the skin friction coefficients for the  $L/d_0 = 10$  rough surface were determined for freestream velocities of 6 and 12 m/s. The skin friction coefficients for the  $L/d_0 = 4$  and  $L/d_0 = 2$  rough surfaces were obtained for freestream velocities of 12 and 58 m/s.

Figure 4.33 shows the local skin friction coefficient distributions for the smooth and the rough ( $L/d_0 = 10$ ) surfaces determined by hot-wire anemometry versus the momentum thickness Reynolds number ( $Re_{\delta_2}$ ) computed from the measured momentum thickness at each profile station. The smooth wall skin friction correlation (Eq. 3.2) is also shown for reference with a  $\pm 10\%$  range indicated. The skin friction coefficient data for the  $L/d_0 = 10$  rough surface at free-stream velocities of 6 and 12 m/s fall within the scatter of the smooth wall data and overlap the  $\pm 10\%$  range of the smooth wall correlation.

Figure 4.34 presents the skin friction coefficients for the  $L/d_0 = 4$  and  $L/d_0 = 2$  rough surfaces for nominal freestream velocities of 12 and 58 m/s. Also shown for reference is the smooth wall correlation. This figure clearly exhibits the influence of the roughness on the friction coefficients and shows that as the surface becomes rougher, the skin friction coefficient increases. The skin friction coefficient,  $C_f$ , at an  $Re_{\delta_2}$  of about 13,000 is 0.00234 for the smooth wall and for the  $L/d_0 = 4$  rough surface is 0.00418, which corresponds to a 78% increase. The skin friction coefficient for the roughest surface ( $L/d_0 = 2$ ) at about the same  $Re_{\delta_2}$  is 0.00620. This corresponds to a significant increase of about 165% with respect to the smooth wall skin friction coefficient.

These same data are plotted against the ratio of momentum thickness to roughness height in Figure 4.35. These coordinates were first suggested by Healzer (1974) as the most appropriate coordinates for presenting rough wall skin friction coefficient

data. Using the Stanford rough surface, he measured turbulent boundary layer mean velocity profiles, calculated momentum thicknesses, and subsequently obtained skin friction coefficients based on the momentum integral equation. Due to the data uncertainty, he could not make a firm assessment on any velocity dependence of his data. Pimenta (1975) obtained skin friction distributions over the same rough surface using hot-wire anemometry and stated that in the fully rough state of the boundary layer, friction coefficient  $C_f/2$  is independent of Reynolds number and a function only of local momentum thickness. He observed that his fully rough skin friction distributions plotted versus momentum thickness normalized by roughness height collapsed together and that the one transitionally rough data set appeared to be a little lower. The curve representing Pimenta's fully rough data from the Stanford surface is shown in the figure, along with smooth wall curves (Eq. 3.2) for several velocities (using  $k = 0.0635$  mm to normalize the smooth wall momentum thickness values).

Figure 4.35 shows that the THTF skin friction coefficient data for each surface, irrespective of transitionally rough or fully rough regimes, collapse together within the data uncertainty. Also, it is apparent that for each rough surface, the data collapse to a different curve. In these coordinates, the THTF  $L/d_0 = 2$  surface is "roughest", followed by the Stanford surface, then by the THTF  $L/d_0 = 4$  surface.



#### 4.5 ADDITIONAL COMMENTS ON THE CLASSIFICATION OF FLOW REGIMES

The classification of the flow regimes for the boundary layers over the three rough surfaces investigated in this research effort was previously discussed based on the shape of the near-wall axial turbulent intensity suggested by Pimenta (1975) and supported by Ligrani (1979). In addition, it is useful to consider the calculated values of  $R_\tau$  using the discrete element method [as proposed by Taylor et al. (1984) and set by Scaggs et al. (1988a)] to distinguish between flow regimes. Recall from Chapter 2 that  $R_\tau$  is the ratio of the apparent shear stress due to roughness elements to the total apparent shear stress as calculated using the discrete element method.

Figure 4.36 shows a plot of calculated values of  $R_\tau$  using the discrete element method for nominal freestream velocities of 6, 12, 28, 43, 58, and 67 m/s for the three rough surfaces ( $L/d_0 = 10$ ,  $L/d_0 = 4$ , and  $L/d_0 = 2$ ). Based on the limits between smooth, transitionally rough and fully rough flow regimes suggested by Scaggs et al. of  $R_\tau$  about 0.5-0.10 and 0.6 respectively, the  $L/d_0 = 10$  rough surface results for all freestream velocities correspond to transitionally rough flow regimes except for the  $u_\infty = 6$  m/s case, which could be classified as smooth or on the lower end of transitionally rough. For the  $L/d_0 = 4$  surface, based on the same limits for  $R_\tau$ , the 6 and 12 m/s results would definitely be classified as transitionally rough, while the 28 m/s run (with  $R_\tau = 0.56$ ) would fall in the upper range of transitionally rough or lower range of fully rough, and the 43, 58 and 67 m/s runs (with  $R_\tau = 0.60-0.65$ ) would be

classified in the lower range of the fully rough state. The 12, 28, 43, 58, and 67 m/s results for the  $L/d_0 = 2$  rough surface are classified as fully rough according to the limit on  $R_\tau$ . The 6 m/s results would fall in the lower range of the fully rough regime or the upper range of the transitionally rough regime. From observations of the  $\overline{u'^2}$  behavior, the 6 m/s results appear to have transitionally rough characteristics.

The flow regime classifications based on  $\overline{u'^2}$  and  $R_\tau$  are summarized in Table 4.1.

# Hemispherical Roughness

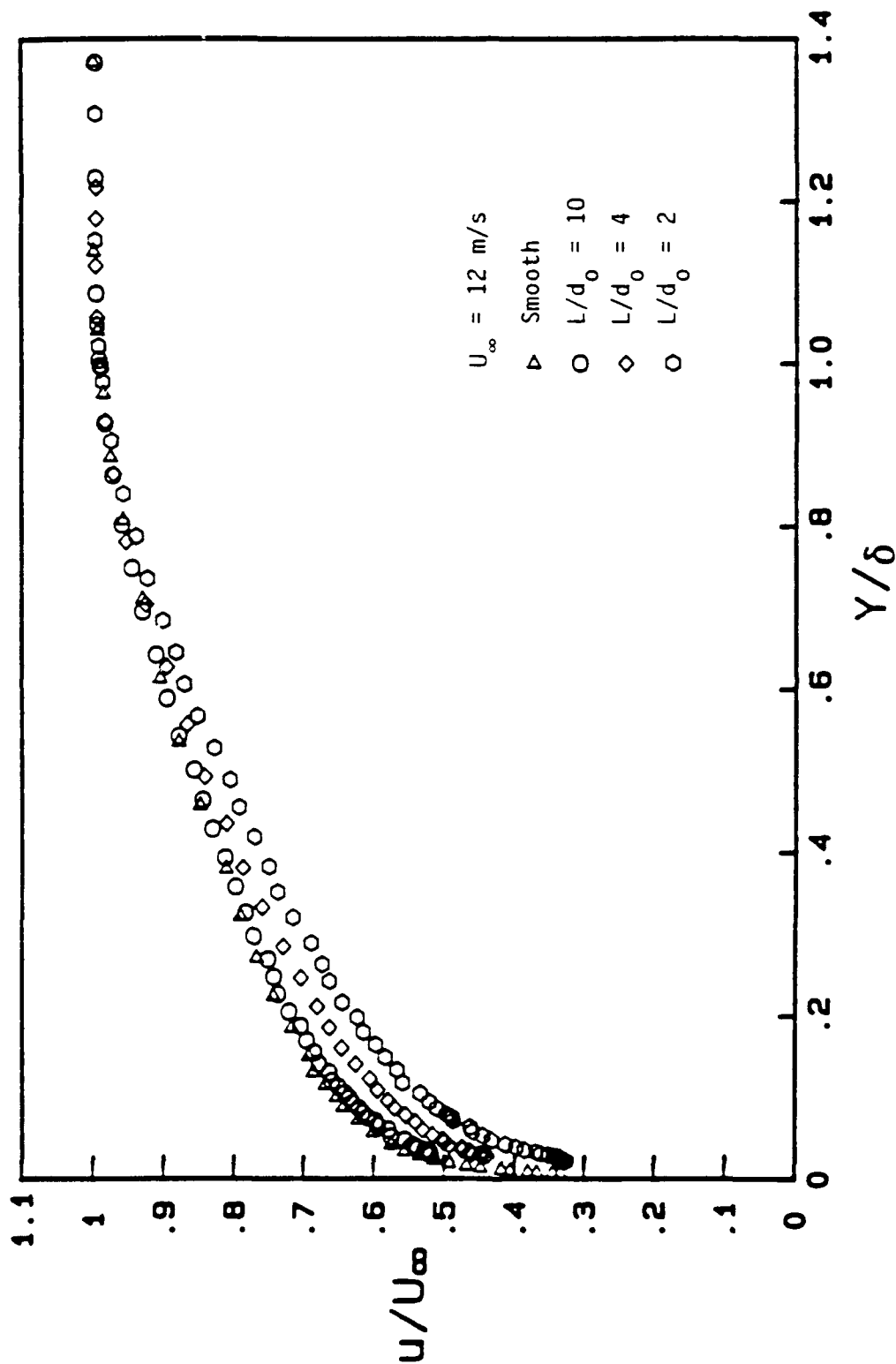


Figure 4.1 Comparison of mean velocity profiles for the smooth and the three rough surfaces plotted in  $u/U_{\infty}$  vs.  $y/\delta$  coordinates.

# Hemispherical Roughness

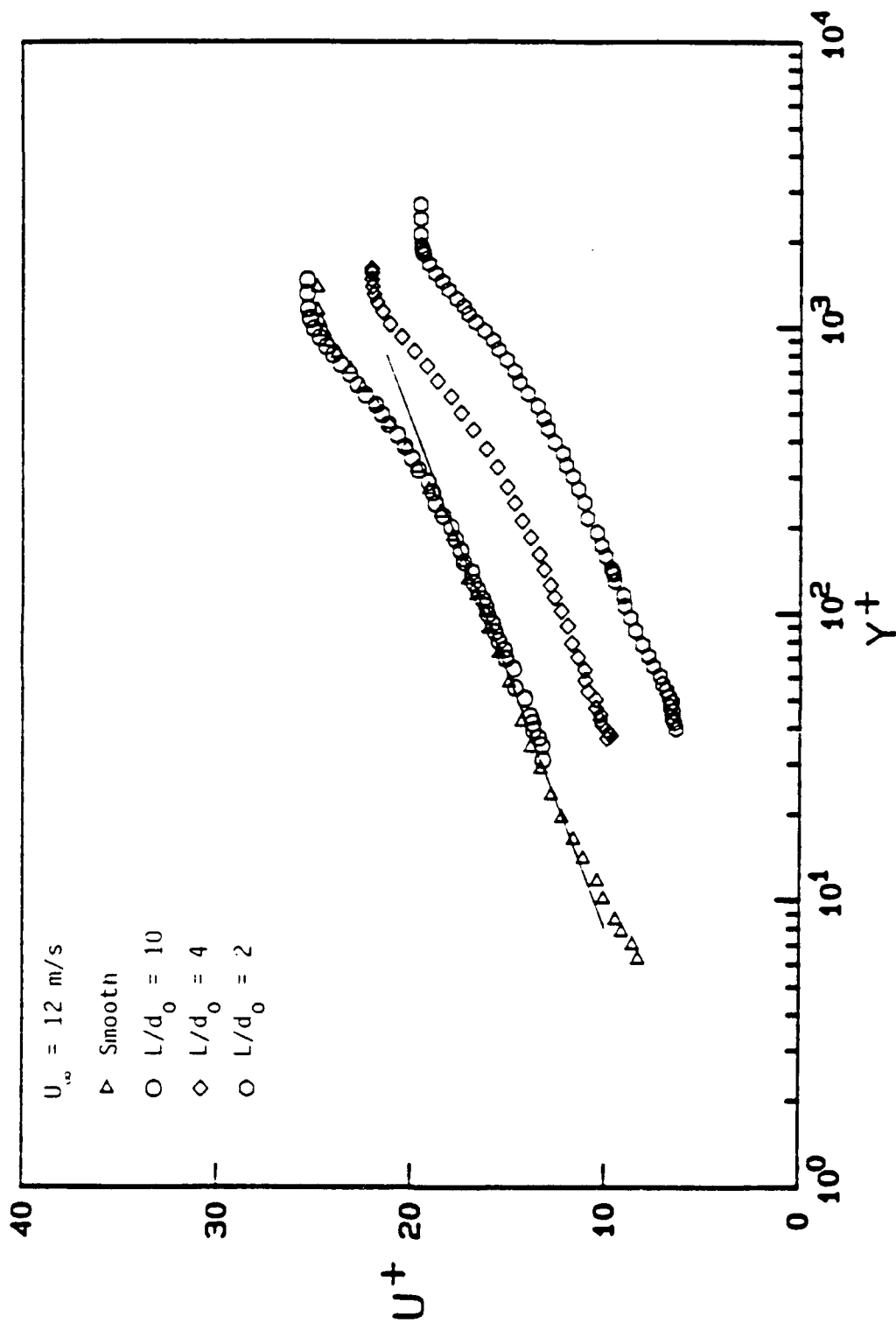


Figure 4.2 Mean velocity profiles for the smooth and the three rough surfaces compared with the smooth wall law of the wall.

# Hemispherical Roughness

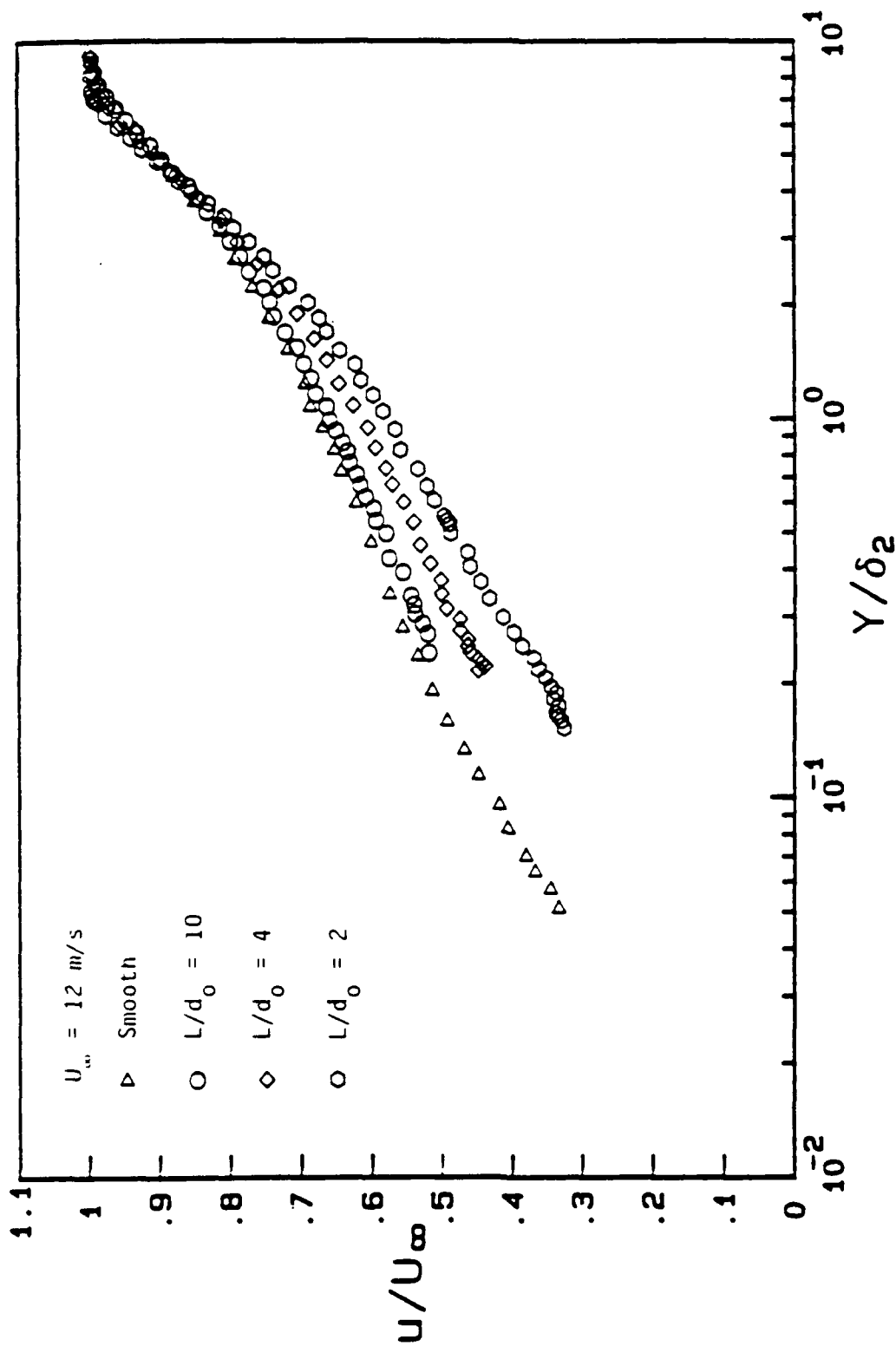


Figure 4.3 Comparison of mean velocity profiles for the smooth and the rough surfaces plotted in  $u/U_{\infty}$  vs.  $y/\delta_2$  coordinates.

# Hemispherical Roughness

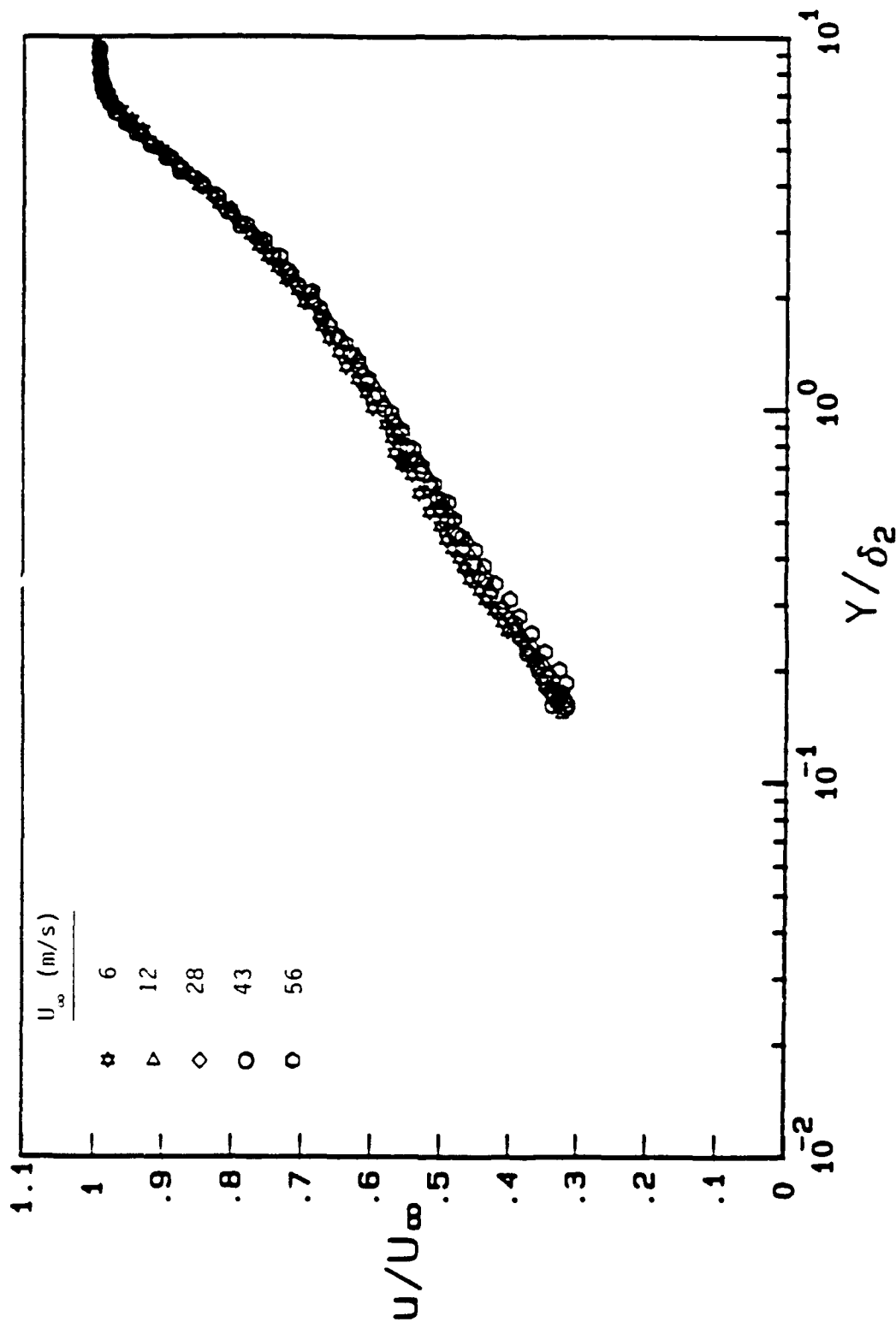


Figure 4.4 Mean velocity profiles for the  $L/d_0 = 2$  surface illustrating similarity in  $u/U_\infty$  vs.  $y/\delta_2$  coordinates.

# Hemispherical Roughness

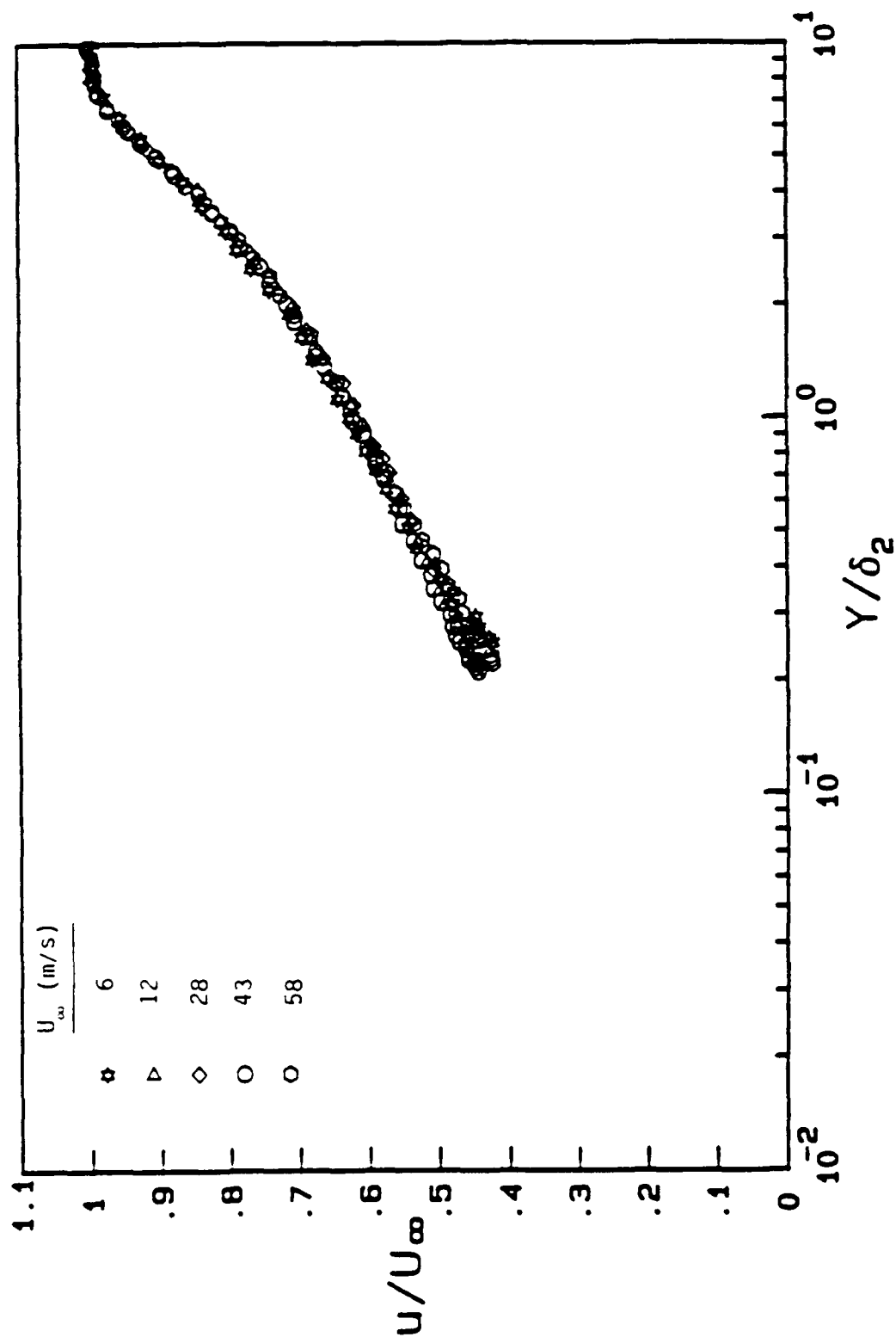


Figure 4.5 Mean velocity profiles for the  $L/d_0 = 4$  surface illustrating similarity in  $u/U_\infty$  vs.  $y/\delta_2$  coordinates.

# Hemispherical Roughness

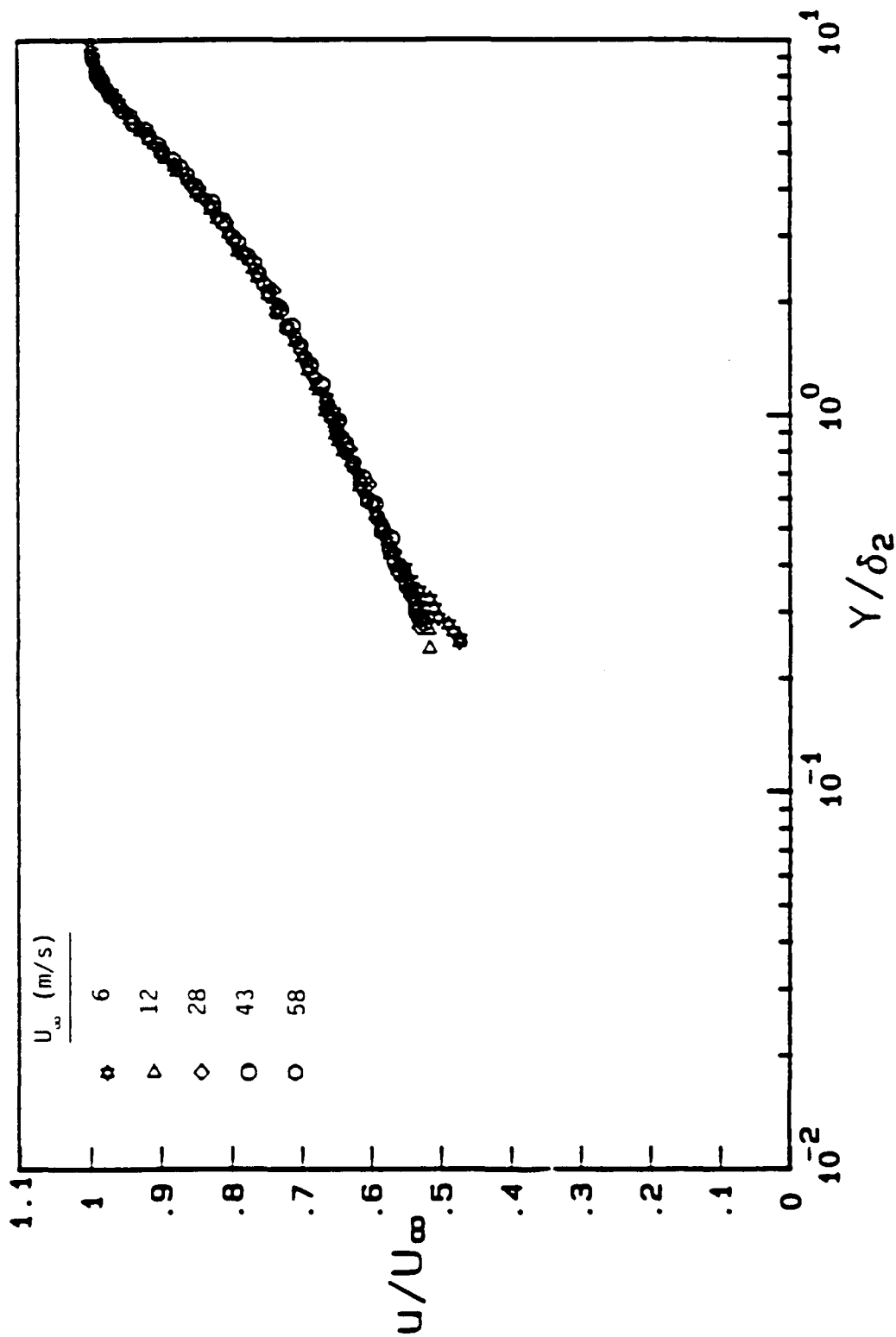


Figure 4.6 Mean velocity profiles for the  $L/d_0 = 10$  surface illustrating similarity in  $u/U_\infty$  vs.  $y/\delta_2$  coordinates.



# Hemispherical Roughness

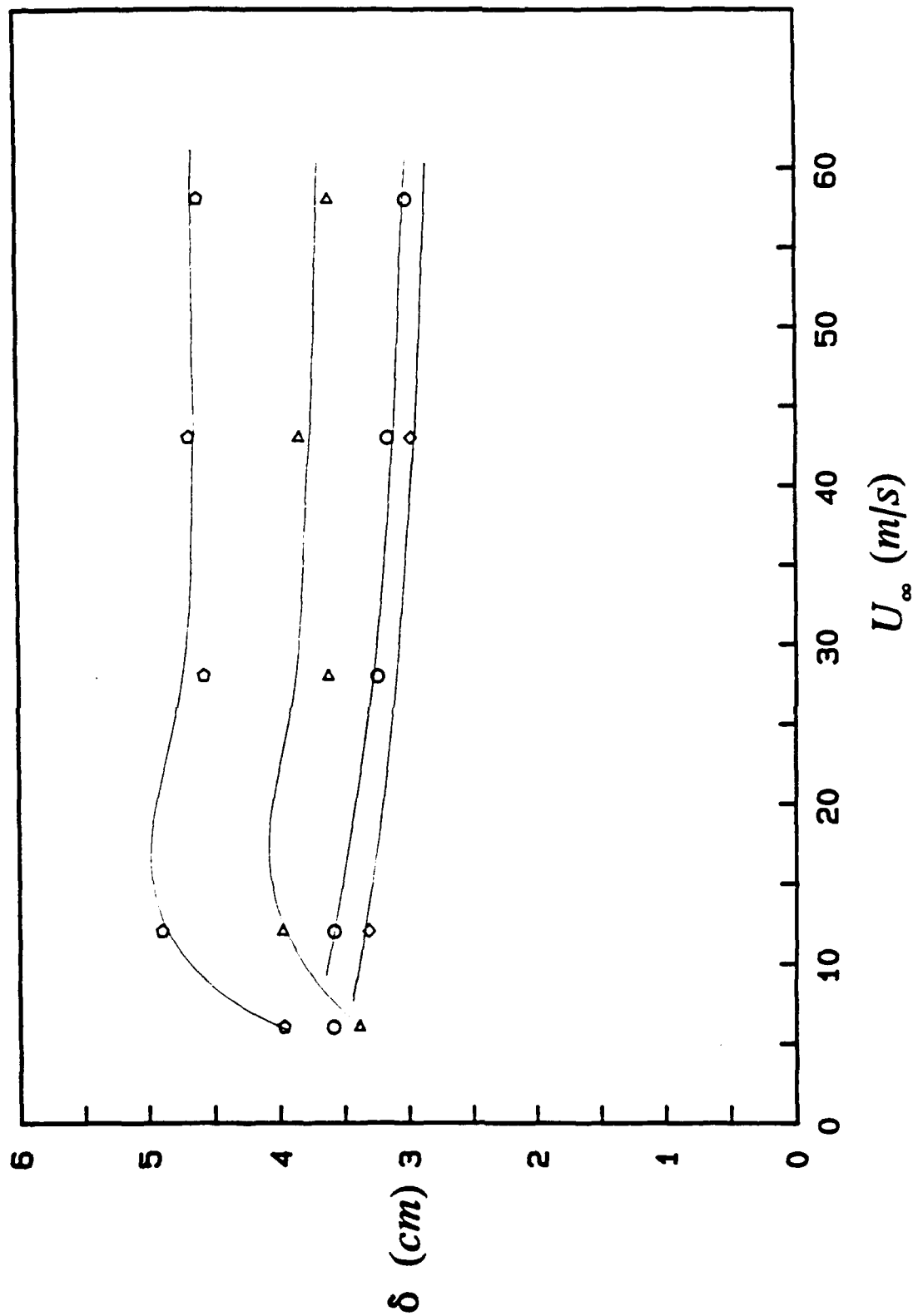


Figure 4.7 Influence of increasing freestream velocity on the behavior of the boundary layer thickness for the smooth and the rough surfaces.

# Hemispherical Roughness

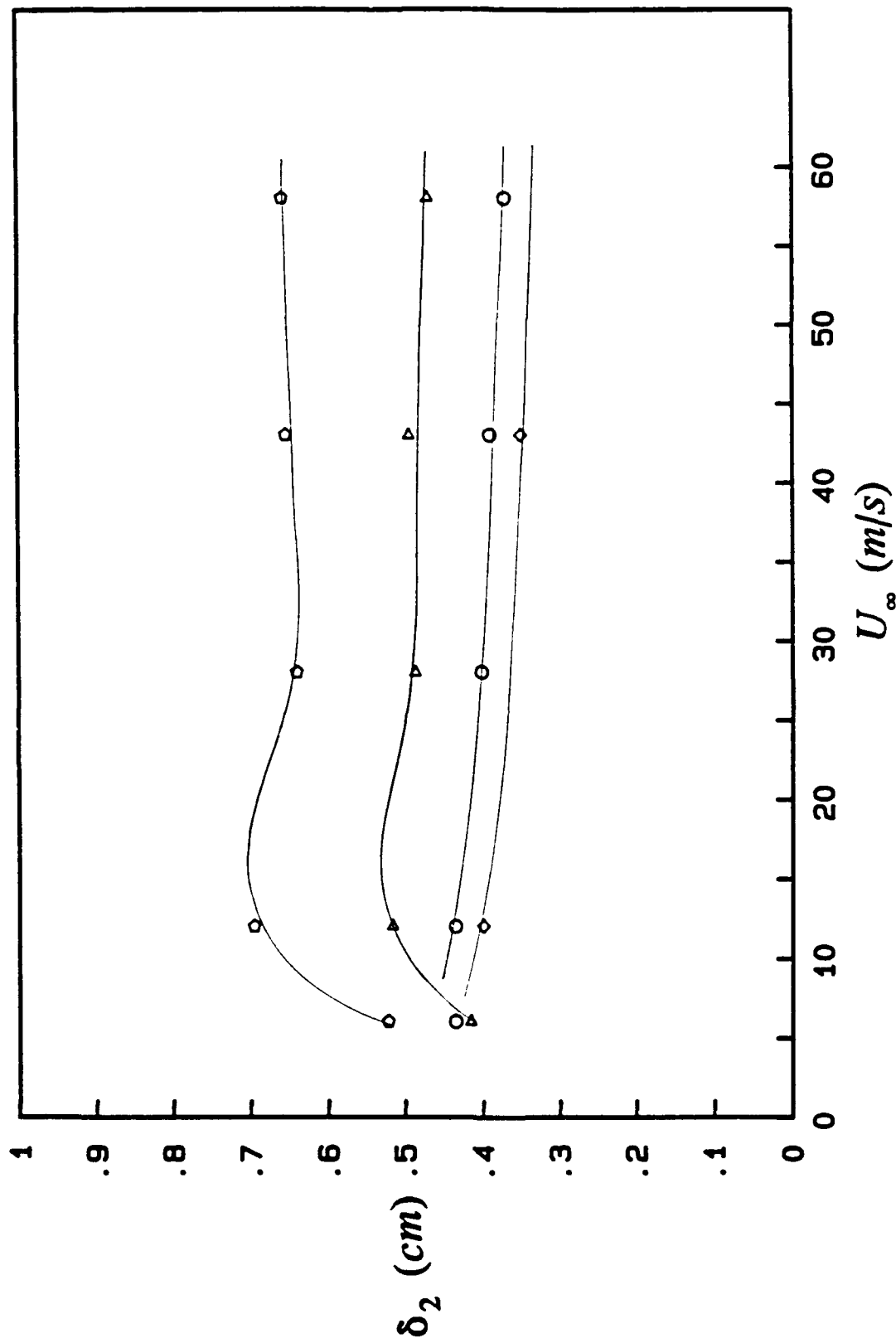


Figure 4.8 Influence of increasing freestream velocity on the behavior of the momentum thickness for the smooth and the rough surfaces.

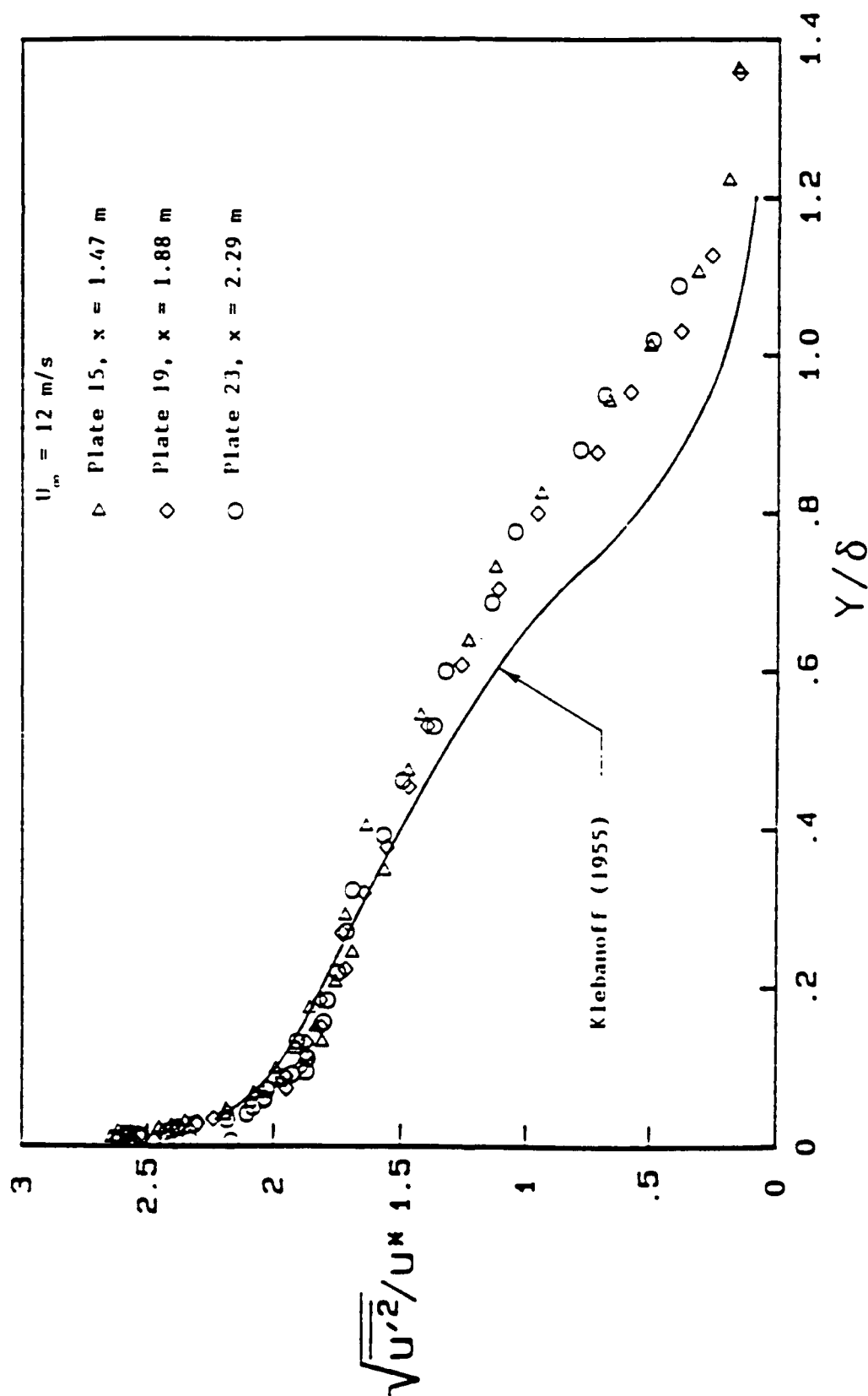


Figure 4.9 The THTF smooth wall axial turbulence intensity profiles compared with the data of Klebanoff (1955).

# Hemispherical Roughness

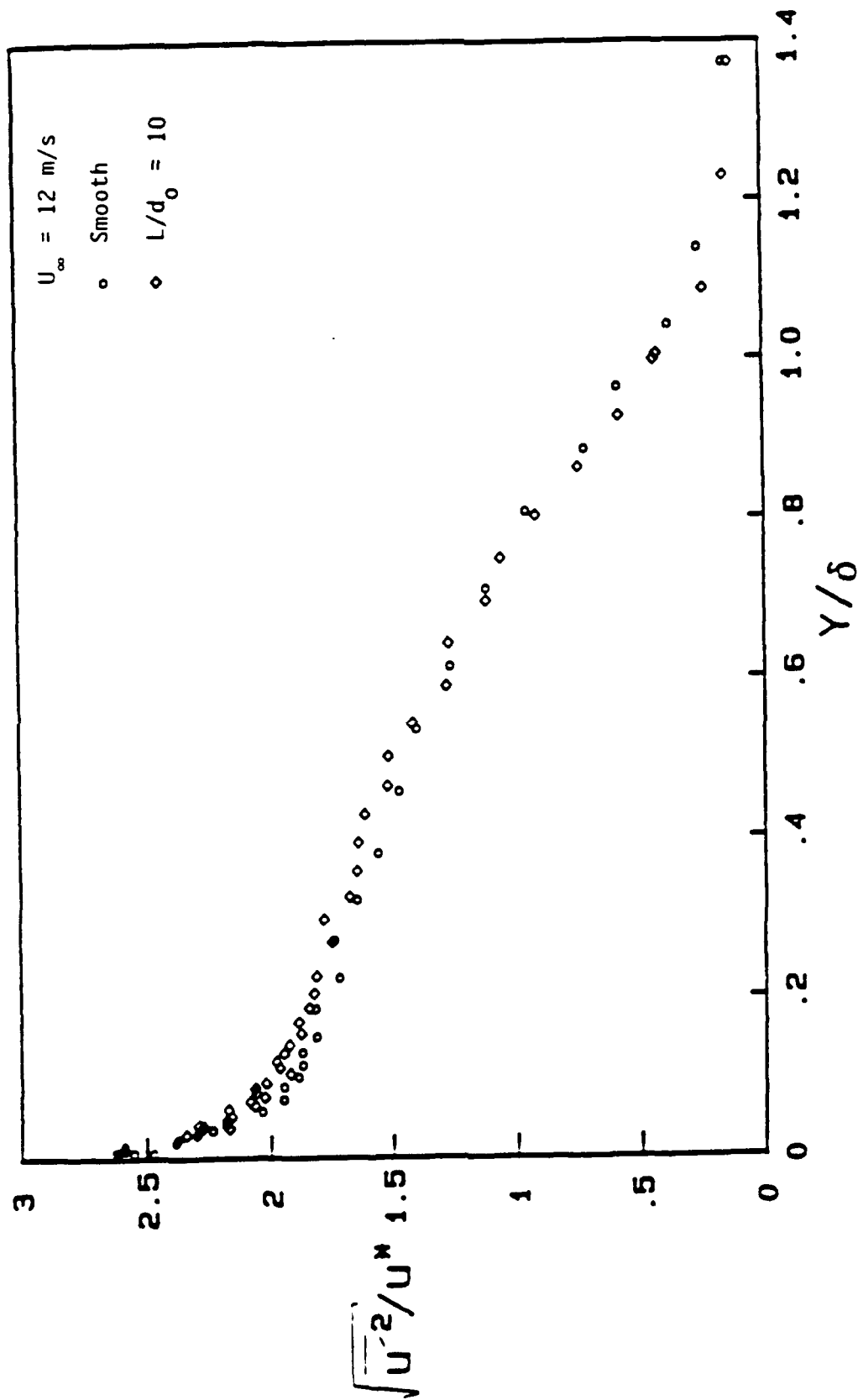


Figure 4.10 Comparison of the axial turbulence intensity profiles for the smooth and  $L/d_0 = 10$  rough surfaces.

# Hemispherical Roughness

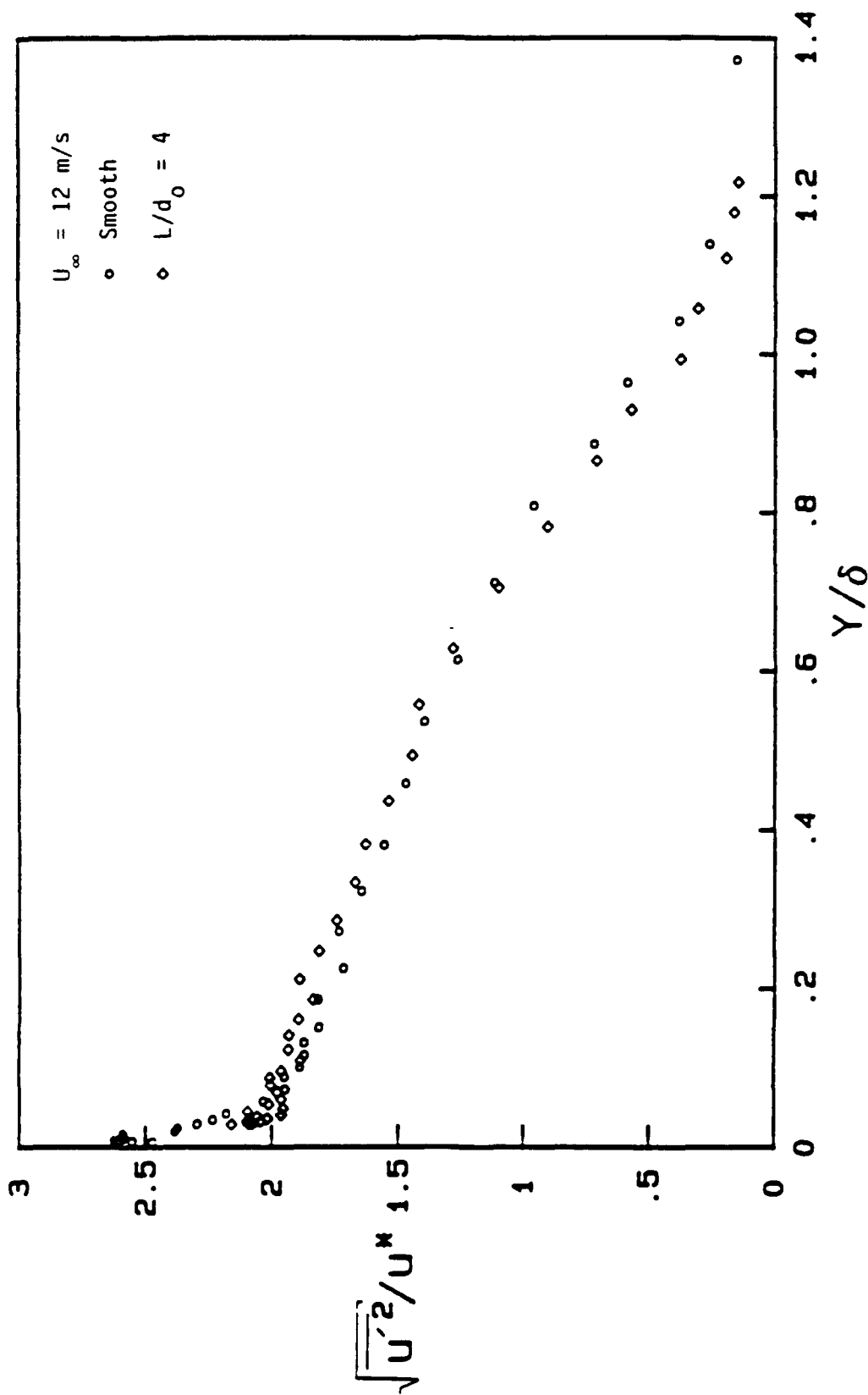


Figure 4.11 Comparison of the axial turbulence intensity profiles for the smooth and  $L/d_0 = 4$  rough surfaces.

# Hemispherical Roughness

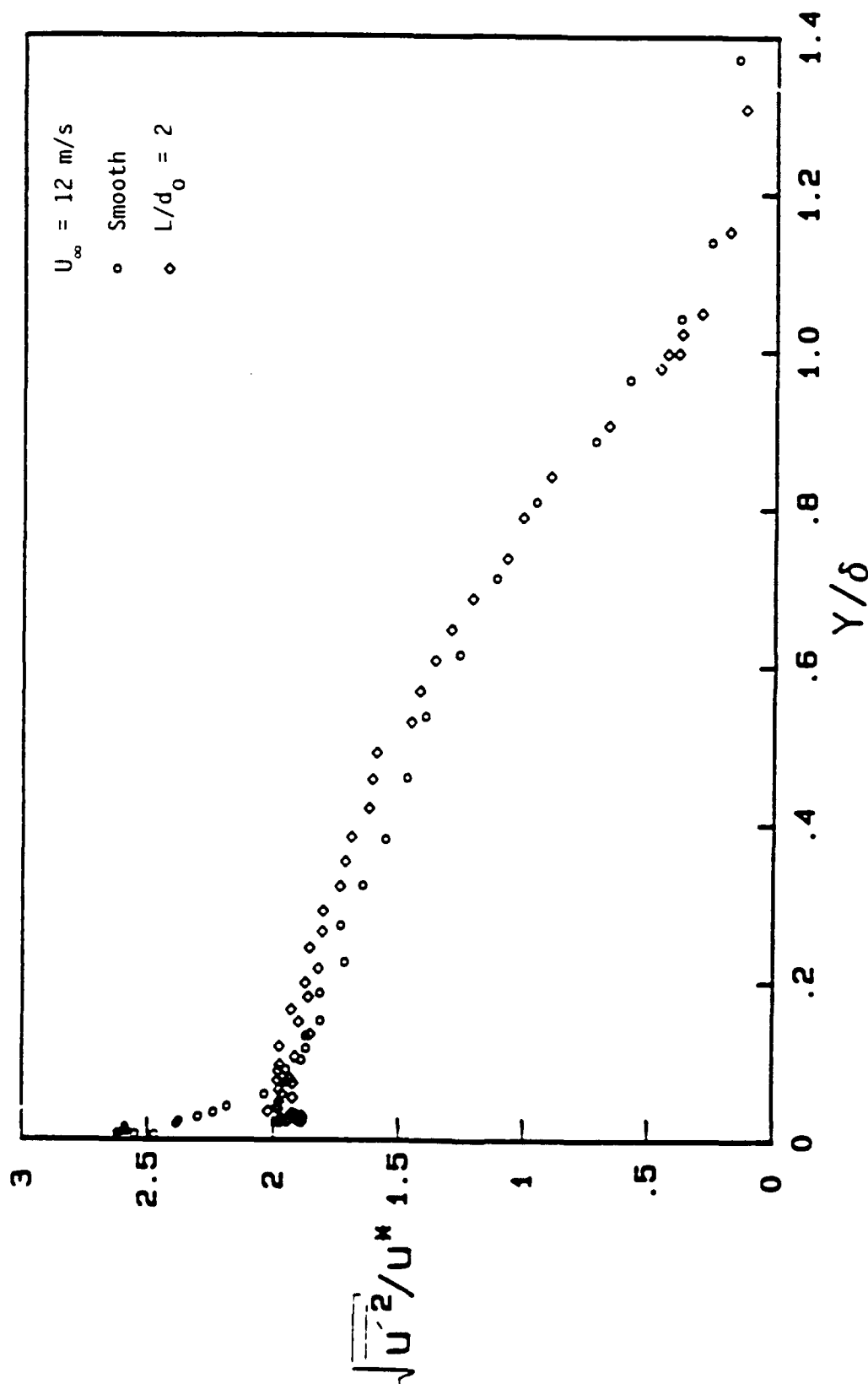


Figure 4.12 Comparison of the axial turbulence intensity profiles for the smooth and  $L/d_0 = 2$  rough surfaces.

# Hemispherical Roughness

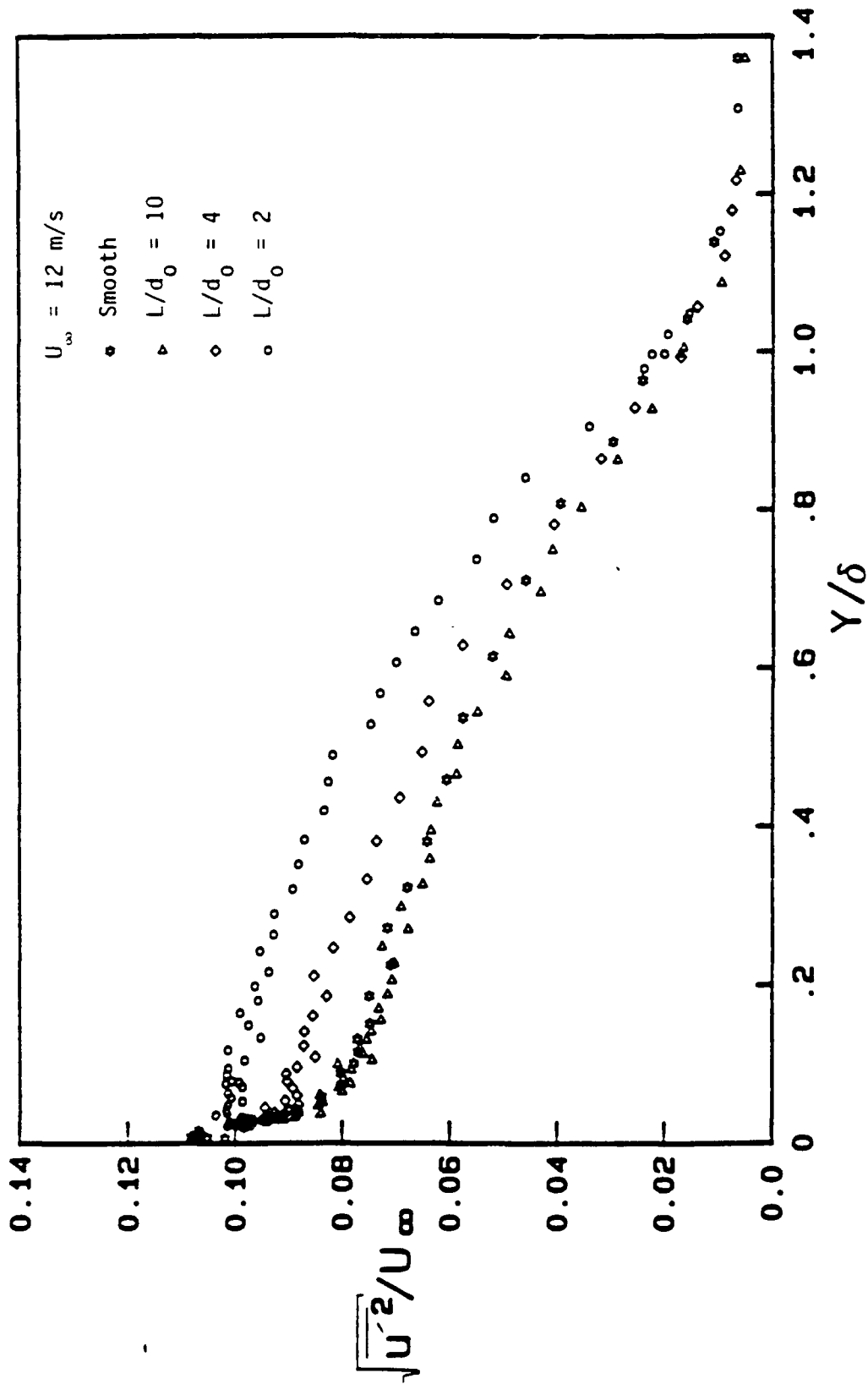


Figure 4.13 Composite plot of the axial turbulence intensity profiles for the smooth and the rough surfaces illustrating roughness effects.

# Hemispherical Roughness

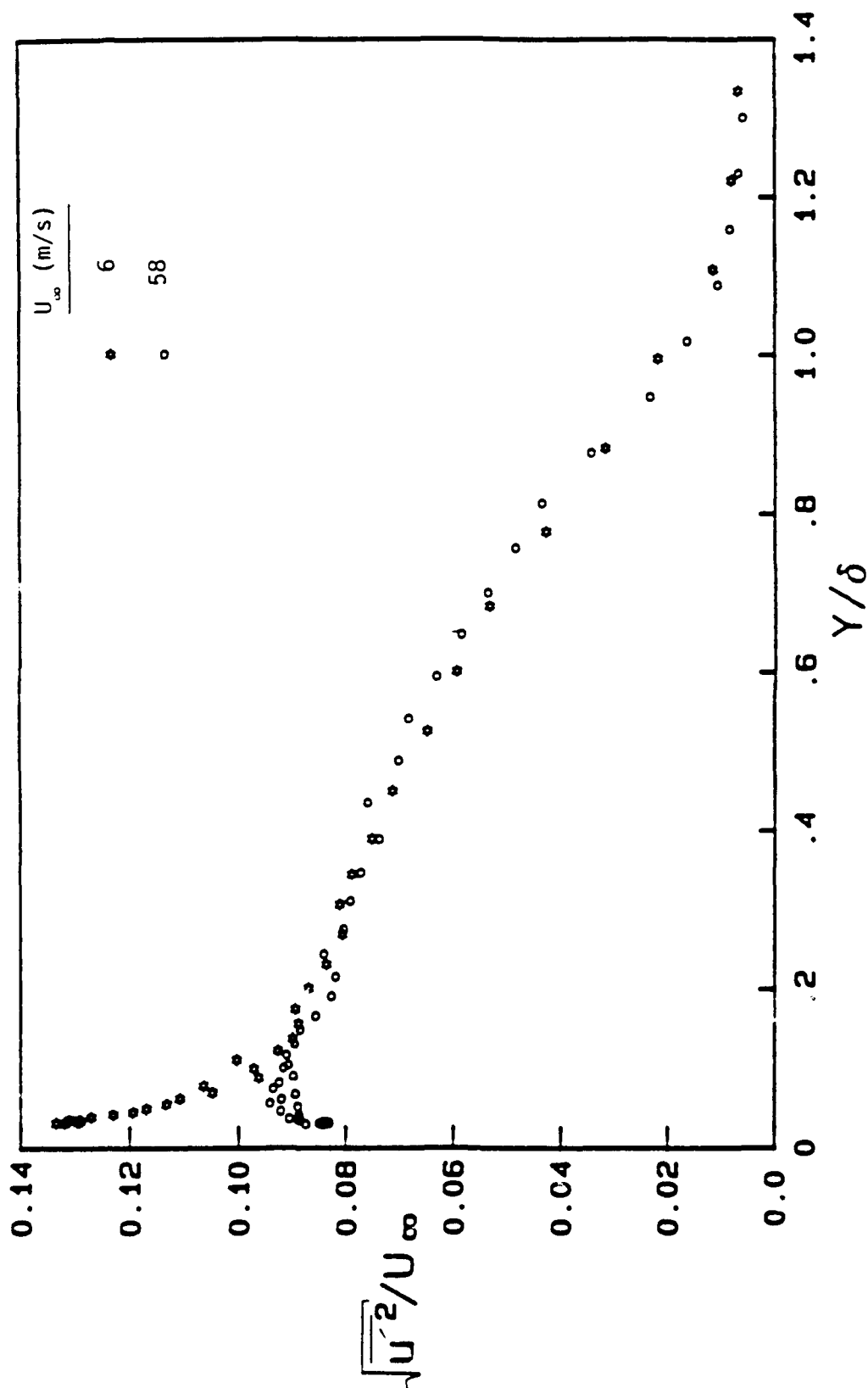


Figure 4.14 Comparison of the axial turbulence intensity profiles in transitionally rough and fully rough flow regimes for the  $L/d_0 = 4$  surface.



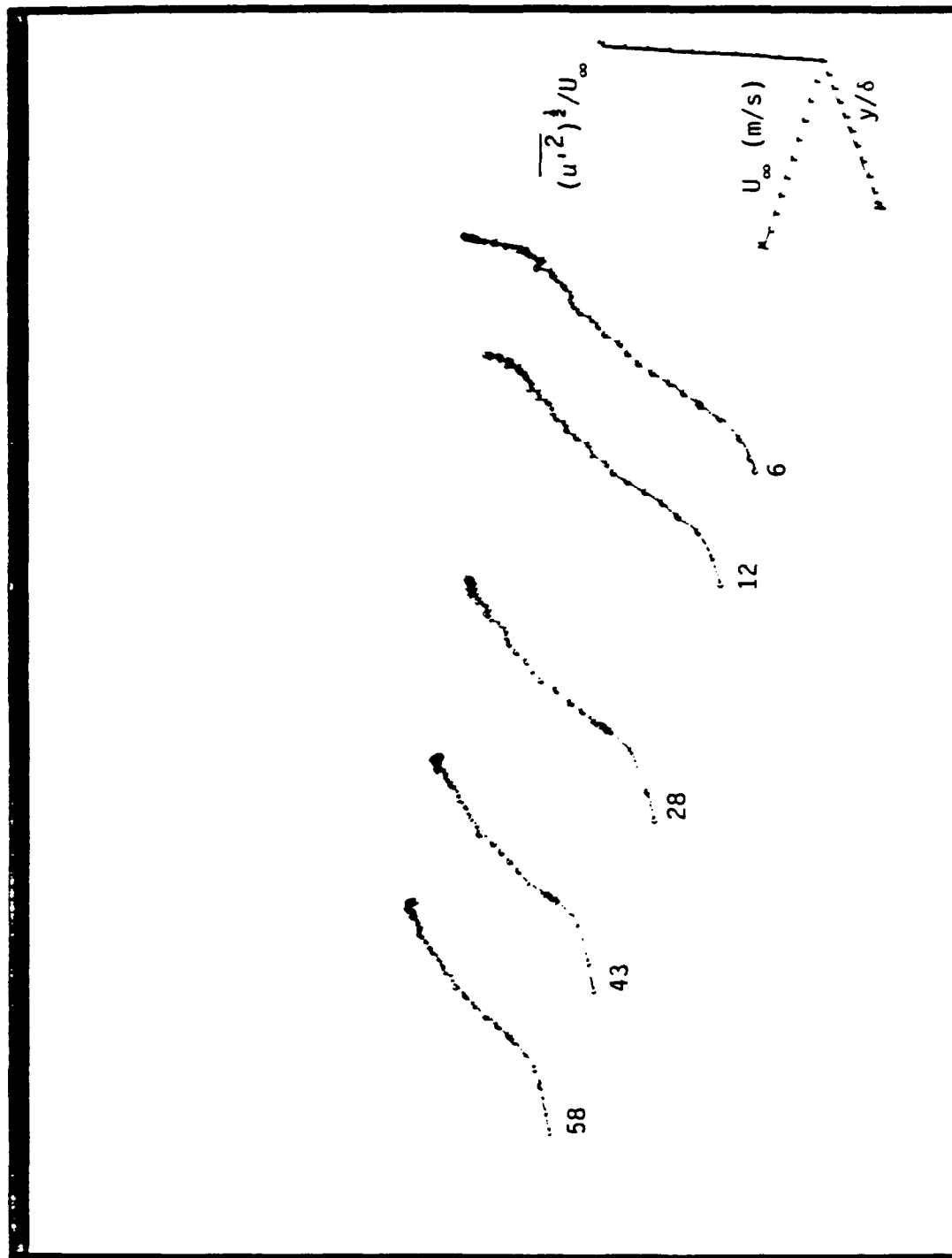


Figure 4.15 Profiles of the axial turbulence intensity for  $U_\infty = 6, 12, 28, 43$  and  $58$  m/s for the  $L/d_0 = 10$  surface illustrating the near-wall peak behavior.

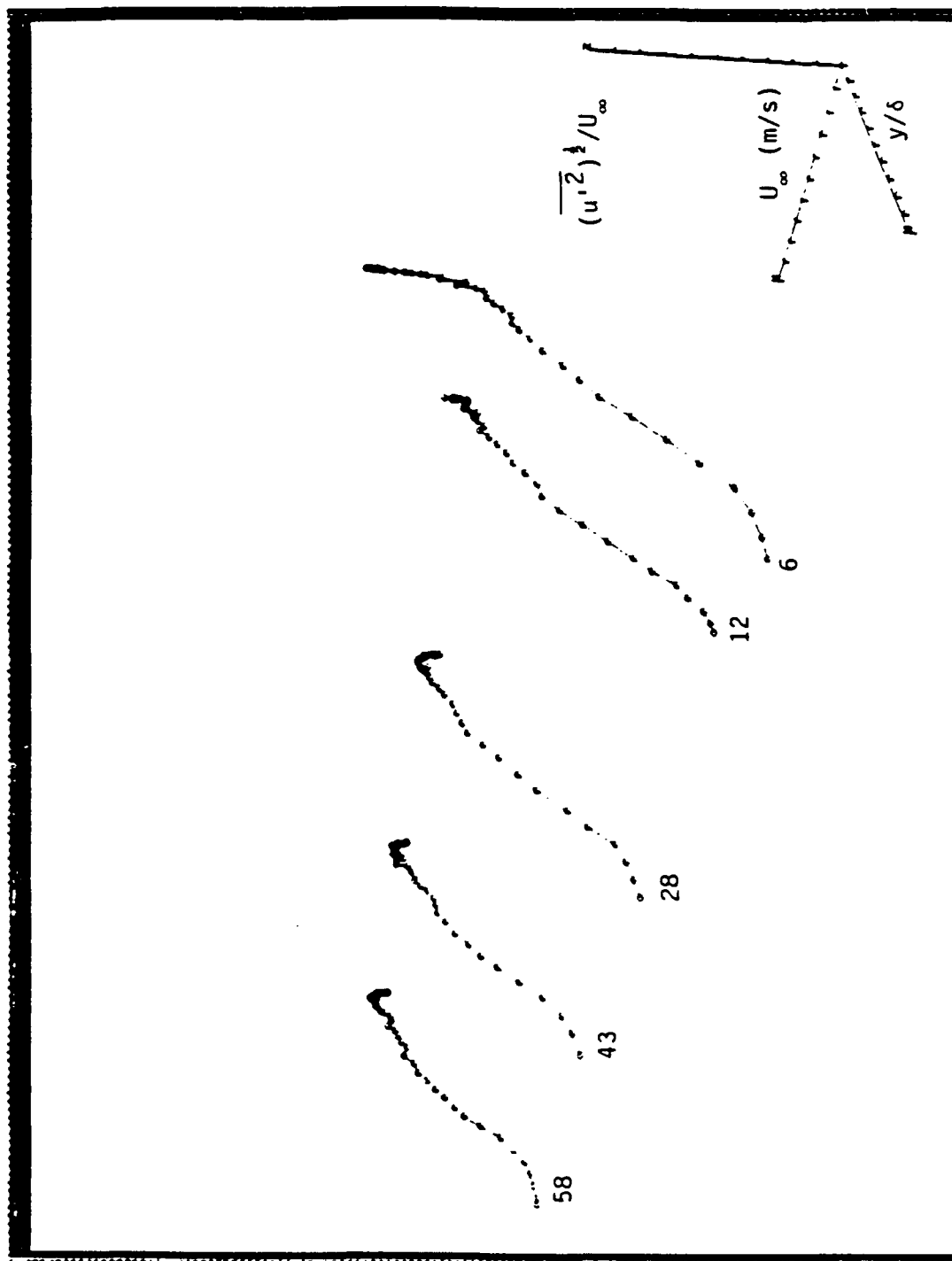


Figure 4.16 Profiles of the axial turbulence intensity for  $U_\infty = 6, 12, 28, 43$  and  $58$  m/s for the  $L/d_0 = 4$  surface illustrating the near-wall peak behavior.

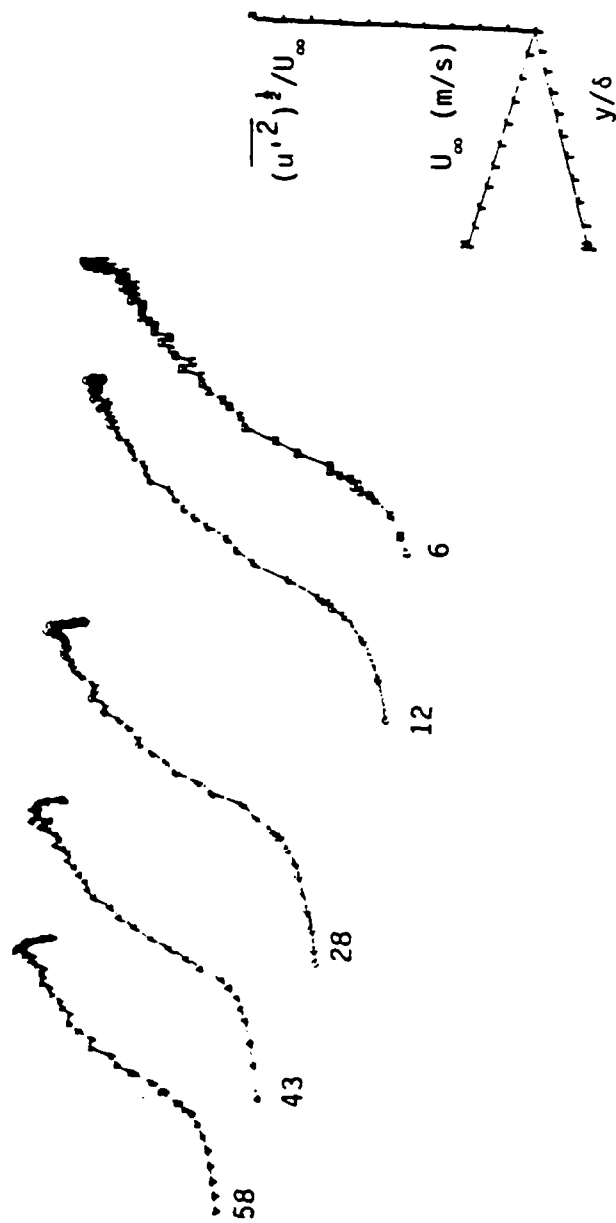


Figure 4.17 Profiles of the axial turbulence intensity for  $U_\infty = 6, 12, 28, 43$  and  $58$  m/s for the  $L/d_0 = 2$  surface illustrating the near-wall peak behavior.

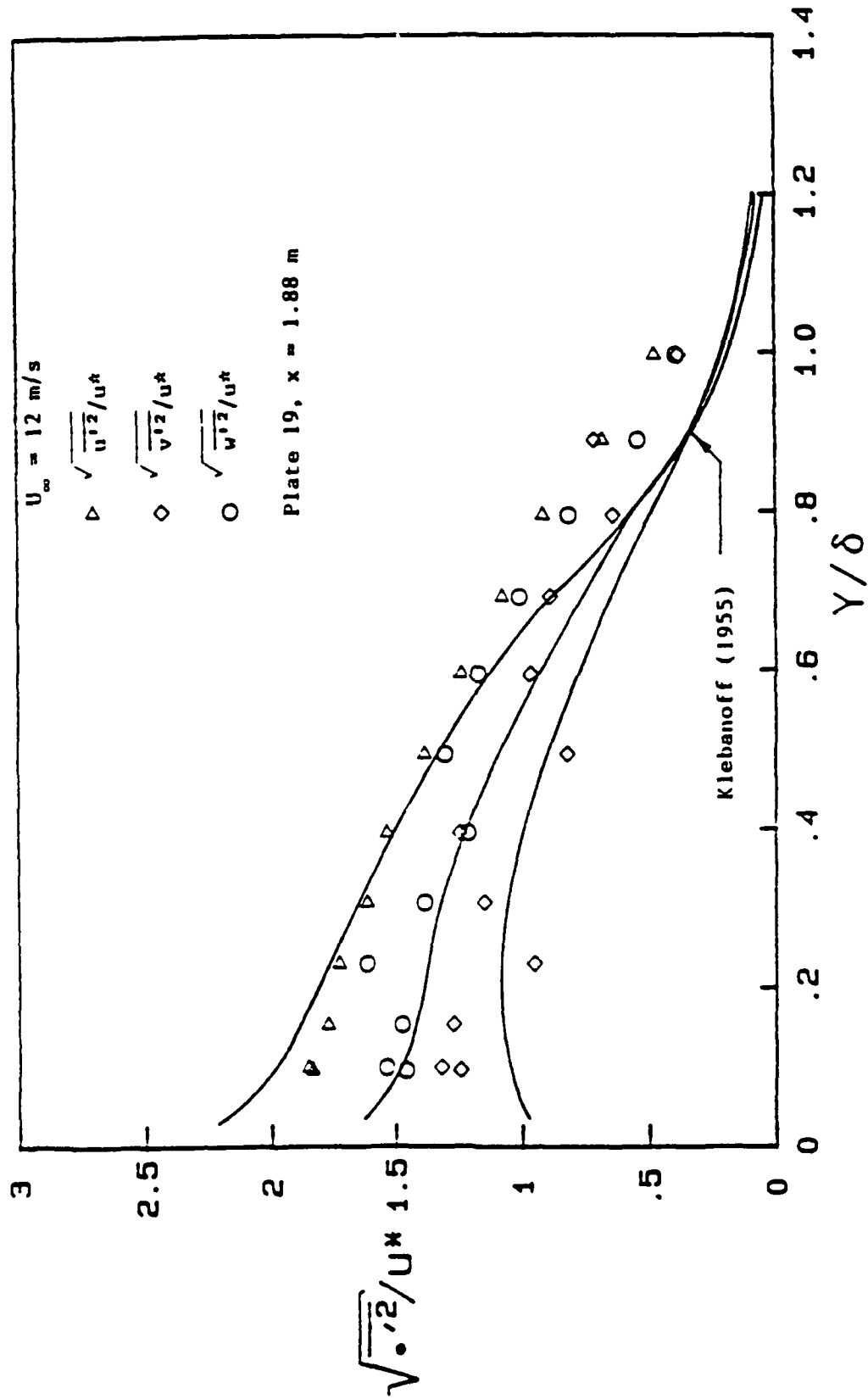


Figure 4.18 Comparison of the THTF smooth wall profiles of all three Reynolds normal stresses with the data of Klebanoff (1955).

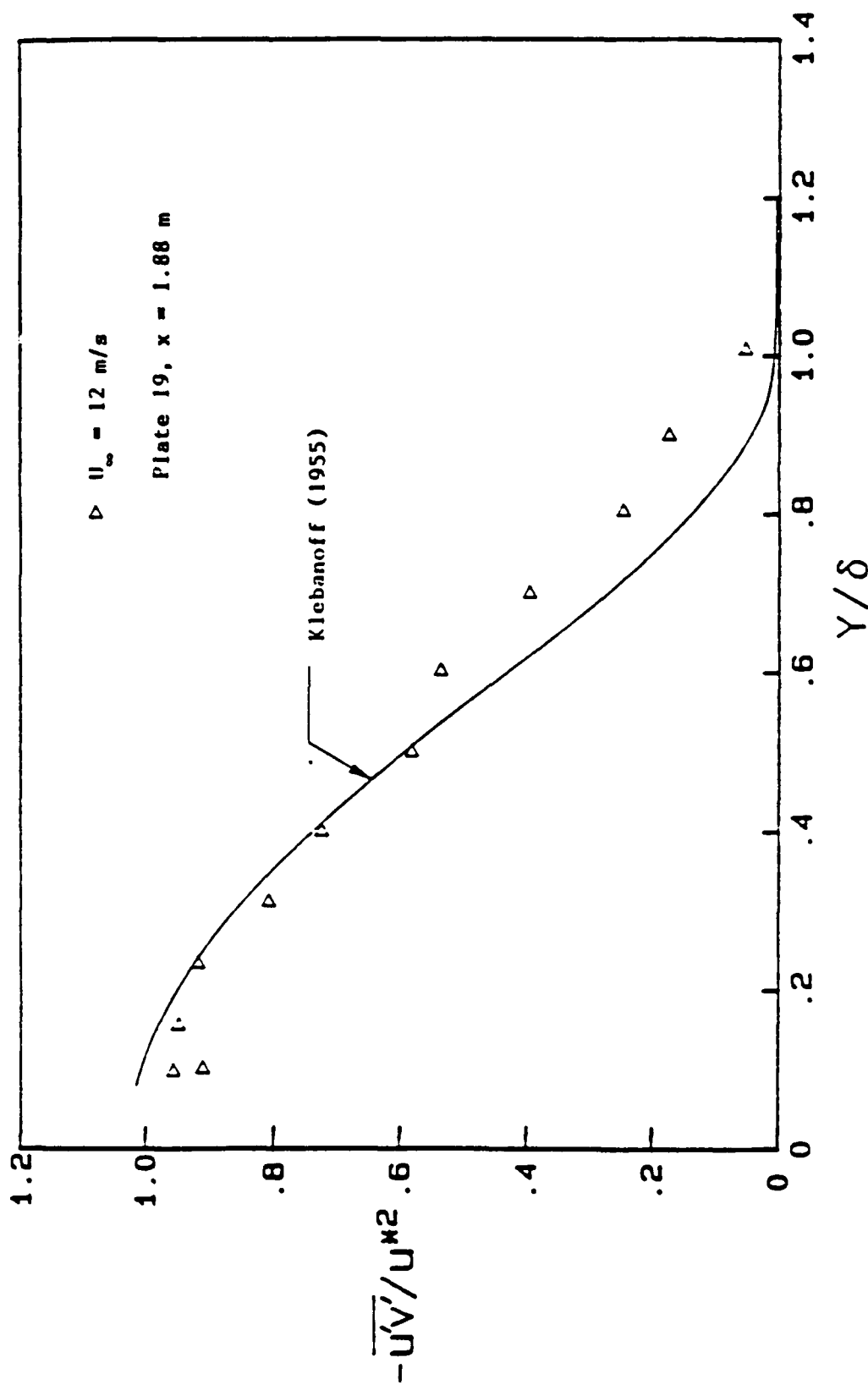


Figure 4.19 Comparison of the THTF smooth wall profiles of Reynolds shear stress compared with the data of Klebanoff (1955).

# Hemispherical Roughness

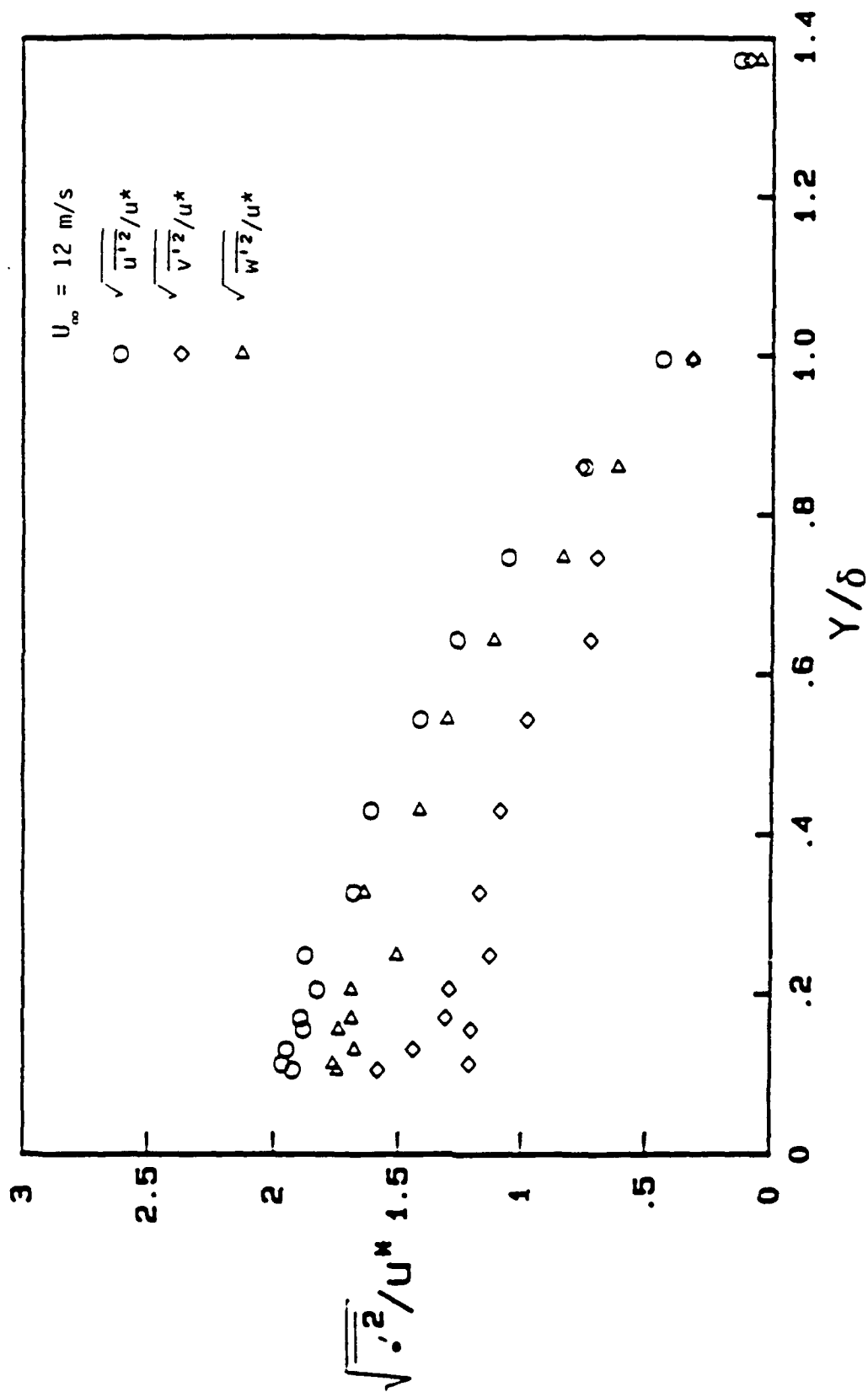


Figure 4.20 Profiles of all three Reynolds normal stresses for the  $L/d_0 = 10$  rough surface.

# Hemispherical Roughness

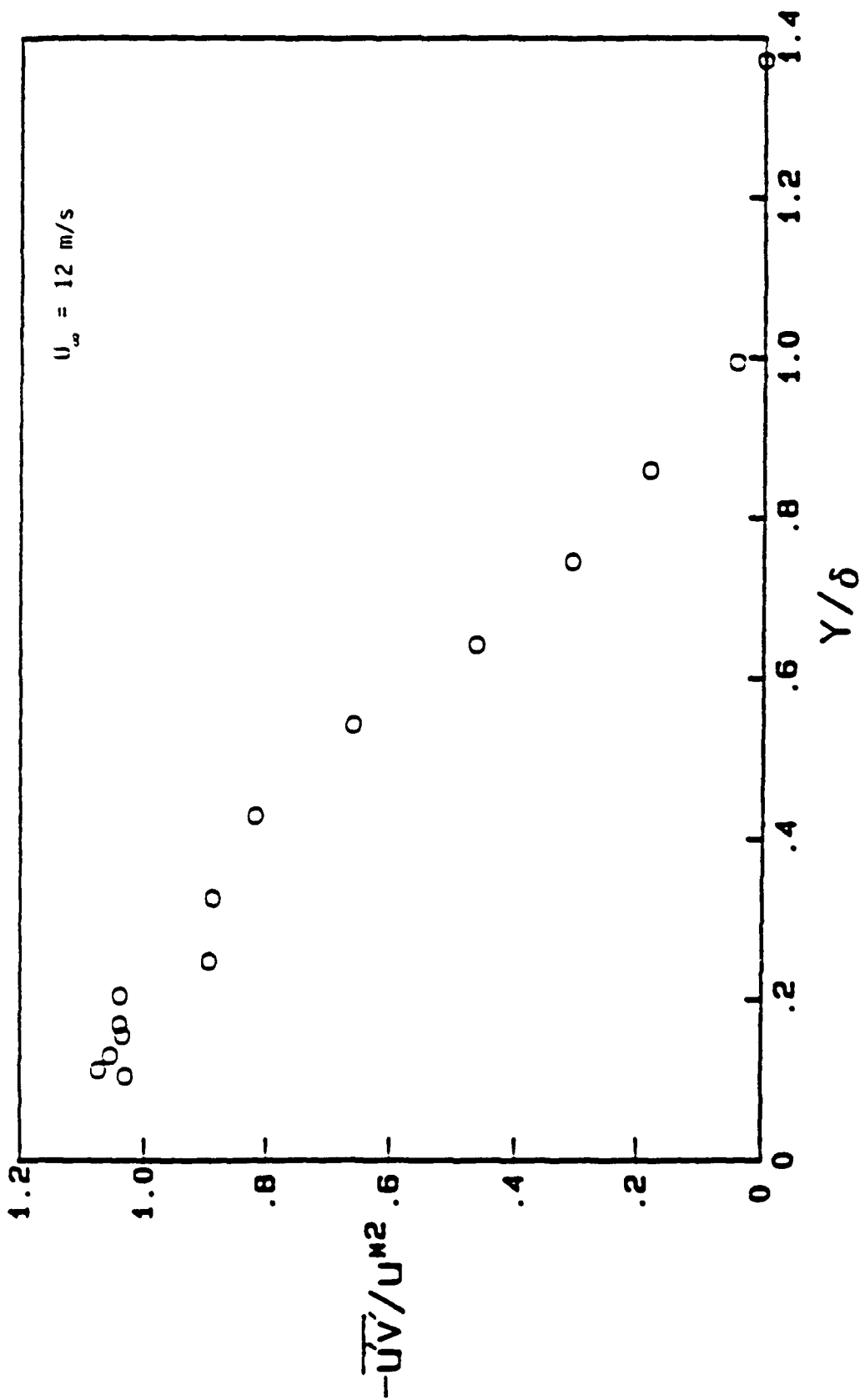


Figure 4.21 Profile of Reynolds shear stress for the  $L/d_0 = 10$  surface.

# Hemispherical Roughness

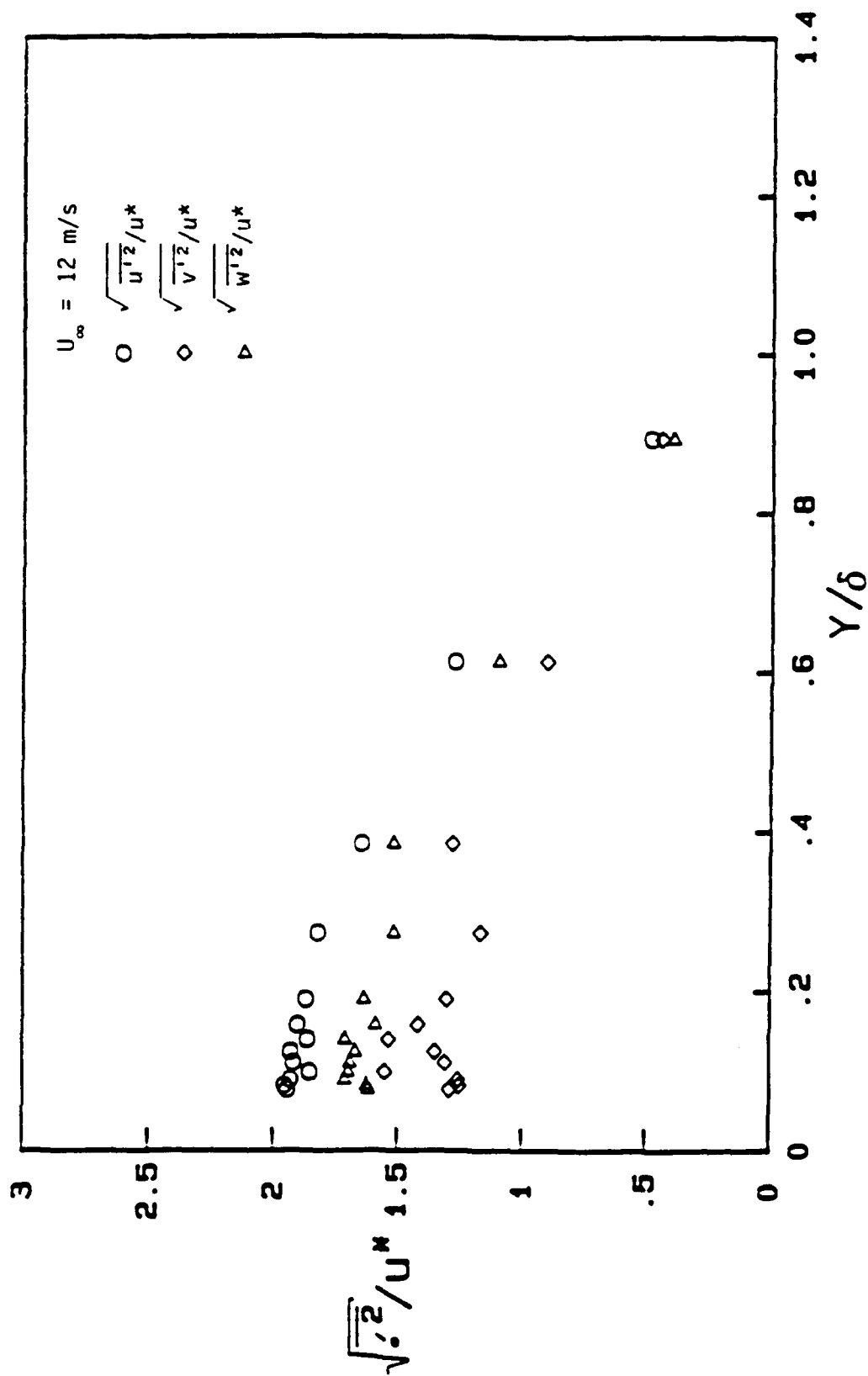


Figure 4.22 Profiles of all three Reynolds normal stresses for the  $L/d_0$   
 - 4 rough surface.



# Hemispherical Roughness

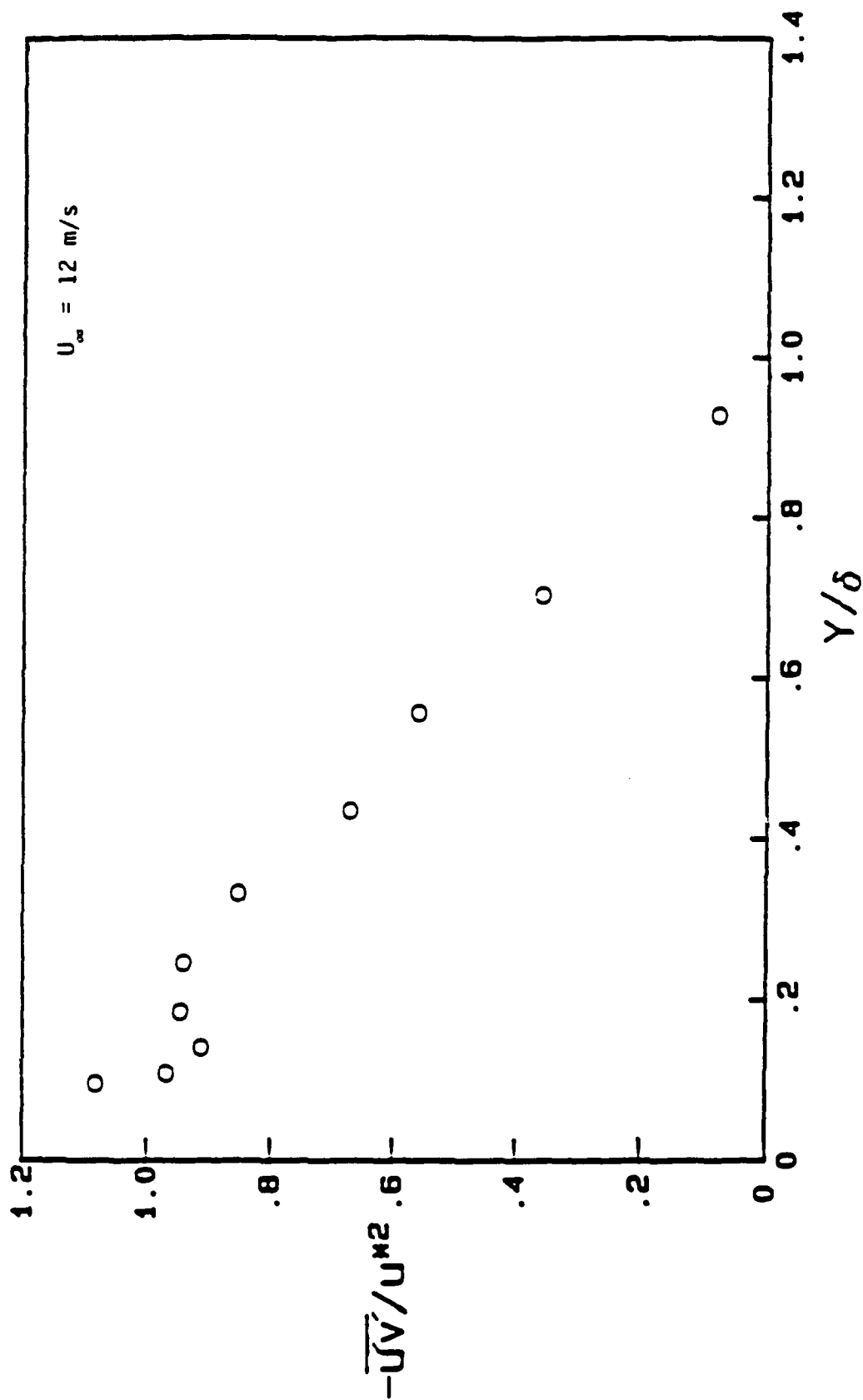


Figure 4.23 Profile of Reynolds shear stress for the  $L/d_0 = 4$  surface.

# Hemispherical Roughness

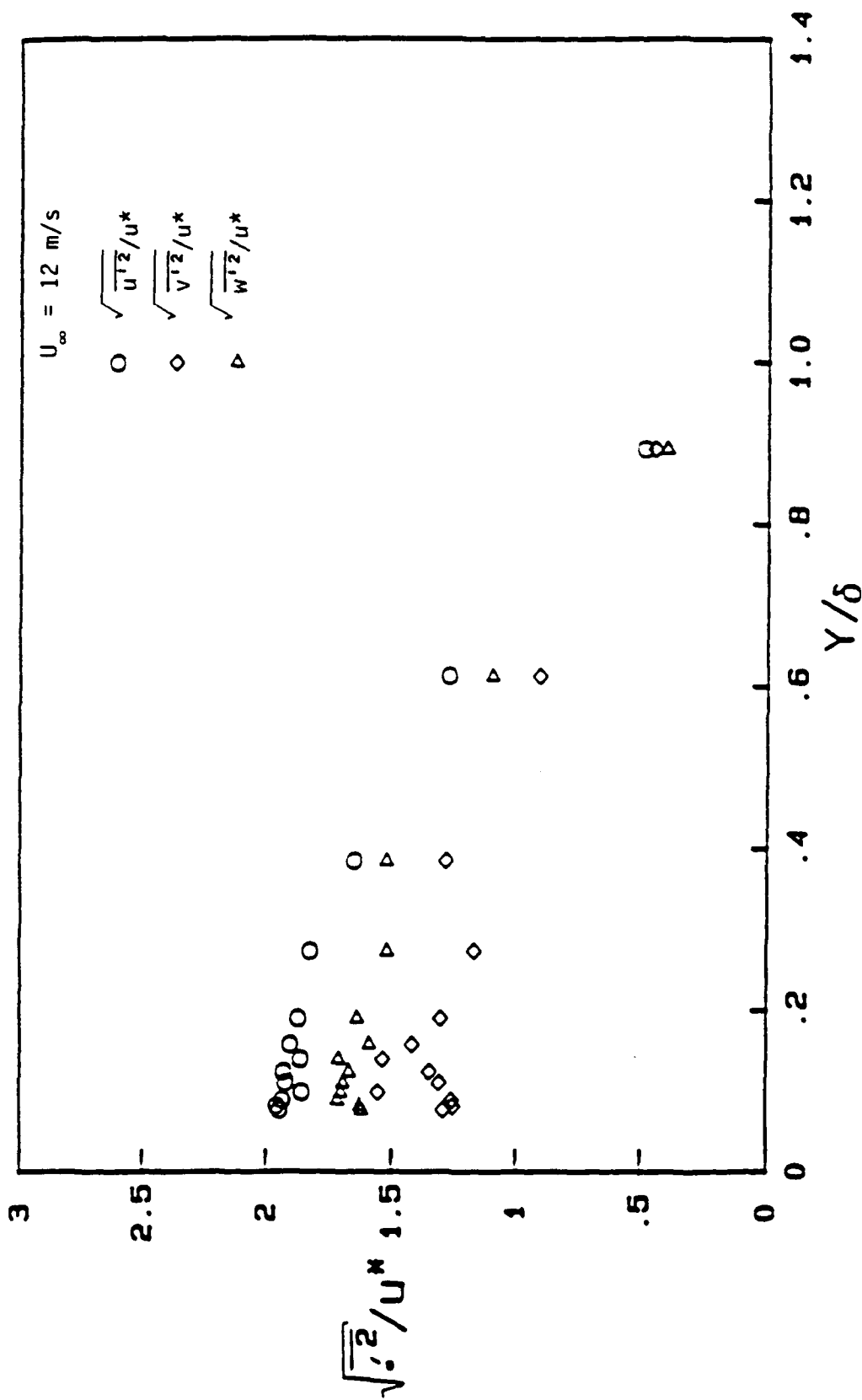


Figure 4.24 Profiles of all three Reynolds normal stresses for the  $l/d_0$  - 2 rough surface.

# Hemispherical Roughness

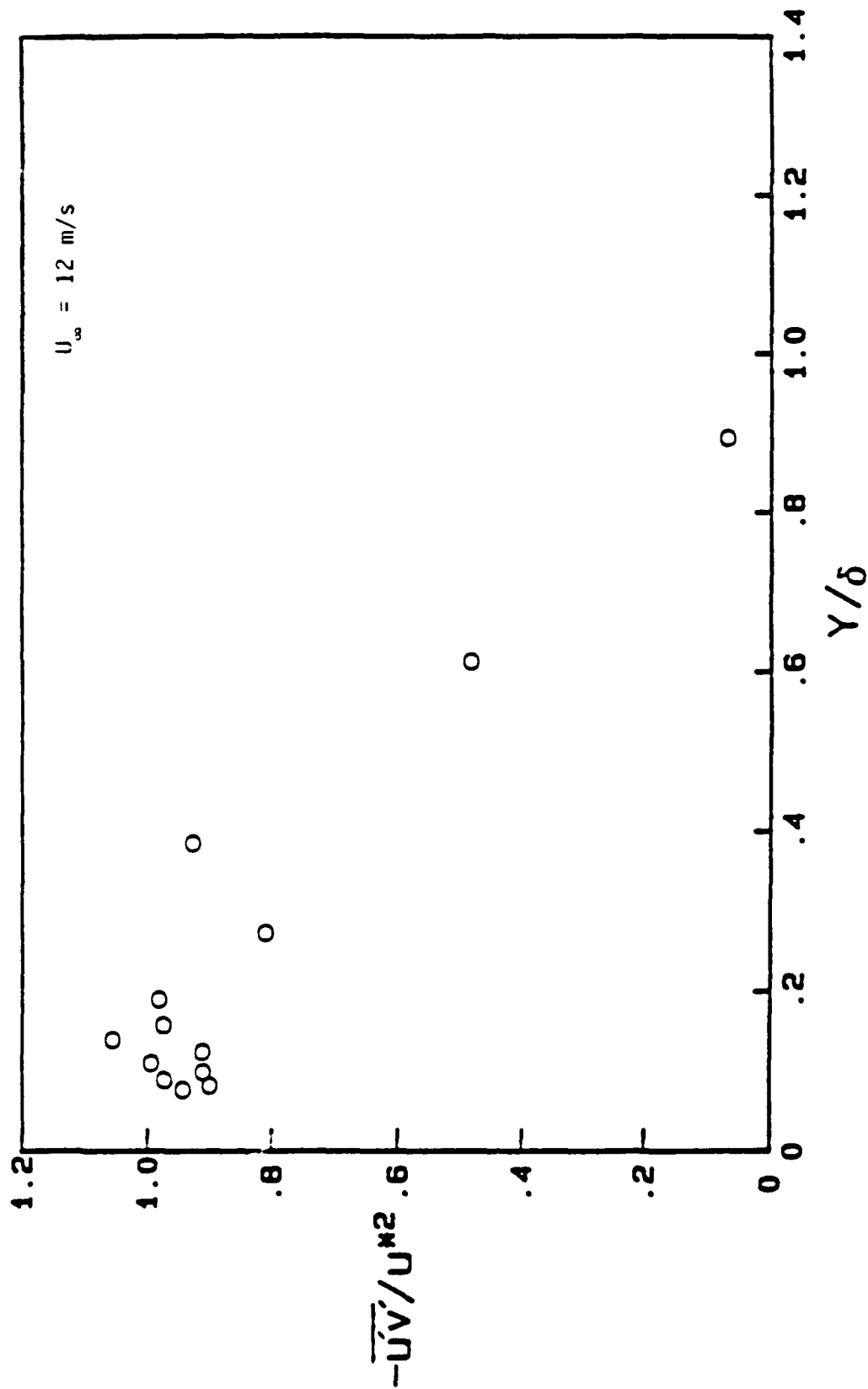


Figure 4.25 Profile of Reynolds shear stress for the  $L/d_0 = 2$  surface.

# Hemispherical Roughness

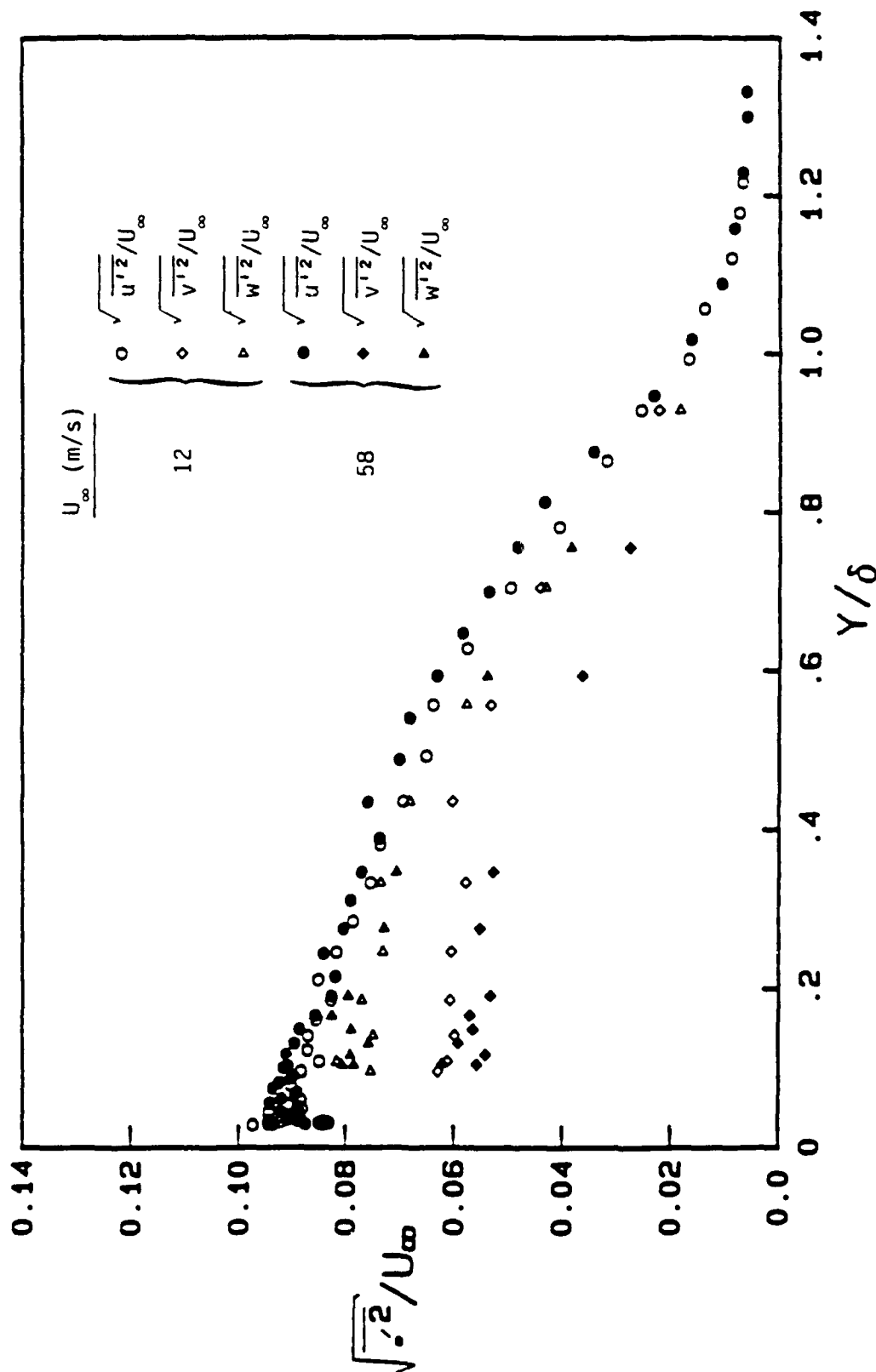


Figure 4.26 Reynolds normal stresses normalized by freestream velocity vs.  $y/\delta$  for the  $L/d_0 = 4$  surface illustrating the influence of freestream velocity.

# Hemispherical Roughness

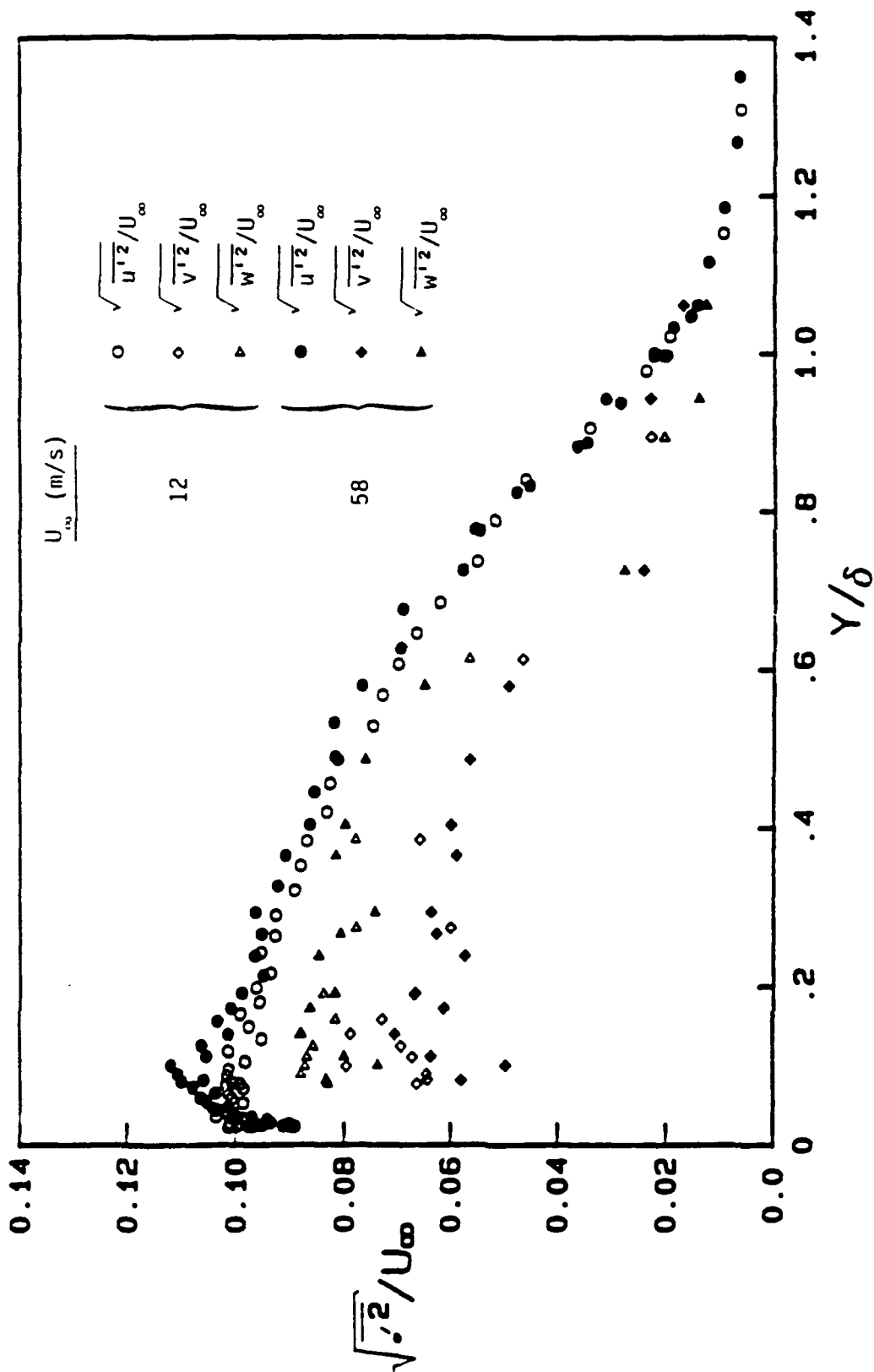


Figure 4.27 Reynolds normal stresses normalized by freestream velocity vs.  $y/\delta$  for the  $L/d_0 = 2$  surface illustrating the influence of freestream velocity.

# Hemispherical Roughness

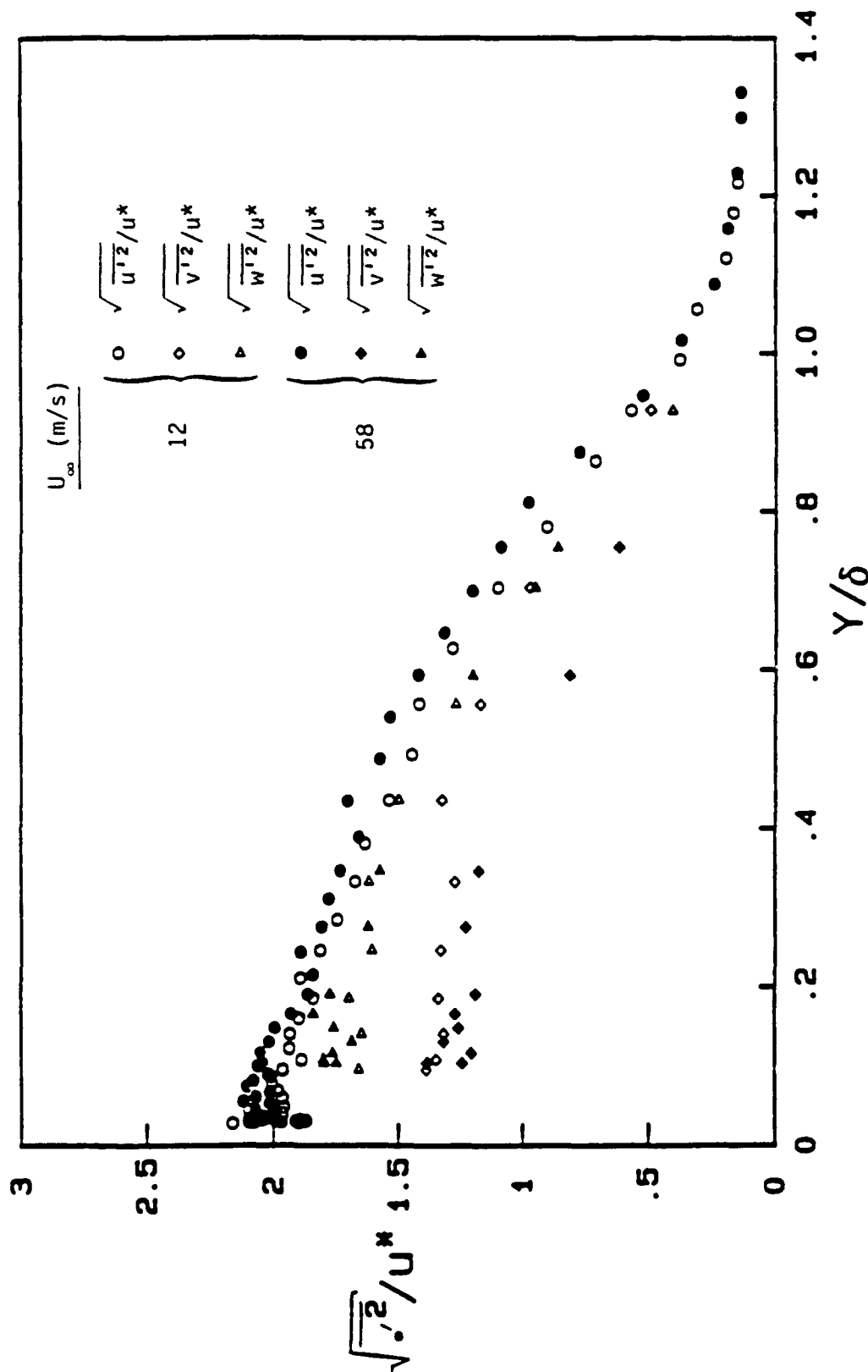


Figure 4.28 Reynolds normal stresses normalized by friction velocity vs.  $y/\delta$  for the  $L/d_0 = 4$  surface illustrating the influence of freestream velocity.

# Hemispherical Roughness

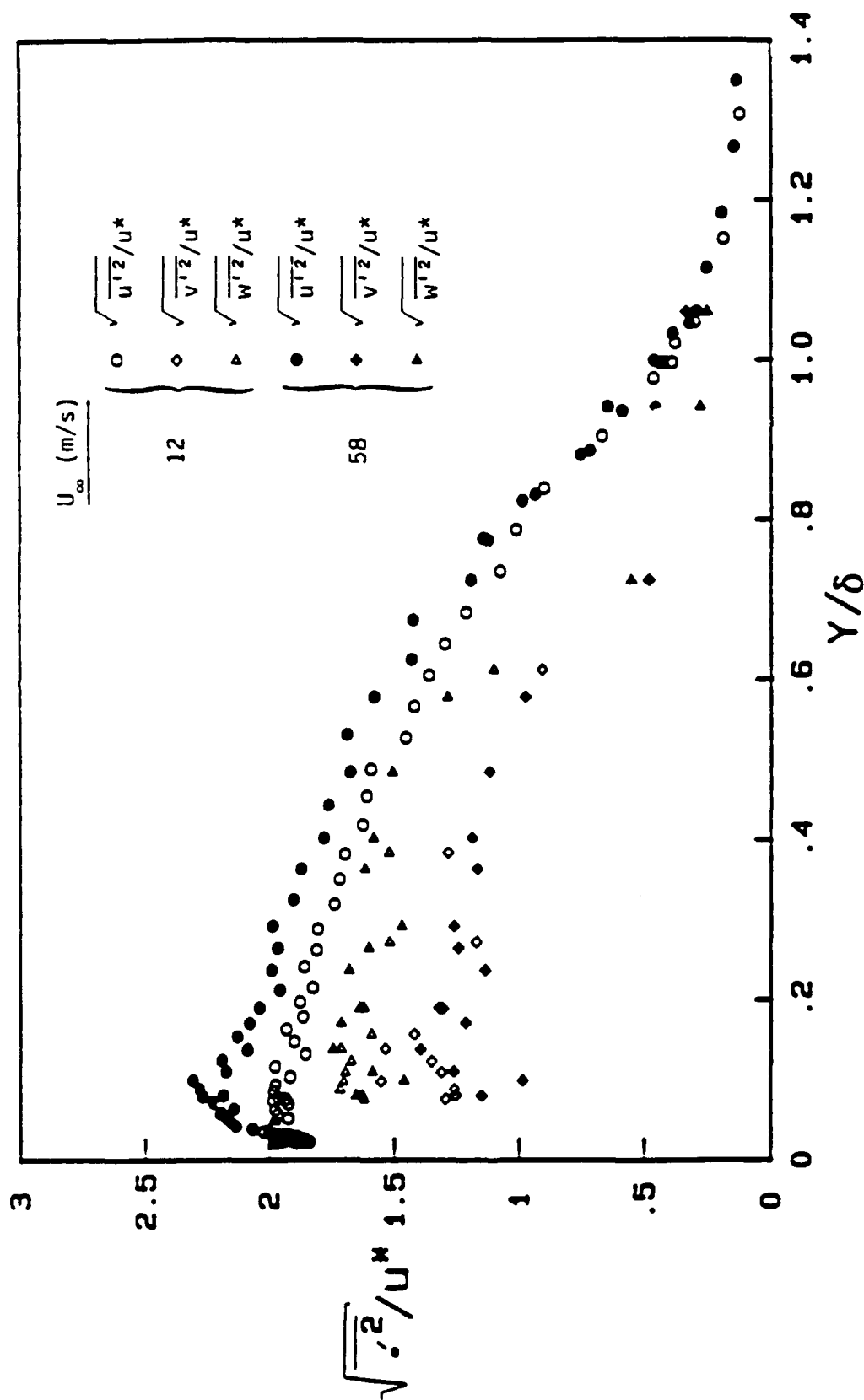


Figure 4.29 Reynolds normal stresses normalized by friction velocity vs.  $y/\delta$  for the  $L/d_0 = 2$  surface illustrating the influence of freestream velocity.

# Hemispherical Roughness

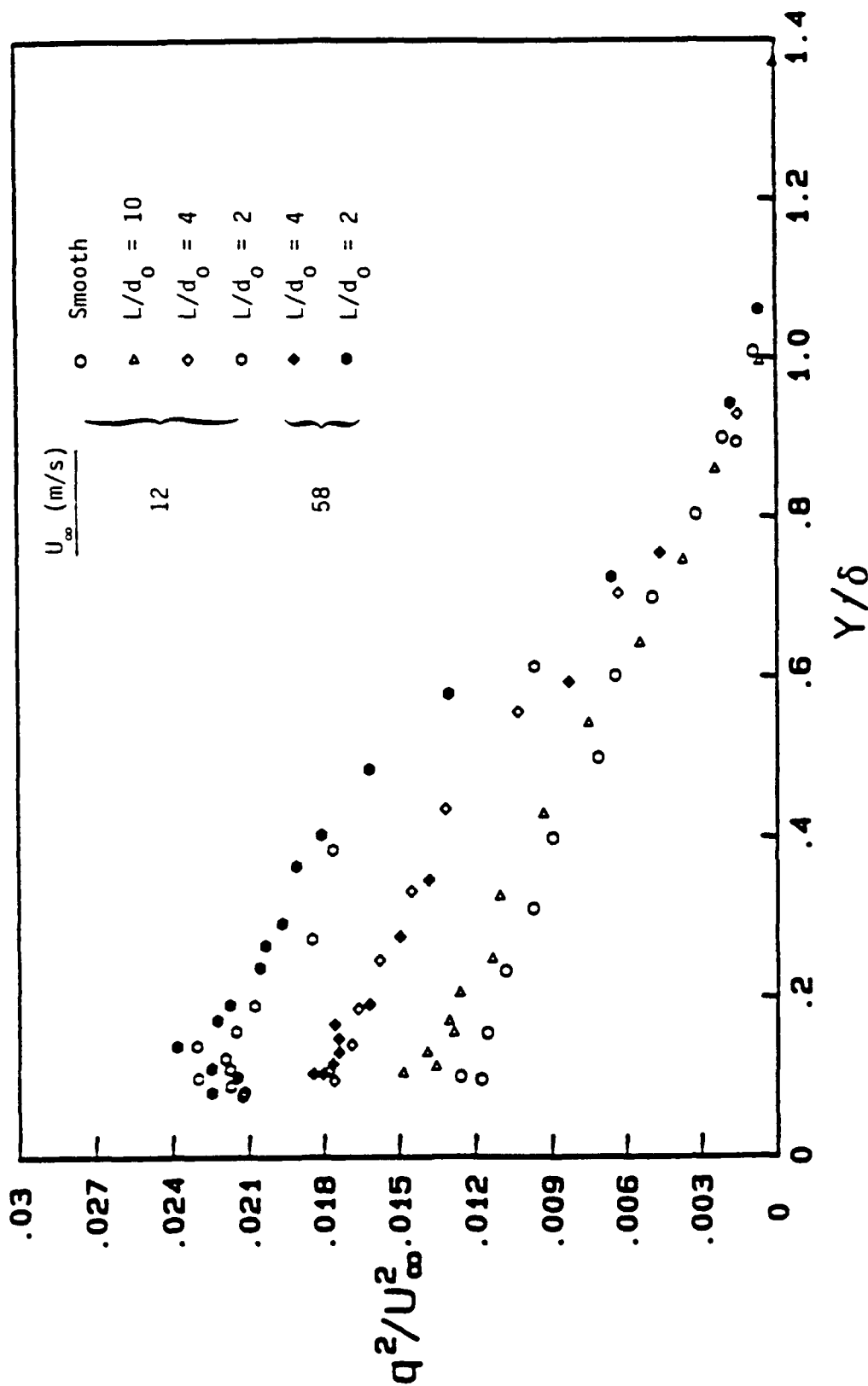


Figure 4.30 Comparison of the turbulent kinetic energy profiles normalized by freestream velocity for the smooth and the three rough surfaces.



# Hemispherical Roughness

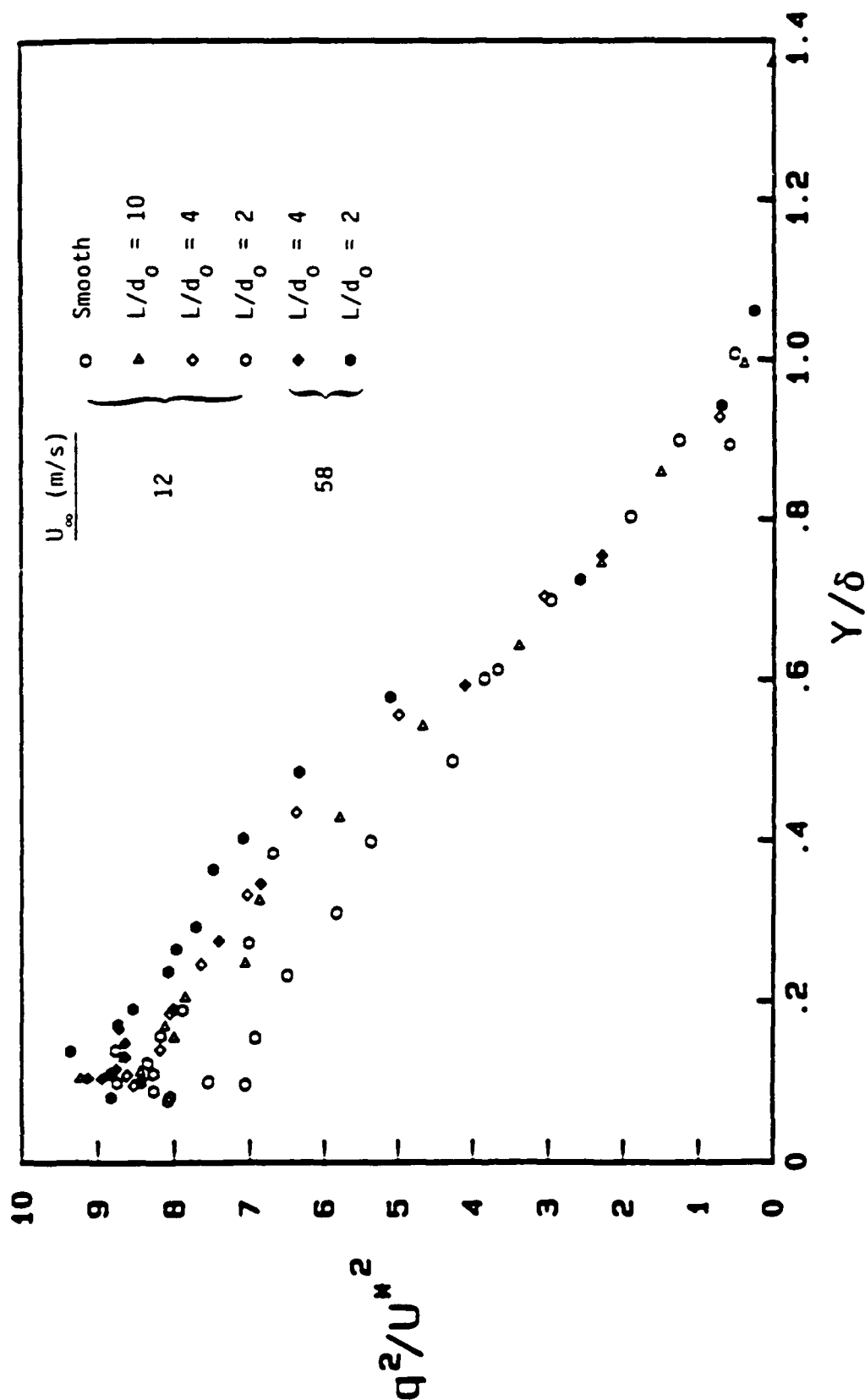


Figure 4.31 Comparison of the turbulent kinetic energy profiles normalized by friction velocity for the smooth and the three rough surfaces.

# Hemispherical Roughness

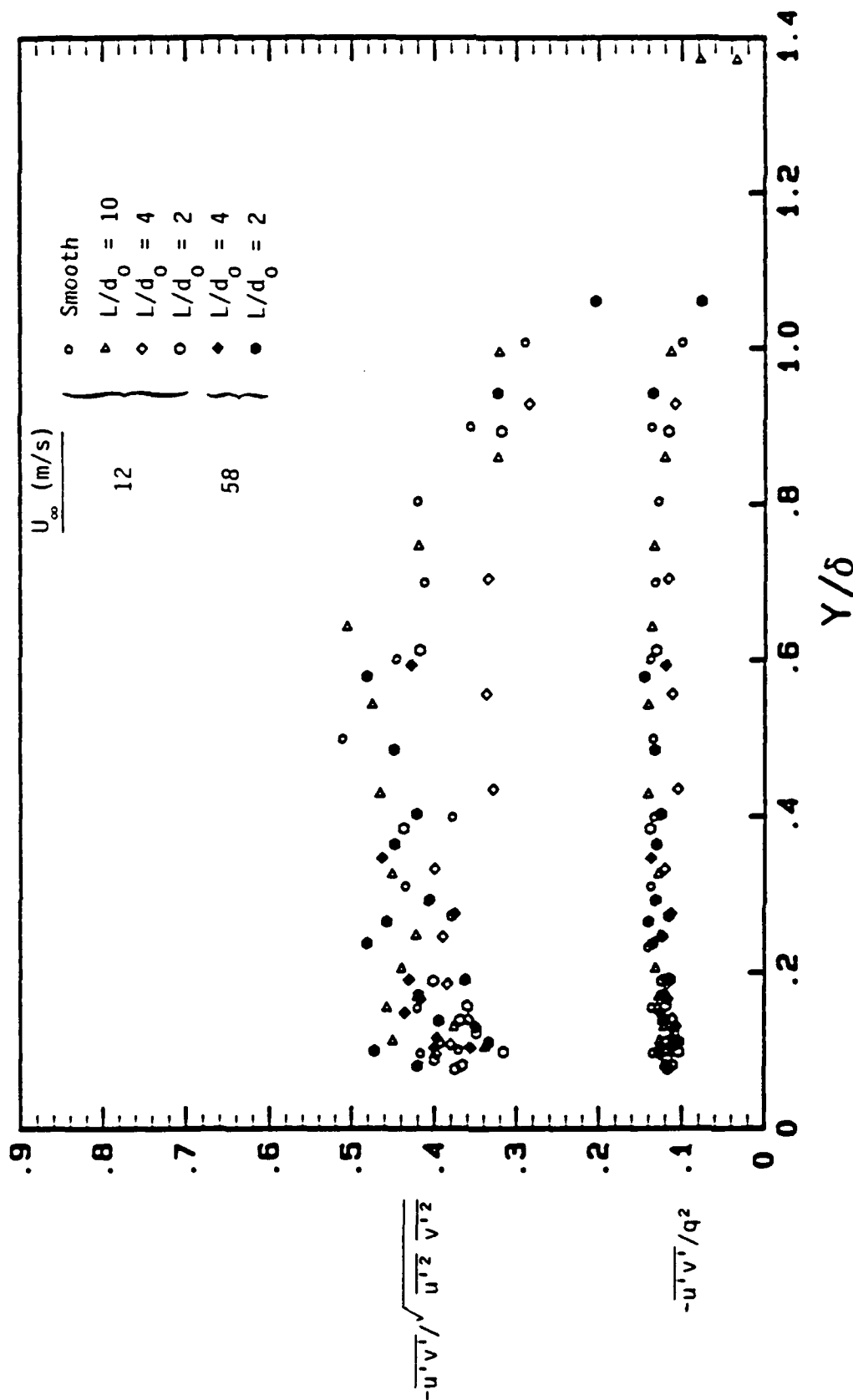


Figure 4.32 Distribution of Reynolds shear stress correlation coefficients through the boundary layer.

# Hemispherical Roughness

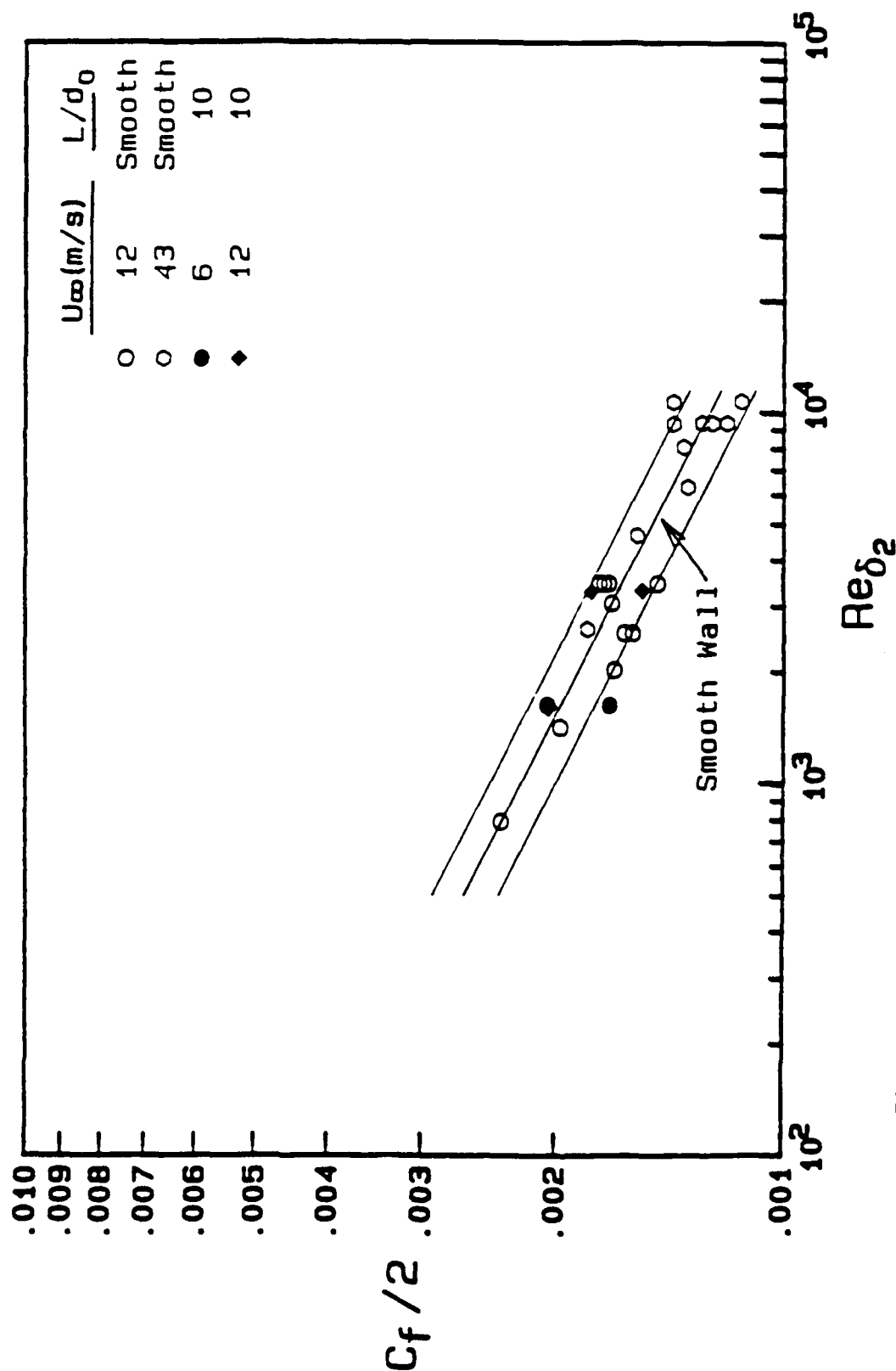


Figure 4.33 Skin friction coefficient distributions for the smooth and the  $L/d_0 = 10$  rough surfaces compared with the  $Re_{\delta_2}$  correlation (Eq. 3.2).

# Hemispherical Roughness

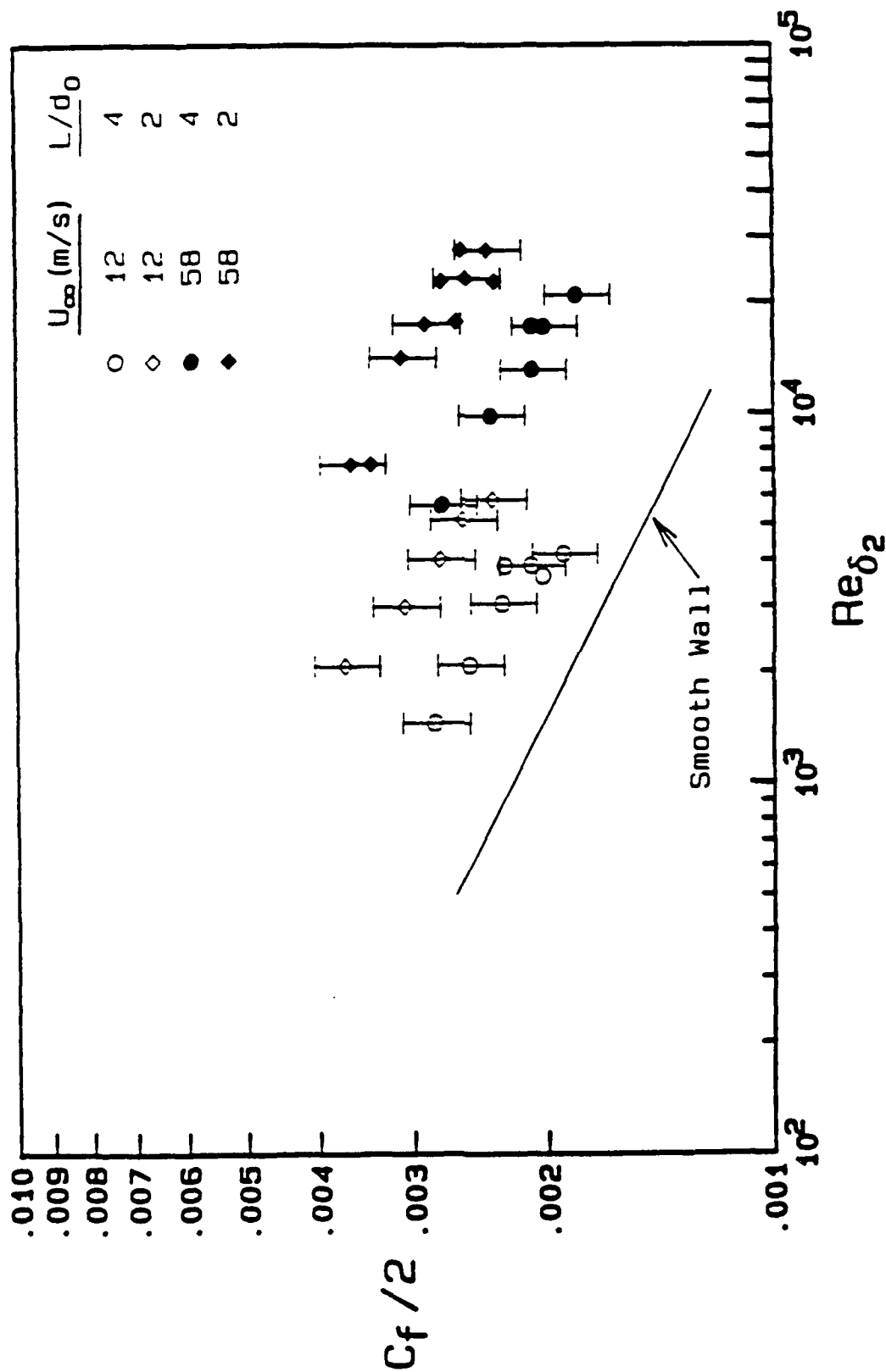


Figure 4.34 Comparison of the skin friction coefficient distributions for the  $L/d_0 = 4$  and  $L/d_0 = 2$  surfaces in  $Re_{\delta_2}$  coordinates.

# Hemispherical Roughness

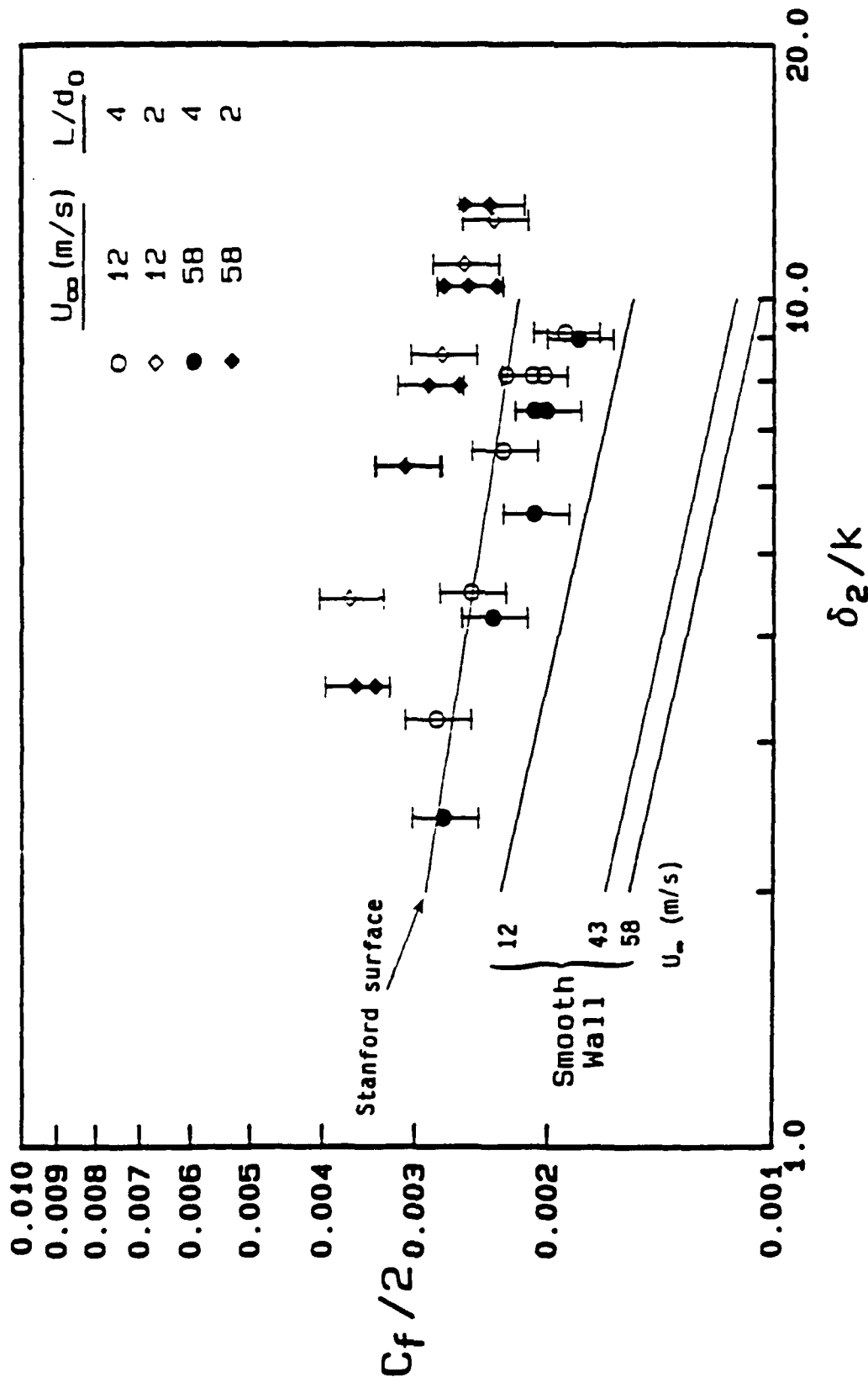


Figure 4.35 Comparison of the skin friction coefficient distributions for the  $L/d_0 = 4$  and  $L/d_0 = 2$  surfaces in  $\delta_2/k$  coordinates.

# Hemispherical Roughness

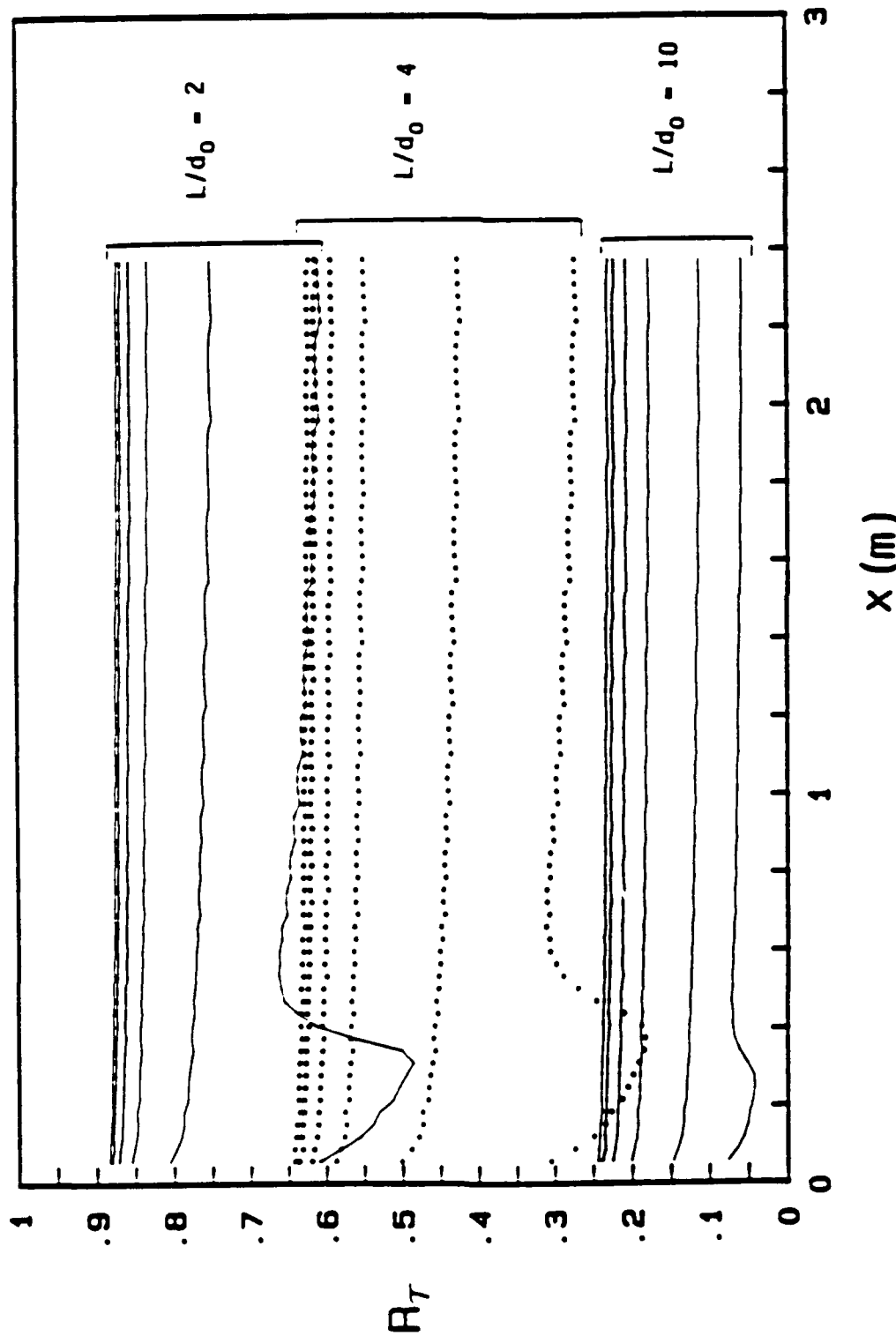


Figure 4.36 Comparison of the calculated values of  $R_T$  from the discrete element method for the THTF rough surfaces. For each surface  $R_T$  increases with  $U_\infty$  (6, 12, 28, 43, 58 and 67 m/s).

Table 4.1 Classification of flow regimes for the hemispherically-roughened THTF surfaces based on  $\overline{u'^2}$  behavior and calculated  $R_\tau$  values.

$U_\infty$ (m/s)	$L/d_0 = 10$		$L/d_0 = 4$		$L/d_0 = 2$	
	$\overline{u'^2}$	$R_\tau$	$\overline{u'^2}$	$R_\tau$	$\overline{u'^2}$	$R_\tau$
6	TR	S/LOWER TR	TR	TR	TR	LOWER FR
12	TR	TR	TR	TR	UPPER TR/ LOWER FR	FR
28	TR	TR	FR	UPPER TR/ LOWER FR	FR	FR
43	--	TR	FR	LOWER FR	FR	FR
58	--	TR	FR	LOWER FR	FR	FR
67	--	TR	--	LOWER FR	--	FR

S - Smooth  
 TR - Transitionally Rough  
 FR - Fully Rough

## CHAPTER 5

### HEAT TRANSFER RESULTS

One of the most important aspects of this research program is the development of boundary layer heat transfer data on well-defined rough surfaces which can be used to formulate and refine energy transport predictive models. Since there exists a critical need for boundary layer heat transfer data on well-defined rough surfaces, extreme care was taken to obtain accurate, comprehensive sets of data over a number of freestream velocities between 6 and 67 m/s on five different rough surfaces such that the total sets of data thoroughly cover behavior in the aerodynamically smooth, transitionally rough, and fully rough regimes.

This chapter presents the experimental heat transfer results obtained for turbulent boundary layer flow over the three different well-defined rough surfaces with hemispherical elements for nominal freestream velocities of 6, 12, 28, 43, 58, and 67 m/s. The primary results are the Stanton number measurements in the Turbulent Heat Transfer Test Facility (THETF) for the three rough surfaces. In addition, the characteristics of thermal boundary layers for rough wall flow regimes (aerodynamically smooth, transitionally rough, and fully rough) are investigated.

Furthermore, the THETF Stanton number data are compared with the Stanford data taken on a single rough surface comprised of 1.27 mm diameter spheres packed in the most dense array. The three THETF



rough surfaces were composed of 1.27 mm diameter hemispheres spaced 2, 4 and 10 diameters apart. The Stanford surface and the THTF surfaces can be considered to be in the same family of rough surfaces if one assumes that surfaces of 1.27 mm spheres and 1.27 mm hemispheres spaced in the most dense array appear similar to a turbulent boundary layer.

All of the THTF data are for zero pressure gradient, constant wall temperature, incompressible boundary layer flow. The boundary layer was tripped at the leading edge of the test surface.

#### 5.1 STANTON NUMBER DATA

The THTF Stanton number data were determined from energy balances on each test plate, as discussed in detail in Appendix I. The data of the present study are presented using a definition of the Stanton number which is based on the difference between the wall temperature and the freestream total temperature, as did Healzer (1974), Pimenta (1975), Coleman (1976) and Ligrani (1979) for the Stanford surface. This is in contrast to the traditional choice of wall temperature minus recovery temperature traditionally used for smooth wall Stanton numbers. There are indications that the plate recovery temperature is a function of the surface roughness (Hodge, Taylor and Coleman (1986)), and the freestream total temperature is thus a more firmly defined variable.

Stanton number data sets are presented graphically in two formats: (1) with an ordinate of  $St$  and abscissa of  $Re_x$ , and (2) with an ordinate of  $St$  and abscissa of  $\Delta_2/k$ , where  $\Delta_2$  is the

enthalpy thickness and  $k$  is the roughness height (which corresponds to the sphere radius,  $r$ , used in the original Stanford surface data presentations). Values of  $Re_x$  were computed with the length scale ( $x$ ) taken as the distance from the leading edge of the first plate. To compute  $\Delta_2/k$ , the enthalpy thickness corresponding to each Stanton number was determined by numerical integration of the applicable form of the integral energy equation (Kays and Crawford, 1980)

$$St = d\Delta_2/dx \quad (5.1)$$

In order to contrast the data for rough surfaces with the smooth wall results, each plot of rough wall Stanton number data includes a curve representing the smooth wall correlation. In plots of  $St$  versus  $Re_x$ , the smooth wall Stanton number correlation expression described in Chapter 3

$$St = 0.185 (\log_{10} Re_x)^{-2.584} Pr^{-0.4} \quad (3.3)$$

is used.

As described in Appendix I, the uncertainty analysis of the Stanton number determinations was based on the ANSI/ASME Standard on Measurement Uncertainty (1986), following the procedures of Coleman and Steele (1989). As was discussed in Chapter 3, a detailed uncertainty analysis of the determination of Stanton numbers using the THTTF was made during the design and construction phase of the test facility. This analysis showed that the precision limits corresponding to the measured variables were negligible relative to the bias limits. This meant that replications of Stanton number at a given experimental set point ( $U_\infty$ ) should show negligible scatter, since any significant errors were estimated to be bias errors that

would be the same in all replications. The Stanton numbers for smooth wall runs at  $U_\infty = 12$  m/s and the rough wall runs at 6 m/s showed a small but noticeable scatter and the estimate of zero precision limit (no scatter) for these runs was not valid. Investigation showed that at low freestream velocities-- $U_\infty \leq 12$  m/s for the smooth wall tests and  $U_\infty \leq 6$  m/s for the rough wall tests--the heat transfer coefficients are relatively low and the time constant of THTTF is thus increased. At these conditions the time constant of the THTTF is large enough so that the relatively long period variations in facility line voltage to the test plate heater circuits and the temperature of the incoming make-up water for the heat exchanger loop affect the ability to hold a tight steady state condition. These unexpected annoyances were not accounted for in the uncertainty analysis during the design phase. Observations of the Stanton number results for eight smooth wall runs and three rough wall runs produced a 95 percent confidence estimate of a precision limit in Stanton numbers of 3 percent for these conditions. The 3 percent precision limit contribution was combined by root-sum-square with the estimated bias limit to obtain the overall uncertainty in Stanton numbers. The plots of Stanton numbers presented in this chapter include uncertainty bands on selected data points which show typical overall uncertainty limits on Stanton numbers.

Figure 5.1 shows a composite plot of the THTTF Stanton number data for nominal freestream velocities of 12, 28, 43, 58, 67 m/s for the three rough surfaces and the smooth THTTF surface. The 6 m/s data sets are not included in this plot since the trip at the nozzle

exit did not immediately trip the boundary layer turbulent at this freestream velocity. Thus at this velocity there existed transition regions from laminar to turbulent flow at different  $Re_x$  for the three rough surfaces. This would make such a composite plot hopelessly cluttered if such data were included. This figure clearly shows the influence of roughness on the Stanton numbers, as Stanton number increases with increased roughness density.

It was shown for the smooth surface in Figure 3.7 that, in these coordinates, data sets corresponding to 5 different freestream velocities collapsed to a single curve, as expected. For the three rough surfaces, the Stanton number data sets appear to collapse to single curves for  $U_\infty = 28$  m/s and greater. However, the Stanton numbers at  $U_\infty = 12$  m/s for all three rough surfaces exhibit a distinct shift from corresponding data sets taken at higher freestream velocities.

Figure 5.2 shows Stanton number data sets reported by Healzer (1974) and Pimenta (1975) for constant wall temperature, zero pressure gradient turbulent boundary layer flows over the Stanford surface plotted in  $St$  versus  $Re_x$  coordinates. These data exhibit similar behaviors to the three THTF rough surfaces in that the data for the highest freestream velocities appear to collapse together in these coordinates. However, for this surface the data for  $U_\infty = 27$  m/s fall below the higher  $U_\infty$  data rather than collapsing together with them. Neither Healzer nor Pimenta stressed the apparent ap-

proach of the  $St$  data to a single curve versus  $Re_x$  as  $U_\infty$  increased. Rather, they postulated such behavior in  $St$  versus  $\Delta_2/r$  coordinates, as will be discussed later.

Figures 5.3, 5.4, and 5.5 present the THTF Stanton number data plotted versus  $Re_x$  for nominal freestream velocities of 6, 12, 28, 43, 58, and 67 m/s for the  $L/d_0 = 2$ ,  $L/d_0 = 4$ , and  $L/d_0 = 10$  rough surfaces, respectively. As seen in these figures, except for the lower freestream velocities (6 and 12 m/s), the THTF Stanton number data sets for different freestream velocities do not exhibit freestream velocity dependency. In fact, the Stanton number data for freestream velocities of 28 m/s and higher for each of the three different rough surfaces are coherent in these coordinates, considering the data uncertainty. It appears that the Stanton number data for freestream velocities of 12 m/s and less correspond to a different flow regime.

Figure 5.6 shows Stanton number data for nominal freestream velocities of 9, 16, 27, 40, 58, and 74 m/s from the Stanford surface plotted versus  $\Delta_2/r$ , where  $r$  is the radius of the spherical roughness elements. Healzer proposed that the  $St$  versus  $\Delta_2/r$  coordinates are more appropriate for presenting rough wall Stanton number results. He postulated that since his data showed no apparent velocity dependence in these coordinates, the Stanton number was a function only of  $\Delta_2/r$  for all velocities.

Pimenta (1975) studied both the Stanton number behavior and the turbulence characteristics of the boundary layer using the same rough porous surface. He concluded that, for the Stanford surface,

Stanton number behavior was independent of Reynolds number in the fully rough flow regime. He postulated that in the fully rough regime the Stanton number data plotted in  $St$  versus  $\Delta_2/r$  collapse together and that this characteristic may be used to distinguish rough wall flow regimes. He used this criterion for classification of his own three Stanton number runs for freestream velocities of 16, 27, and 40 m/s presented in Figure 5.7. He identified the 16 m/s run as transitionally rough and the 27 and 40 m/s runs as fully rough. However, he pointed out that the difference in the data for his 16 m/s transitionally rough run and the 27 and 40 m/s fully rough runs was small when plotted in these coordinates. He supported his classification of the 16 m/s run as transitionally rough using the  $\overline{u'^2}$  behavior discussed earlier in Chapter 4. Pimenta's final classification of flow regimes for the Stanford surface based on both  $St$  versus  $\Delta_2/r$  behavior and boundary layer structural studies was that the 9 and 16 m/s data were in the transitionally rough regime, and the data for  $U_\infty \geq 27$  m/s were in the fully rough regime.

Figures 5.8, 5.9, and 5.10 present THTTF Stanton number data for freestream velocities of 6, 12, 28, 43, 58, and 67 m/s for the  $L/d_0 = 2$ ,  $L/d_0 = 4$ , and  $L/d_0 = 10$  rough surfaces plotted in  $St$  versus  $\Delta_2/k$  coordinates. (Note that  $k$  corresponds to  $r$  for hemispherical elements, and that this value is numerically the same for the Stanford surface and the THTTF surfaces.) Figure 5.8 shows the  $L/d_0 = 2$  rough surface data, and only the 58 and 67 runs collapse together. If the criterion proposed by Pimenta were to be used, these two runs would be classified as fully rough and the others as

transitionally rough. This classification could not be supported by either the criterion based on the shape of the  $\overline{u'^2}$  profile or the criterion set by the magnitude of  $R_\tau$ , both of which indicate that the 12, 28, and 43 m/s data are in the fully rough regime. The classification of flow regimes for the  $L/d_0 = 10$  surface results based on the behavior of  $St$  versus  $\Delta_2/k$  (Figure 5.10) would be even more perplexing. Again, the 58 and 67 m/s results are coherent and would be classified as in the fully rough flow regime. However, based on  $\overline{u'^2}$  behavior and  $R_\tau$  values none of the runs on this surface correspond to the fully rough regime.

Based on observation of the data from the three THTF rough surfaces and the Stanford surface, it appears that the idea of roughness flow regimes based on heat transfer behavior in  $St$  versus  $\Delta_2/k$  or  $\Delta_2/r$  coordinates is not viable. The data do not support the idea that fully rough Stanton numbers are functions only of  $\Delta_2/r$ .

## 5.2 THERMAL BOUNDARY LAYER PROFILES

Mean temperature profiles were measured by traversing the boundary layer with a thermocouple probe as discussed in Appendix II. Mean temperature profiles were measured for freestream velocities of 6, 12, 28, 43, and 58 m/s for the  $L/d_0 = 2$ ,  $L/d_0 = 4$ , and  $L/d_0 = 10$  rough surfaces.

Non-dimensional temperature profiles for the smooth and the three rough surfaces for a freestream velocity of 12 m/s are presented in Figure 5.11 versus  $y/\Delta$ .

Previous studies have shown that temperature profiles along smooth flat plates of constant temperature in a zero pressure gradient, turbulent flow agree with the law of the wall for a thermal boundary layer as given by Kays and Crawford (1980)

$$T^+ = 2.195 \ln y^+ + 13.2 \text{ Pr} - 5.66 \quad (5.2)$$

Figure 5.12 shows the temperature profiles for a nominal flow velocity of 12 m/s for the smooth and the rough surfaces plotted in  $T^+$  versus  $y^+$  coordinates along with Eq. (5.2).



# Hemispherical Roughness

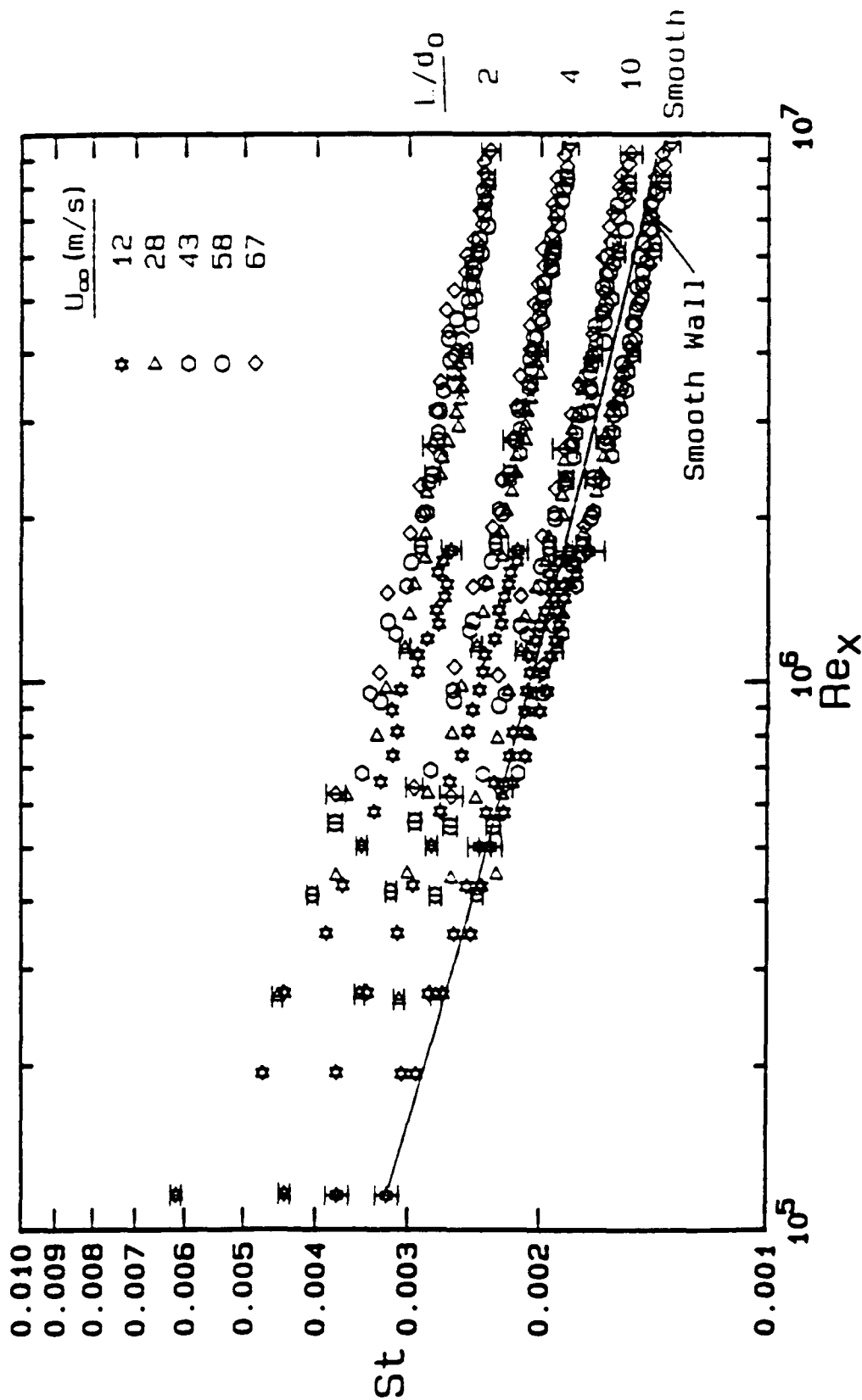


Figure 5.1 Composite plot of Stanton number data vs.  $Re_x$  for the TITTF smooth and rough surfaces.

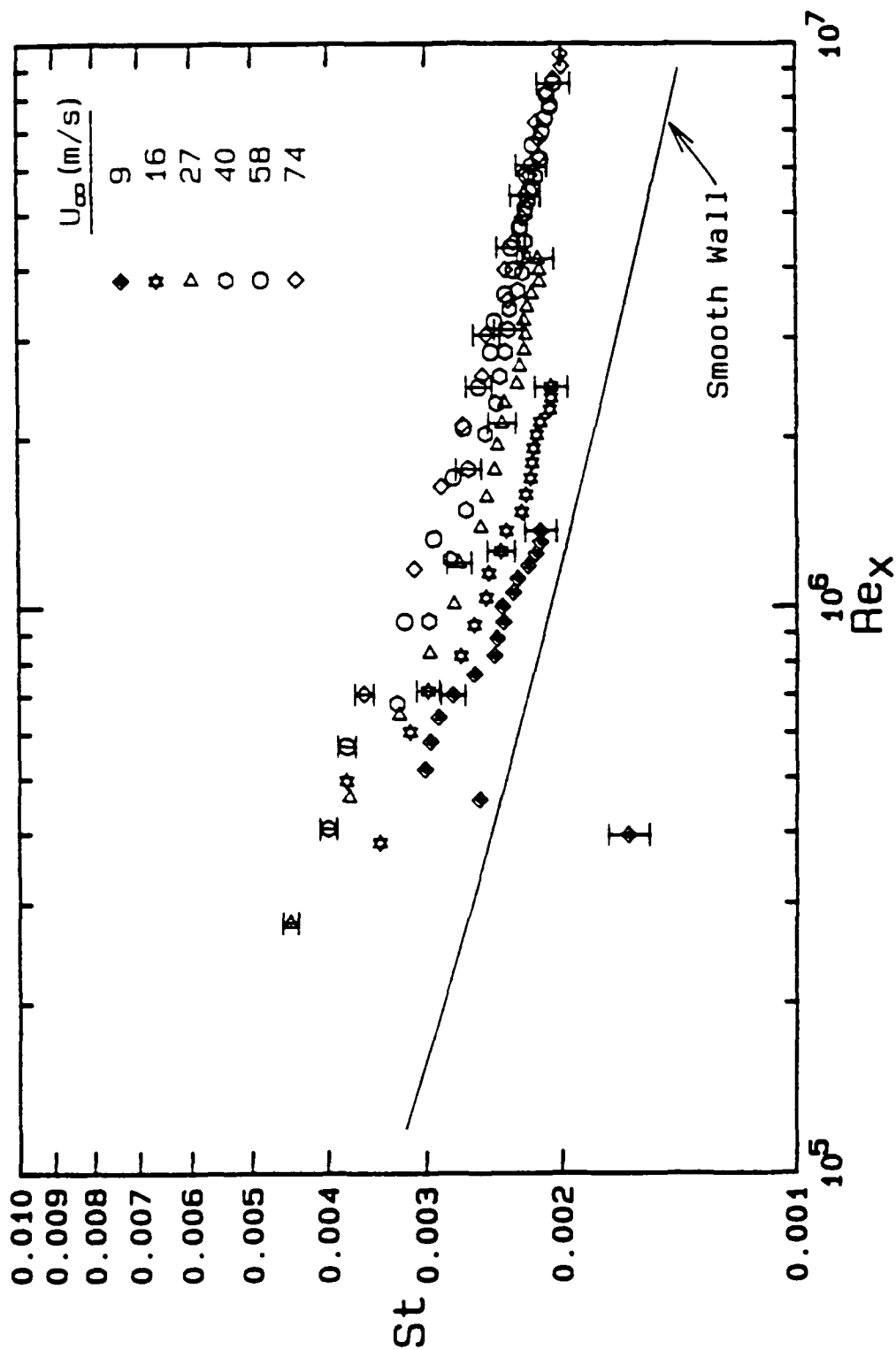


Figure 5.2 Composite plot of Stanton number data vs.  $Re_x$  for the Stanford surface reported by Healzer (1974) and Pimenta (1975).

# Hemispherical Roughness

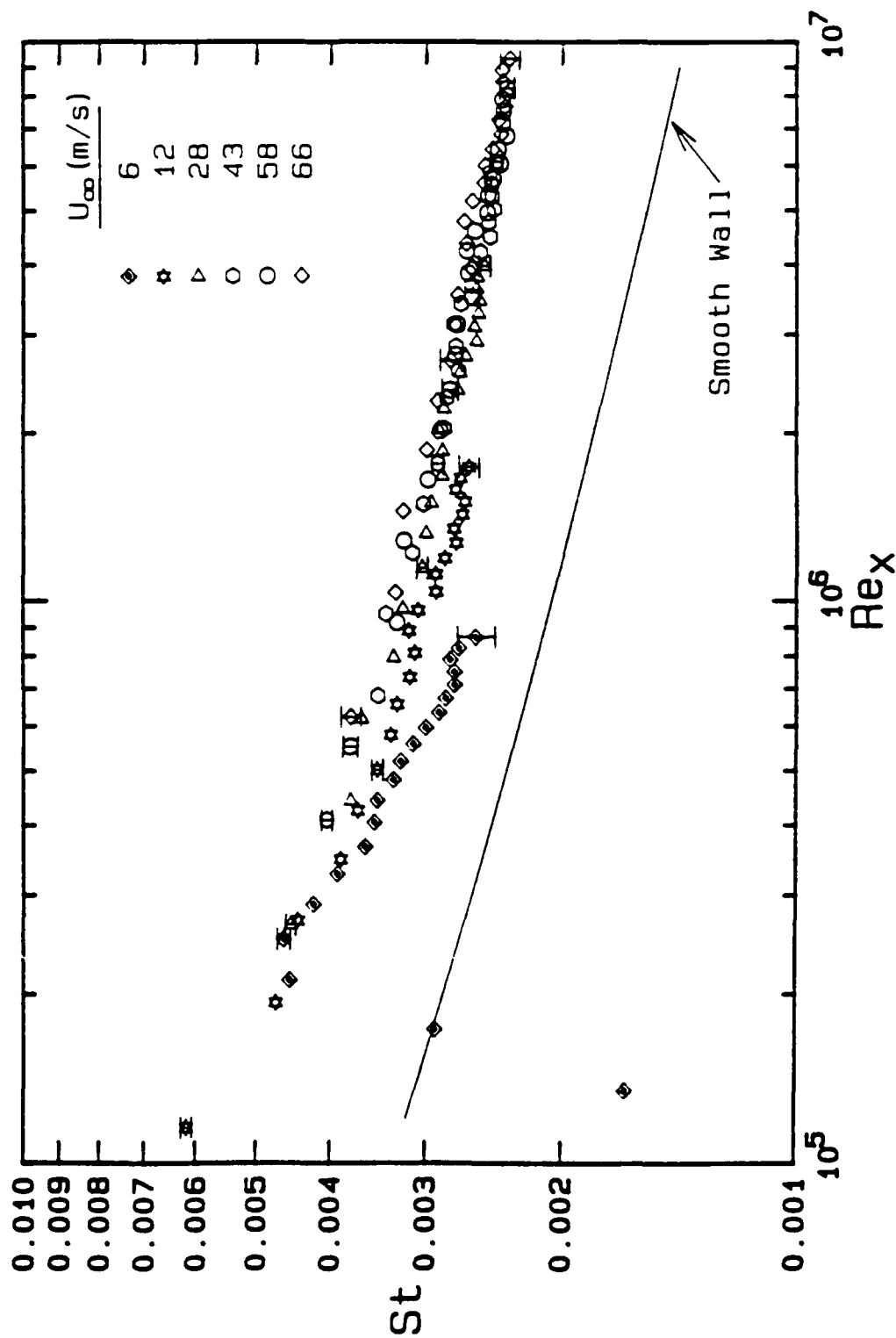


Figure 5.3 The IHTIF Stanton number data vs.  $Re_x$  for  $U_\infty = 6, 12, 28, 43, 58$  and  $67$  m/s for the  $L/d_0 = 2$  rough surface.

# Hemispherical Roughness

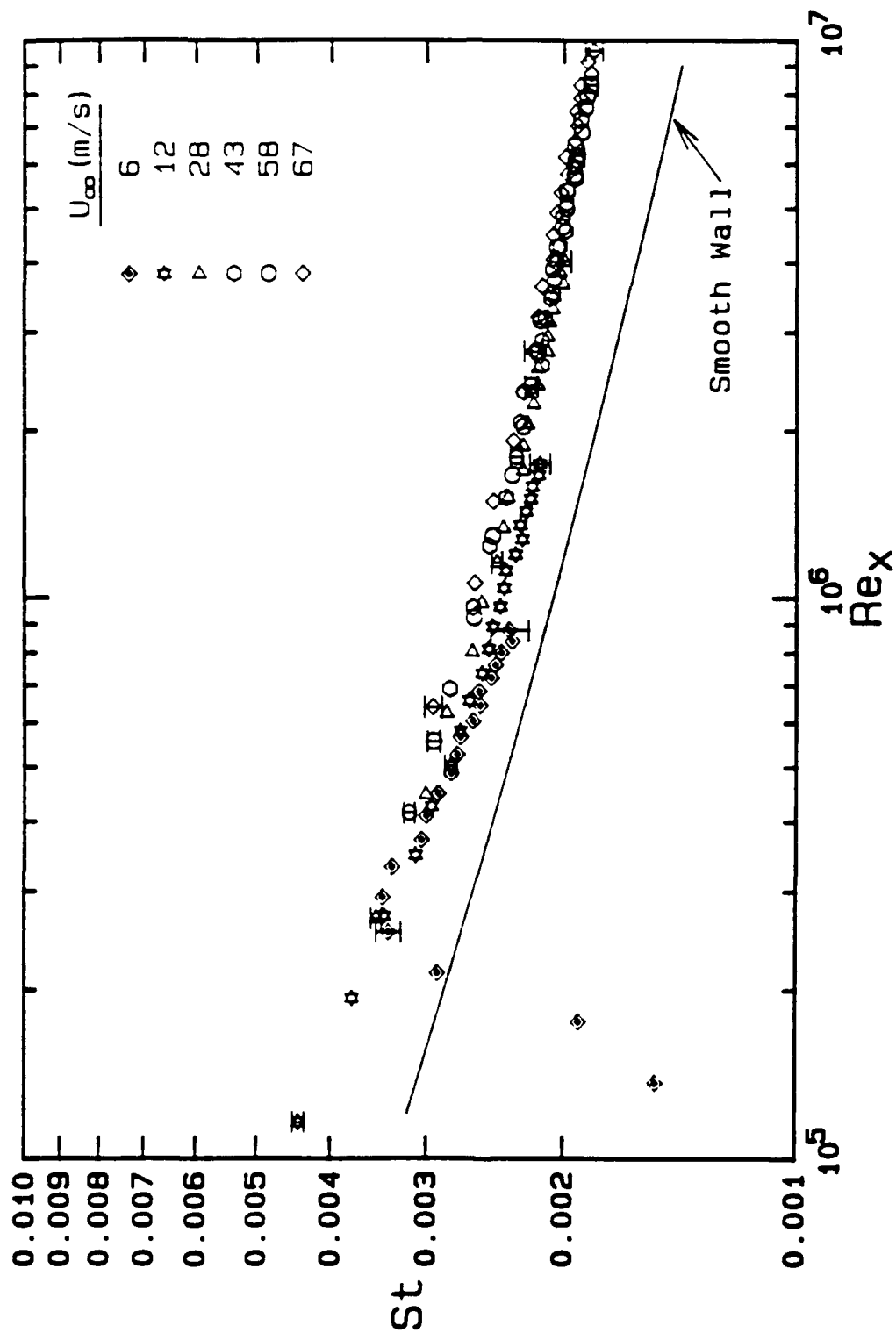


Figure 5.4 The THITF Stanton number data vs.  $Re_x$  for  $U_{\infty} = 6, 12, 28, 43, 58$  and  $67$  m/s for the  $L/d_0 = 4$  rough surface.

# Hemispherical Roughness

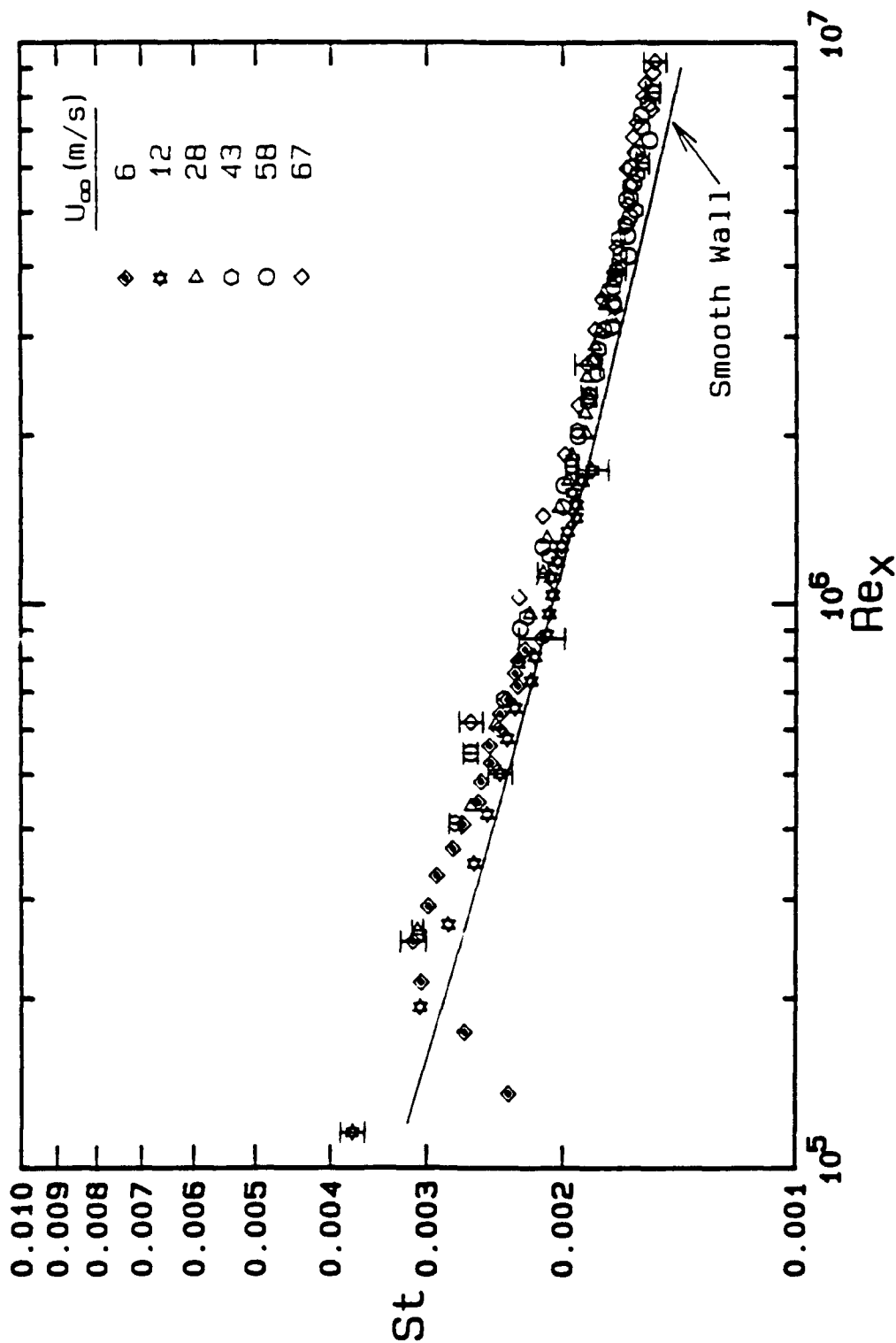


Figure 5.5 The IHTIF Stanton number data vs.  $Re_x$  for  $U_\infty = 6, 12, 28, 43, 58$  and  $67$  m/s for the  $L/d_0 = 10$  rough surface.

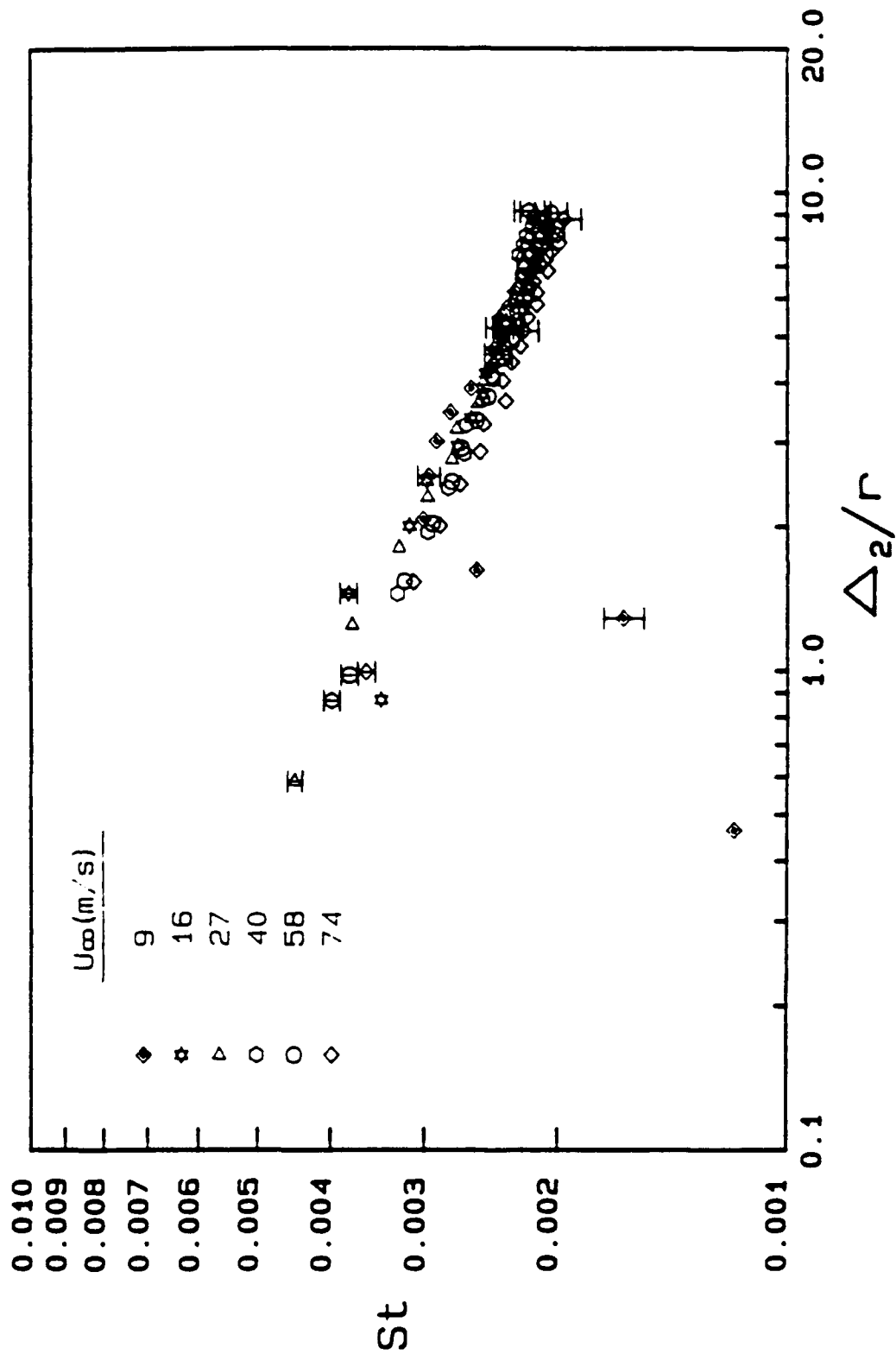


Figure 5.6 Composite plot of Stanton number data vs.  $\Delta_2/r$  for the Stanford surface reported by Healzer (1974) and Pimenta (1975).

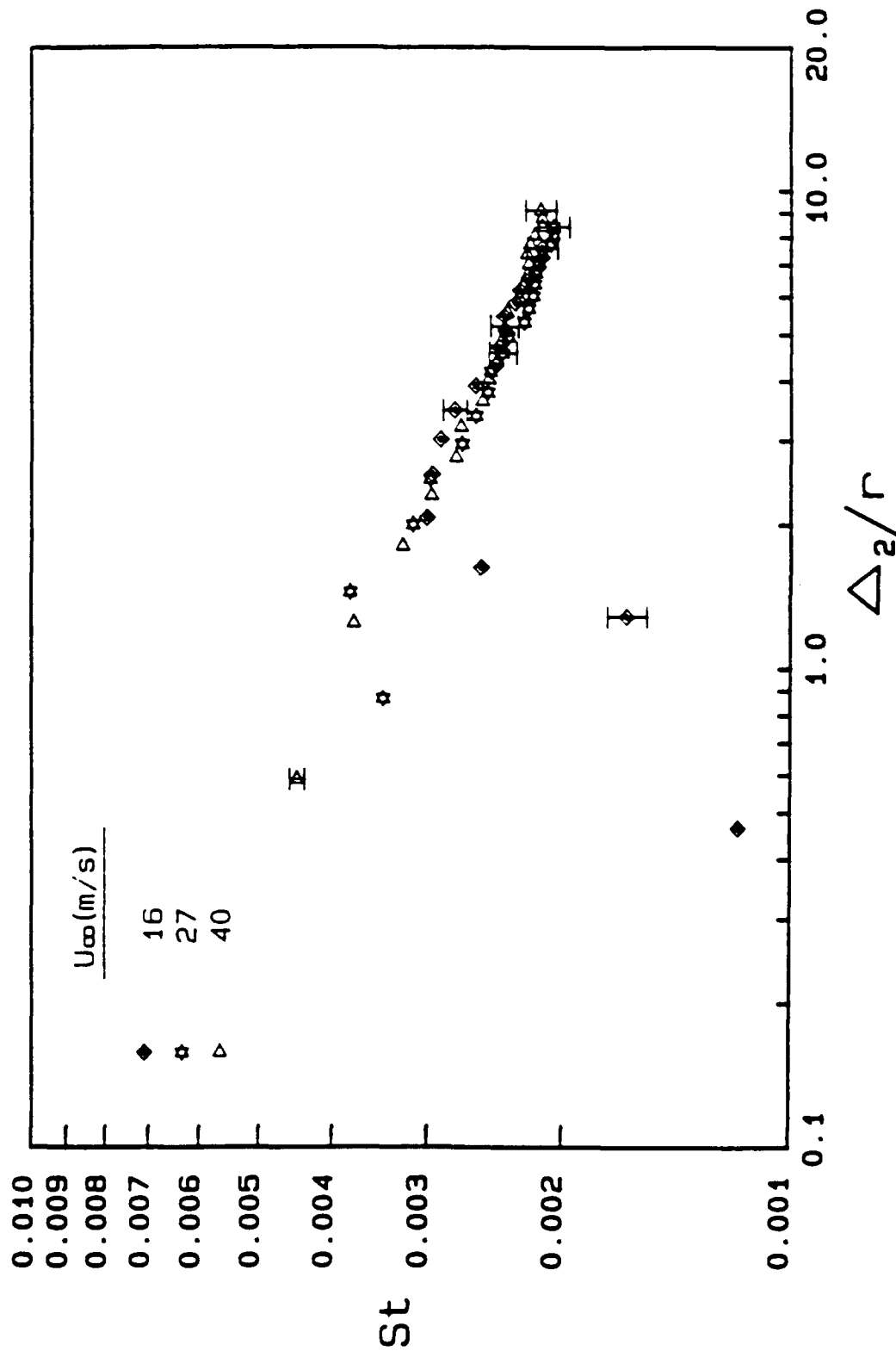


Figure 5.7 Stanton number data vs.  $\Delta_2/r$  for  $U_\infty = 16, 27$  and  $40$  m/s for the Stanford surface reported by Pimenta (1975).

# Hemispherical Roughness

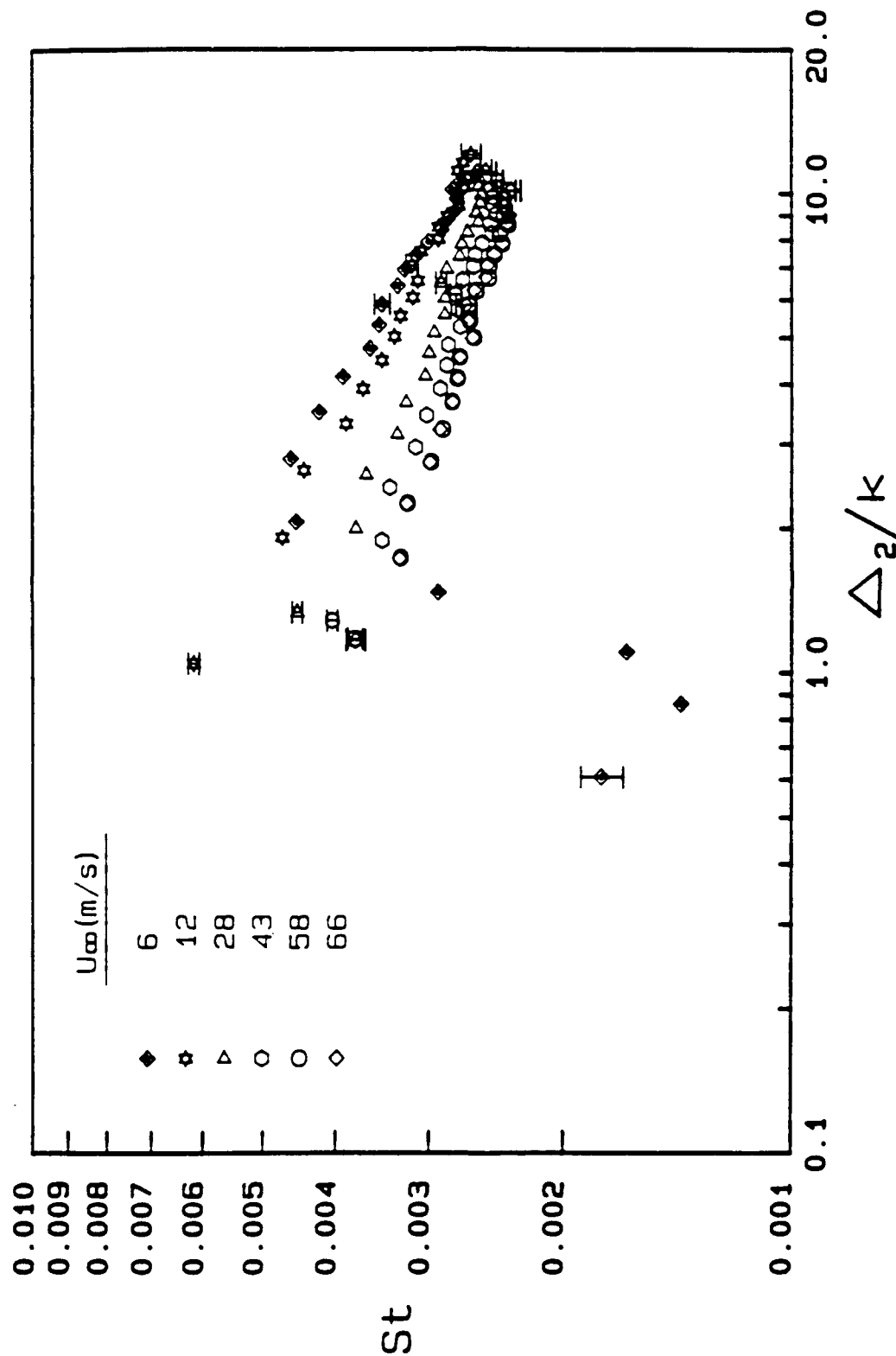


Figure 5.8 The THTF Stanton number data vs.  $\Delta_2/k$  for  $U_{\infty} = 6, 12, 28, 43, 58$  and  $67$  m/s for the  $L/d_0 = 2$  rough surface.



# Hemispherical Roughness

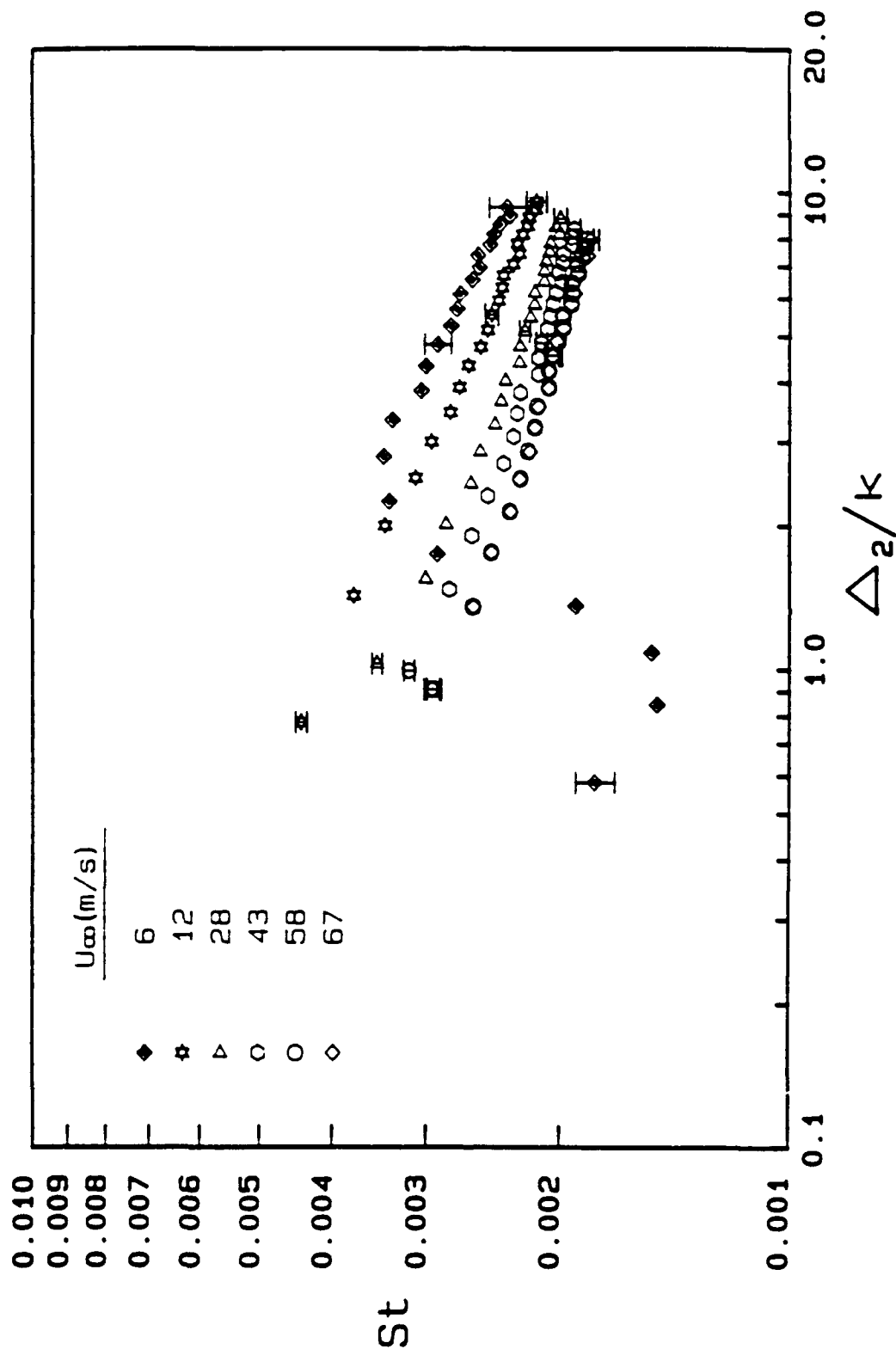


Figure 5.9 The THTF Stanton number data vs.  $\Delta_2/k$  for  $U_{\infty} = 6, 12, 28, 43, 58$  and  $67$  m/s for the  $L/d_0 = 4$  rough surface.

# Hemispherical Roughness

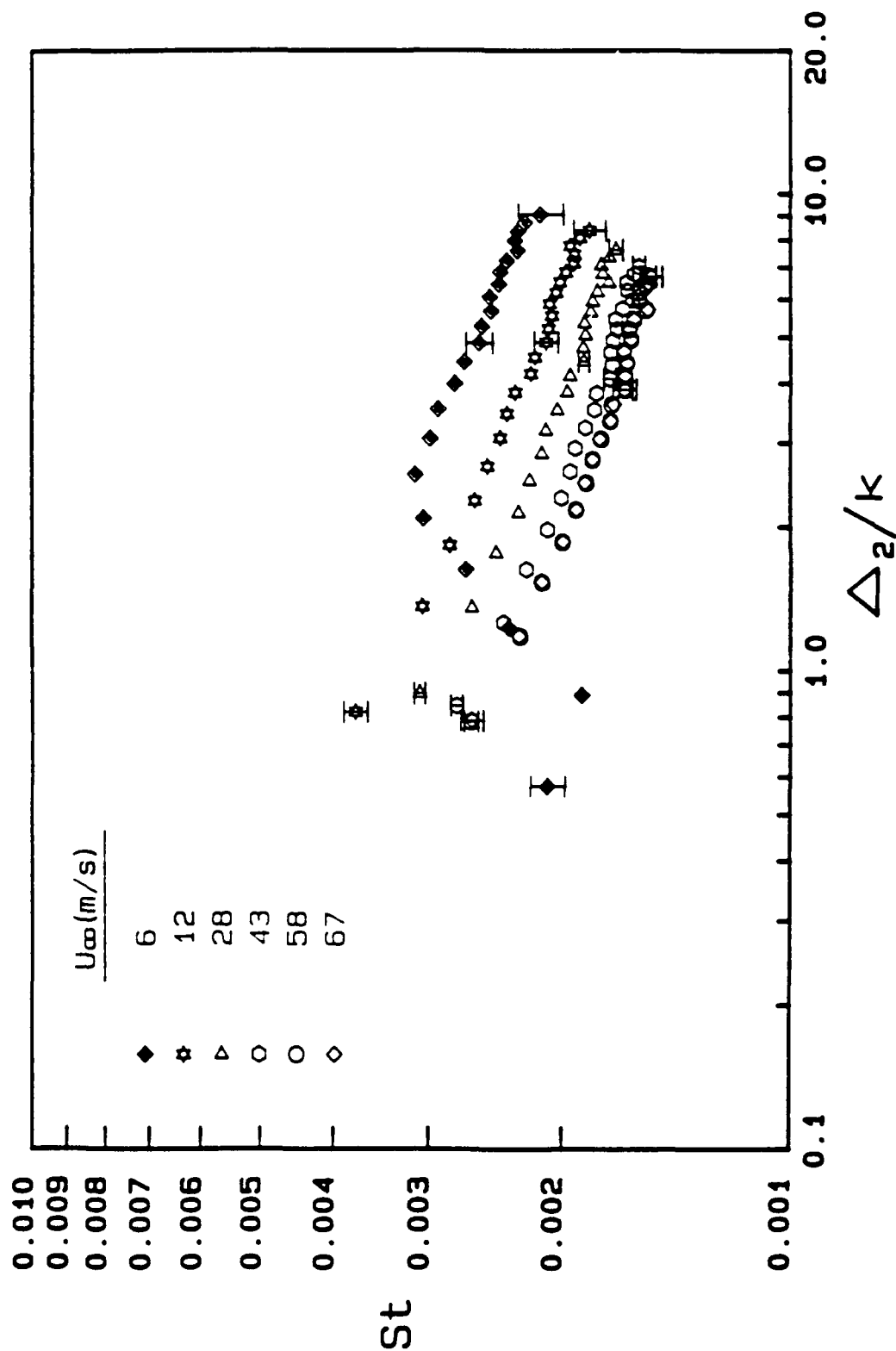


Figure 5.10 The THTF Stanton number data vs.  $\Delta_2/k$  for  $U_\infty = 6, 12, 28, 43, 58$  and  $67$  m/s for the  $L/d_0 = 10$  rough surface.

# Hemispherical Roughness

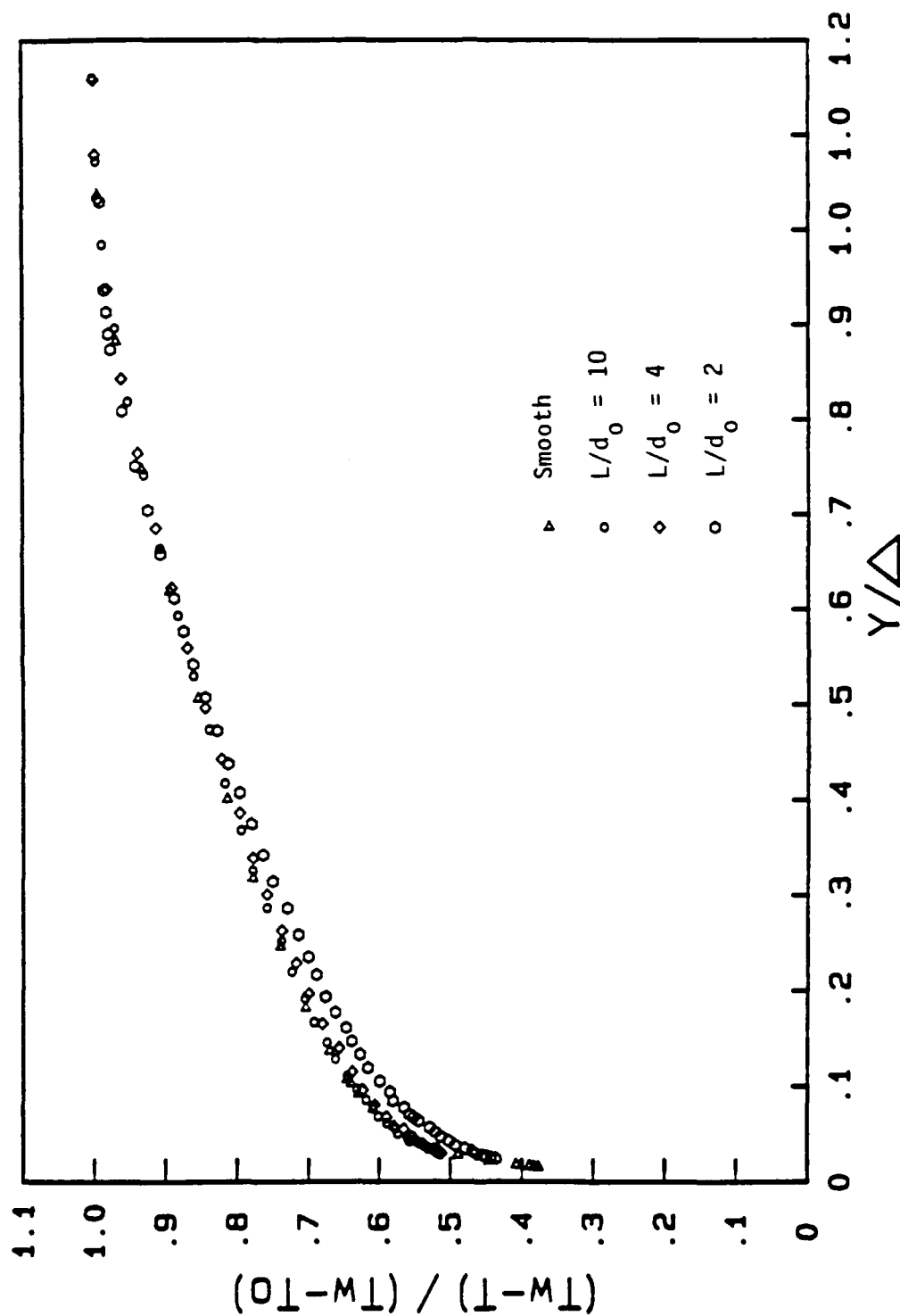


Figure 5.11 Nondimensional temperature profiles vs.  $y/\Delta$  for  $U_\infty = 12$  m/s for the THTF smooth and rough surfaces.

# Hemispherical Roughness

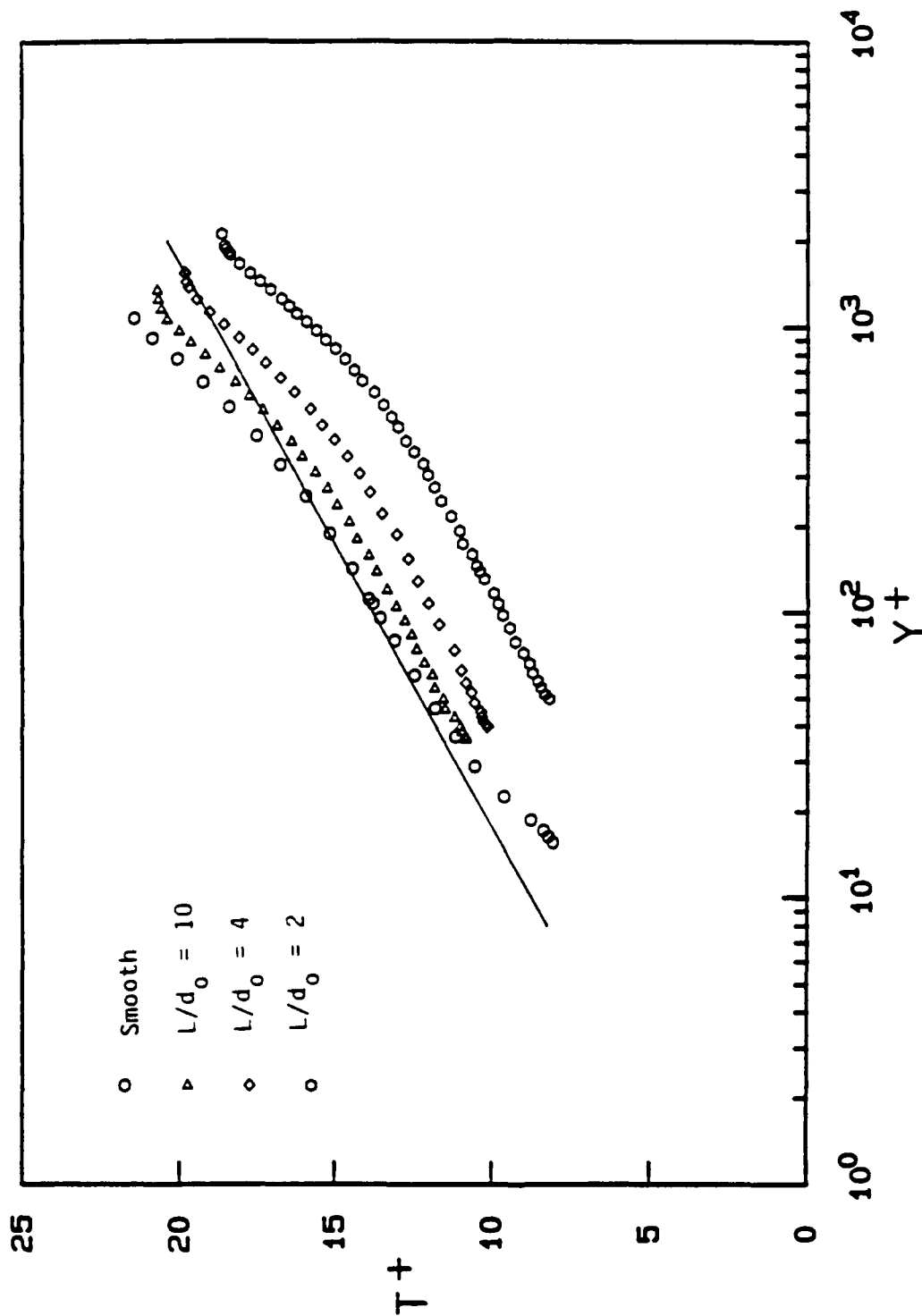


Figure 5.12 Temperature profiles for  $U_\infty = 12$  m/s for the THTF smooth and rough surfaces compared with the law of the wall.

## CHAPTER 6

### ROUGH-WALL BOUNDARY LAYER PREDICTIONS (Hemispherical Elements)

The purpose of this chapter is to compare fluid dynamics and heat transfer prediction results obtained using the discrete element method with experimental data for the Stanford surface and the three rough surfaces with hemispherical elements investigated in the Turbulent Heat Transfer Test Facility (THTTF). Moreover, this chapter presents the latest roughness element momentum and energy transport models used in the discrete element prediction method. These models are responsible for incorporating the effects of roughness into the partial differential equations which describe the behavior of turbulent boundary layer flows; therefore, their validity plays a major role in the success of the discrete element prediction scheme. The momentum transport ( $C_D$ ) model presented and used is unchanged from that reported by Taylor et al. (1984). The energy transport ( $Nu_d$ ) model is new, however, and has been developed during the course of the present work. Finally, a new computational measure ( $R_q$ ) for heat transfer characterization of rough wall flows is introduced.

#### 6.1 OVERVIEW OF THE DISCRETE ELEMENT METHOD

The development of the discrete element prediction method was discussed in Chapter 2. Only an overview is presented here so that the importance of accurate roughness models is explored. The basic

idea of the discrete element approach is to treat the roughness as a collection of individual entities and to account for the blockage, form drag, and heat transfer on the elements. The discrete element prediction approach used in this work is formulated for roughness elements with three dimensional shapes (as opposed to transverse ribs, for example) for which the element cross-section can be approximated as circular with diameter,  $d$ , at every height,  $y$ . Thus, the geometric description of the roughness element,  $d(y)$ , is easily included in this prediction scheme. Consequently, the element shape descriptor and the blockage parameters which are functions only of roughness geometry require no empirical fluid mechanics input. However, the necessary empirical information for rough surfaces is contained in the roughness models for the roughness element drag coefficient,  $C_D$ , and the roughness element Nusselt number,  $Nu_d$ . The roughness element drag coefficient,  $C_D$ , is used in the boundary layer momentum equation to model the drag force exerted on the fluid by each element. The roughness element Nusselt number,  $Nu_d$ , is utilized in the energy equation to model the local heat transfer between the fluid and each element. The final form of these models which were used in the discrete element approach for calculation of results presented here are discussed next.

## 6.2 MOMENTUM TRANSPORT MODEL

The discrete element prediction method contains a term to account for the drag force exerted by the roughness elements on the fluid. This drag is cast in terms of a nondimensional drag coeffi-

cient,  $C_D$ . It is this drag coefficient that contains the necessary empirical information on the relationship between the roughness elements and surrounding flow. The  $C_D$  model developed by Taylor et al. (1984) is

$$\begin{aligned} \log C_D &= -0.125 \log(Re_d) + 0.375 & Re_d \leq 6 \times 10^4 \\ C_D &= 0.6 & Re_d \geq 6 \times 10^4 \end{aligned} \quad (6.1)$$

where  $Re_d = u(y) d(y)/\nu$ . This  $C_D$  model has been tested for values of  $Re_d$  up to about 25,000 [Taylor et al. (1984), Scaggs et al. (1988a)], and was used unchanged for the predictions discussed here.

### 6.3 ENERGY TRANSPORT MODEL

The energy transport model in the discrete element method accounts for the local convective heat transfer between the fluid and the roughness elements. The model for the roughness element heat transfer coefficient requires empirical input in the form of a roughness Nusselt number,  $Nu_d$ . As with the momentum transport model, this model in its initial form was developed by Taylor et al. (1984). They developed a  $Nu_d = f(Re_d, Pr)$  model for roughness Reynolds numbers up to  $Re_d = 1000$  using the heat transfer data on the single rough surface from the Stanford series of tests. They chose the 27 m/s experimental run by Pimenta (1975) to calibrate their model.

A modified  $Nu_d$  model was formulated during the course of the current work using that of Taylor et al. (1984) as a starting point. The new model is

$$Nu_d = 1.7 Re_d^{0.49} Pr^{0.4} \quad (6.2)$$

This model has been tested up to  $Re_d = 2200$  in the comparisons with the THTF and Stanford data presented in this chapter. In Figure 6.1 a comparison is made between the current and former models for  $Nu_d$ .

#### 6.4 PREDICTION RESULTS FOR THTF RUNS

Results obtained using the discrete element prediction method are compared with the data taken on the three hemispherically-roughened surfaces in the THTF. The THTF rough surfaces were composed of 1.27 mm diameter hemispheres spaced 2 diameters ( $L/d_0 = 2$ ), 4 diameters ( $L/d_0 = 4$ ), and 10 diameters ( $L/d_0 = 10$ ) apart. All of the THTF data are for zero pressure gradient, constant wall temperature, incompressible turbulent boundary layer flow.

##### 6.4.1 Fluid Dynamics

The skin friction coefficient data from the THTF taken at nominal freestream velocities of 12 and 58 m/s on the  $L/d_0 = 2$  and  $L/d_0 = 4$  rough surfaces are compared with the calculations made using the discrete element prediction scheme in Figures 6.2 and 6.3, respectively. Figure 6.4 shows comparison of the skin friction data and corresponding discrete element predictions for the  $L/d_0 = 10$  rough surface from the THTF for freestream velocities of 6 and 12 m/s. Skin friction coefficient distributions are plotted versus momentum thickness Reynolds number in these figures. The uncer-



tainty bands represent the estimated  $\pm 10\%$  uncertainty in  $C_f$ . The curves represent the predictions and the smooth wall correlation, Eq. (3.2).

Comparison of the data and predictions shows that the agreement is excellent, with the predictions matching the data within the  $\pm 10\%$  uncertainty. These comparisons essentially cover the aerodynamically smooth, transitionally rough and fully rough flow regimes.

#### 6.4.2 Heat Transfer

The Stanton number data for the  $L/d_0 = 2$ ,  $L/d_0 = 4$ , and  $L/d_0 = 10$  rough surfaces from the THTF for nominal freestream velocities of 6, 12, 28, 43, 58, and 67 m/s are compared with the calculations made using the discrete element prediction method in  $St$  versus  $Re_x$  coordinates in Figures 6.5, 6.6, and 6.7, respectively. The uncertainty bands on selected data points indicate the uncertainties as computed using the techniques discussed in Appendix I. The curves represent the predictions and the smooth wall correlation as given by Eq. (3.3). As shown, the discrete element method predicts the data sets extremely well over the range of roughness spacings and for smooth, transitionally rough and fully rough flow regimes.

Figures 6.8, 6.9, and 6.10 present comparisons between the same data and predictions but in  $St$  versus  $\Delta_2/k$  coordinates, where as before  $\Delta_2$  is the enthalpy thickness and  $k$  is the roughness height. As seen in these figures, the agreement is excellent except for the lowest velocities on the  $L/d_0 = 2$  and 4 surfaces, where the predictions fall slightly outside the uncertainty bands.

## 6.5 PREDICTION RESULTS FOR STANFORD RUNS

The discrete element method has been used to make predictions corresponding to the boundary layer experiments performed using the Stanford surface as reported by Healzer (1974) and Pimenta (1975). Both Healzer and Pimenta reported skin friction coefficients and Stanton numbers for both transitionally rough and fully rough zero pressure gradient flow over a constant temperature rough surface. All data sets were taken on the single rough surface composed of 1.27 mm diameter spheres packed in the most dense array. Since this surface did not have a solid base smooth wall, an effective base wall location 0.2 sphere diameter below the crests of the spherical elements as determined by Taylor et al. (1984) was used. It should also be noted that the correct specification for element spacing is 1.0 and 0.866 sphere diameters in the x and z directions, respectively. Thus the  $L^2$  factor in the discrete element Eqs. (2.2-2.7) is  $(1.0)(0.866)(1.27 \text{ mm})^2$  for this surface.

One of the concerns of the Stanford series of experiments was the study of the effects of surface transpiration; therefore, both blown and unblown runs were reported. Since transpiration is not considered in the present work, only the unblown cases are considered and neither the discrete element prediction method nor the calculations presented herein include transpiration effects.

### 6.5.1 Fluid Dynamics

The zero pressure gradient skin friction coefficient distributions for the Stanford rough surface reported by Healzer (1974) and Pimenta (1975) are compared with the calculations made with the discrete element method in Figure 6.11. The uncertainty bands represent the estimated  $\pm 10\%$  uncertainty in reported  $C_f$  data. The curves are the predictions and the smooth wall correlation given by equation (3.2). The predictions for every run fall either within or just outside the data uncertainty limits, indicating agreement with the data within 10-12%.

### 6.5.2 Heat Transfer

In Figure 6.12, the zero pressure gradient Stanton number data sets for the Stanford rough surface reported by Healzer (1974) and Pimenta (1975) are compared with calculations made with the discrete element method. The calculations for freestream velocities of 9, 16, 27, 40, and 58 m/s are in excellent agreement with Pimenta's data. For the freestream velocity of 74 m/s, the discrete element model predicts Healzer's data to almost within the data uncertainty of  $\pm 0.0001$  St units. Figure 6.13 shows comparisons of these Stanford data sets with the predictions in St versus  $\Delta_2/r$  coordinates where  $\Delta_2$  is the enthalpy thickness and  $r$  is the roughness radius. The agreement between the data and predictions is excellent in these coordinates. This is especially encouraging, since the

discrete element model properly predicts the somewhat different behavior of the Stanford and THTF data in  $St$  versus  $\Delta_2/r$  coordinates

## 6.6 CHARACTERIZATION OF FLOW REGIMES BASED ON PREDICTIONS

Various experimental measures for classification of flow regimes based on observations of fluid dynamics and heat transfer behaviors of rough wall data were discussed in previous chapters. The only non-sandgrain computational delimiter for identification of rough wall flow conditions available is that of Taylor et al. (1984). As was discussed previously, they proposed that the ratio of the apparent shear stress due to the roughness elements to the total apparent shear stress ( $R_\tau = \tau_R/\tau_T$ ) be used to distinguish between aerodynamically smooth, transitionally rough and fully rough regimes. Scaggs et al. (1988a), based on their extensive fluid dynamic data set and the corresponding calculations of  $\tau_T$  and  $\tau_R$  made using their discrete element model, suggested that a value of  $R_\tau$  about 0.6 might be considered as an appropriate boundary between the transitionally rough and fully rough flow regimes. The parameter  $R_\tau$ , of course, is based only on the fluid dynamics character of rough wall flows. An analogous parameter based on the effects of roughness elements on the heat transfer characteristics of rough wall flows is discussed next.

The ratio of the rate of heat transfer to the roughness elements to the total rate of heat transfer to the surface

$$R_q = q_R/q_T \quad (6.3)$$

is the heat transfer equivalent to  $R_T$ . Figure 6.14 shows a plot of calculated values of  $R_q$  using the energy transport model for nominal freestream velocities of 6, 12, 28, 43, 58, and 67 m/s for the three THTTF rough surfaces ( $L/d_0 = 2$ ,  $L/d_0 = 4$ , and  $L/d_0 = 10$ ). Also presented in Figure 6.14 is a plot of calculated values of  $R_T$  using the momentum transport model (previously presented as Figure 4.36) for comparison to the  $R_q$  values. A similar plot is presented in Figure 6.15 for the zero pressure gradient Stanford data sets.

The behavior of  $R_q$  seems to mirror the behavior of the Stanton number data when viewed in  $Re_x$  coordinates. For each THTTF surface, the  $R_q$  values collapse to essentially a constant value except for the lowest freestream velocities of 6 and 12 m/s. The constant value, however, increases with an increase of surface roughness for these surfaces, being approximately  $R_q = 0.07$ , 0.3, and 0.65 for the  $L/d_0 = 10$ , 4, and 2 surfaces, respectively.

For the Stanford surface, the collapse of  $R_q$  to a constant value appears to occur at a slightly higher freestream velocity than for the THTTF surfaces. In addition, the constant value of  $R_q$  of about 0.77 is higher than that for the  $L/d_0 = 2$  THTTF surface (0.65), although the  $L/d_0 = 2$  surface appeared "rougher" than the Stanford surface in the  $C_f$  vs.  $\delta_2/k$  coordinates of Figure 4.35.

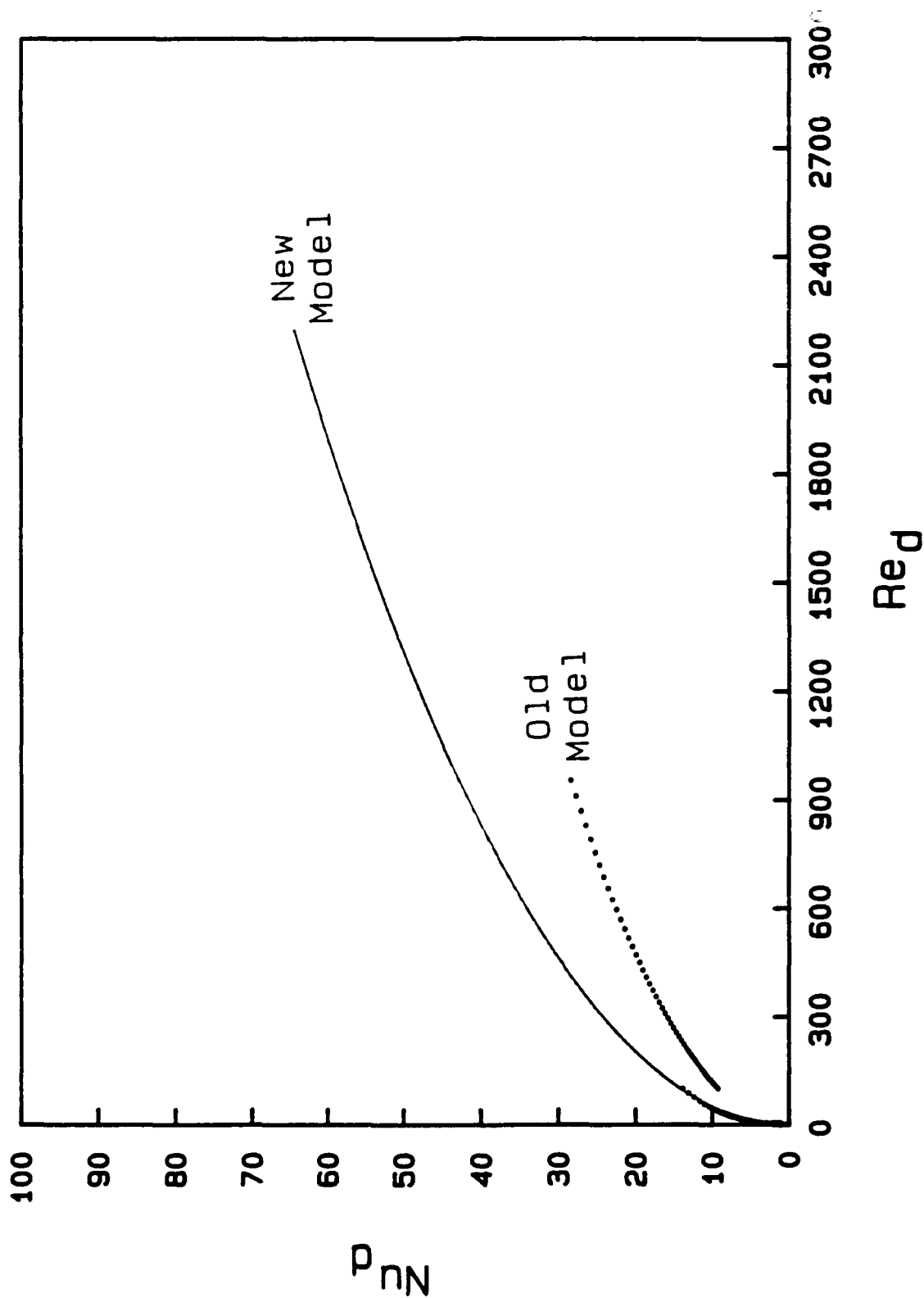


Figure 6.1 Comparison of the current and former models for the roughness element Nusselt number,  $Nu_d$ , up to the extent of their validation.

# Hemispherical Roughness

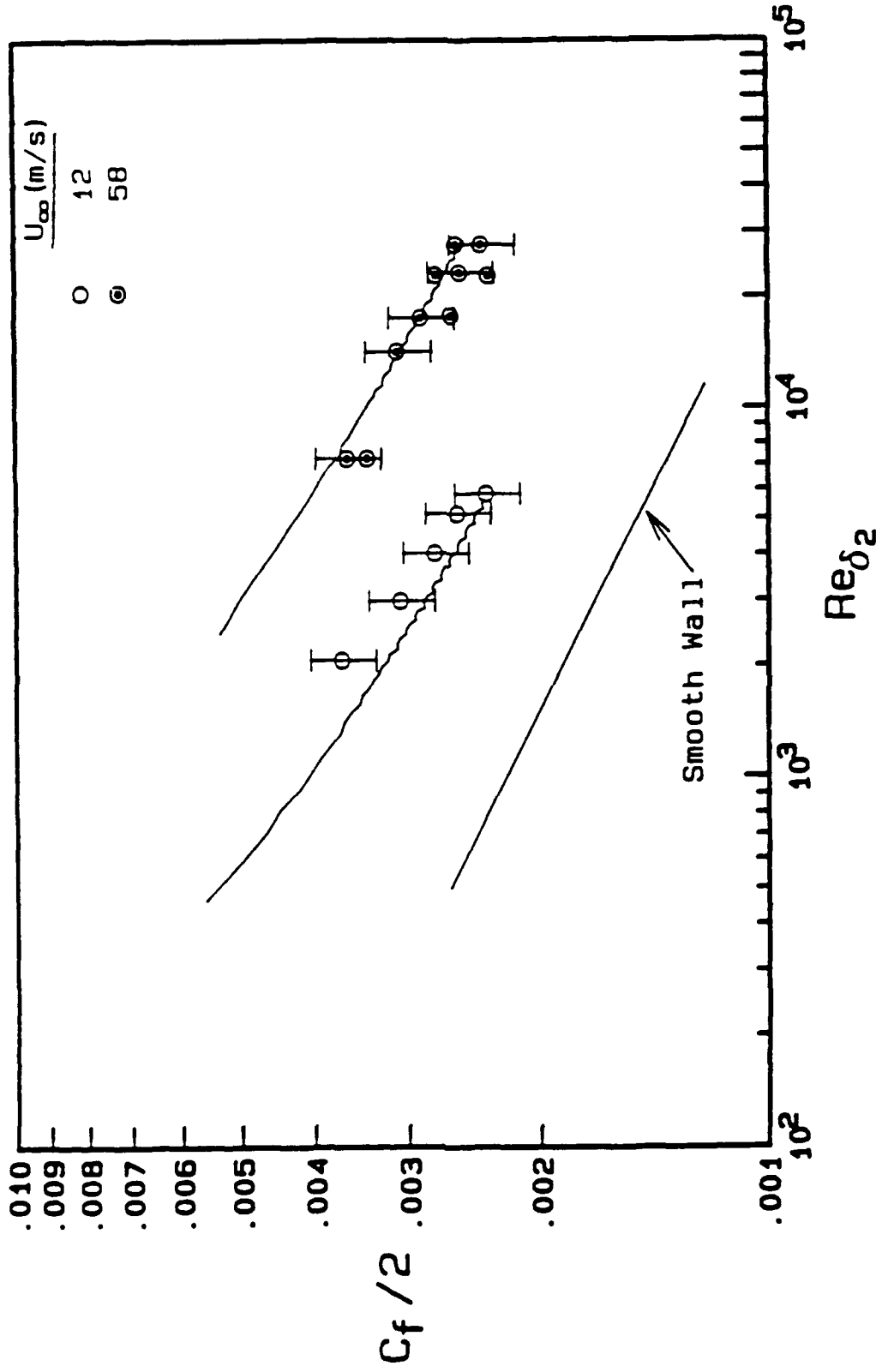


Figure 6.2 Comparison of  $C_f$  data and predictions for the  $L/d_0 = 2$  surface.

# Hemispherical Roughness

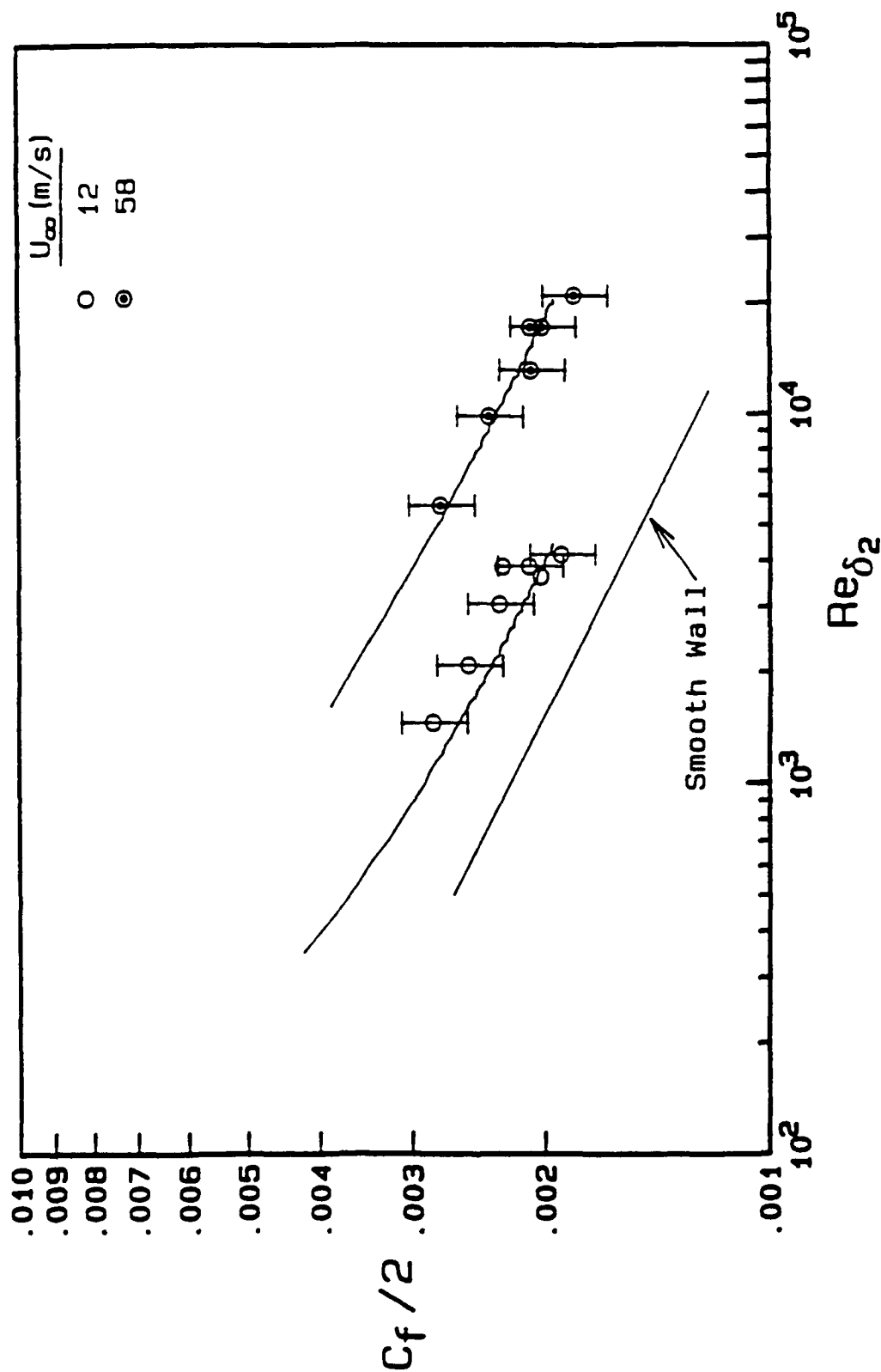


Figure 6.3 Comparison of  $C_f$  data and predictions for the  $L/d_0 = 4$  surface.



# Hemispherical Roughness

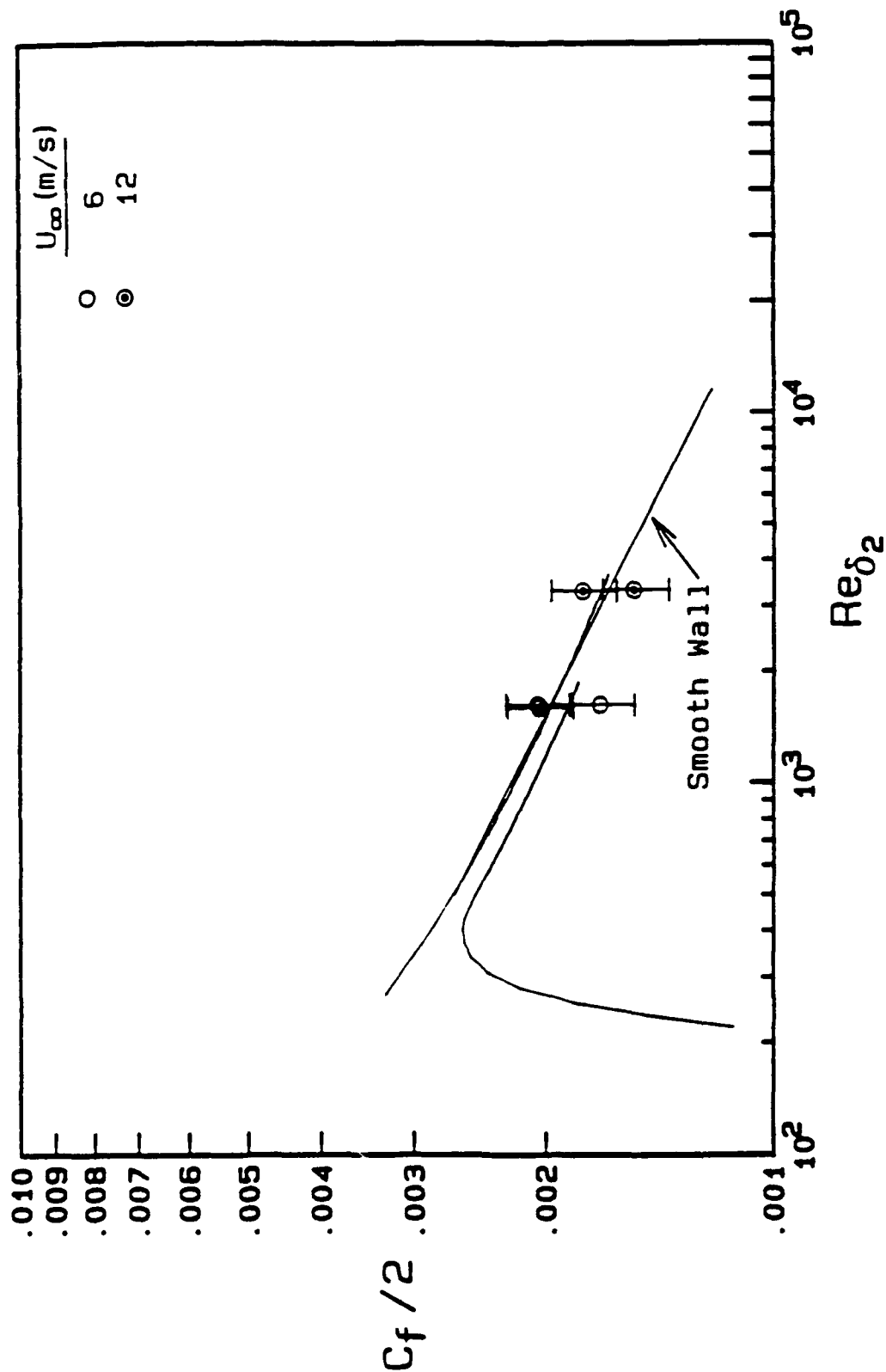


Figure 6.4 Comparison of  $C_f$  data and predictions for the  $L/d_0 = 10$  surface.

# Hemispherical Roughness

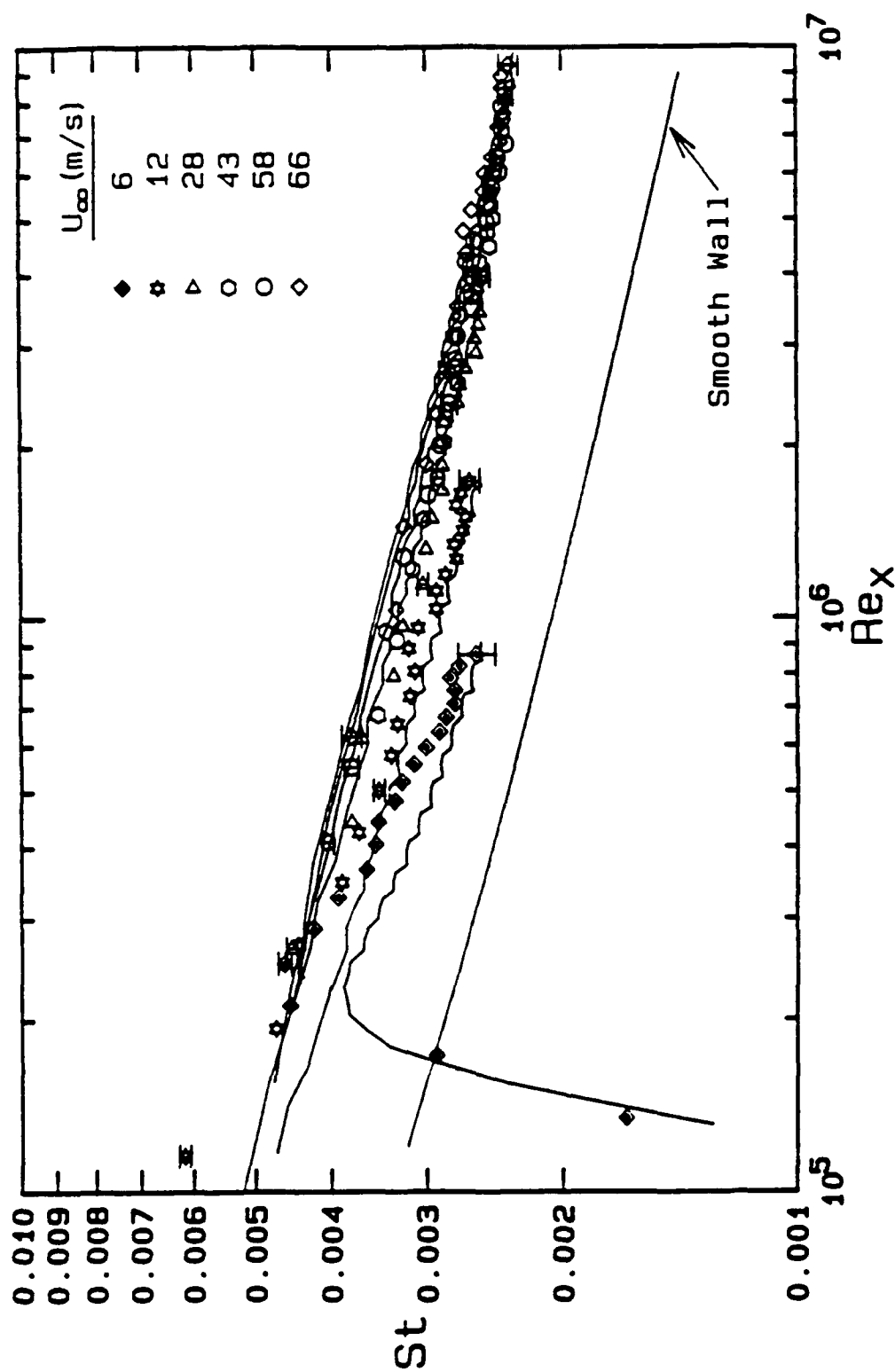


Figure 6.5 Comparison of St data and predictions in  $Re_x$  coordinates for the  $L/d_0 = 2$  surface.

# Hemispherical Roughness

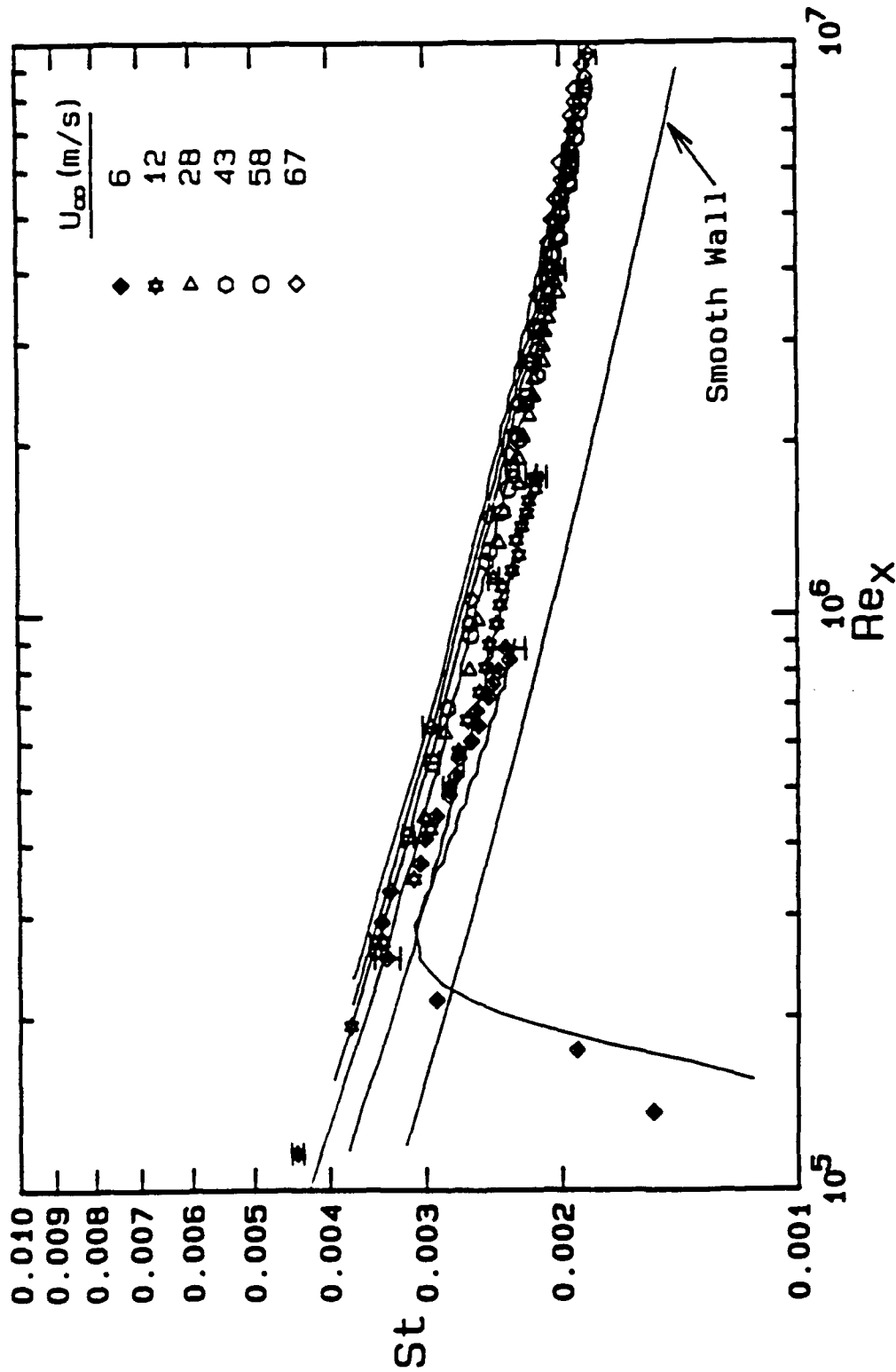


Figure 6.6 Comparison of St data and predictions in  $Re_x$  coordinates for the  $L/d_0 = 4$  surface.

# Hemispherical Roughness

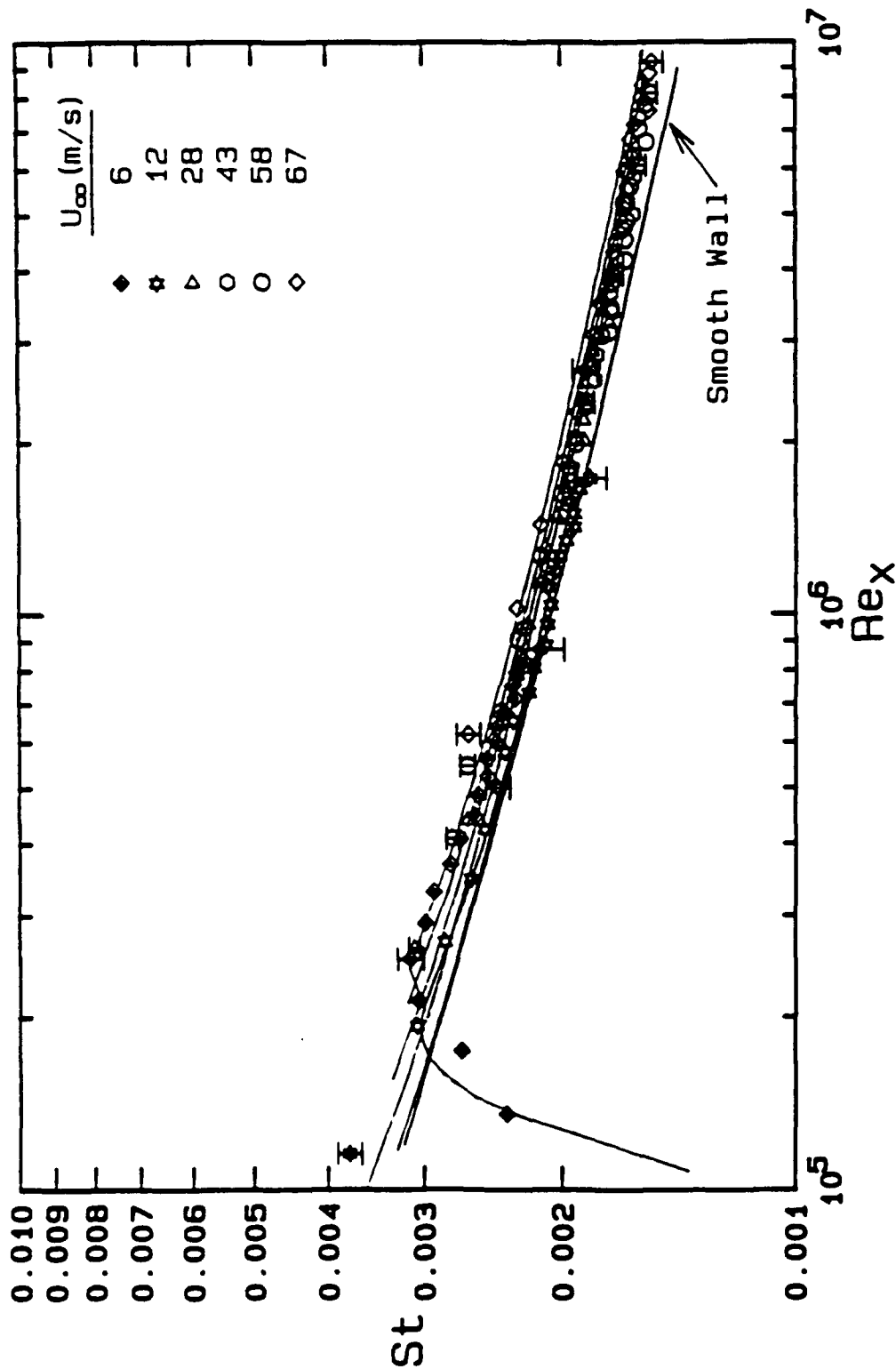


Figure 6.7 Comparison of  $St$  data and predictions in  $Re_x$  coordinates for the  $L/d_0 = 10$  surface.

# Hemispherical Roughness

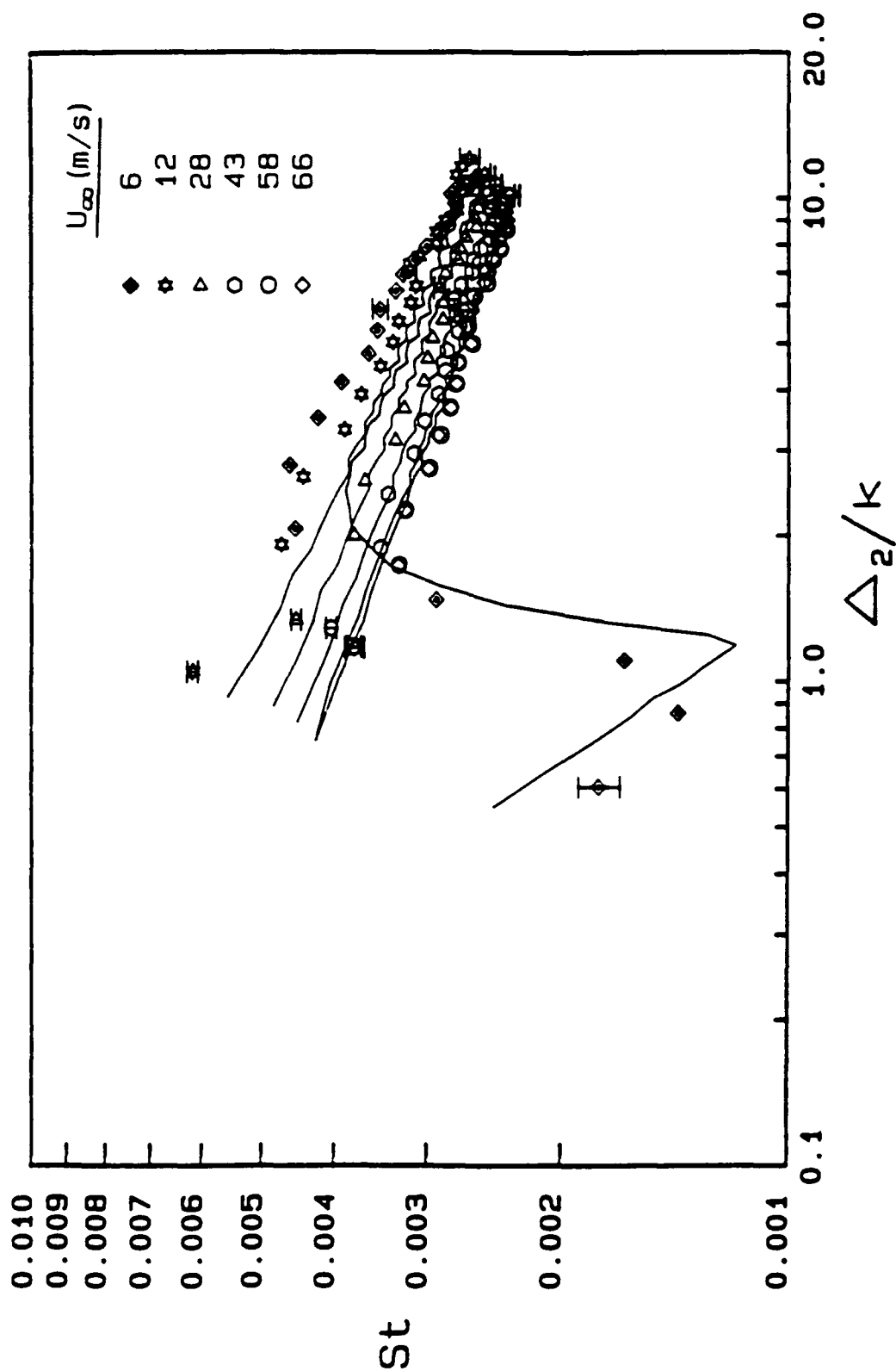


Figure 6.8 Comparison of St data and predictions in  $\Delta_2/k$  coordinates for the  $L/d_0 = 2$  surface.

# Hemispherical Roughness

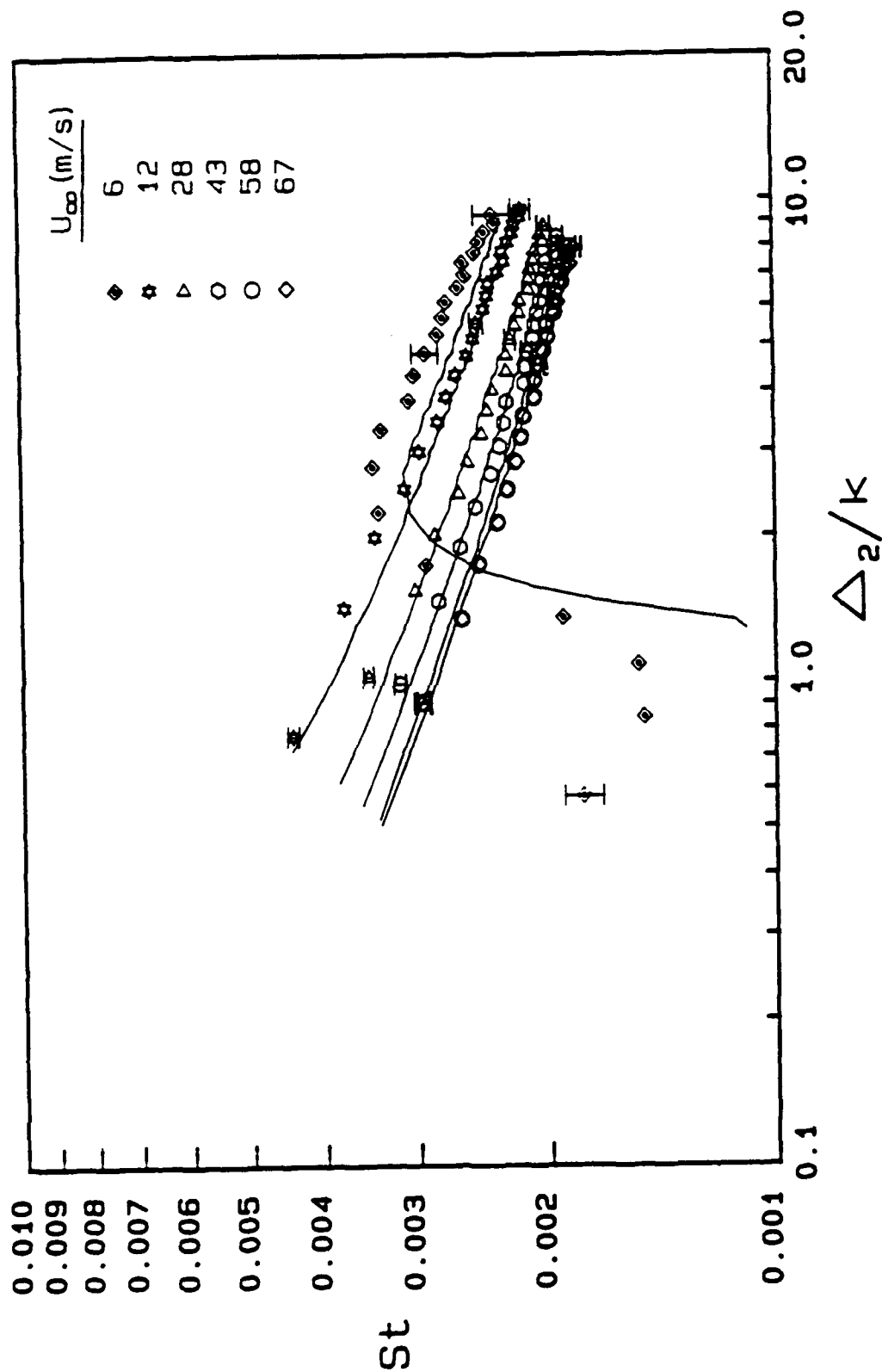


Figure 6.9 Comparison of  $St$  data and predictions in  $\Delta_2/k$  coordinates for the  $L/d_0 = 4$  surface.

# Hemispherical Roughness

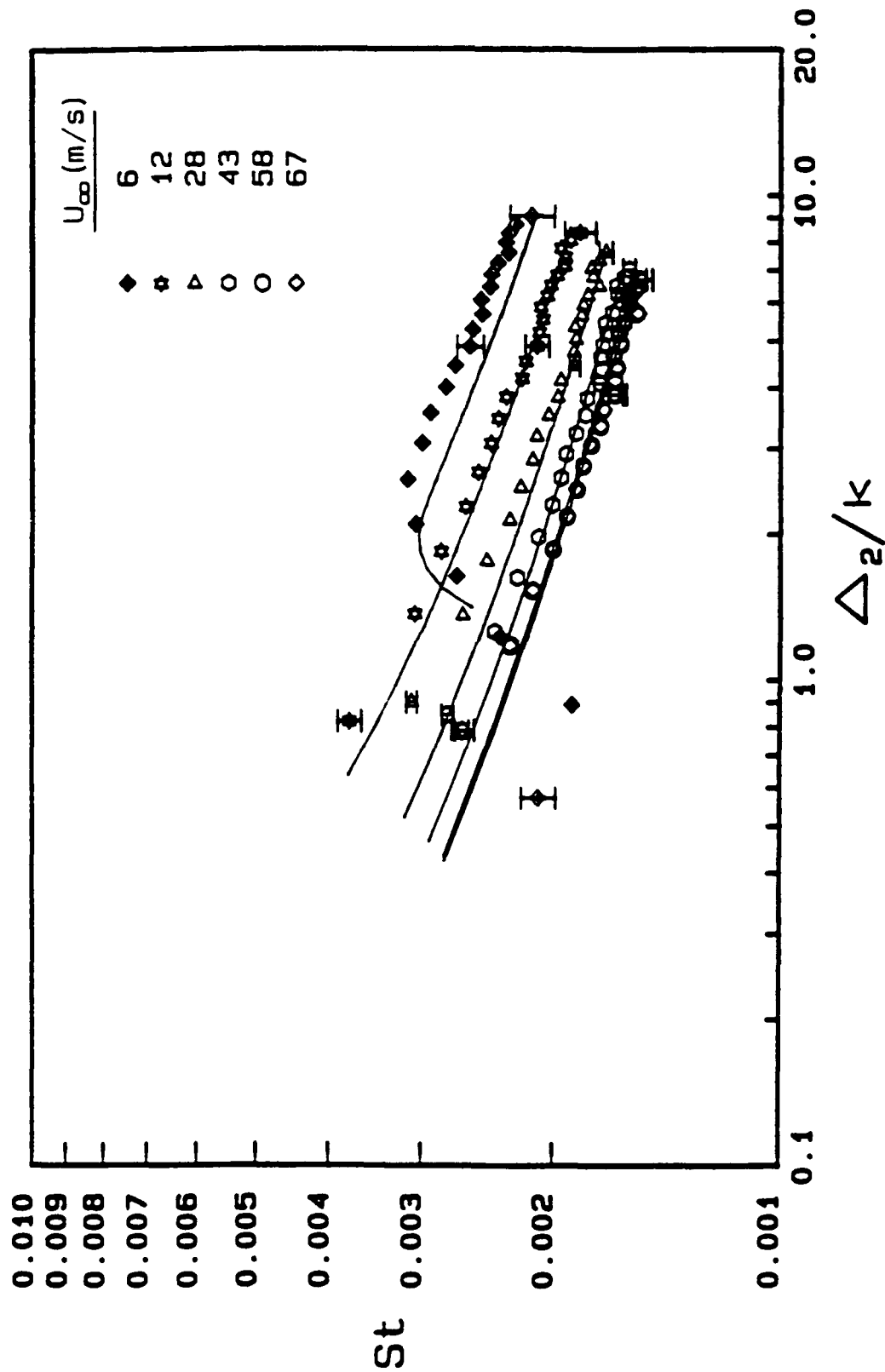


Figure 6.10 Comparison of  $St$  data and predictions in  $\Delta_2/k$  coordinates for the  $L/d_0 = 10$  surface.

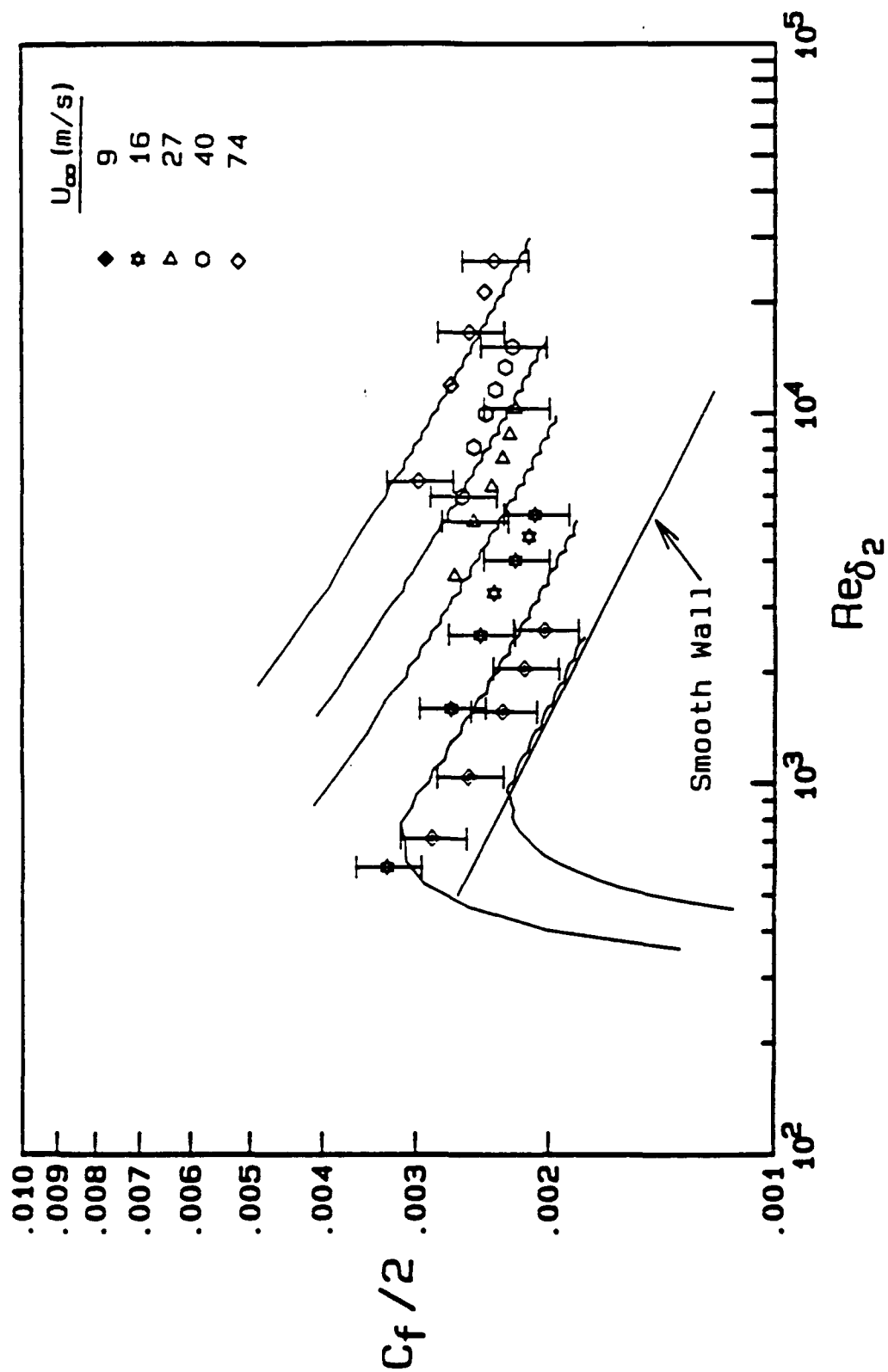


Figure 6.11 Comparison of  $C_f$  data and predictions for the Stanford surface. Data of Healzer (1974) and Pimenta (1975).



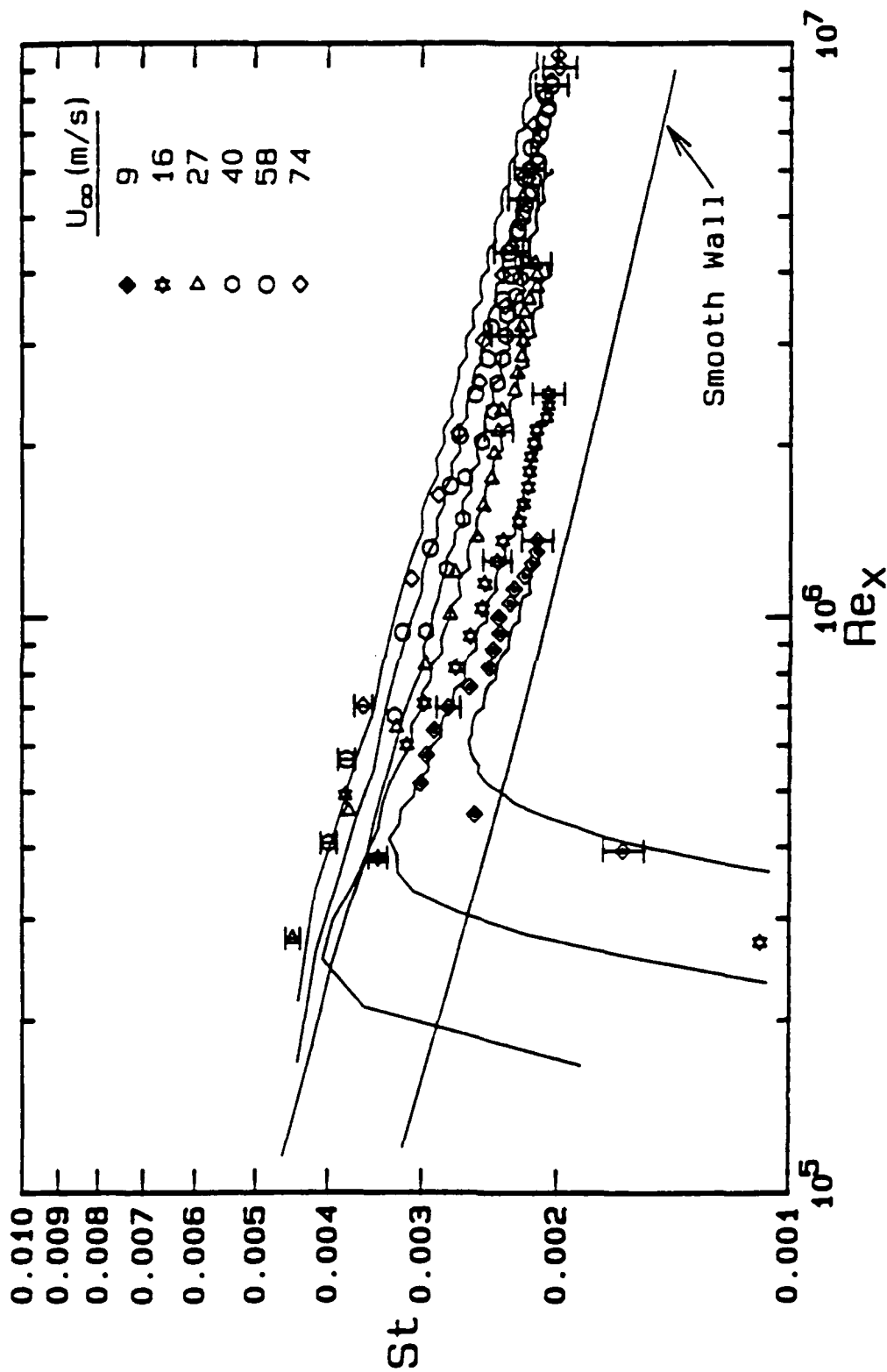


Figure 6.12 Comparison of St data and predictions in  $Re_x$  coordinates for the Stanford surface. Data of Healzer (1974) and Pimenta (1975).

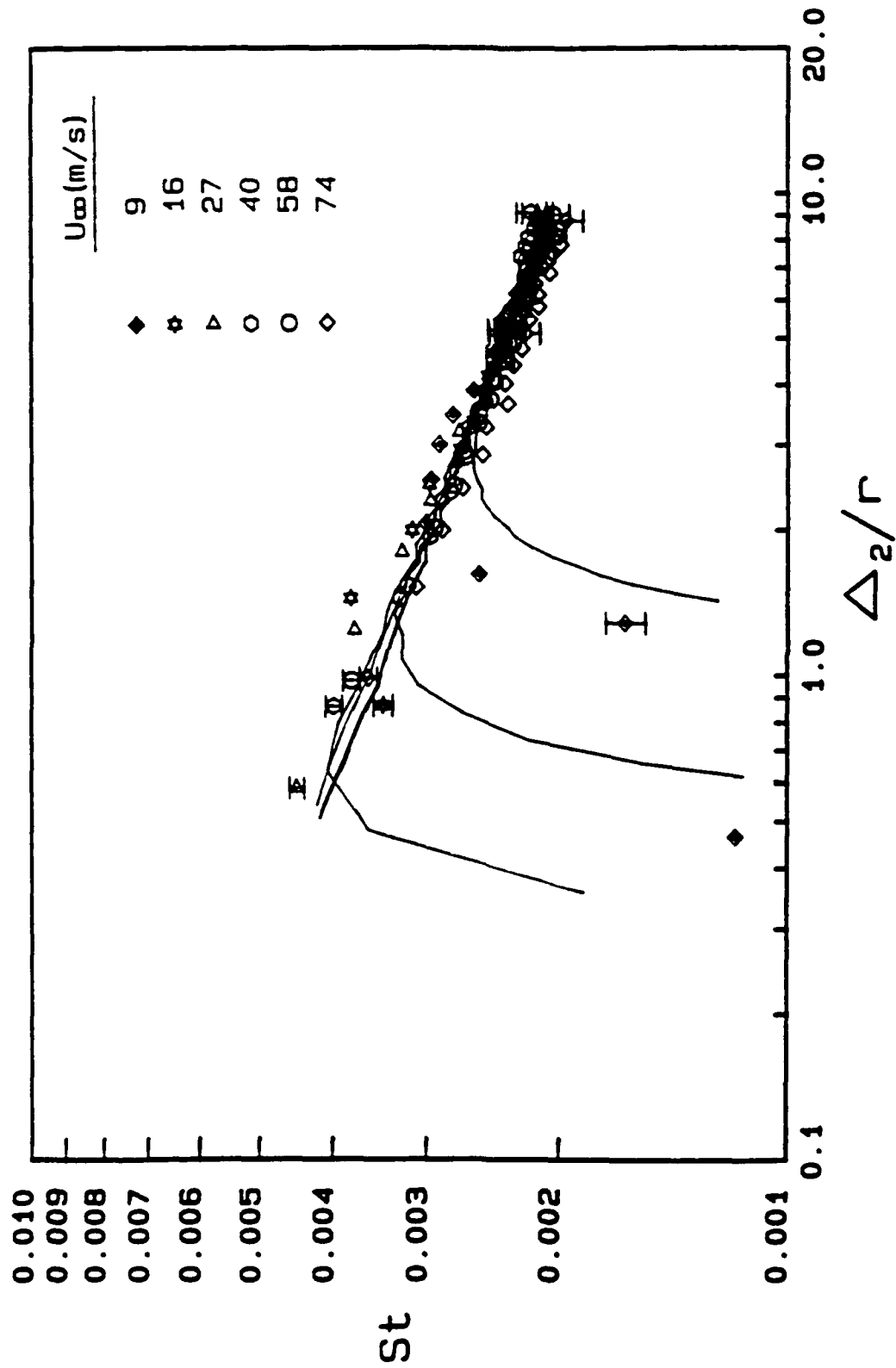


Figure 6.13 Comparison of  $St$  data and predictions in  $\Delta_2/r$  coordinates for the Stanford surface. Data of Healzer (1974) and Pimenta (1975).

# Hemispherical Roughness

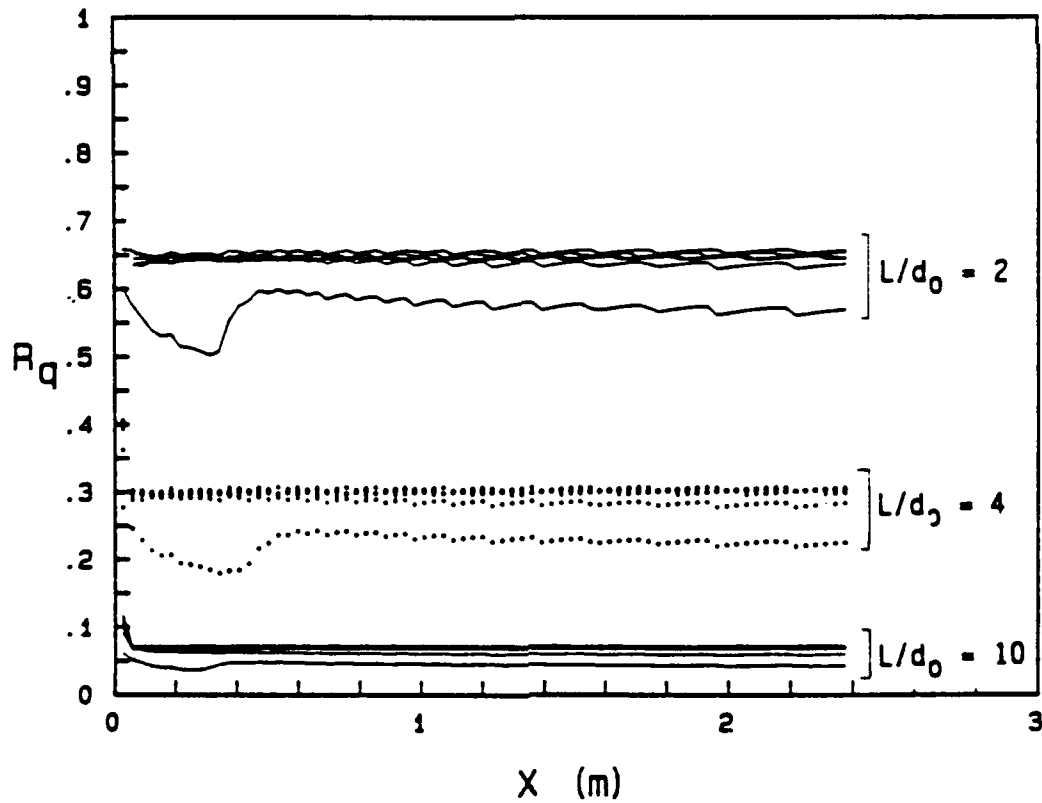
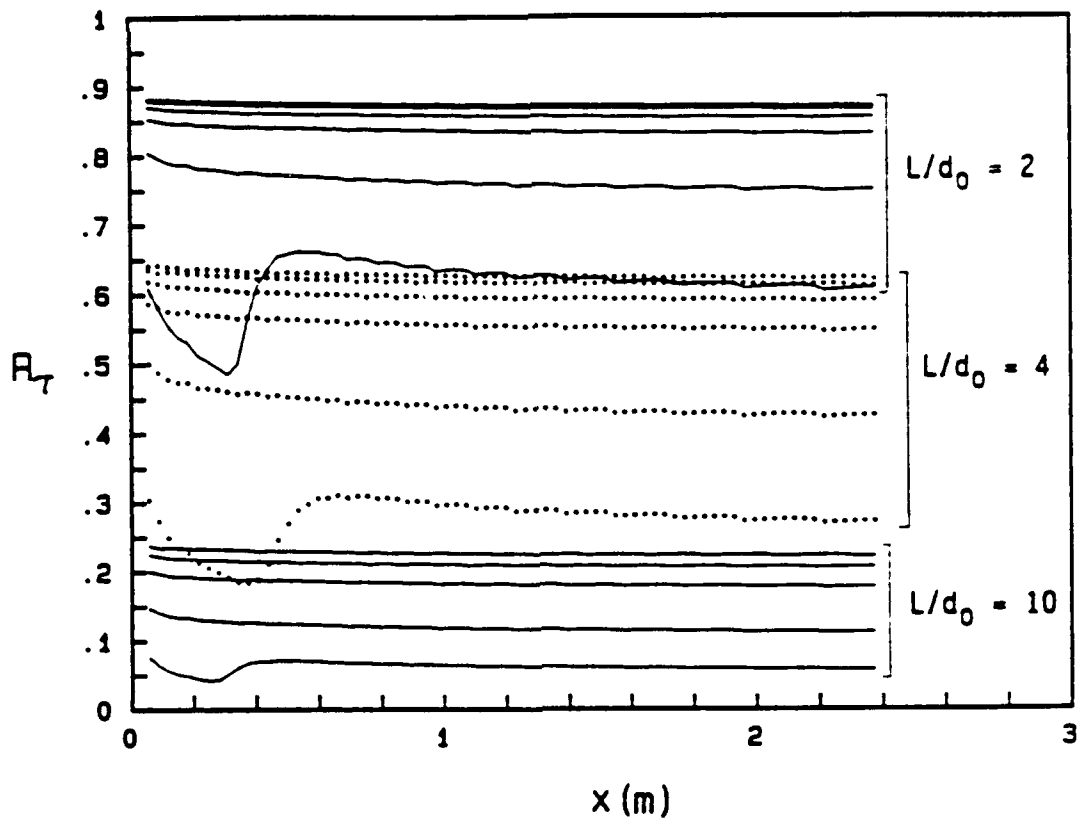


Figure 6.14 Calculated values of  $R_T$  and  $R_Q$  for  $U_\infty = 6, 12, 28, 43, 58$  and  $67$  m/s from the discrete element method for the THTF rough surfaces.

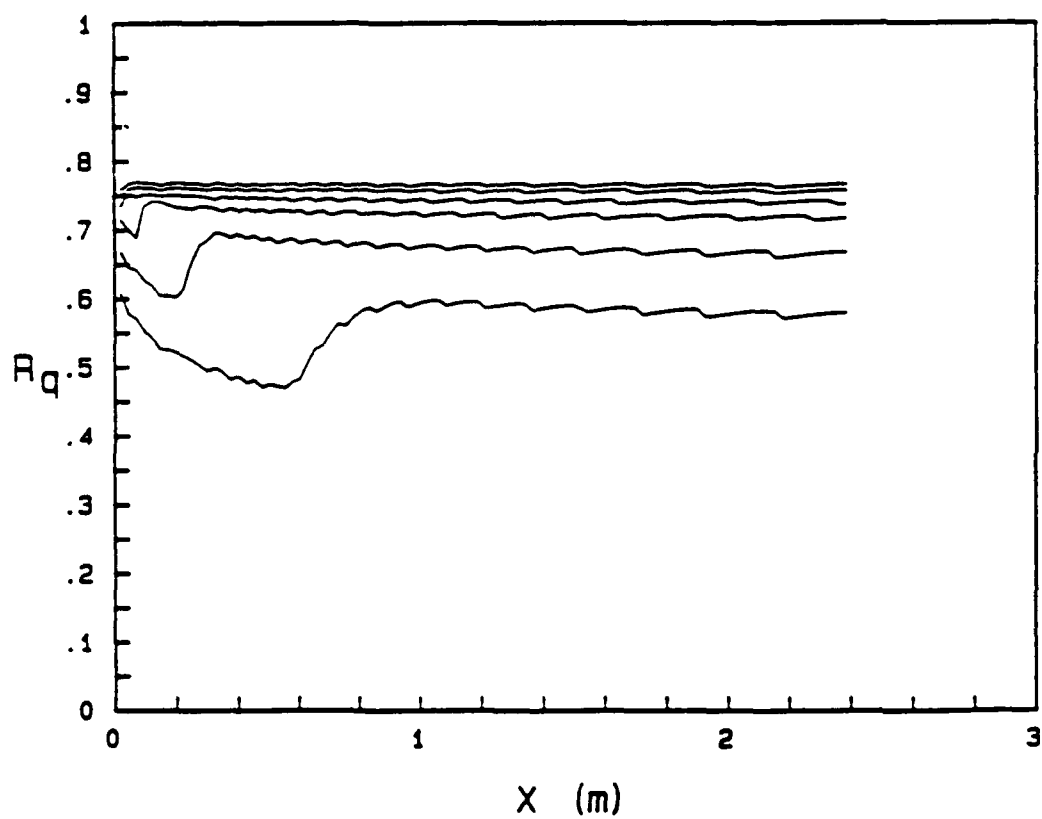
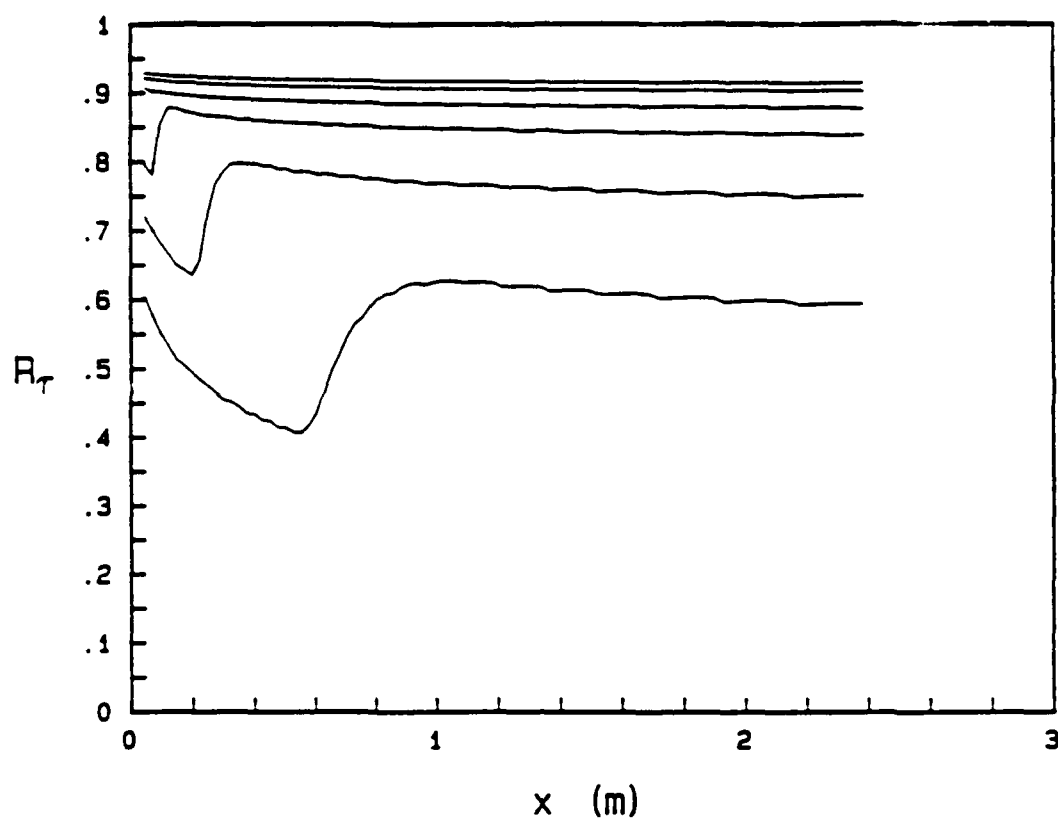


Figure 6.15 Calculated values of  $R_T$  and  $R_Q$  for  $U_\infty = 9, 16, 27, 40, 58$  and  $74$  m/s from the discrete element method for the Stanford rough surface.

## CHAPTER 7

### EFFECTS OF ROUGHNESS ELEMENT SHAPE

The portion of the research effort discussed in this chapter was conducted as an investigation of surface roughness shape effects on flat plate, turbulent boundary layer flow and heat transfer. This chapter considers the influence of truncated right circular cone roughness elements which are uniformly distributed 2 and 4 base diameters apart. To investigate roughness element shape effects on heat transfer and fluid dynamic characteristics, the data collected for the test surfaces roughened with truncated cones are compared with data obtained under similar flow conditions over the equivalently spaced hemisphere roughened surfaces. The two analogous test surfaces are similar in that both roughness element geometries have a base diameter of 1.27 mm and a height of 0.635 mm and the elements are spaced equally apart. They differ in the shape, surface area, and projected frontal area of the roughness elements. The area ratio of hemispheres to truncated cones is 1.35 for the projected area and 1.32 for the surface area.

As discussed in previous chapters, the turbulent boundary layer flows over the  $L/d_0 = 4$  hemisphere roughened surface were classified as being in the transitionally rough regime for  $U_\infty = 6$  and 12 m/s and in the lower fully rough regime for  $U_\infty = 43, 58,$  and 67 m/s. The flow for  $U_\infty = 28$  m/s was classified as upper transitionally rough/lower fully rough. For the  $L/d_0 = 2$  hemisphere roughened

surface, the flow for  $U_{\infty} = 6$  m/s was classified as lower fully rough and for  $U_{\infty} \geq 12$  m/s as fully rough. Based on the data of Scaggs et al. (1988), it was anticipated that the flows over the current surfaces roughened with truncated cones would exhibit the same flow regime characteristics with increasing freestream velocity. Scaggs et al. found, for fully developed pipe flows, that surfaces roughened with hemispheres and with truncated cones with the same height, spacing and aspect ratio exhibited identical friction factor versus Reynolds number behavior within the uncertainty of the data.

In Figure 7.1, skin friction coefficient distributions for the truncated cone surfaces are compared with  $C_f$  results from the comparable hemisphere surfaces for freestream velocities of 12 and 58 m/s. This figure shows that skin friction coefficients for both THTF roughness shapes for both the  $L/d_0 = 2$  and  $L/d_0 = 4$  surfaces are the same within the indicated uncertainty bounds associated with the hot-wire measurement technique. The smooth wall line is Eq. (3.2), the turbulent flat plate boundary layer correlation from Kays and Crawford (1980).

Mean velocity profiles were measured across the boundary layer using the horizontal hot-wire. In Figure 7.2 velocity profiles from flows over the surfaces with cones and hemispheres at both  $L/d_0 = 2$  and  $L/d_0 = 4$  are compared in the inner variable coordinates  $u^+$  versus  $y^+$  for the two freestream velocities. Also shown for reference is the "law of the wall" for smooth surfaces [Kays and Crawford (1980)]

$$u^+ = 2.44 \ln(y^+) + 5.0 \quad (7.1)$$

In these coordinates, mean velocity profiles at a given freestream velocity show no difference due to the difference in roughness element shape when the data uncertainties are considered.

Figures 7.3 and 7.4 present comparisons of profiles of the axial turbulence intensity in flows over the rough surfaces for freestream velocities of 12 and 58 m/s, respectively. These profiles are normalized by  $U_\infty$  and plotted versus the  $y$ -position normalized by the boundary layer thickness  $\delta$ . Considering the data uncertainty, it can not be concluded that there is any difference in the character of axial turbulence profiles due to the difference in roughness shape.

Profiles of all three Reynolds normal stress components for the  $L/d_0 = 2$  and  $L/d_0 = 4$  surfaces are shown in Figure 7.5 for a freestream velocity of 58 m/s. As in the preceding figures, it can not be concluded that there is a shape effect when the uncertainty of the measurements is considered.

In Figure 7.6, Reynolds shear stress profiles at plate 17 ( $x = 1.68$  m) are shown for a freestream velocity of 58 m/s for the  $L/d_0 = 2$  and  $L/d_0 = 4$  rough surfaces. These profile data are presented in the non-dimensional coordinates  $-\overline{u'v'}/u^*2$  versus  $y/\delta$ . The data from the surfaces with different roughness shapes are indistinguishable from one another considering the data uncertainties.

## 7.2 HEAT TRANSFER RESULTS

Stanton number measurements and thermal boundary layer profiles which were measured for a constant wall temperature boundary condition constitute the heat transfer data considered in this investigation. Stanton number data were taken for freestream velocities of 6, 12, 28, 43, 58, and 66 m/s and a nominal wall temperature of 44 C. Temperature profiles of the thermal boundary layer were measured with a thermocouple probe for freestream velocities of 6, 12, 43, 66 m/s at the prescribed wall temperature of 44 C.

Figure 7.7 presents the complete set of THTTF Stanton number distributions for the  $L/d_0 = 2$  and  $L/d_0 = 4$  surfaces with truncated cone roughness. These Stanton number data are for nominal freestream velocities of 6, 12, 28, 43, 58, and 66 m/s, corresponding to  $x$ -Reynolds numbers up to 10 million. The Stanton number data for  $U_\infty = 28, 43, 58,$  and  $66$  m/s seem to collapse to a single curve, whereas the data for  $U_\infty = 6$  and  $12$  m/s deviate somewhat from this common curve. As was seen in Figures 5.3 and 5.4, the Stanton number data for the  $L/d_0 = 2$  and  $L/d_0 = 4$  hemisphere roughened surfaces exhibit the same behavior. In all of the Stanton versus Reynolds number presentations, the curve shown is the smooth surface turbulent flat plate boundary layer correlation, Eq. (3.3).

Figures 7.8 through 7.13 show comparisons of the Stanton number data from the  $L/d_0 = 2$  and  $L/d_0 = 4$  surfaces with truncated cone roughness to that from the surfaces with the hemispherical roughness



for matched flow conditions at nominal freestream velocities of 6, 12, 28, 43, 58, and 66 m/s, respectively. These figures show that Stanton numbers are larger for the hemisphere roughened surfaces than for similar surfaces with truncated cone roughness. Typically, the Stanton number data are about 10% higher for the  $L/d_0 = 2$  and 2-4% higher for the  $L/d_0 = 4$  surfaces roughened with hemispheres compared with equivalent surfaces roughened with truncated cones.

This apparent effect of the roughness element shape difference on Stanton number is believed real and physically meaningful, even though the observed difference is marginally the same as the uncertainty in Stanton number for the  $L/d_0 = 4$  cones. The experimental apparatus and methods used to obtain these Stanton number distributions were the same; thus the bias error is the same for both test surfaces. As shown in Figure 7.14 for the  $L/d_0 = 4$  surfaces, the repeatability of a Stanton number distribution for a given  $U_\infty$  is excellent. This figure shows replications for both surfaces at a representative velocity of 12 m/s. Replications of all THTTF Stanton runs demonstrate this run-to-run precision with the exception of the  $U_\infty = 6$  m/s cases, which reflect the 3% precision limit discussed in Chapter 3.

Profiles of the mean temperature within the thermal boundary layer were measured for the prescribed constant wall temperature boundary condition of 44 C. As described in Chapter 3, a thermocouple probe was used to measure these profiles of the thermal boundary layer for representative freestream velocities of 6, 12, 43, and 66 m/s. Prior THTTF studies using the smooth test surface

produced thermal boundary layer profiles which are consistent with the law of the wall for the thermal boundary layer, Eq. (5.2), as given by Kays and Crawford (1980). Figure 7.15 shows a comparison of temperature profiles from  $U_\infty = 12$  m/s runs for both  $L/d_0 = 4$  rough surfaces. These data are also compared with the thermal law of the wall in the  $T^+$  versus  $y^+$  coordinates. The temperature profiles from the flows over the two surfaces are the same within the data uncertainty.

### 7.3 COMPARISONS OF PREDICTIONS WITH DATA

The empirical models for  $C_D$  and  $Nu_D$  used to generate the discrete element method predictions presented in this chapter were those as discussed previously in Chapter 6. No adjustments to these models were made based on data from the current surfaces roughened with truncated cones. As discussed previously, the  $C_D$  model had been developed and tested against a wide range of rough surfaces; however, the  $Nu_D$  model has previously been tested only for the Stanford rough surface composed of spheres packed in the most dense array and the three THTTF surfaces roughened with hemispherical elements.

In Figure 7.16, skin friction coefficient data for the  $L/d_0 = 2$  and  $L/d_0 = 4$  surfaces with truncated cone and hemisphere roughness are compared with  $C_f$  calculations made using the discrete element prediction scheme for freestream velocities of 12 m/s and 58 m/s. Comparisons of skin friction coefficient data and predictions plotted versus the momentum thickness Reynolds number show that the

predictions exhibit a behavior that is typical of the data. For a freestream velocity of 58 m/s, predictions and data agree within the data uncertainty. For a freestream velocity of 12 m/s, the data and predictions for the hemisphere roughness agree within the data uncertainty for both  $L/d_0 = 2$  and  $L/d_0 = 4$ , but predictions for the truncated cone roughness fall slightly below the uncertainty bounds of the data. The indicated smooth wall line is the turbulent flat plate boundary layer correlation from Kays and Crawford (1980).

The Stanton number data for the  $L/d_0 = 2$  and  $L/d_0 = 4$  surfaces roughened with truncated cones are compared with predicted Stanton number distributions in Figure 7.17 for nominal freestream velocities of 6, 12, 28, 43, 58, and 66 m/s. This figure shows that the agreement of the data and predictions for the  $L/d_0 = 4$  surface is excellent, with both exhibiting identical behavior with increasing velocity. However, the prediction model slightly over predicts the data for the  $L/d_0 = 2$  surface. The smooth wall curve shown is the smooth surface flat plate boundary layer correlation, Eq. (3.3).

Figures 7.18 through 7.23 compare Stanton number data for the  $L/d_0 = 2$  and  $L/d_0 = 4$  surfaces with conical roughness with the predictions for freestream velocities of 6, 12, 28, 43, 58, and 66 m/s, respectively. These figures show the excellent agreement between the experimentally determined Stanton numbers and the discrete element predictions for the  $L/d_0 = 4$  surface. For the  $L/d_0 = 2$  surface, the predictions are about 2 to 12% higher than the data, but the trend of the data is accurately predicted.

The effects of surface roughness shape on discrete element predictions of Stanton number are demonstrated in Figure 7.24 for the  $L/d_0 = 2$  and  $L/d_0 = 4$  surfaces roughened with truncated cones and with hemispheres for nominal freestream velocities of 6 and 66 m/s. The predicted Stanton number distributions for the hemisphere roughened surfaces are higher than for the truncated cone roughened surfaces. This behavior is consistent with that of the experimental data.

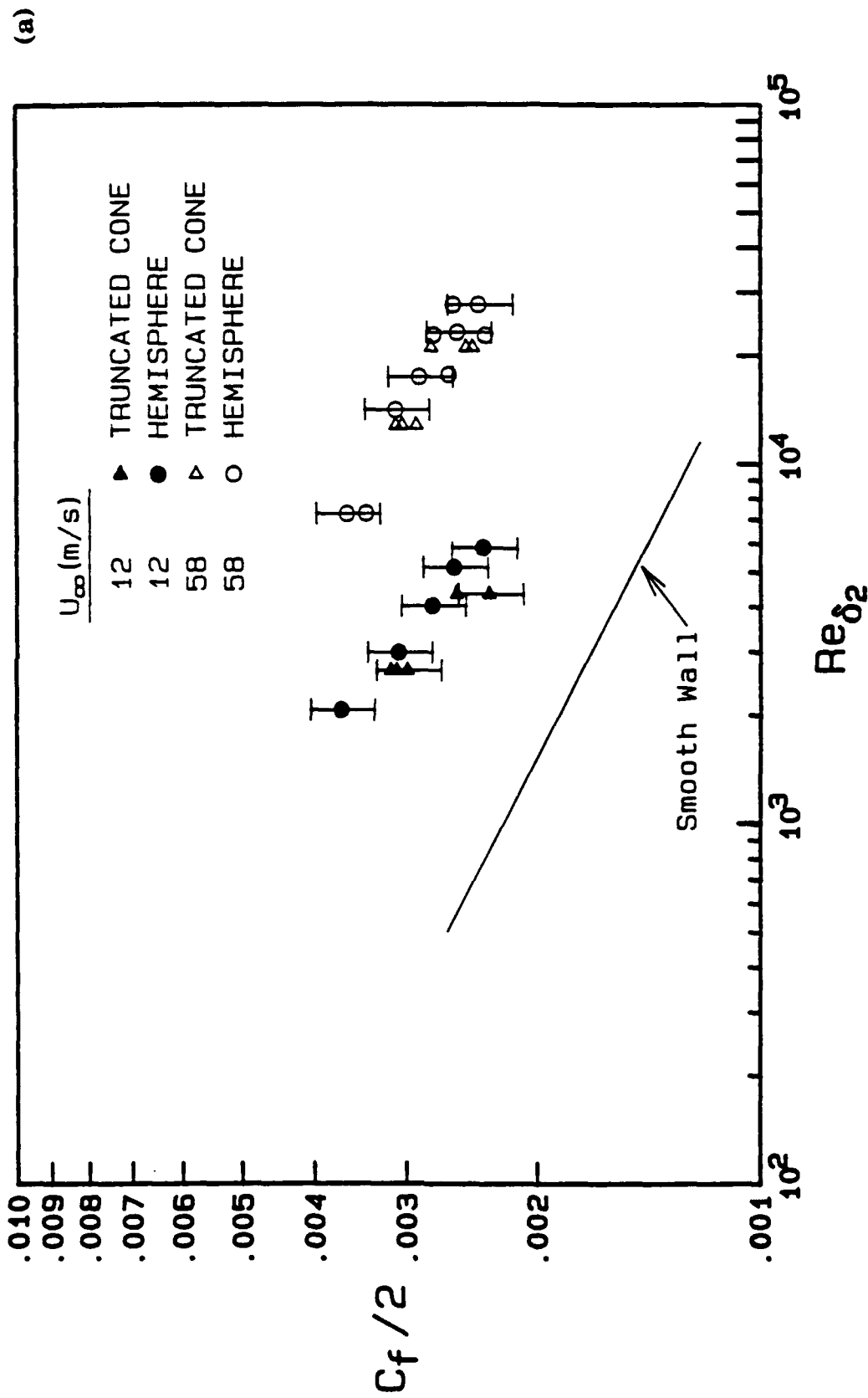


Figure 7.1 Comparison of skin friction coefficient distributions vs. momentum thickness Reynolds number. (a)  $L/d_o = 2$ ; (b)  $L/d_o = 4$ .

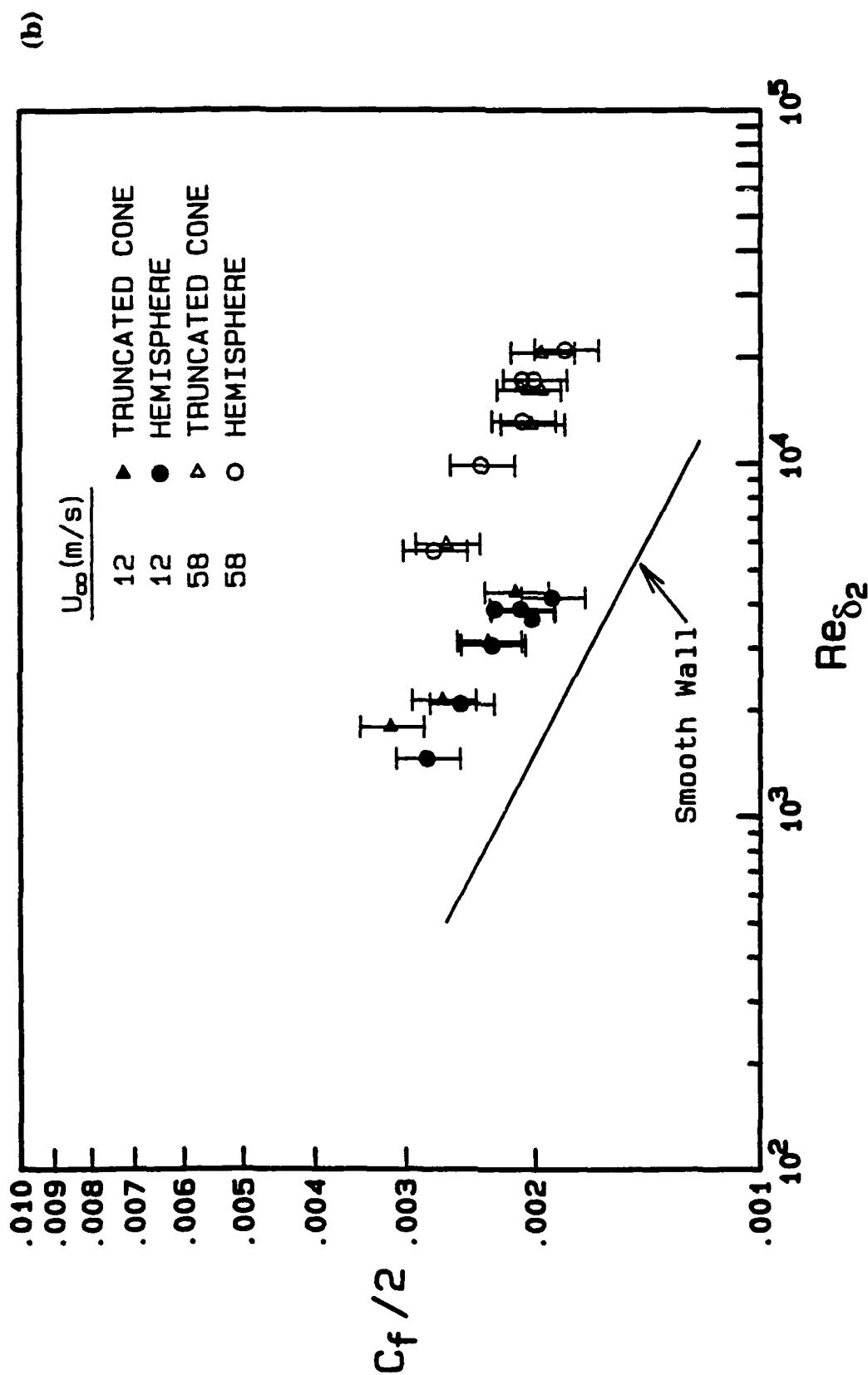


Figure 7.1 Comparison of skin friction coefficient distributions vs. momentum thickness Reynolds number. (a)  $L/d_o \approx 2$ ; (b)  $L/d_o = 4$ .

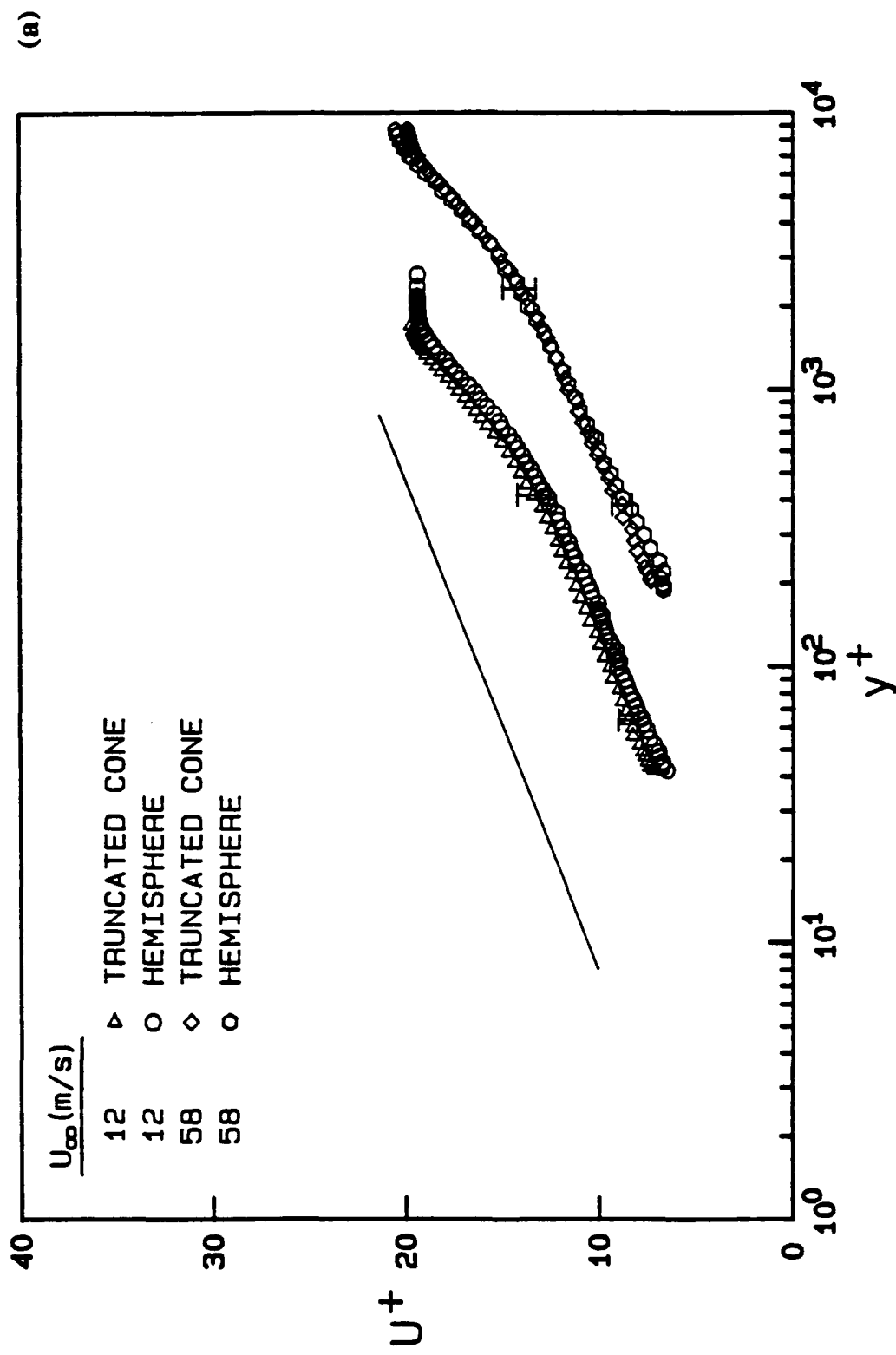


Figure 7.2 Mean velocity profiles in inner coordinates compared with the smooth law of the wall. (a)  $L/d_0 = 2$ ; (b)  $L/d_0 = 4$ .

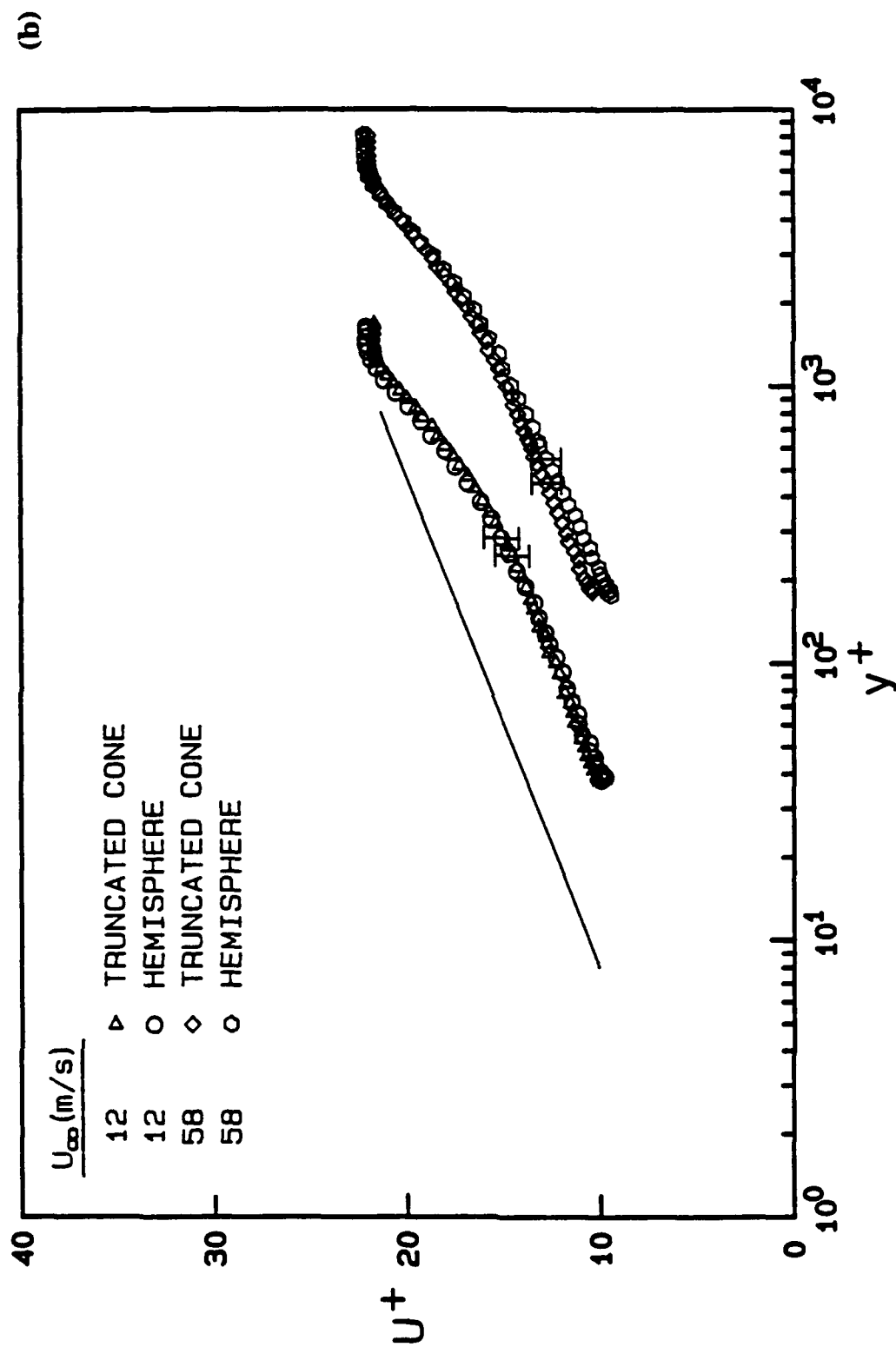


Figure 7.2 Mean velocity profiles in inner coordinates compared with the smooth law of the wall. (a)  $L/d_0 = 2$ ; (b)  $L/d_0 = 4$ .



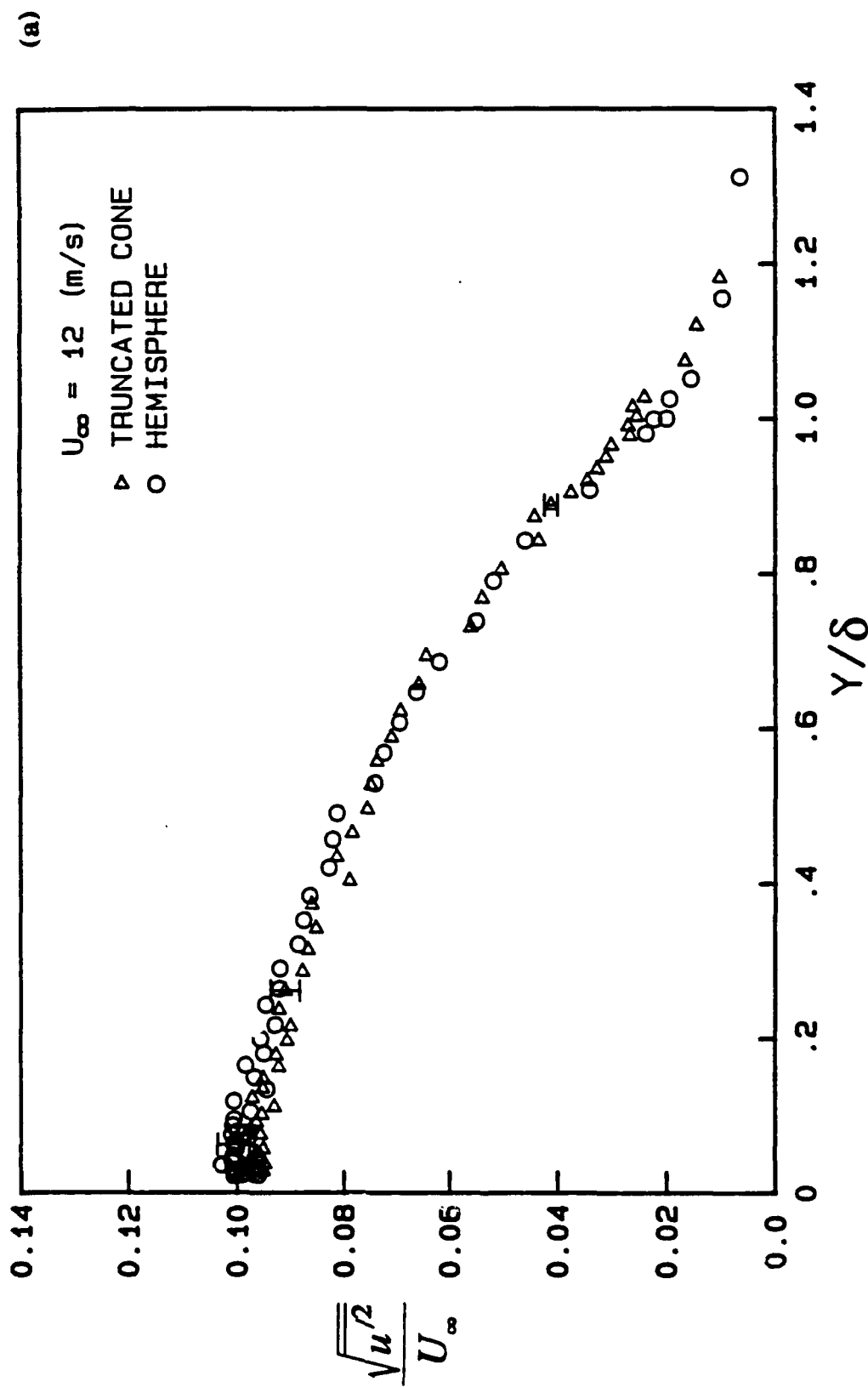


Figure 7.3 Comparison of the axial turbulence intensity profiles to illustrate similarity of profiles at  $U_{\infty} = 12 \text{ m/s}$ . (a)  $L/d_0 = 2$ ; (b)  $L/d_0 = 4$ .

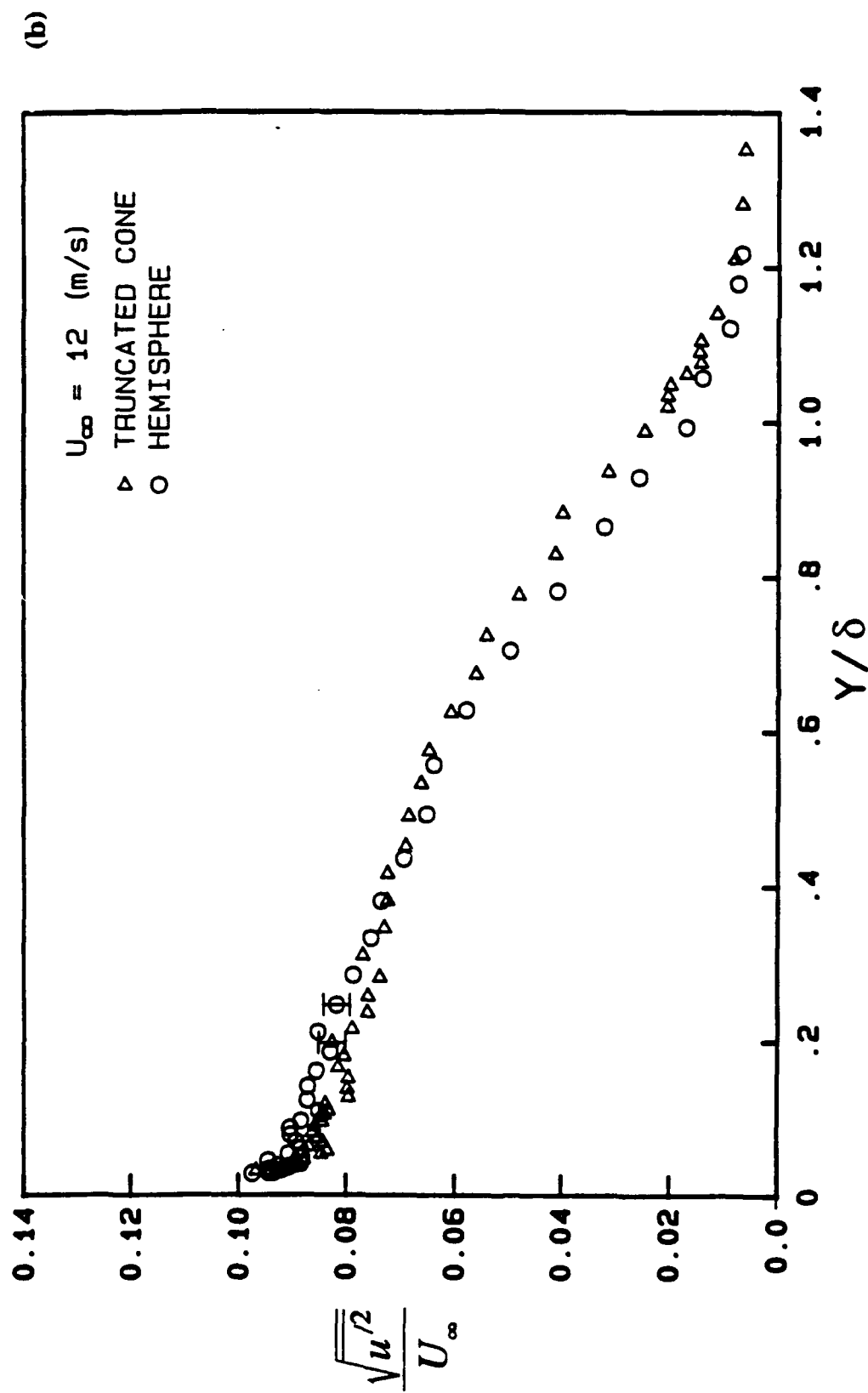


Figure 7.3 Comparison of the axial turbulence intensity profiles to illustrate similarity of profiles at  $U_\infty = 12 \text{ m/s}$ . (a)  $L/d_o = 2$ ; (b)  $L/d_o = 4$ .

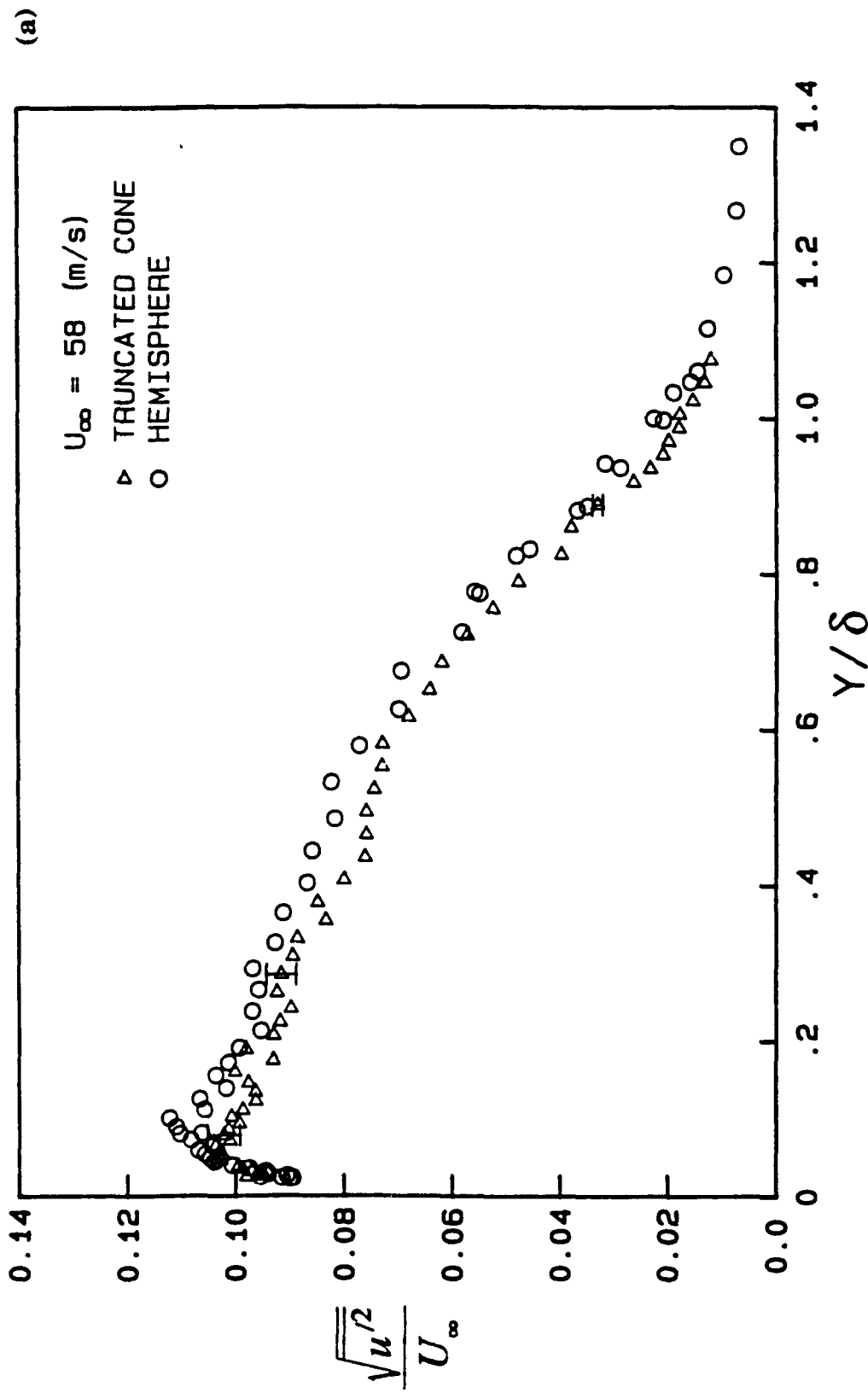


Figure 7.4 Comparison of the axial turbulence intensity profiles to illustrate similarity of profiles at  $U_{\infty} = 58 \text{ m/s}$ . (a)  $L/d_0 = 2$ ; (b)  $L/d_0 = 4$ .

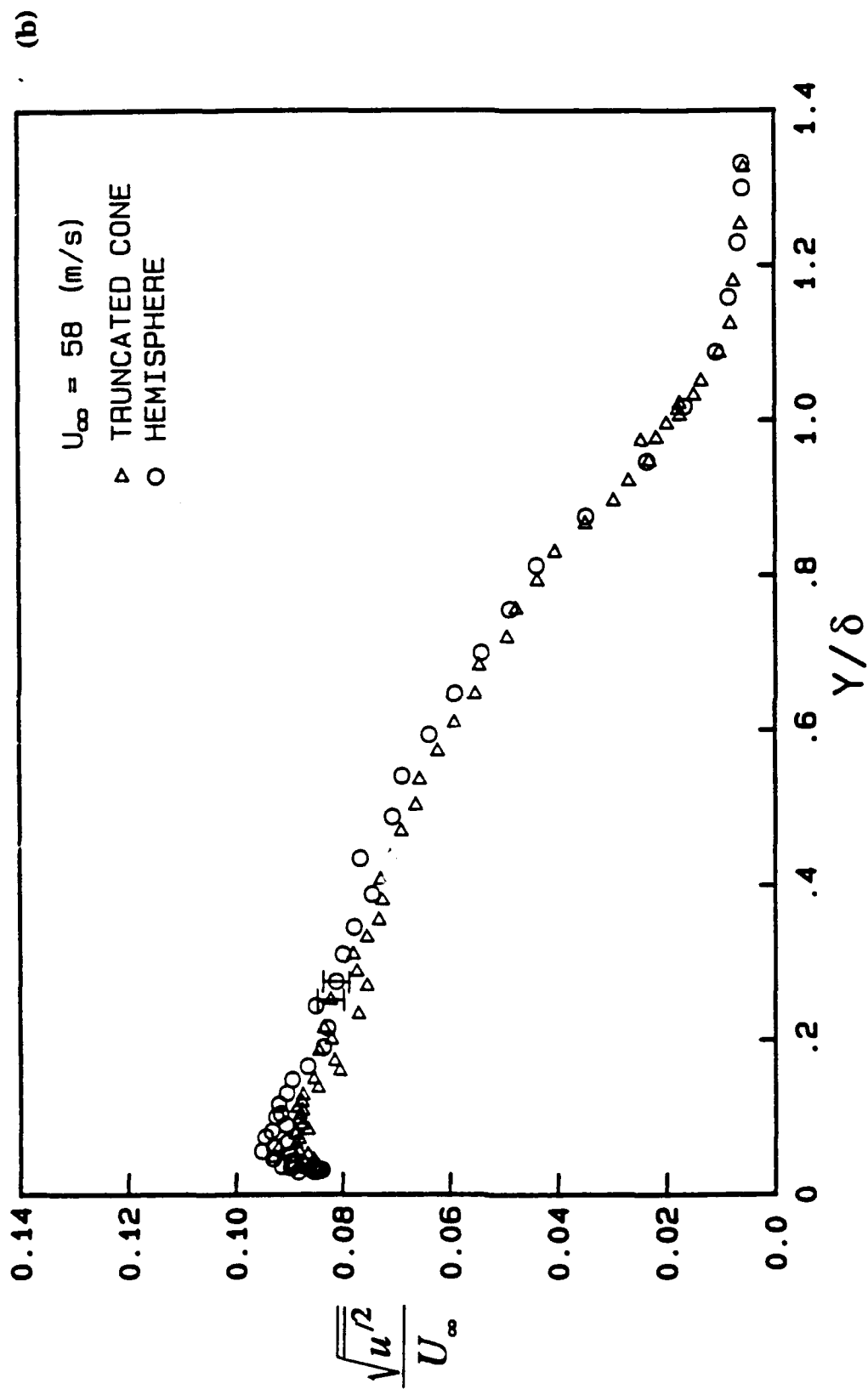


Figure 7.4 Comparison of the axial turbulence intensity profiles to illustrate similarity of profiles at  $U_{\infty} = 58 \text{ m/s}$ . (a)  $L/d_0 = 2$ ; (b)  $L/d_0 = 4$ .

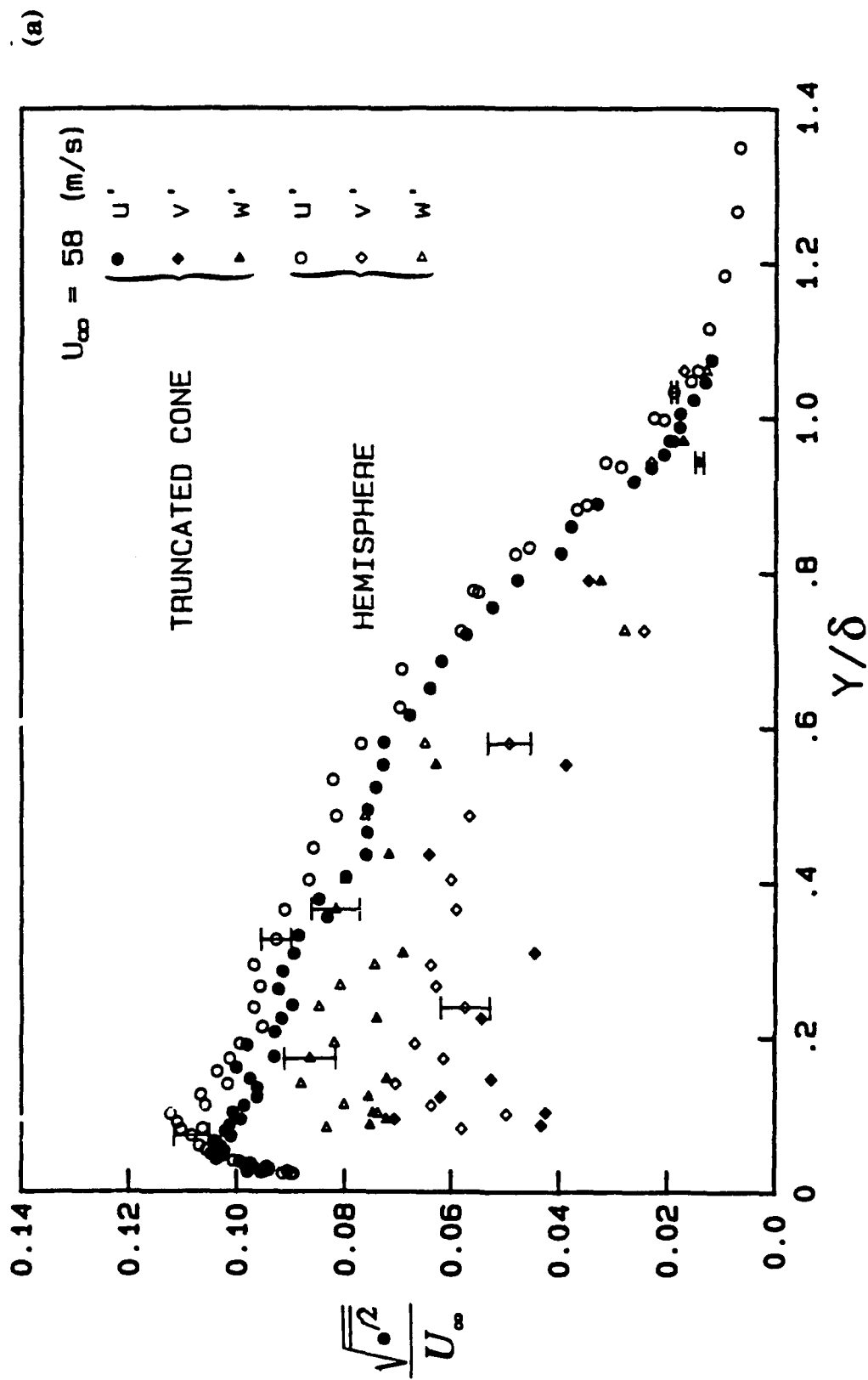


Figure 7.5 Comparison of the Reynolds normal stresses in normalized coordinates.  
(a)  $L/d_0 = 2$ ; (b)  $L/d_0 = 4$ .

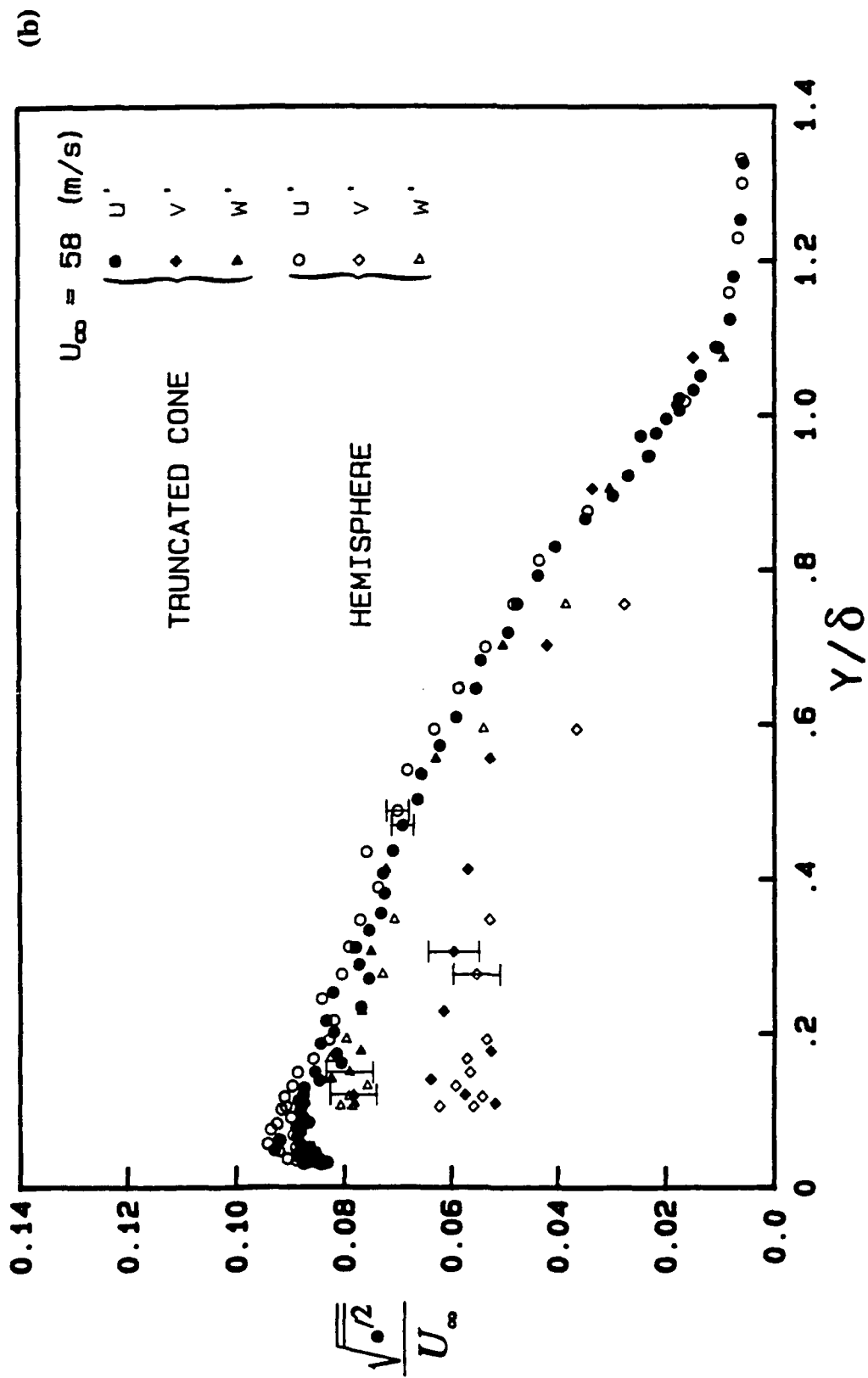


Figure 7.5 Comparison of the Reynolds normal stresses in normalized coordinates.  
(a)  $L/d_0 = 2$ ; (b)  $L/d_0 = 4$ .

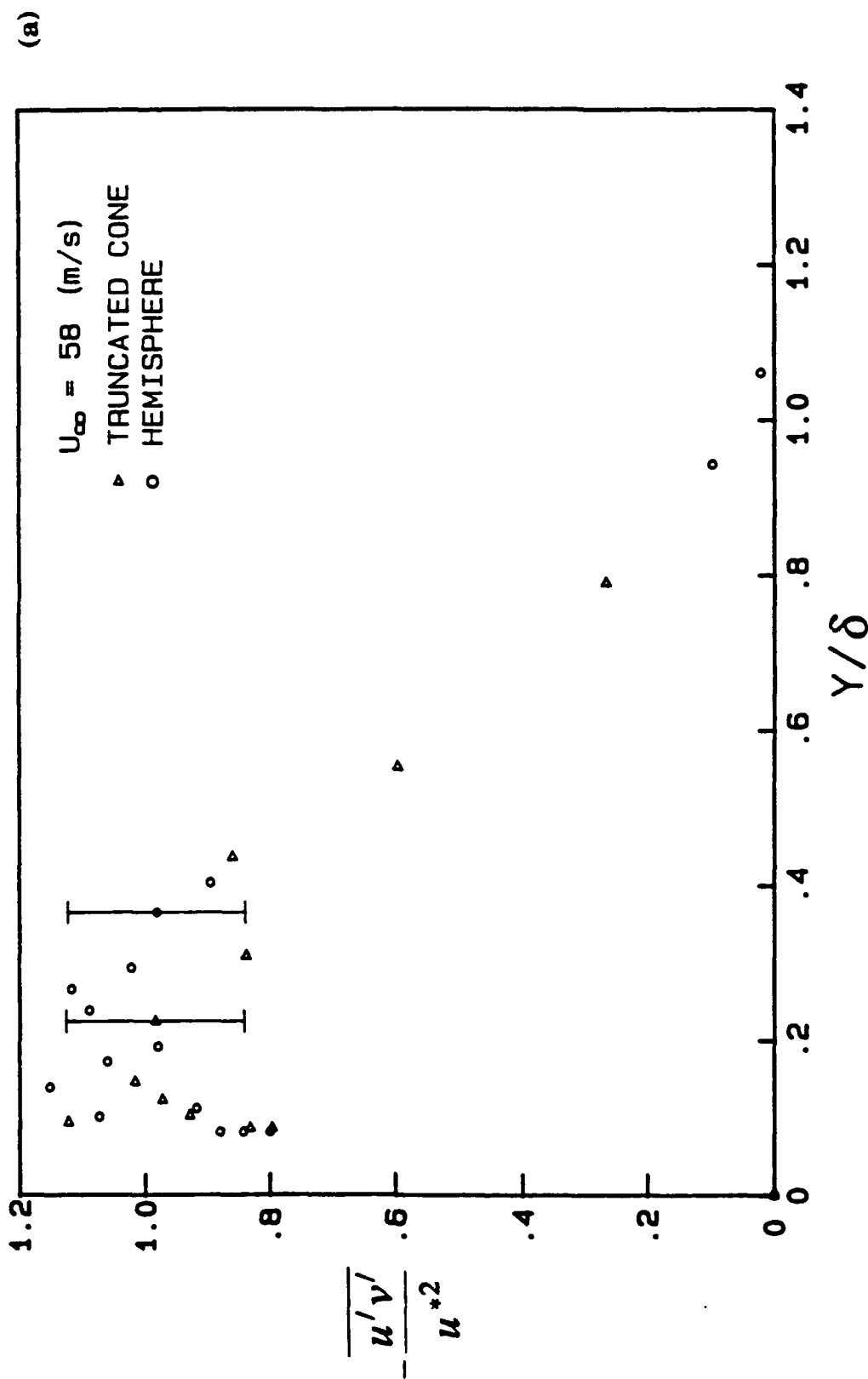


Figure 7.6 Comparison of Reynolds shear stress profiles normalized by friction velocity.  
 (a)  $L/d_0 = 2$ ; (b)  $L/d_0 = 4$ .

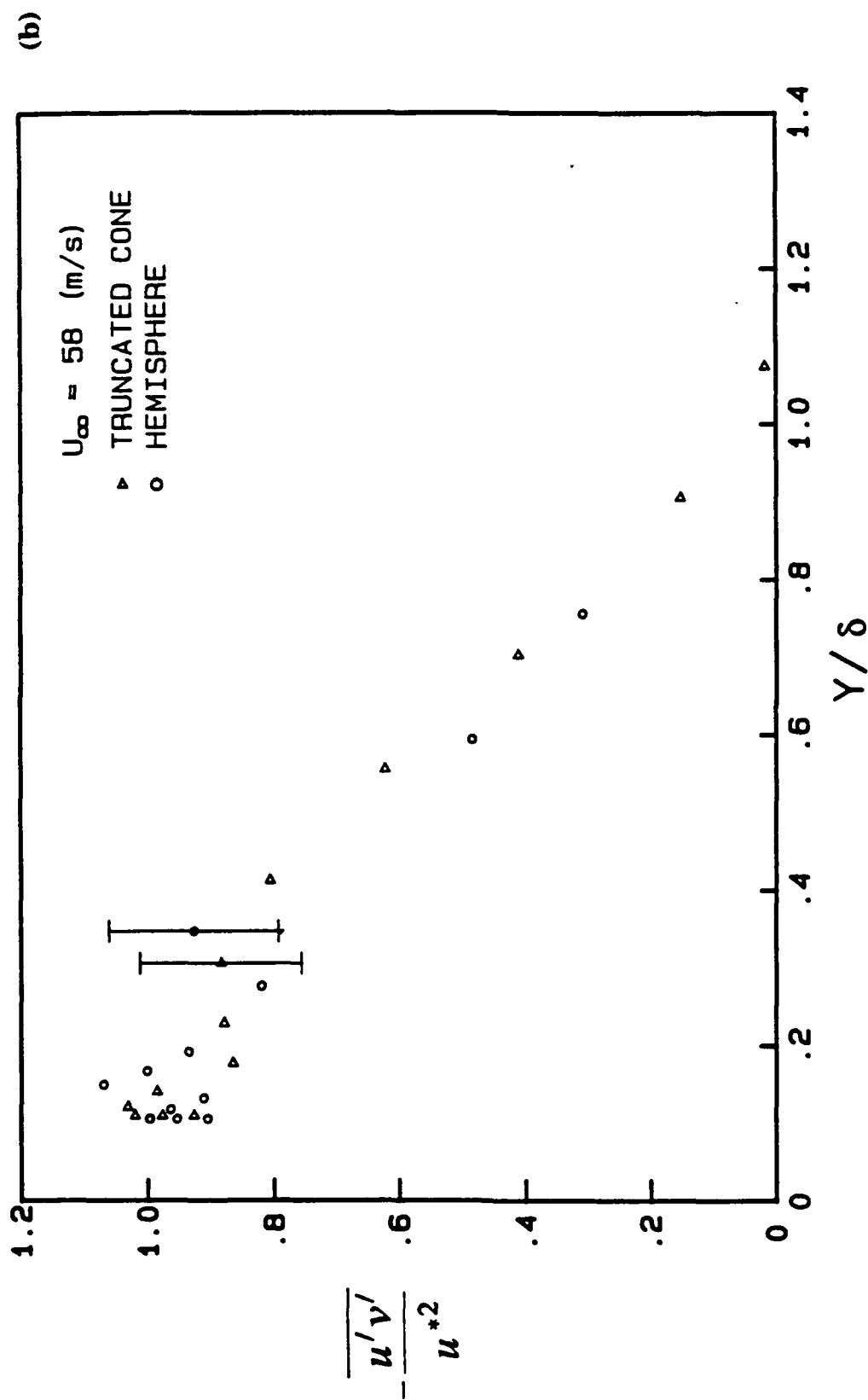


Figure 7.6 Comparison of Reynolds shear stress profiles normalized by friction velocity.  
(a)  $L/d_o = 2$ ; (b)  $L/d_o = 4$ .



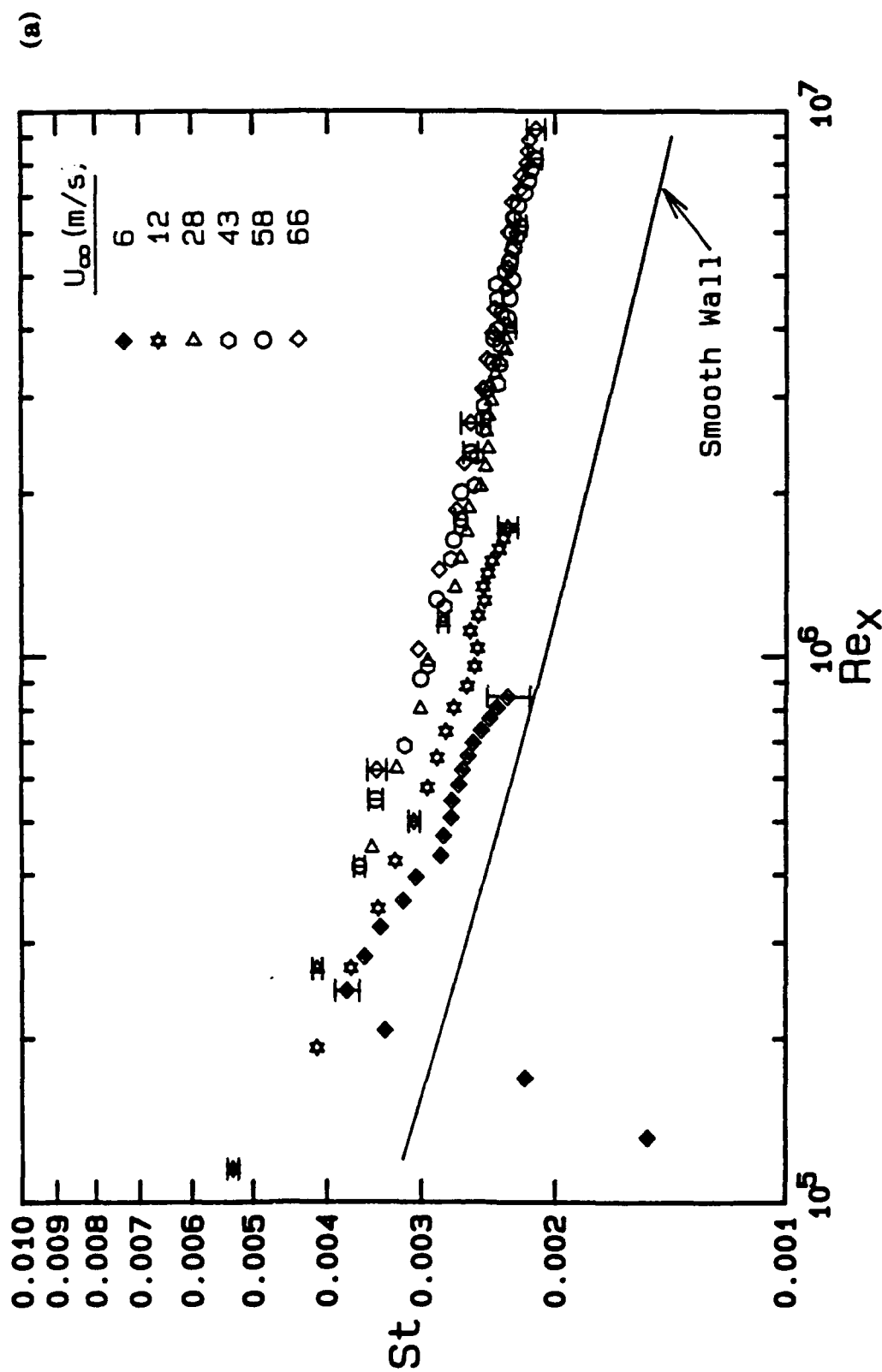


Figure 7.7 Composite plot of THTF Stanton number data vs.  $Re_x$  for surfaces with truncated cone roughnesses. (a)  $L/d_o = 2$ ; (b)  $L/d_o = 4$ .

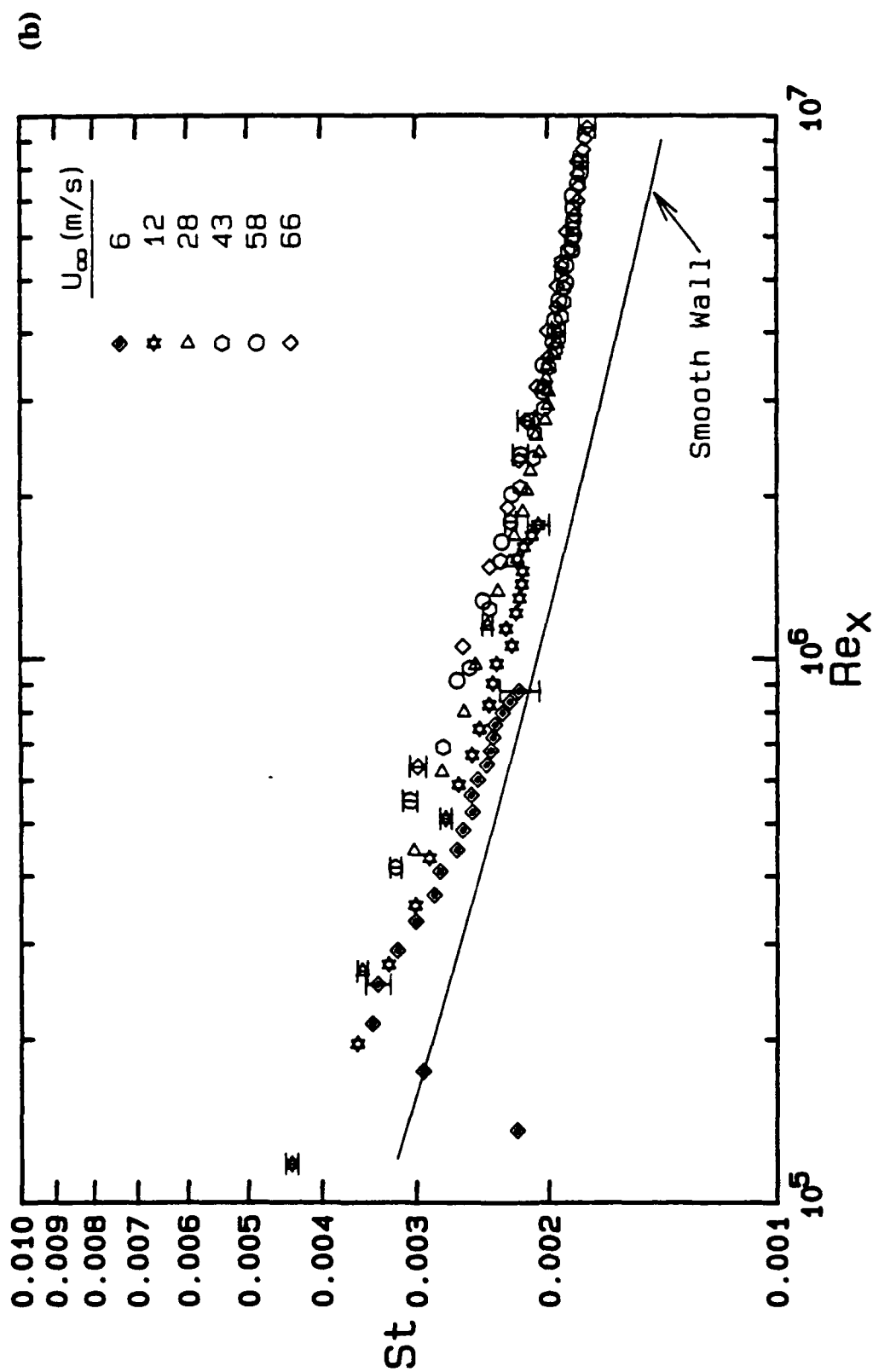


Figure 7.7 Composite plot of THETF Stanton number data vs.  $Re_x$  for surfaces with truncated cone roughnesses. (a)  $L/d_o = 2$ ; (b)  $L/d_o = 4$ .

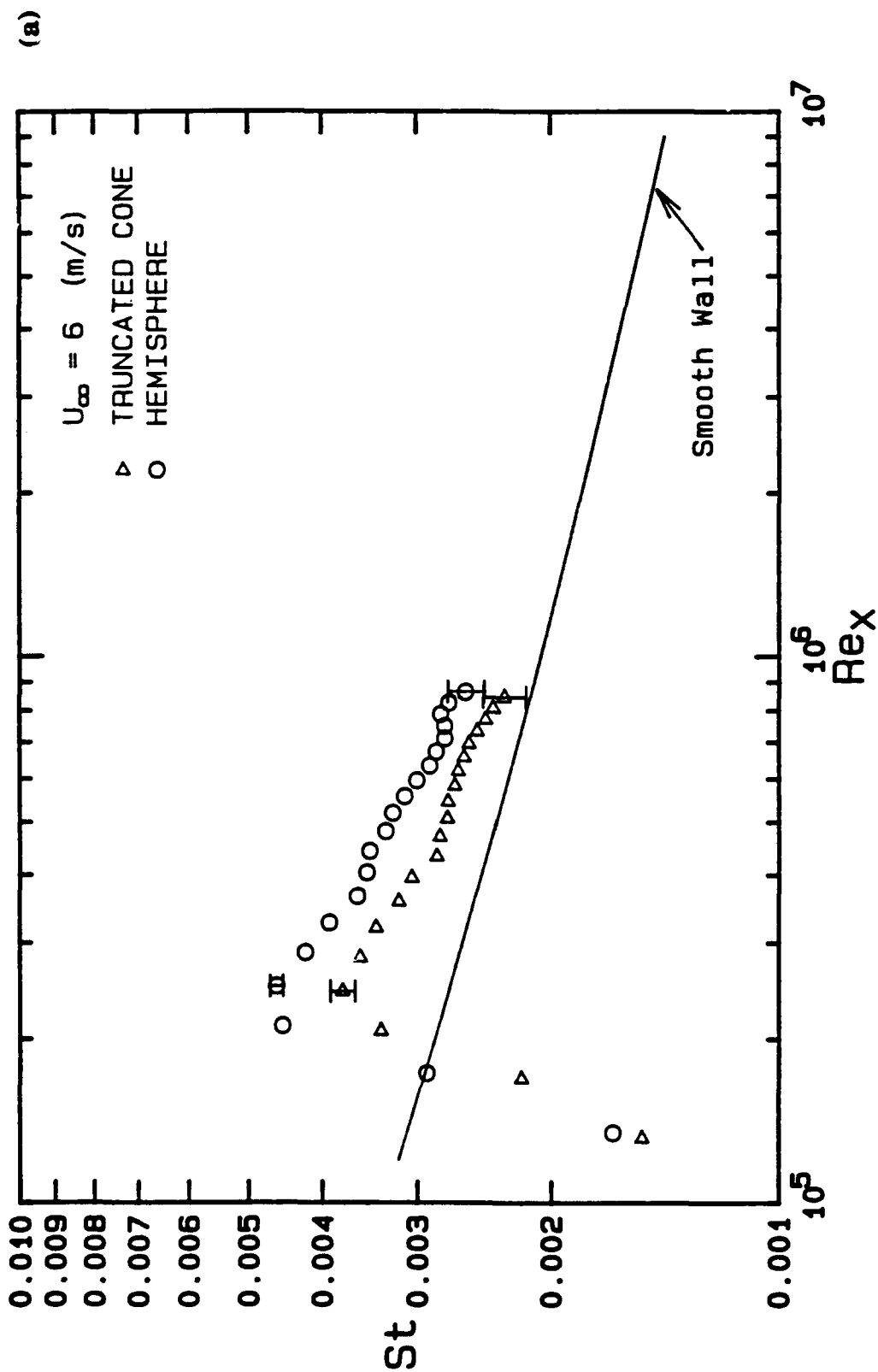


Figure 7.8 Comparison of THTF Stanton number data vs.  $Re_x$  at  $U_{\infty} = 6 \text{ m/s}$  for the truncated cone and hemisphere roughness. (a)  $L/d_0 = 2$ ; (b)  $L/d_0 = 4$ .

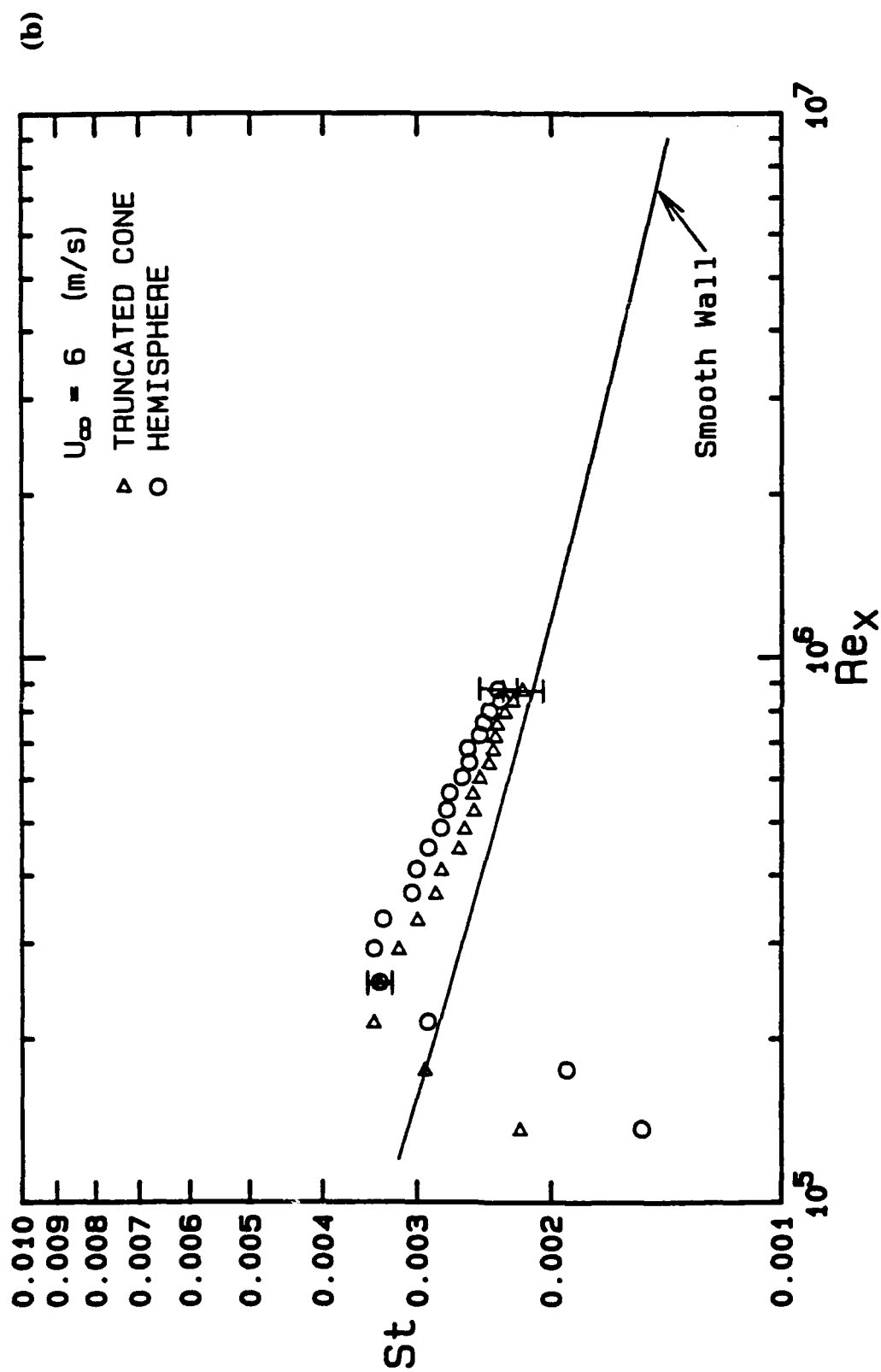


Figure 7.8 Comparison of THTF Stanton number data vs.  $Re_x$  at  $U_{\infty} = 6 \text{ m/s}$  for the truncated cone and hemisphere roughness. (a)  $L/d_0 = 2$ ; (b)  $L/d_0 = 4$ .

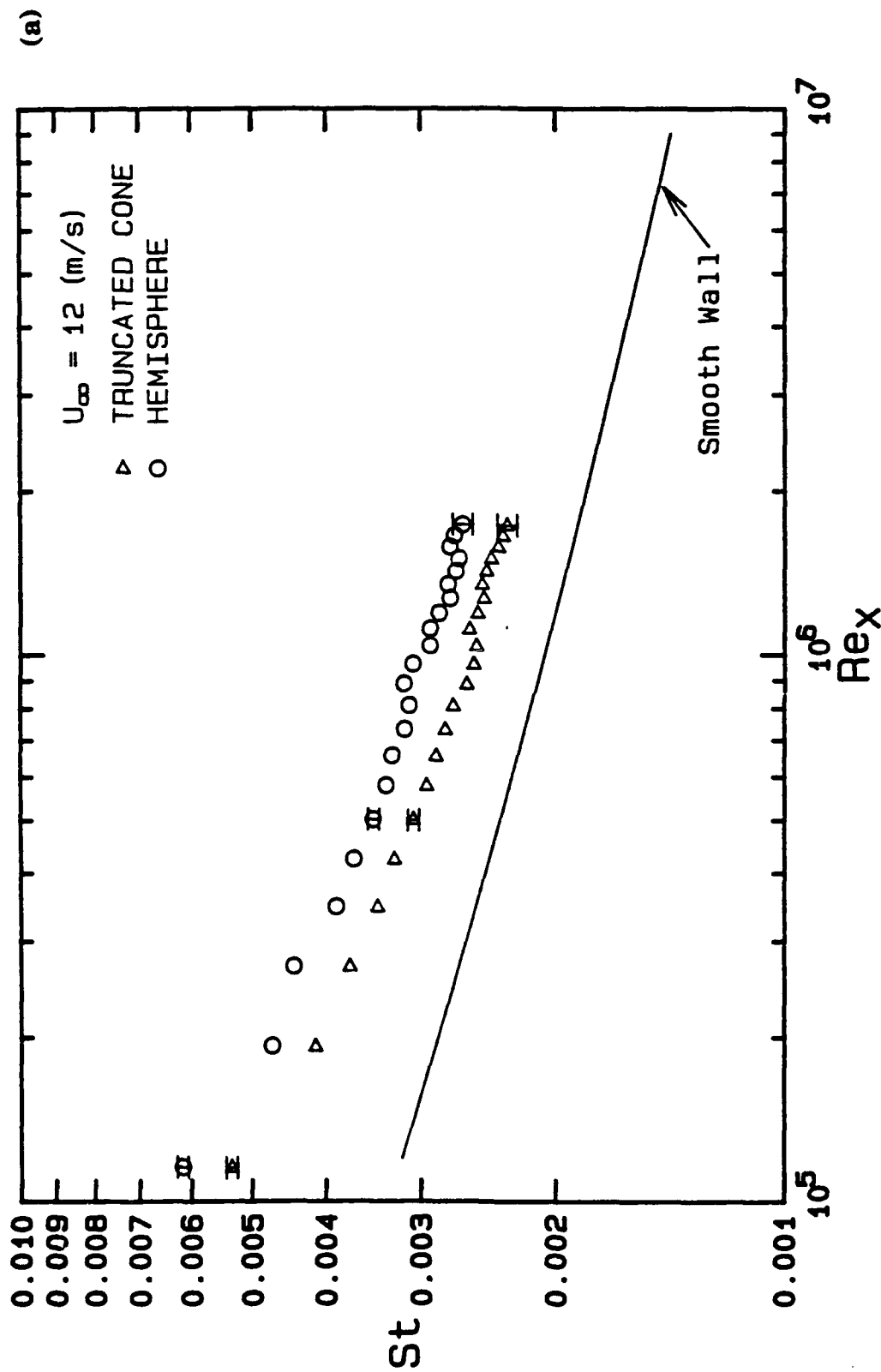


Figure 7.9 Comparison of THETF Stanton number data vs.  $Re_x$  at  $U_{\infty} = 12 \text{ m/s}$  for the truncated cone and hemisphere roughness. (a)  $L/d_o = 2$ ; (b)  $L/d_o = 4$ .

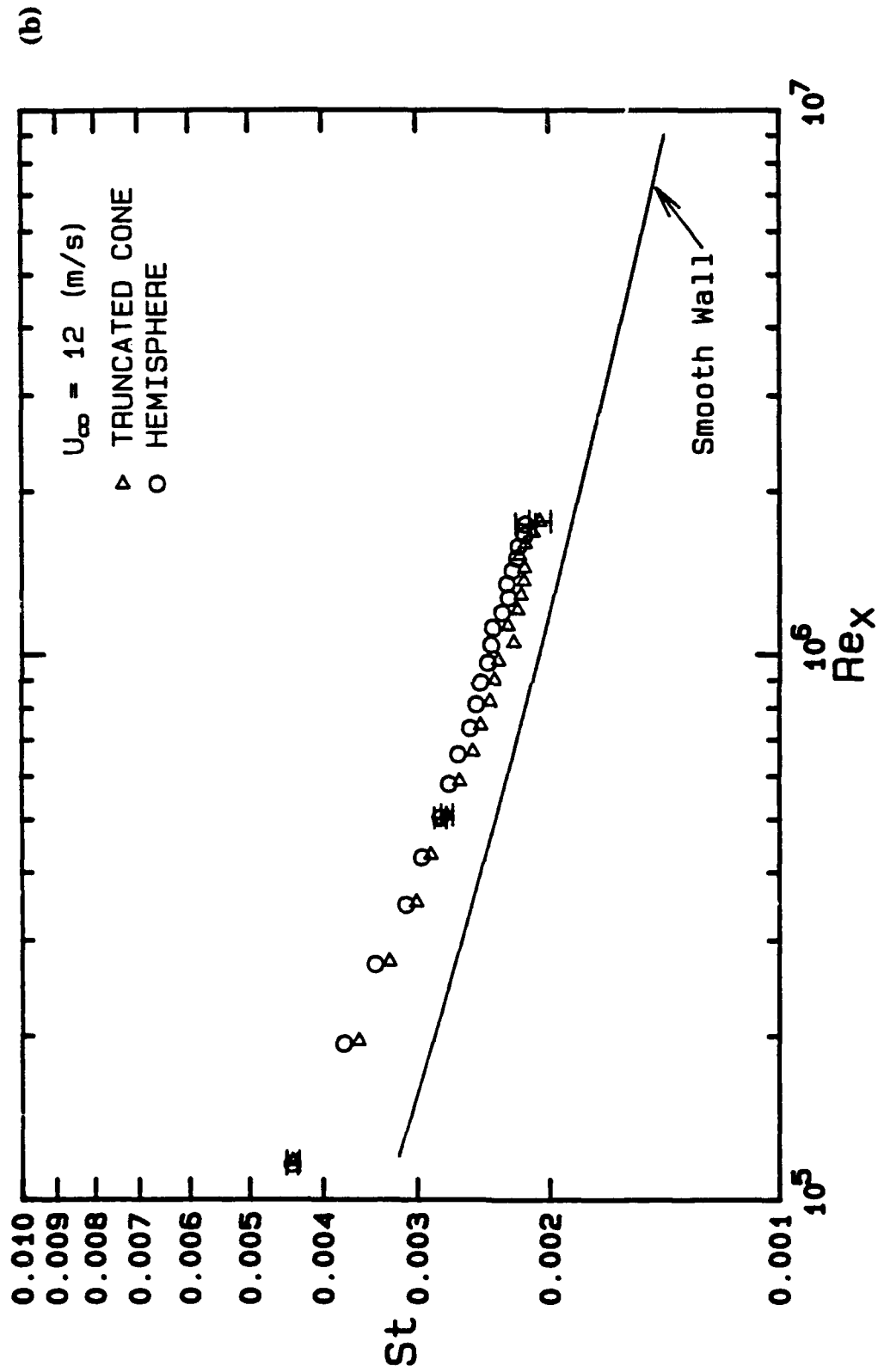


Figure 7.9 Comparison of THETF Stanton number data vs.  $Re_x$  at  $U_{\infty} = 12 \text{ m/s}$  for the truncated cone and hemisphere roughness. (a)  $L/d_0 = 2$ ; (b)  $L/d_0 = 4$ .

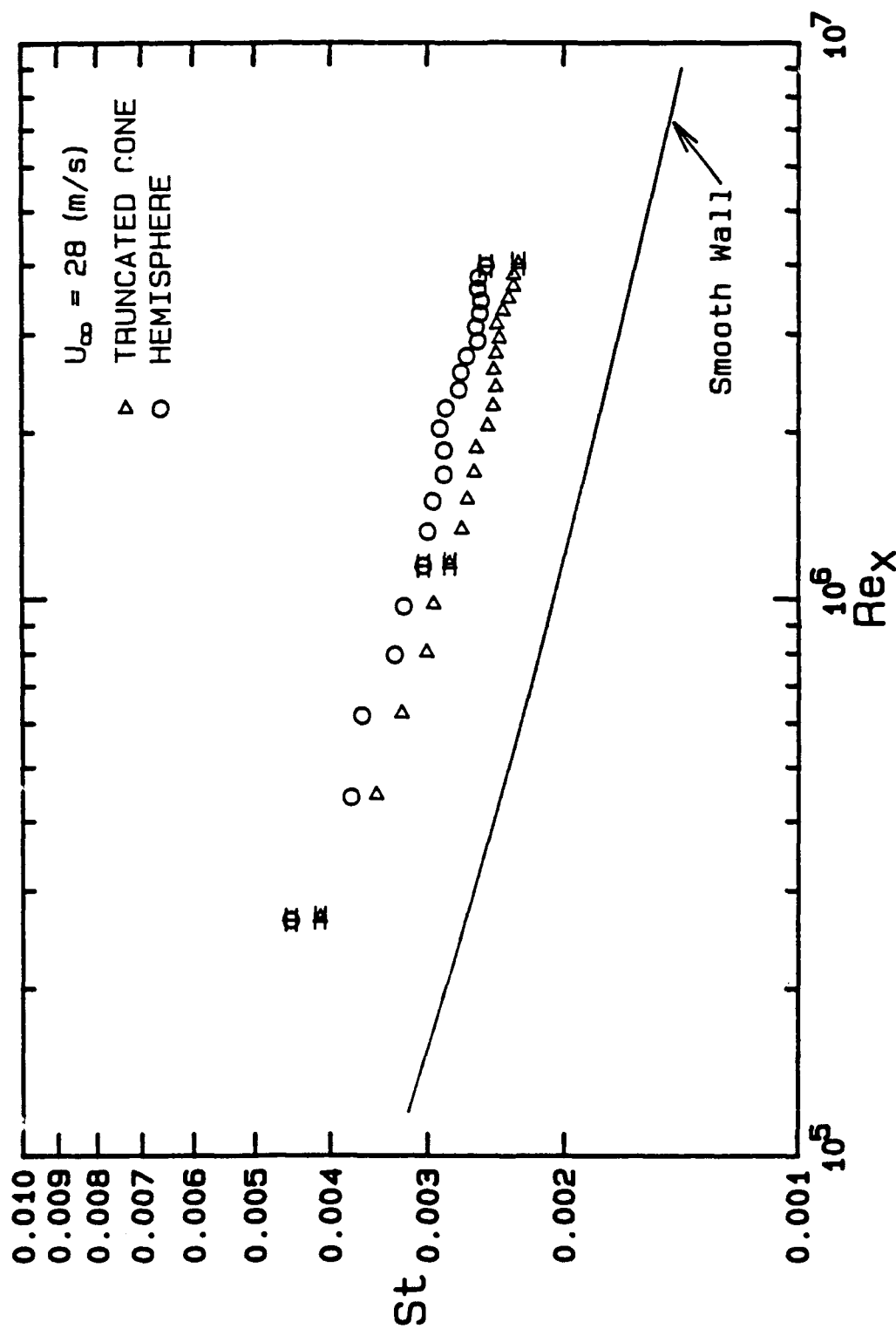


Figure 7.10 Comparison of THETF Stanton number data vs.  $Re_x$  at  $U_{\infty} = 28 \text{ m/s}$  for the truncated cone and hemisphere roughness. (a)  $L/d_0 = 2$ ; (b)  $L/d_0 = 4$ .

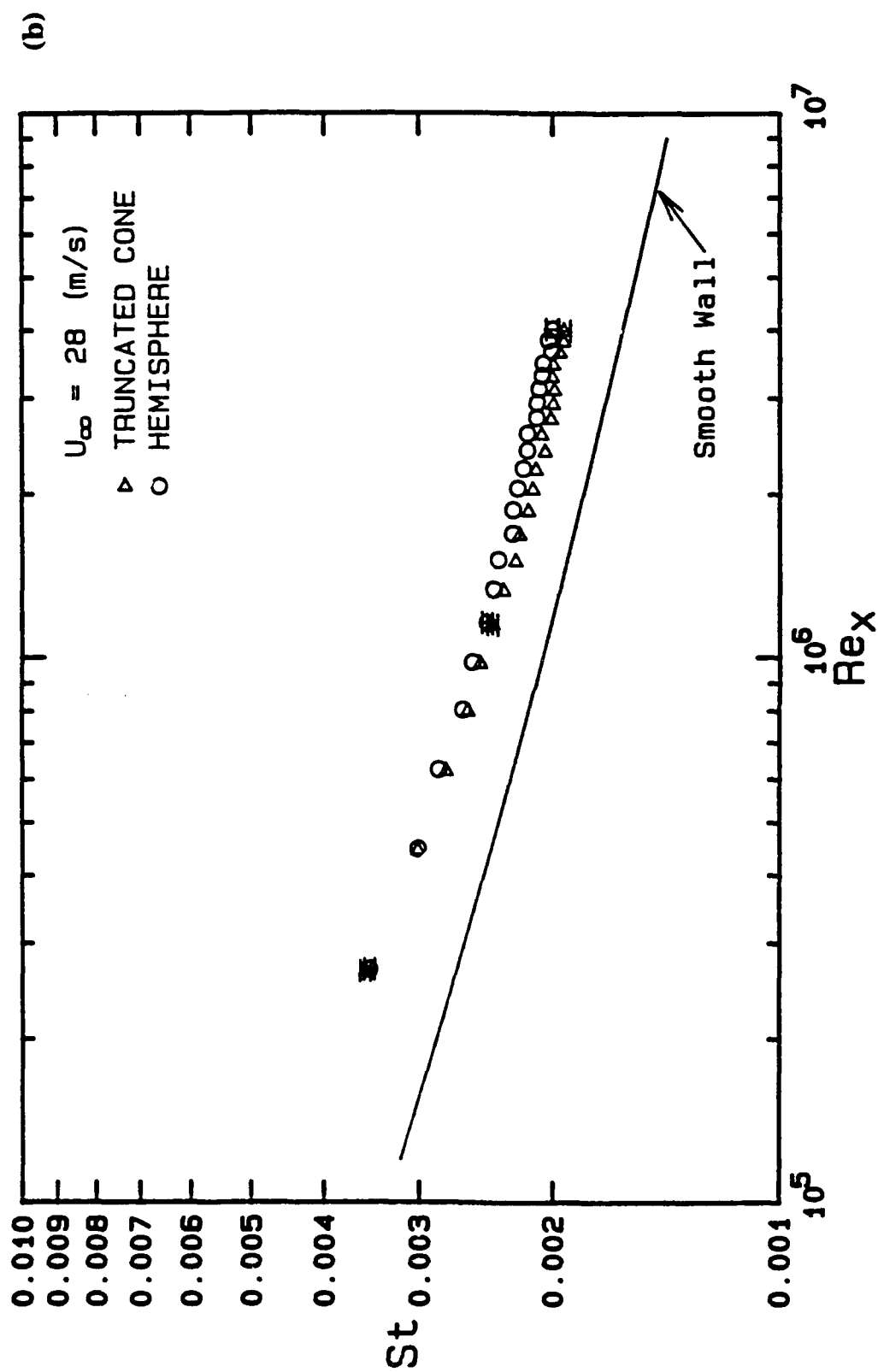


Figure 7.10 Comparison of THETF Stanton number data vs.  $Re_x$  at  $U_{\infty} = 28 \text{ m/s}$  for the truncated cone and hemisphere roughness. (a)  $L/d_o = 2$ ; (b)  $L/d_o = 4$ .



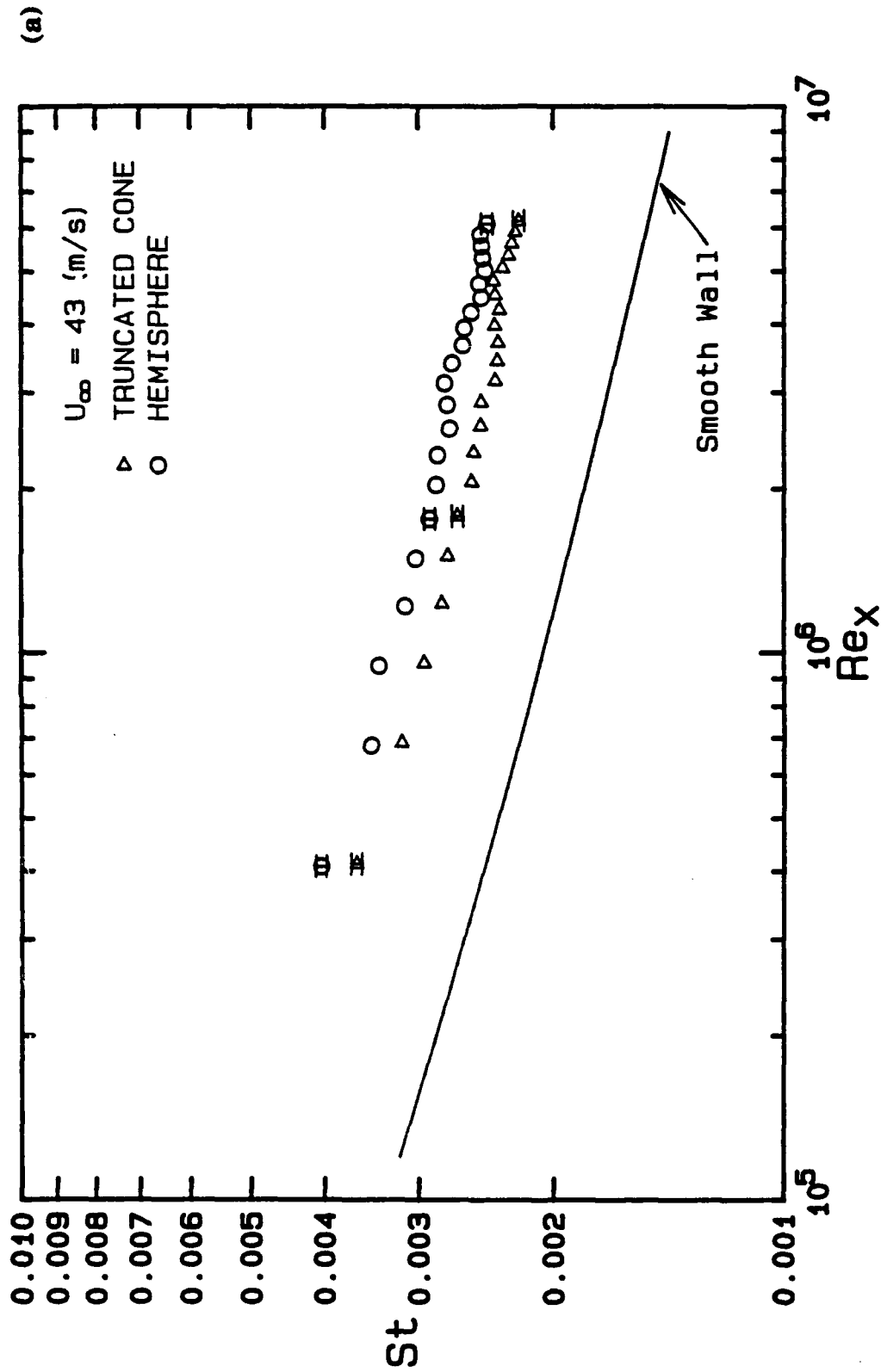


Figure 7.11 Comparison of THETF Stanton number data vs.  $Re_x$  at  $U_\infty = 43 \text{ m/s}$  for the truncated cone and hemisphere roughness. (a)  $L/d_0 = 2$ ; (b)  $L/d_0 = 4$ .

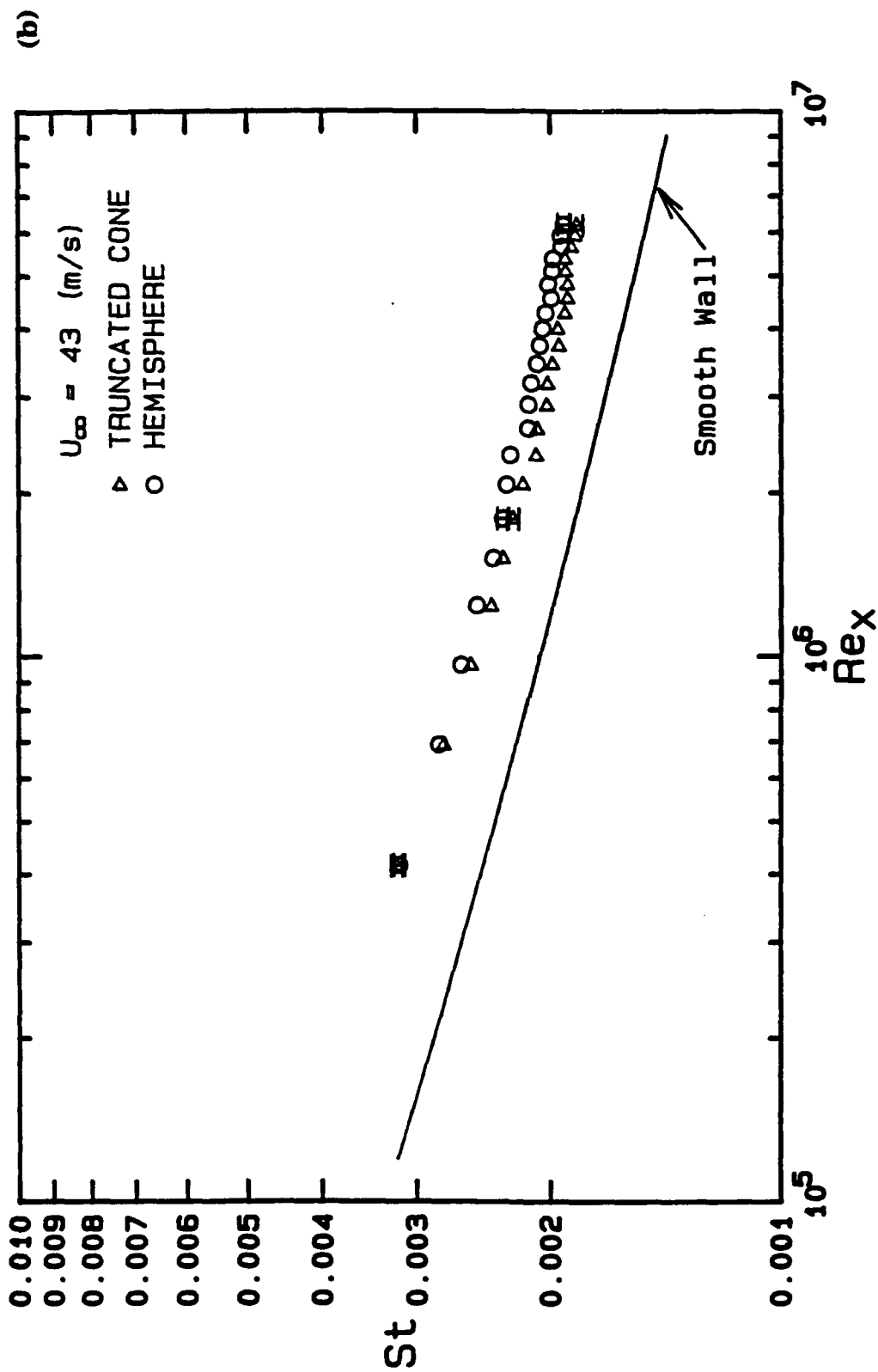


Figure 7.11 Comparison of THETF Stanton number data vs.  $Re_x$  at  $U_{\infty} = 43 \text{ m/s}$  for the truncated cone and hemisphere roughness. (a)  $L/d_o = 2$ ; (b)  $L/d_o = 4$ .

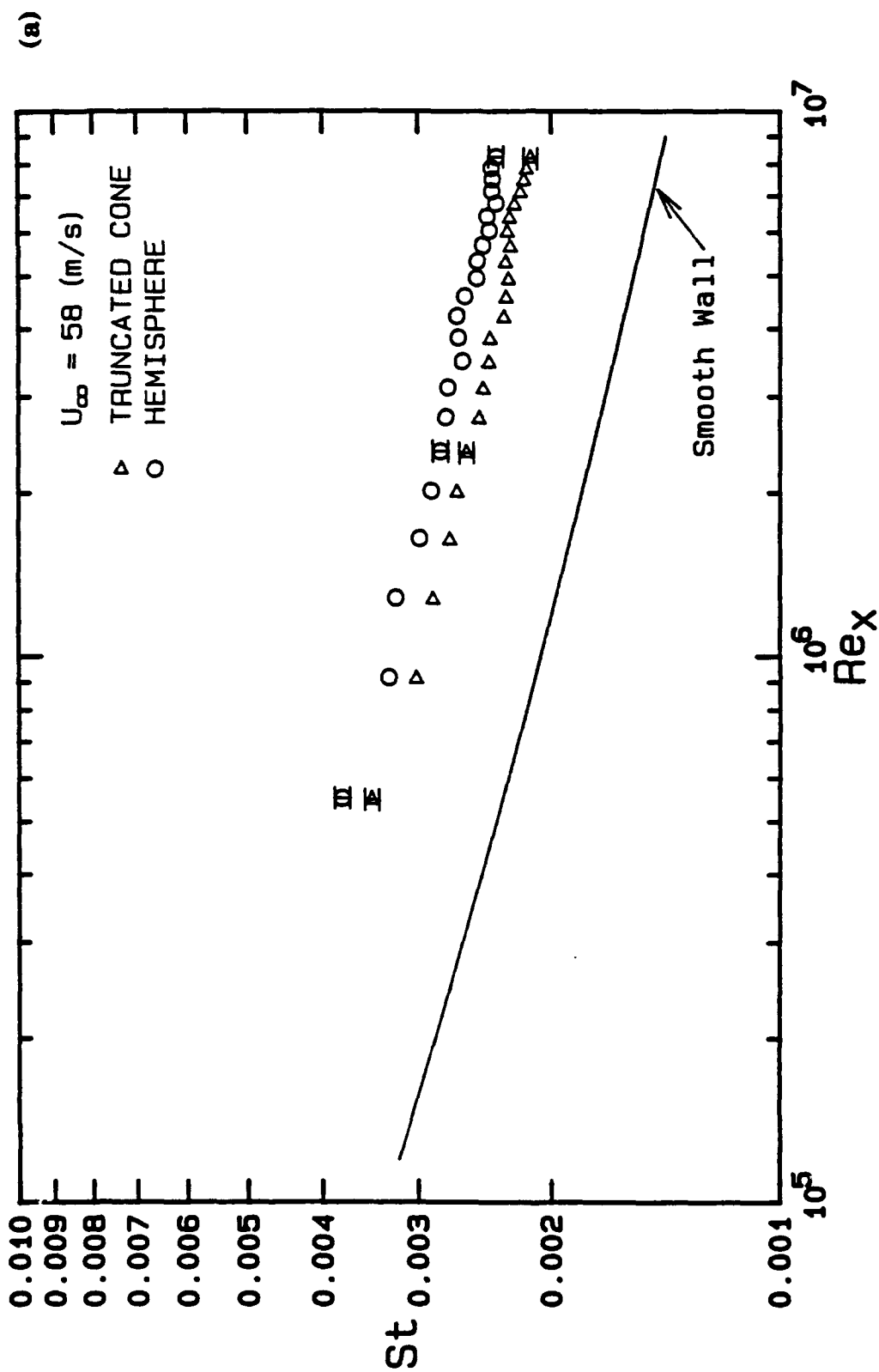


Figure 7.12 Comparison of THETF Stanton number data vs.  $Re_x$  at  $U_{\infty} = 58 \text{ m/s}$  for the truncated cone and hemisphere roughness. (a)  $L/d_o = 2$ ; (b)  $L/d_o = 4$ .

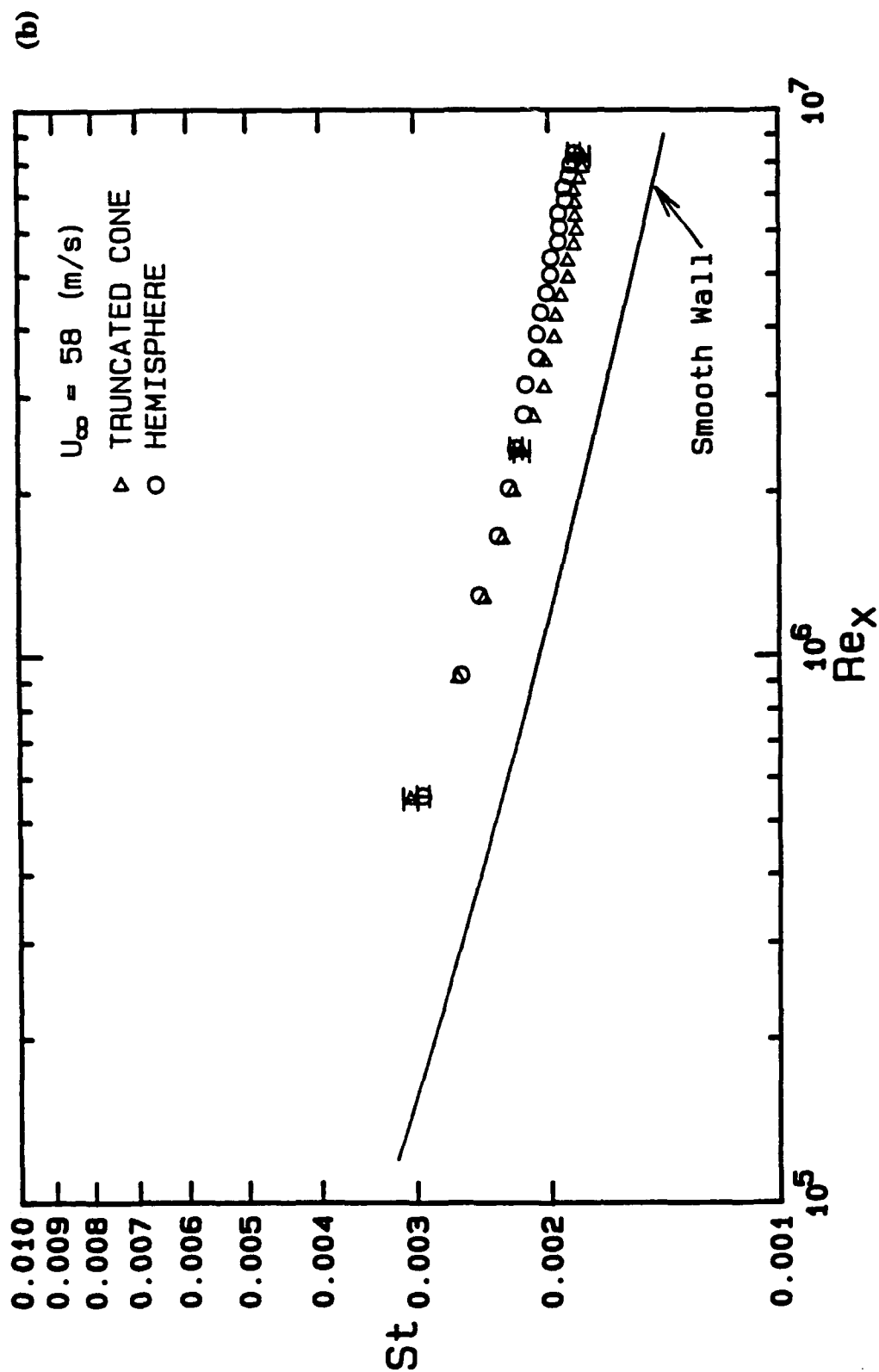


Figure 7.12 Comparison of THITF Stanton number data vs.  $Re_x$  at  $U_{\infty} = 58 \text{ m/s}$  for the truncated cone and hemisphere roughness. (a)  $L/d_0 = 2$ ; (b)  $L/d_0 = 4$ .

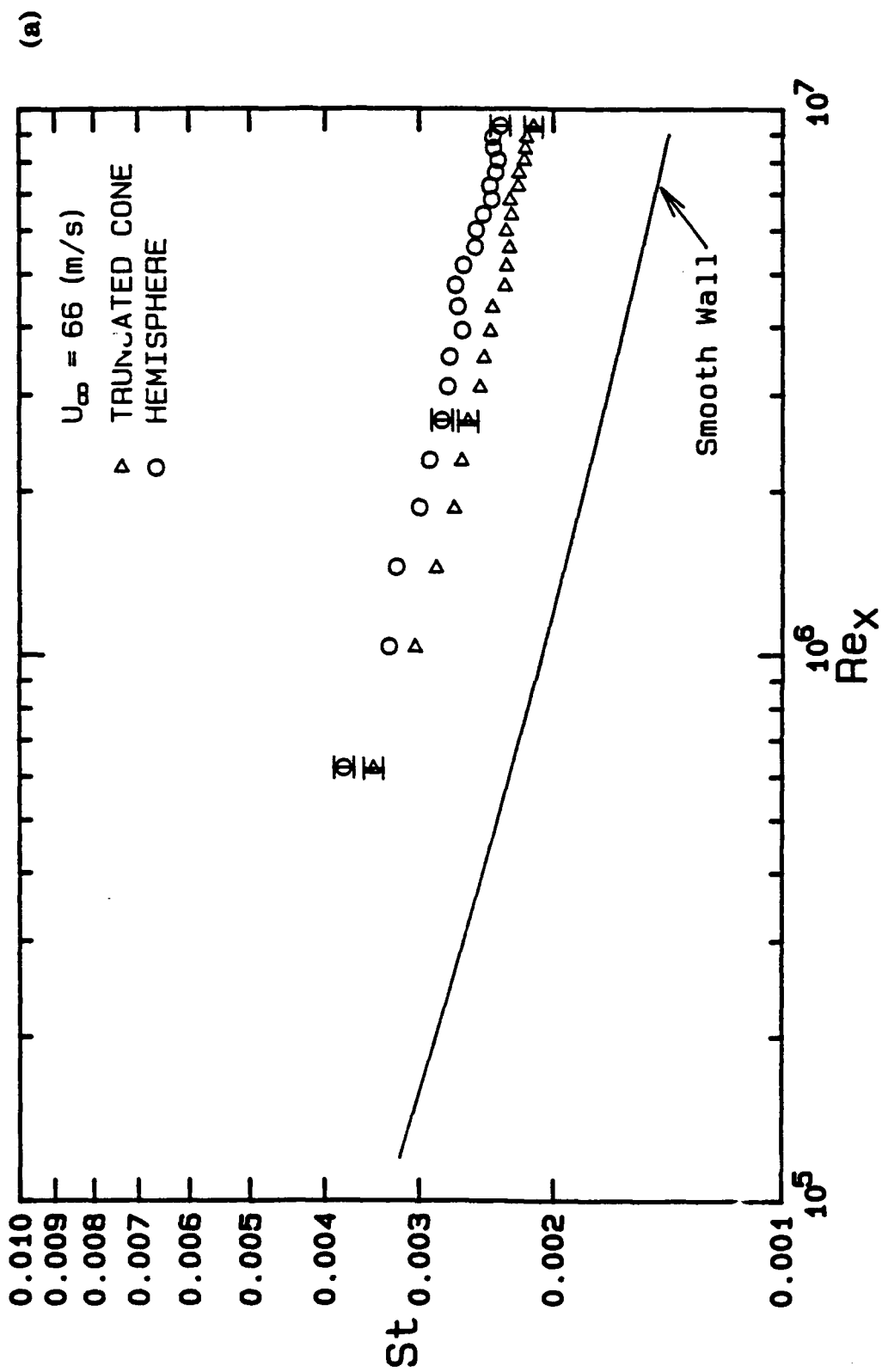


Figure 7.13 Comparison of THITTF Stanton number data vs.  $Re_x$  at  $U_{\infty} = 66 \text{ m/s}$  for the truncated cone and hemisphere roughness. (a)  $L/d_0 = 2$ ; (b)  $L/d_0 = 4$ .

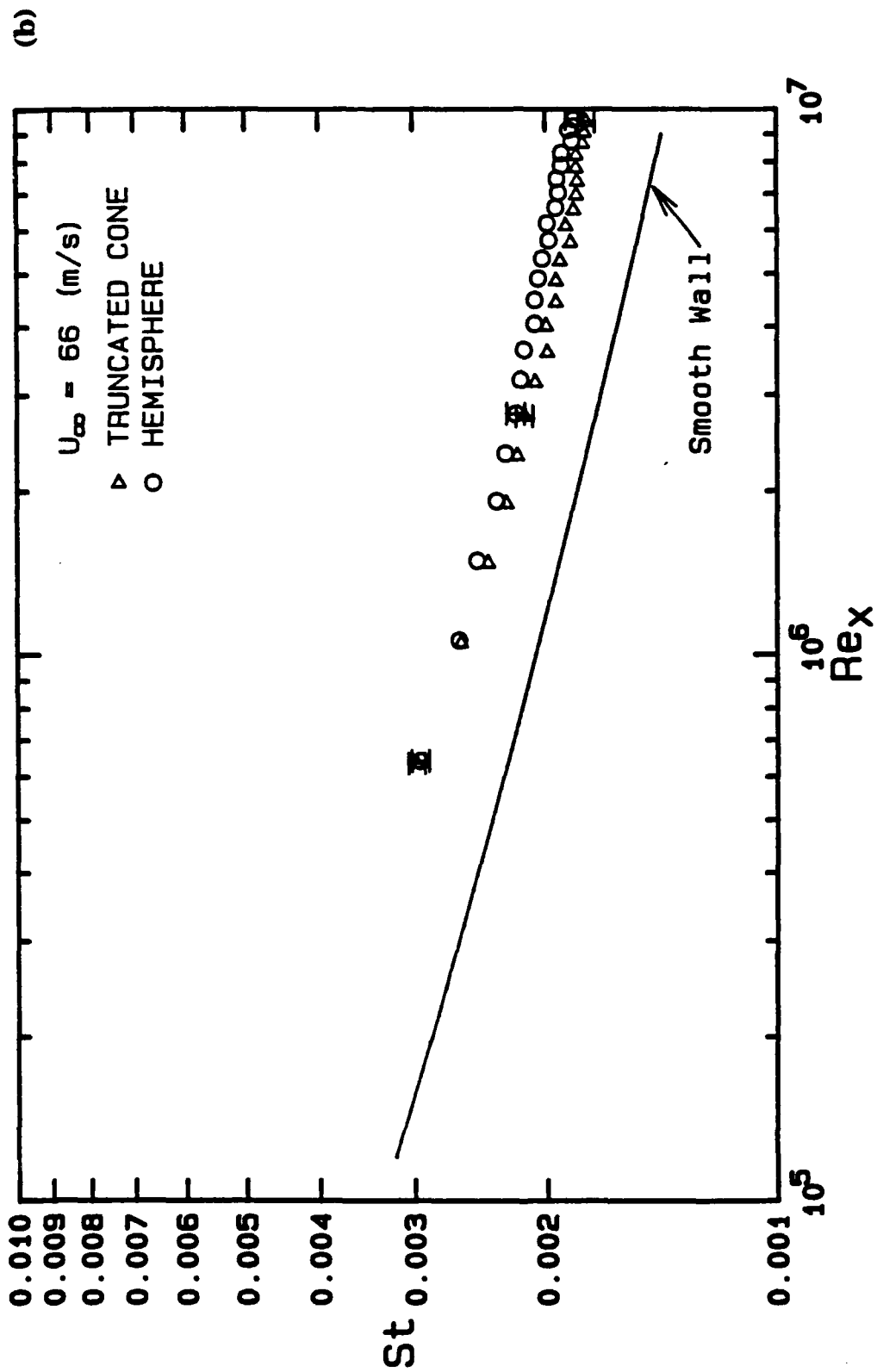


Figure 7.13 Comparison of THETF Stanton number data vs.  $Re_x$  at  $U_{\infty} = 66 \text{ m/s}$  for the truncated cone and hemisphere roughness. (a)  $L/d_0 = 2$ ; (b)  $L/d_0 = 4$ .

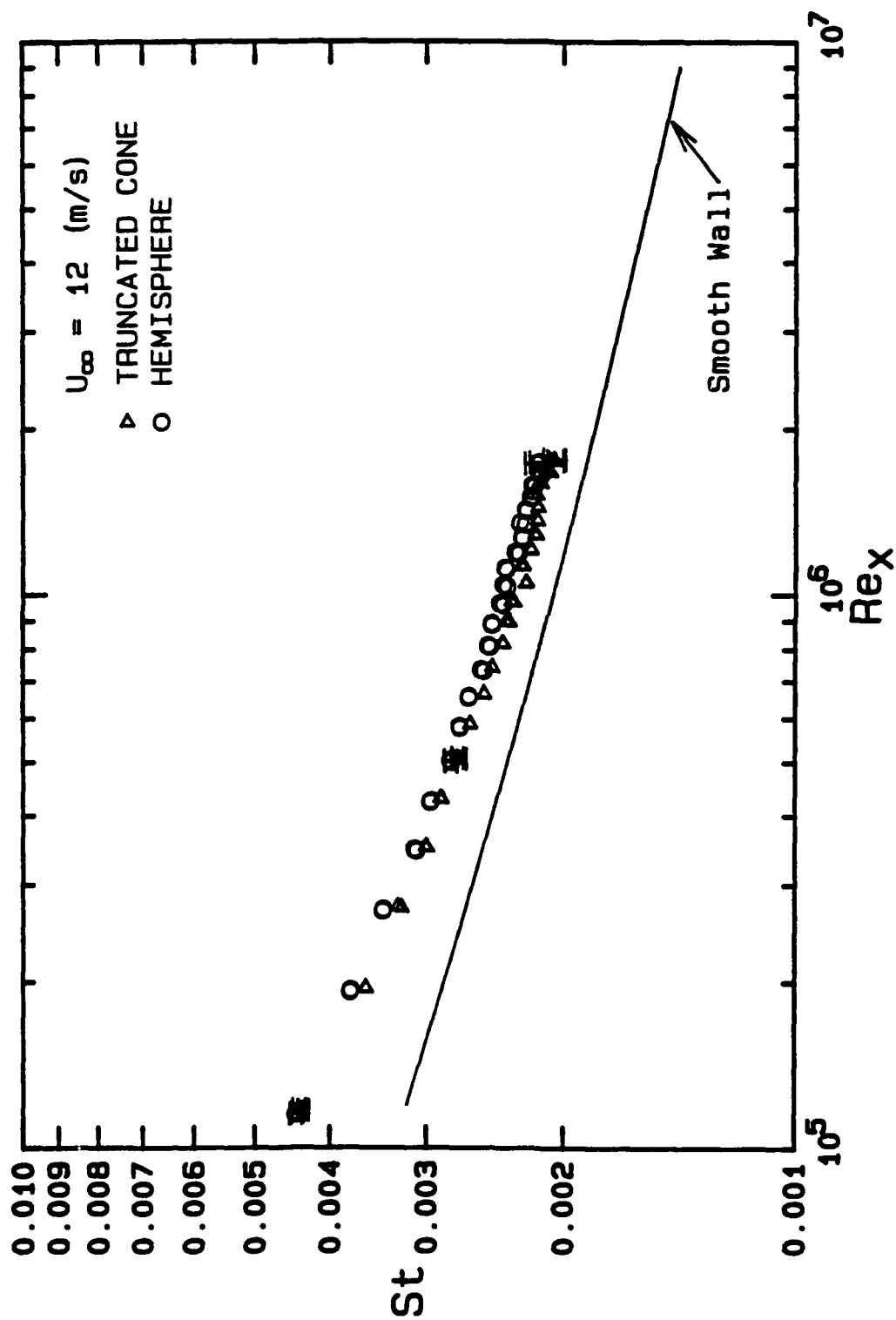


Figure 7.14 Replications of THTF Stanton number data for the  $L/d_0 = 4$  surfaces at  $U_{\infty} = 12 \text{ m/s}$  to illustrate repeatability of Stanton number distributions.

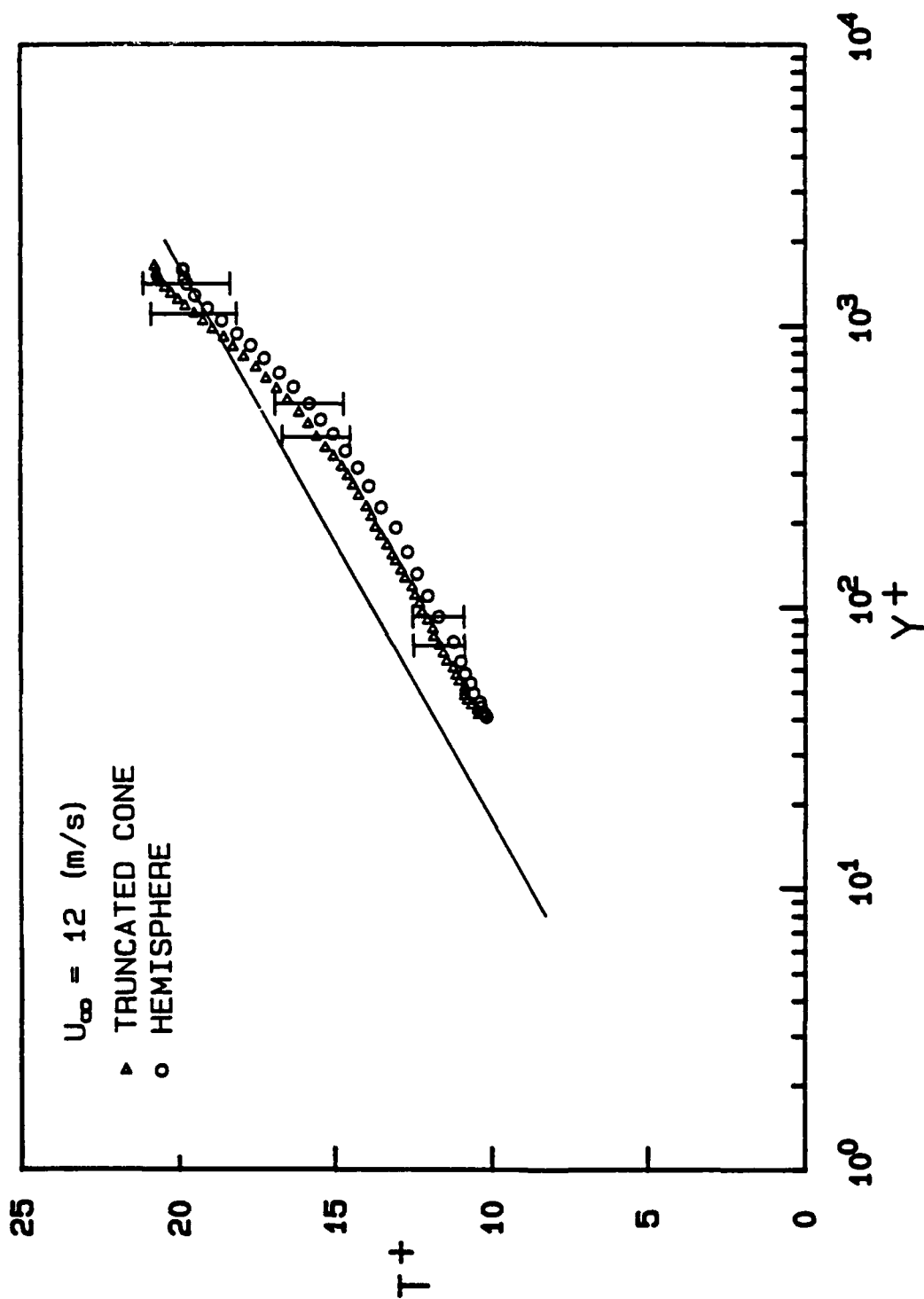


Figure 7.15 Thermal law of the wall comparison of THTF mean temperature profiles at  $U_{\infty} = 12 \text{ m/s}$  for the  $L/d_0 = 4$  surfaces.



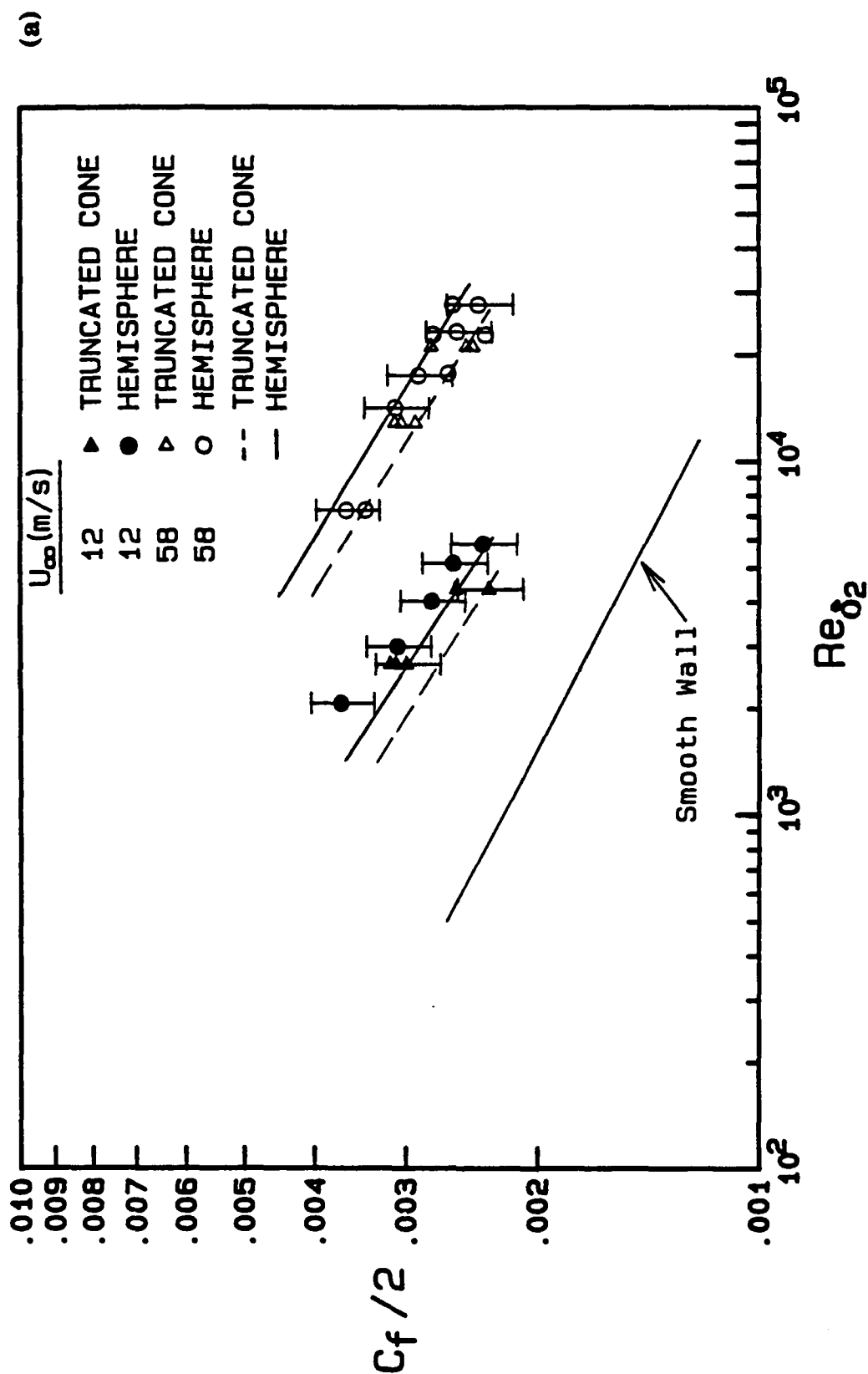


Figure 7.16 Comparison of THITF  $C_f$  data and predictions vs. momentum thickness Reynolds number. (a)  $L/d_o = 2$ ; (b)  $L/d_o = 4$ .

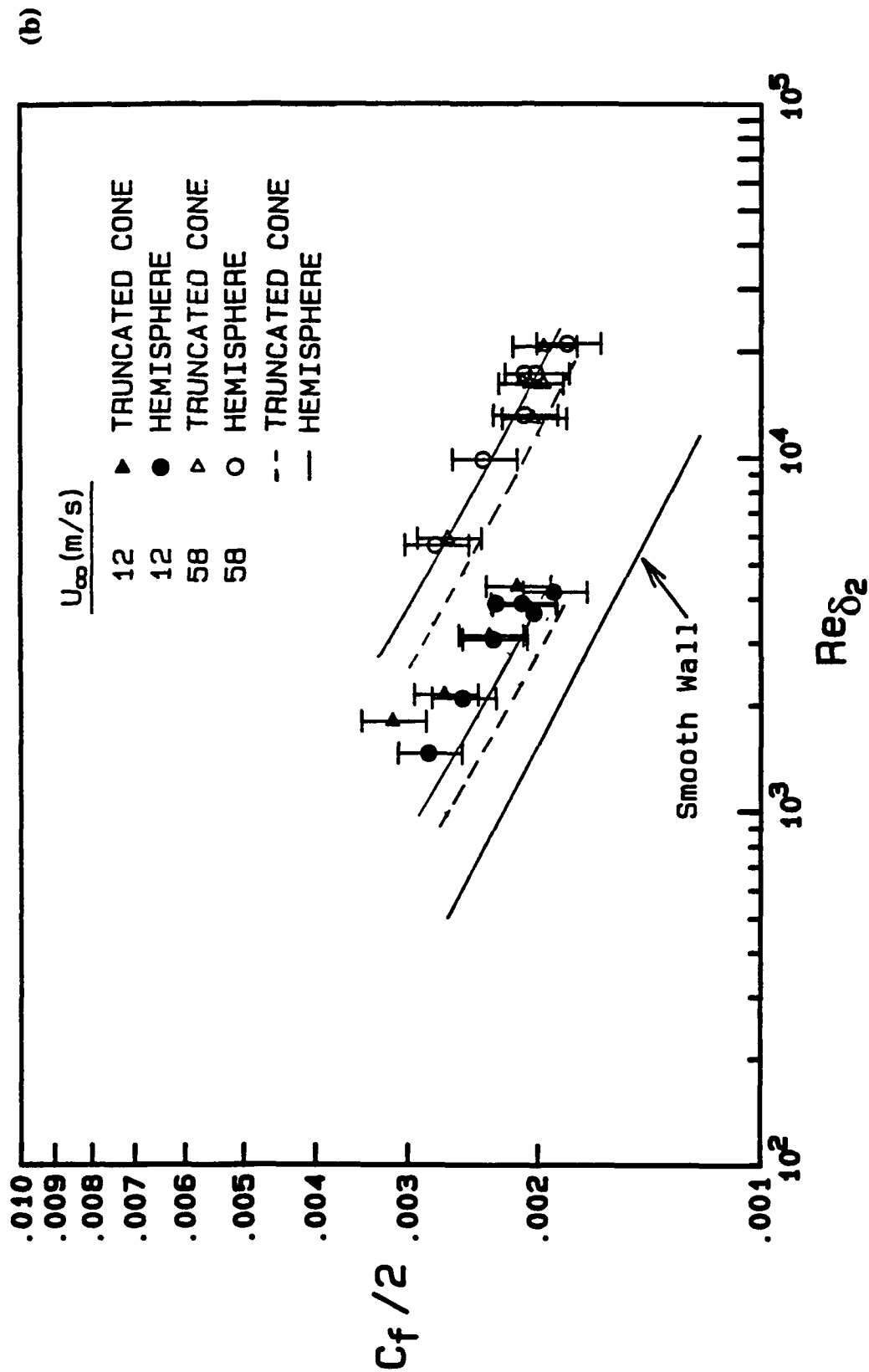


Figure 7.16 Comparison of THTF  $C_f$  data and predictions vs. momentum thickness Reynolds number. (a)  $L/d_o = 2$ ; (b)  $L/d_o = 4$ .

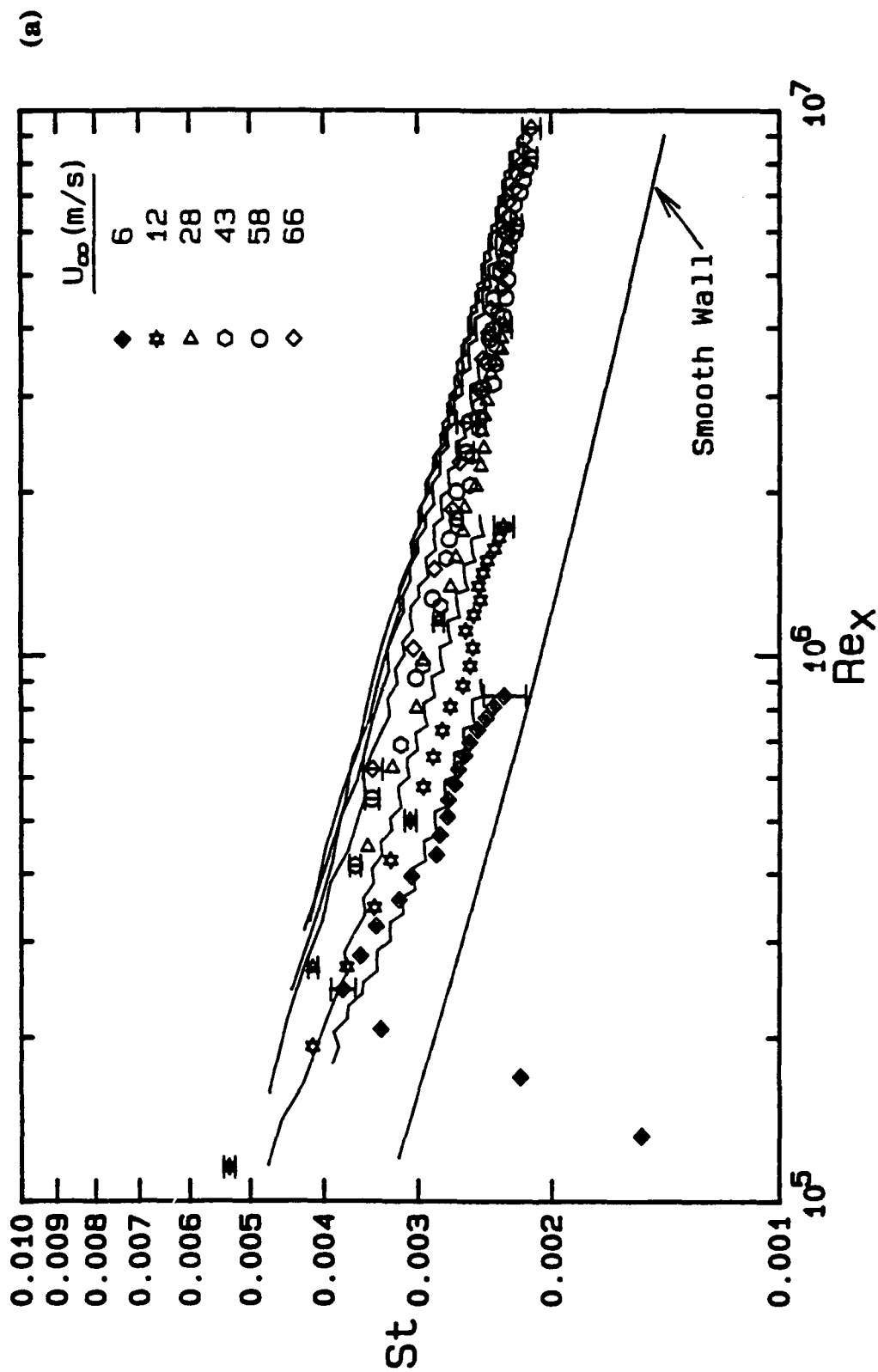


Figure 7.17 Comparison of THTF Stanton number data and predictions vs.  $Re_x$  at  $U_\infty = 6$ , 12, 28, 43, 58, and 66 m/s for the truncated cone surfaces.  
 (a)  $L/d_0 = 2$ ; (b)  $L/d_0 = 4$ .

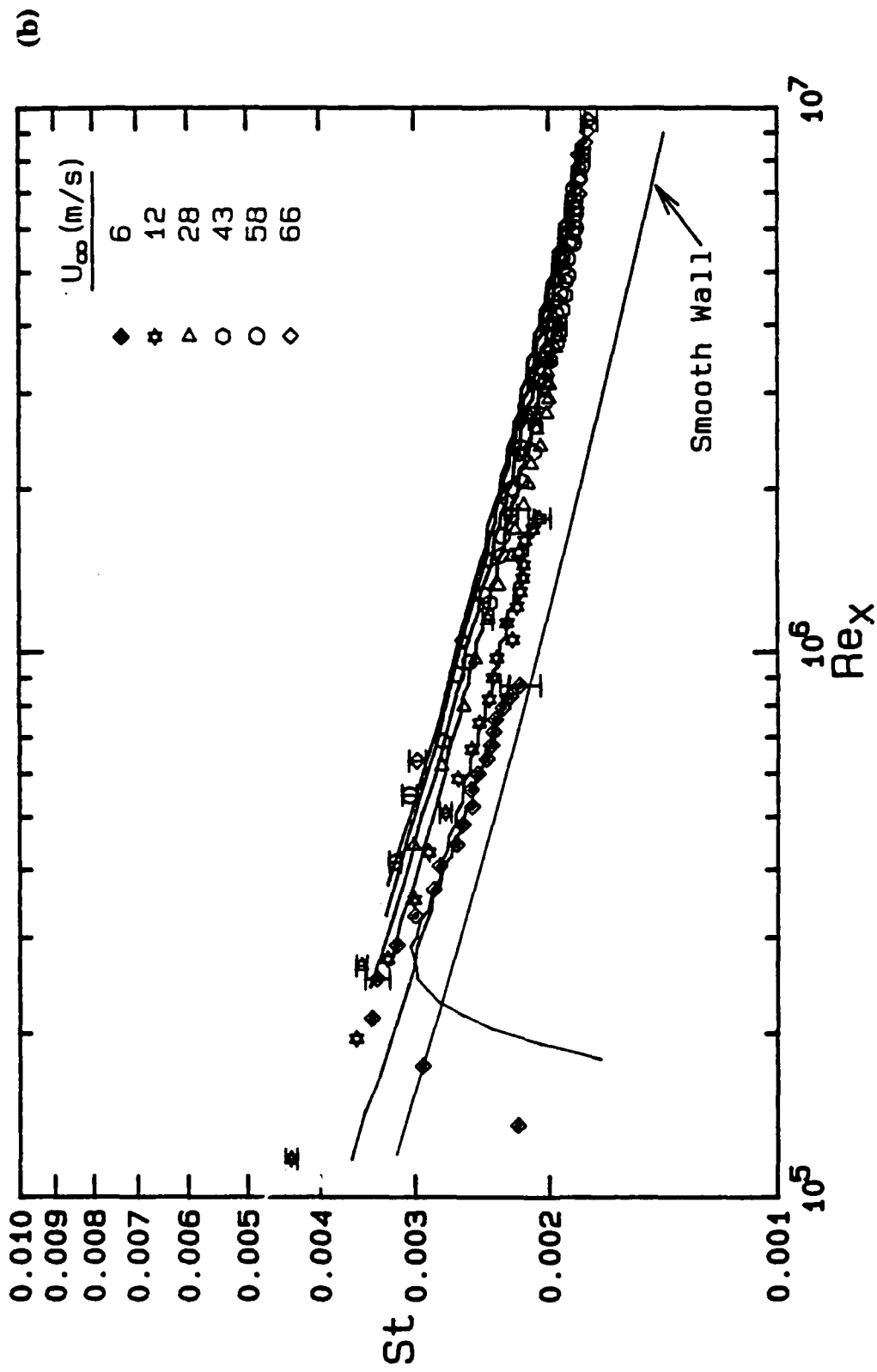


Figure 7.17 Comparison of THETF Stanton number data and predictions vs.  $Re_x$  at  $U_{\infty} = 6$ , 12, 28, 43, 58, and 66 m/s for the truncated cone surfaces.  
 (a)  $L/d_o = 2$ ; (b)  $L/d_o = 4$ .

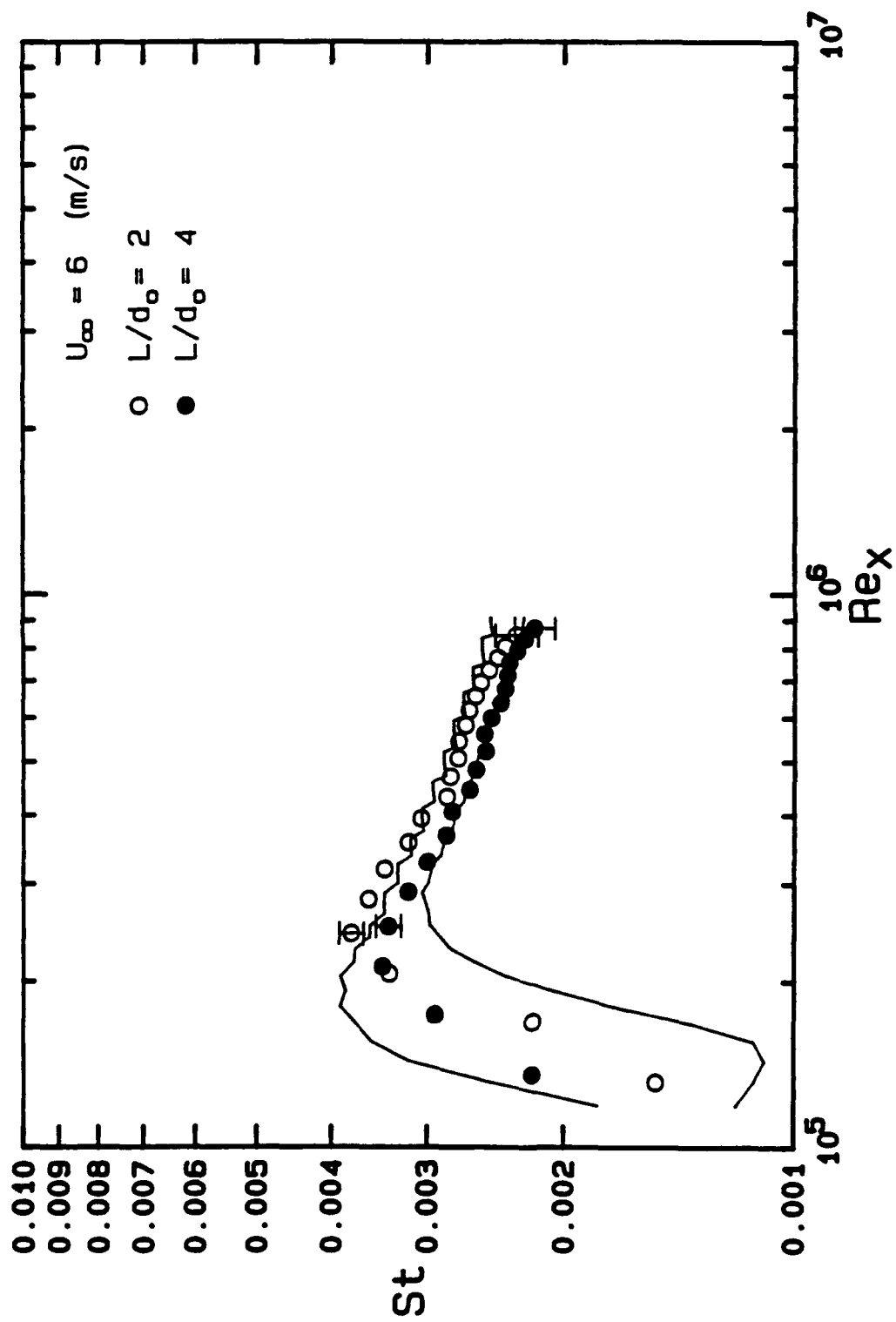


Figure 7.18 Comparison of THTTF Stanton number data and predictions vs.  $Re_x$  at  $U_\infty = 6 \text{ m/s}$  for the truncated cone surfaces.

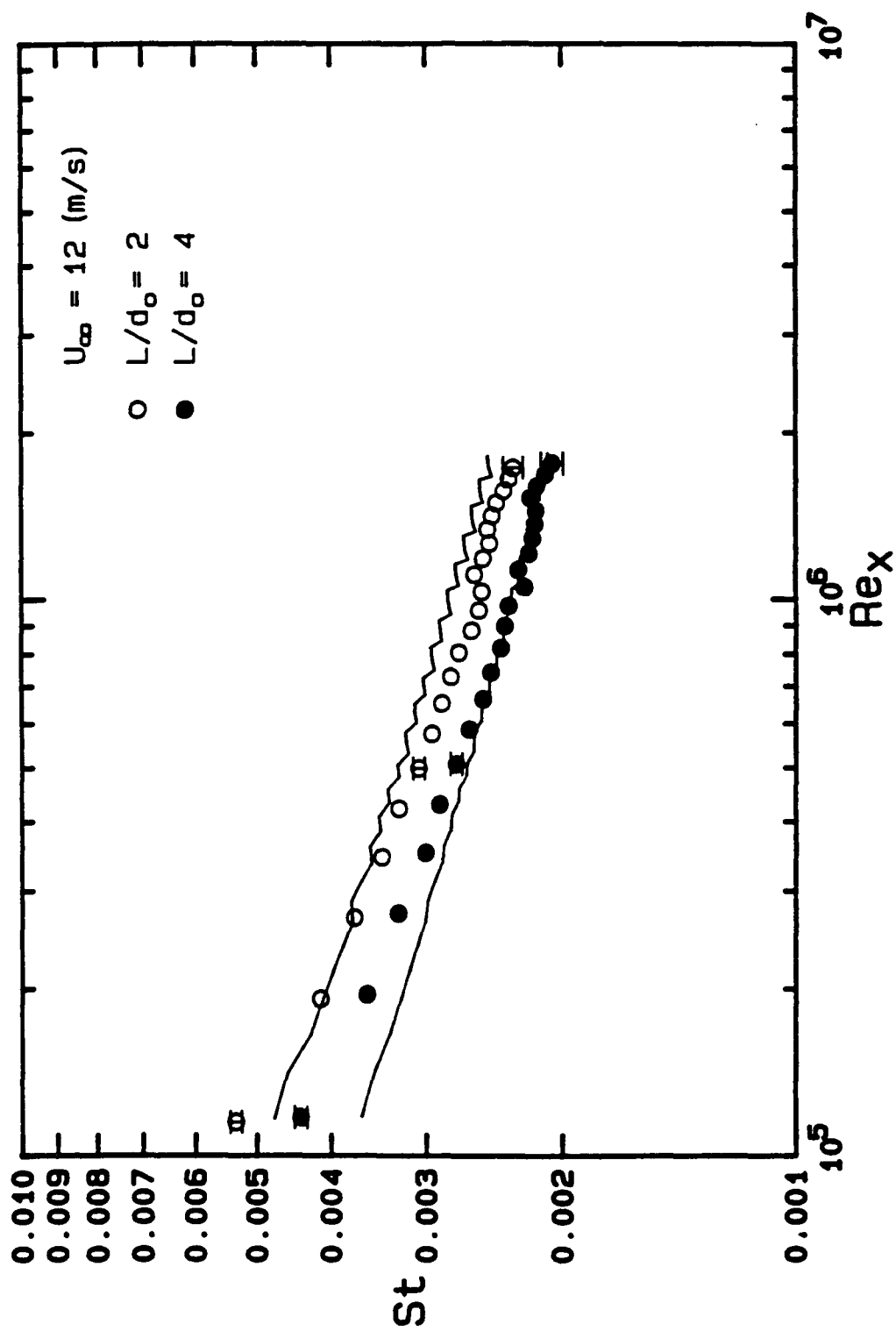


Figure 7.19 Comparison of THETF Stanton number data and predictions vs.  $Re_x$  at  $U_{\infty} = 12 \text{ m/s}$  for the truncated cone surfaces.

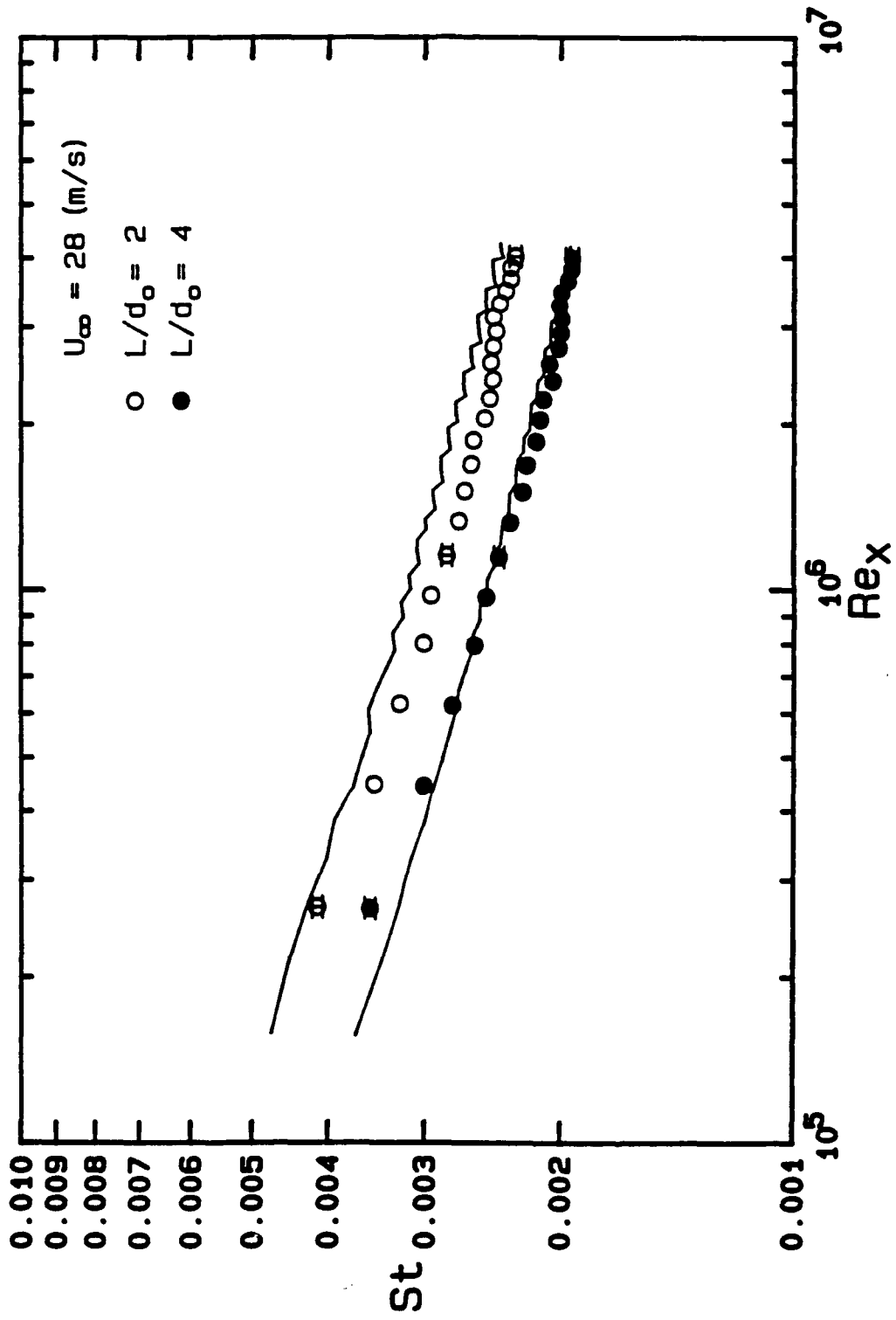


Figure 7.20 Comparison of THTF Stanton number data and predictions vs.  $Re_x$  at  $U_\infty = 28 \text{ m/s}$  for the truncated cone surfaces.

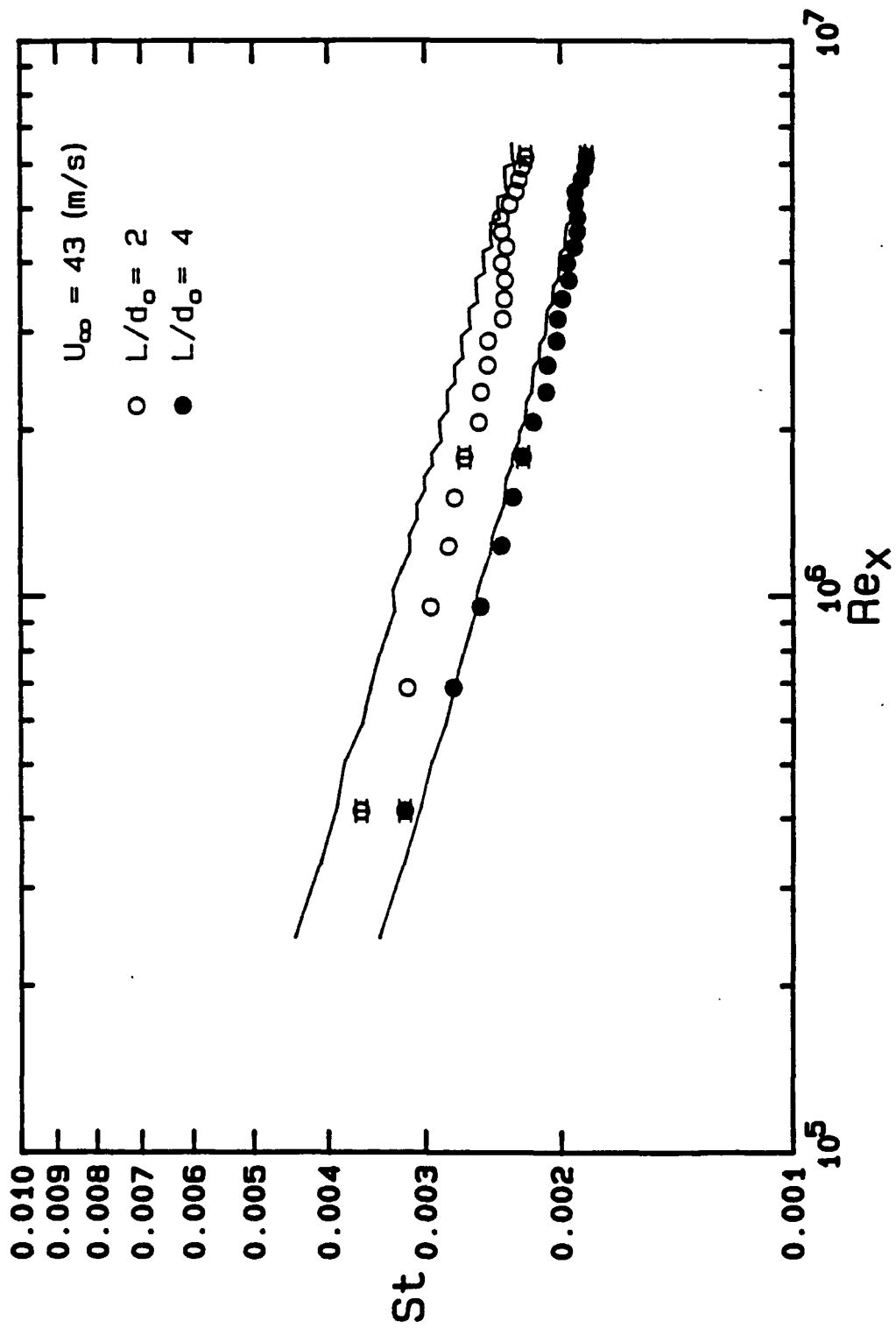


Figure 7.21 Comparison of THTF Stanton number data and predictions vs.  $Re_x$  at  $U_{\infty} = 43 \text{ m/s}$  for the truncated cone surfaces.



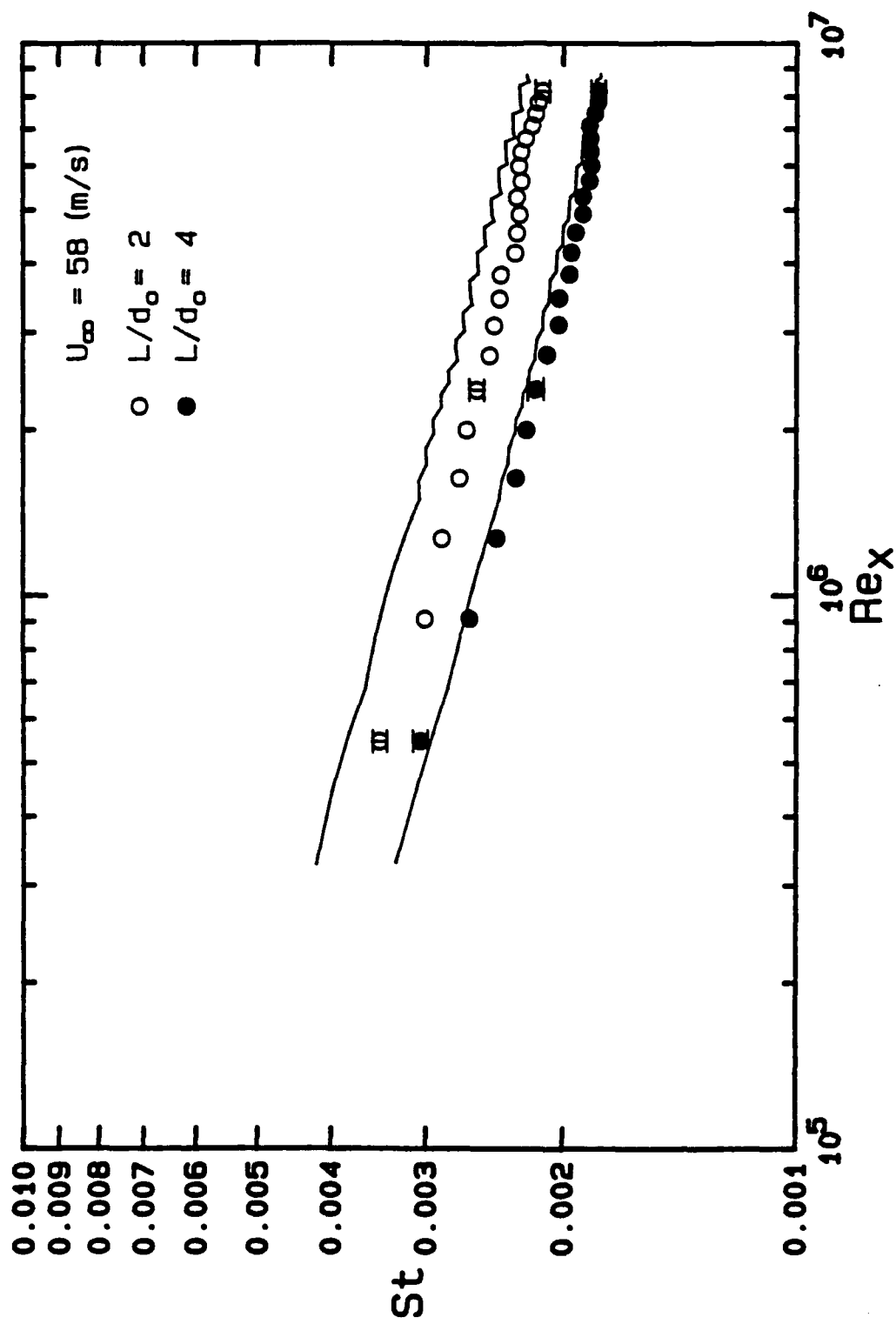


Figure 7.22 Comparison of THITF Stanton number data and predictions vs.  $Re_x$  at  $U_\infty = 58 \text{ m/s}$  for the truncated cone surfaces.

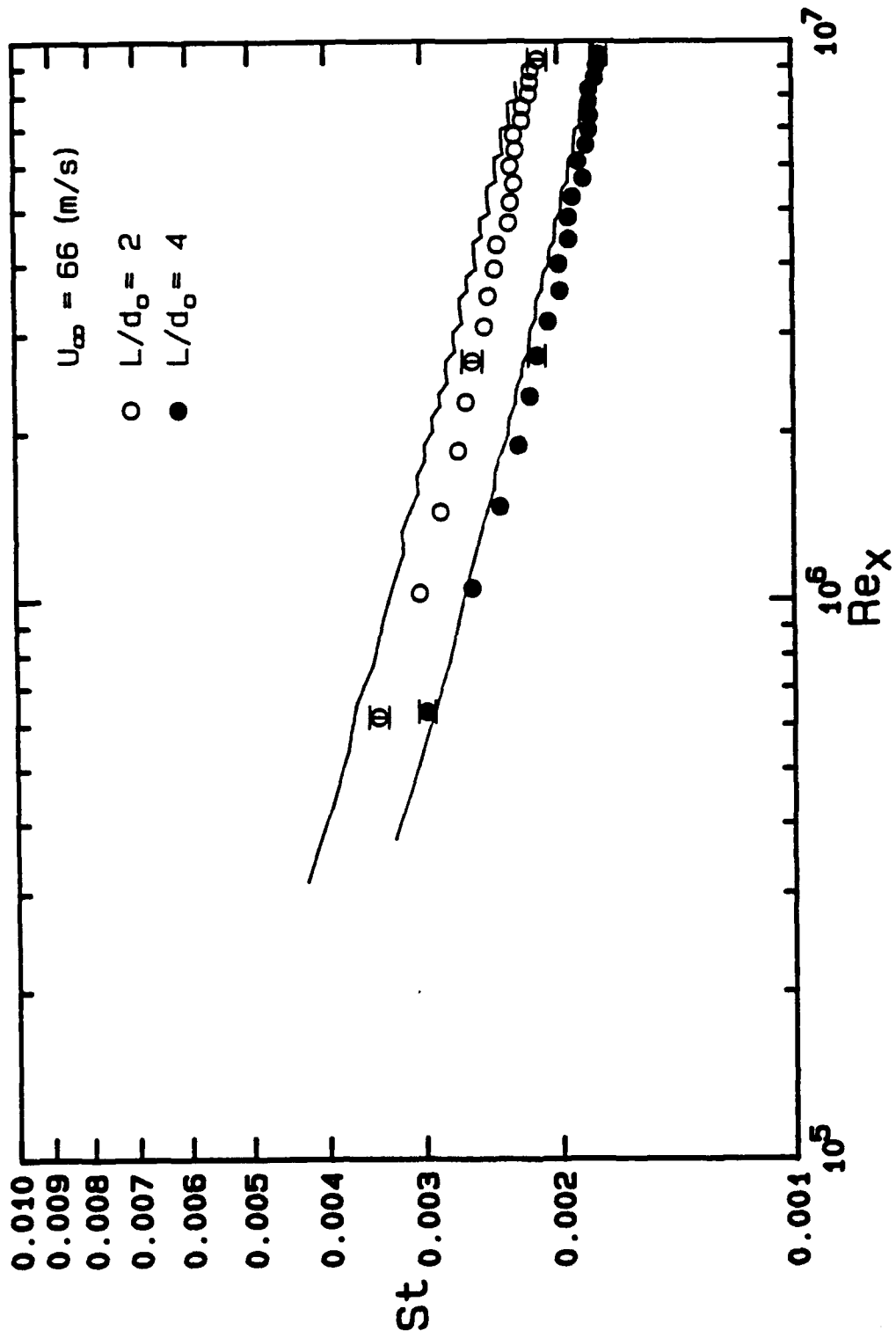


Figure 7.23 Comparison of THETF Stanton number data and predictions vs.  $Re_x$  at  $U_\infty = 66 \text{ m/s}$  for the truncated cone surfaces.

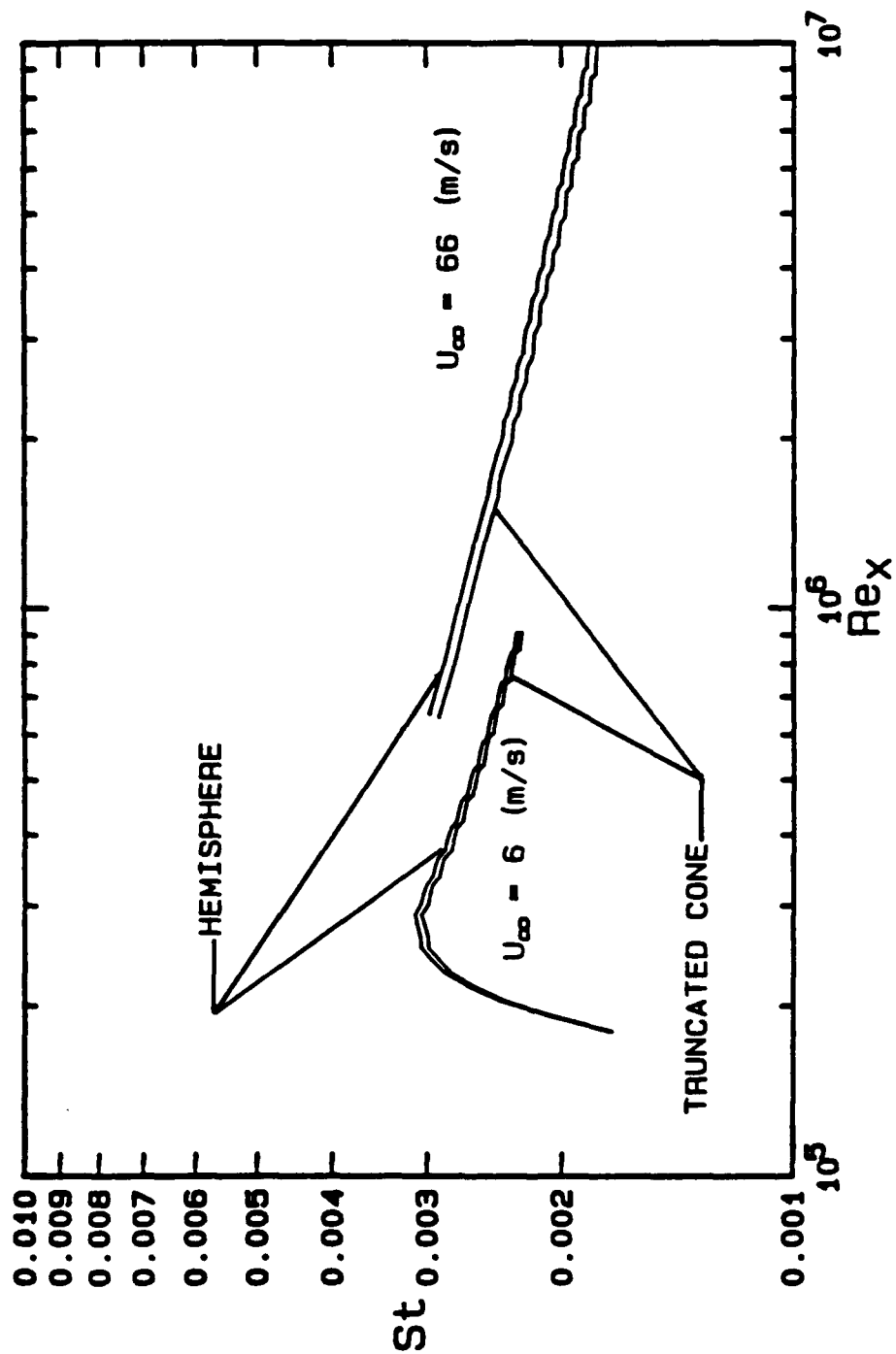


Figure 7.24 Comparison of Stanton number predictions vs.  $Re_x$  at  $U_{\infty} = 6$  and  $66 \text{ m/s}$  for the  $L/d_0 = 4$  truncated cone surfaces.

## CHAPTER 8

### SUMMARY AND CONCLUSIONS

The primary objective of this research program was to investigate the effects of surface roughness on turbulent boundary layer heat transfer by obtaining accurate, comprehensive, quality heat transfer data for zero pressure gradient incompressible air flow over constant temperature test surfaces with well-defined surface roughness geometries. Knowledge gained from the experimental investigation was used to improve and extend the roughness energy transport model used in the discrete element prediction method, thus enhancing and expanding the capability to predict the effects of surface roughness on turbulent flow and heat transfer.

Fluid dynamics and heat transfer data for turbulent boundary layer flow over a smooth and five rough surfaces were taken in the Turbulent Heat Transfer Test Facility (THTTF) for  $x$ -Reynolds numbers ranging up to 10,000,000. The smooth wall data was used for qualification of the THTTF and provided base line data for comparison with the data from rough surfaces. The THTTF smooth wall heat transfer data extended the available incompressible flow Stanton number data range from  $x$ -Reynolds numbers of about 3.5 million to 10 million and were in agreement with the definitive data of Reynolds et al. (1958). The THTTF smooth wall skin friction coefficient data determined by hot-wire anemometry agreed with the  $Re_{\delta_2}$ --correlation of Kays and Crawford (1980) to within the data uncertainty.

The THTF fluid dynamics and heat transfer data taken in aerodynamically smooth, transitionally rough, and fully rough flow regimes over the three well-defined hemispherically roughened surfaces were compared with the Stanford data sets taken using a single well-defined rough surface comprised of spherical elements packed in the most dense array. It was observed that the Stanton numbers for a given surface collapse together in  $St$  versus  $Re_x$  coordinates as the freestream velocity increases, with the Stanton number level being larger for rougher surfaces. This behavior had not been recognized previously. Based on the data from only the Stanford rough surface, it had previously been postulated that such behavior might occur in  $St$  versus enthalpy thickness coordinates. However, the data available now show that this is definitely not the case. It was also observed that the behavior of the  $St$  versus  $Re_x$  data does not correspond to the flow regime characterizations of transitionally rough and fully rough based on fluid mechanics behavior. That is, the Stanton number data collapsed together for the  $L/d_0 = 10$  surface at freestream velocities for which the turbulent boundary layers were clearly in the transitionally rough state, while the same Stanton number behavior was observed for the  $L/d_0 = 2$  surface for freestream velocities corresponding to the fully rough state.

The THTF heat transfer data from the hemispherically roughened surfaces and the Stanford data were used to modify the roughness energy transport model in the discrete element prediction method. This new model was used in calculation of both the fluid dynamics

and heat transfer for the THTTF and Stanford surfaces. The predictions were in excellent agreement with all data sets within the data uncertainty.

Fluid dynamics and heat transfer data were also collected for flows over surfaces with truncated cone roughness elements spaced 2 and 4 base diameters apart in a staggered array to investigate surface roughness shape effects on rough-wall turbulent boundary layer flow and heat transfer. The truncated cone roughness data, when compared with the THTTF data for hemispherical roughness, are the first comprehensive experimental results which consider surface roughness shape effects on heat transfer. Fluid dynamics and heat transfer data for these two roughness shapes were collected under deliberately matched flow conditions and directly compared to determine the surface roughness shape effects on turbulent flow and heat transfer characteristics.

No dependence of skin friction coefficients on roughness element shape could be concluded considering the uncertainty of the hot-wire anemometry technique used to determine  $C_f$ . Other fluid dynamic parameters such as profiles of axial turbulence intensity, mean velocity, and Reynolds stress components showed no conclusive differences due to roughness shape.

The THTTF Stanton number data (which have uncertainties of about 2-4%) exhibit slightly distinguishable differences for the two  $L/d_0 = 4$  surfaces and definitive differences for the two  $L/d_0 = 2$  surfaces. In  $St$  versus  $Re_x$  coordinates, for  $L/d_0 = 4$  the Stanton

numbers are consistently about 2-4% larger for the surface with hemispherical roughness than for the surface with conical roughness. For  $L/d_0 = 2$ , this difference is increased to about 10%.

Discrete element predictions of Stanton number distributions are in excellent agreement with the data from the surface with truncated cone roughness at  $L/d_0 = 4$  and are high about 2-12% for the  $L/d_0 = 2$  cases. Skin friction coefficient data and predictions also agree within the data uncertainty with the exception of the 12 m/s case where predicted skin friction coefficients fell slightly below the data uncertainty bands. In general, the agreement between the data and predictions was very good. This agreement is in spite of the fact that no empirical inputs from the conical roughness were used to refine the  $Nu_d$  and  $C_D$  closure models required for the discrete element approach. A geometric description of the roughness element shape and spacing was the only required input particular to the conical roughness.

APPENDIX I  
EXPERIMENTAL STANTON NUMBER DETERMINATION  
AND ITS UNCERTAINTY ANALYSIS

I.1 STANTON NUMBER DATA REDUCTION EQUATION

The Stanton number is the nondimensional convective heat transfer coefficient and may be defined as

$$St = \frac{h}{\rho C_p U_\infty} \quad (I.1)$$

where

$h$  is the convective heat transfer coefficient

$\rho$  is the density of freestream air

$C_p$  is the specific heat of freestream air

$U_\infty$  is the velocity of freestream air

The rate of convective heat transfer ( $q$ ) from a test plate to the air in the tunnel is defined as

$$q = hA(T_w - T_o) \quad (I.2)$$

where

$A$  is plate area

$T_w$  is wall temperature

$T_o$  is freestream air total temperature

Solving equation (I.2) for the convective heat transfer coefficient and substituting into equation (I.1) gives the Stanton number at each plate as



$$St = \frac{q}{\rho C_p U_\infty A (T_w - T_o)} \quad (I.3)$$

In order to determine the convective heat transfer rate  $q$ , for each plate, the corresponding radiation and conduction heat losses are required. The modes of heat exchange from each plate are depicted graphically in Figure I.1. Application of an energy balance to a plate gives

$$W = q + q_c + q_r \quad (I.4)$$

where

$W$  is power supplied to the plate

$q_r$  is radiation heat loss rate

$q_c$  is conductive heat loss rate

Solving equation (I.4) for the convective heat transfer rate and substituting into equation (I.3) gives

$$St = \frac{W - q_c - q_r}{\rho C_p U_\infty A (T_w - T_o)} \quad (I.5)$$

The radiation heat loss rate is modeled using

$$q_r = \sigma \epsilon A (T_w^4 - T_r^4) \quad (I.6)$$

where

$\sigma$  is the Stefan-Boltzmann constant

$\epsilon$  is the emissivity of the plate surface

$T_r$  is the freestream recovery temperature

The conduction heat loss rate is modeled using

$$q_c = (UA)_{eff} (T_w - T_{rail}) \quad (I.7)$$

where

$(UA)_{\text{eff}}$  is an experimentally-determined effective conductance between a test plate and the side rails

$T_{\text{rail}}$  is the side rail temperature at the axial location of the plate

Substitution of (I.6) and (I.7) into (I.5) gives the final form of the data reduction expression for the Stanton Number

$$St = \frac{W - (UA)_{\text{eff}} (T_w - T_{\text{rail}}) - \sigma \epsilon A (T_w^4 - T_r^4)}{\rho C_p U_{\infty} A (T_w - T_o)} \quad (I.8)$$

This expression shows explicitly most of the variables involved in the experimental Stanton number determination. Additional variables enter in the determination of the static and total temperature of the freestream air and in the moist air property calculations for  $C_p$  and  $\rho$ . The freestream air total and static temperatures are calculated using the measured recovery temperature and a recovery factor,  $r$ , for the probe:

$$T_o = T_r + (1-r) \frac{U_{\infty}^2}{2C_p} \quad (I.9)$$

$$T_{\infty} = T_r - (r) \frac{U_{\infty}^2}{2C_p} \quad (I.10)$$

The functional relationship for the moist air specific heat calculation is

$$C_p = C_p(T_{\infty}, T_{wb}, P_{\text{bar}}, C_{p_{\text{air}}}, C_{p_{\text{water}}})$$

where

$T_{\infty}$  is the freestream air static temperature and is also taken as the dry bulb temperature

$T_{wb}$  is the freestream air wet-bulb temperature

$P_{bar}$  is the barometric pressure

$C_{p_{air}}$  is the dry air specific heat

$C_{p_{water}}$  is the water vapor specific heat

The functional relationship for the moist air density is

$$\rho = \rho(T_{\infty}, T_{wb}, P_{bar})$$

The Stanton number determination for each plate, therefore, involves the following thirteen variables which are either measured or found from a reference source:

- Plate heater power ( $W$ )
- Recovery temperature ( $T_r$ )
- Wall temperature ( $T_w$ )
- Rail temperature ( $T_{rail}$ )
- Wet-bulb temperature ( $T_{wb}$ )
- Effective conductance ( $(UA)_{eff}$ )
- Plate area ( $A$ )
- Barometric pressure ( $P_{bar}$ )
- Specific heat of dry air ( $C_{p_{air}}$ )
- Specific heat of water vapor ( $C_{p_{water}}$ )
- Freestream air velocity ( $U_{\infty}$ )
- Recovery factor ( $r$ )
- Emissivity ( $\epsilon$ )

## I.2 UNCERTAINTY ANALYSIS OVERVIEW

The detailed uncertainty analysis procedure follows Coleman and Steele (1989), which is consistent with the ANSI/ASME Standard on Measurement Uncertainty (1986). Briefly, the true value of a quantity, which is approximated by an experimental result  $r$ , lies within the interval  $r \pm U_r$  with 95% confidence. Here  $U_r$  is the uncertainty in the result determined from the root-sum-square combination of the bias limit of the result,  $B_r$ , and the precision limit of the result,  $P_r$ ,

$$U_r = (B_r^2 + P_r^2)^{1/2} \quad (\text{I.11})$$

For a result (such as  $St$ ) which is a function of  $J$  variables and parameters  $X_i$

$$r = r(X_1, X_2, \dots, X_J) \quad (\text{I.12})$$

the propagation of the precision limits  $P_{X_i}$  of the measured variables into the result is given by

$$P_r = \left[ \sum_{i=1}^J \left[ \frac{\partial r}{\partial X_i} P_{X_i} \right]^2 \right]^{1/2} \quad (\text{I.13})$$

and the propagation of the bias limits  $B_{X_i}$  of the variables into the result is given by

$$B_r = \left\{ \left[ \sum_{i=1}^J \left[ \frac{\partial r}{\partial X_i} B_{X_i} \right]^2 \right] + 2 \left[ \frac{\partial r}{\partial X_1} \right] \left[ \frac{\partial r}{\partial X_2} \right] B'_{X_1} B'_{X_2} + \dots \right\}^{1/2} \quad (\text{I.14})$$

As explained by Coleman and Steele (1989), there is a term such as the second one on the right hand side of equation (I.14) for each pair of variables that have portions ( $B'_{X_1}$  and  $B'_{X_2}$ ) of their bias

limits which are perfectly correlated. These usually arise when the transducers used to measure different variables have been calibrated against the same standard or when two variables (often temperatures or pressures) are measured with the same transducer.

In the current experiments, all of the  $P_{X_1}$ 's are negligible compared to the bias limits, so

$$P_{St} = 0 . \quad (I.15)$$

Exceptions to this occur at low freestream velocities-- $U_\infty \leq 12$  m/sec for the smooth wall tests and  $U_\infty \leq 6$  m/sec for the rough wall tests--for which the heat transfer coefficients are relatively low. At these conditions the time constant of the THTF is large enough so that the relatively long period variations in facility line voltage to the test plate heater circuits and in the temperature of the incoming make-up water for the heat exchanger loop affect the ability to hold a tight steady state condition. These annoyances could be overcome with additional expenditures for power conditioning equipment and a water chiller system; however, the observed run-to-run scatter in  $St$  results at these low velocities is within acceptable limits. Observations of the  $St$  results for eight  $U_\infty = 12$  m/sec replications with the smooth wall and three  $U_\infty = 6$  m/sec replications with the rough wall produced a 95% confidence estimate of  $P_{St} = 3\%$  for those conditions. This is present because of system unsteadiness and not because of measurement uncertainty.

Application of equation (I.14) to the case of equation (I.8) gives

$$\begin{aligned}
B^2_{St} = & \left\{ \frac{\partial St}{\partial T_w} \right\}^2 B^2_{T_w} + \left\{ \frac{\partial St}{\partial T_r} \right\}^2 B^2_{T_r} + \left\{ \frac{\partial St}{\partial T_{rail}} \right\}^2 B^2_{T_{rail}} + \left\{ \frac{\partial St}{\partial T_{wb}} \right\}^2 B^2_{T_{wb}} \\
& + \left\{ \frac{\partial St}{\partial P_{bar}} \right\}^2 B^2_{P_{bar}} + \left\{ \frac{\partial St}{\partial W} \right\}^2 B^2_W + \left\{ \frac{\partial St}{\partial U_{\infty}} \right\}^2 B^2_{U_{\infty}} + \left\{ \frac{\partial St}{\partial r} \right\}^2 B^2_r \\
& + \left\{ \frac{\partial St}{\partial A} \right\}^2 B^2_A + \left\{ \frac{\partial St}{\partial C_{p_{air}}} \right\}^2 B^2_{C_{p_{air}}} + \left\{ \frac{\partial St}{\partial C_{p_{water}}} \right\}^2 B^2_{C_{p_{water}}} \quad (I.16) \\
& + \left\{ \frac{\partial St}{\partial (UA)_{eff}} \right\}^2 B^2_{(UA)_{eff}} + \left\{ \frac{\partial St}{\partial \epsilon} \right\}^2 B^2_{\epsilon} \\
& + 2 \left\{ \frac{\partial St}{\partial T_w} \right\} \left\{ \frac{\partial St}{\partial T_r} \right\} B'_{T_w} B'_{T_r} + 2 \left\{ \frac{\partial St}{\partial T_w} \right\} \left\{ \frac{\partial St}{\partial T_{rail}} \right\} B'_{T_w} B'_{T_{rail}} \\
& + 2 \left\{ \frac{\partial St}{\partial T_r} \right\} \left\{ \frac{\partial St}{\partial T_{rail}} \right\} B'_{T_r} B'_{T_{rail}}
\end{aligned}$$

where, as discussed later, the only portions of biases that are considered correlated are those arising from calibrating the thermistors which measure  $T_w$ ,  $T_r$ , and  $T_{rail}$  against the same reference standard.

### I.3 MEASUREMENTS AND UNCERTAINTIES

The experimental determination of Stanton number requires values for thirteen variables, some of which can be measured directly and some which cannot. Therefore, the methodology used in determination of each variable will be discussed. Discussion of the determination of each variable will include description of the required measurement system, information about the calibration procedures, and uncertainty estimates for each variable.

### I.3.1 Plate Heater Power

The power supplied to the heater pad of each plate is measured by a high precision ac watt transducer coupled to a Hewlett Packard (HP) Model 3054 A Automated Data Acquisition and Control System (ADACS), which in turn is connected to a Model 220 microcomputer. This watt transducer is a single phase transducer with a rated output of 1 ma corresponding to 500 watts. The manufacturer specifies  $\pm 0.2\%$  of reading accuracy and 0 to 1 ma dc current output proportional to electrical power.

A separate power circuit is used for each individual plate heater. There are 24 identical power circuits for the 24 test plates. A single watt transducer (Ohio Semitronics Inc. Model EW5-B) is used for all power measurements. The power delivered to a plate heater is measured by routing the power through the watt transducer by switch closures using the ADACS. Since the ADACS cannot process current signals directly, the transducer's output is measured indirectly. A 7.5 K $\Omega$  resistor is shunted across the transducer's output lines so that the current output is transformed into a measurable voltage. The shunt resistor is sized to compensate for the small current output from the watt transducer. The current output (ma) from the watt transducer is then obtained using Ohm's law

$$i = \left(\frac{V}{R}\right) \left(\frac{1}{1000}\right) \quad (I.17)$$

This current output is then translated into power (watts) using the relationship

$$W = 500 \times i \quad (I.18)$$

A calibration plate heater circuit was used to check the calibration of the watt transducer by comparison of the transducer measurement to the heater power ( $W_{act}$ ) determined using the ADACS. This power was obtained by measuring the ac voltage drop across the plate heater, the resistance of the plate heater, and using

$$W_{act} = \frac{V^2}{R} \quad (I.19)$$

Due to the importance of resistance and voltage measurement in determination of both transducer and actual powers, extreme care was exercised to utilize the ADACS properly. In particular, the resistances from the plate heater and shunt resistor were measured using the four-wire technique. In this method, the resistance of the transmission line is measured and is subtracted from the measured total resistance automatically. Therefore, the resistance obtained by the four-wire technique represents the load resistance alone.

Uncertainties: The high resolution digital voltmeter (3456A) used for both voltage and resistance measurements has a voltage accuracy of  $\pm 0.007\%$  of reading with an ADACS environment temperature of 23 C and an additional 0.0002% error for every 1 C in the environment temperature above or below 23 C. Resistance accuracy for the ADACS is 0.008% of reading, and the environment temperature coefficient is 0.004%/C for four-wire ohm. It was assumed that the manufacturer's specification on the accuracies of the resistance and voltage measurements are the bias limits with 95% confidence



level so that averaging multiple readings would not reduce these estimates. Therefore, the bias limits on the voltage and resistance measurements become

$$\frac{B_V}{V} = \pm 7 \times 10^{-5}$$

$$\frac{B_R}{R} = \pm 8 \times 10^{-5}$$

The bias limit in the determination of the watt transducer output current using equations (I.14) and (I.17) is

$$\left(\frac{B_i}{i}\right)^2 = \left(\frac{B_R}{R}\right)^2 + \left(\frac{B_V}{V}\right)^2$$

$$\left(\frac{B_i}{i}\right) = \pm 0.01\%$$

and the bias limit in the determination of the actual power measurement using equations (I.14) and (I.19) is

$$\left(\frac{B_{W_{act}}}{W_{act}}\right)^2 = \left(\frac{B_R}{R}\right)^2 + \left[2 \frac{B_V}{V}\right]^2$$

$$\left(\frac{B_{W_{act}}}{W_{act}}\right) = \pm 0.02\%$$

These are so small as to be negligible for our purposes. Precision errors were also observed to be negligible.

Although the output from the watt transducer can be measured with high accuracy as indicated above, how well this is translated into power using equation (I.18) must be determined by comparing the power indicated by the watt transducer to the actual power as

found from the calibration tests. (The inductance in the heating element was accounted for, with the power factor being greater than 0.999 (Suryananarayana, 1986).) The power indicated by equation (I.18) from the output of the watt transducer was compared with the actual power as measured by the ADACS (I.19) using 172 points over the 0-250 watt range of interest. Figure I.2 shows the cumulative probability curve of the absolute values of the percent differences. As shown, a 95% confidence estimate of the uncertainty in the watt transducer power measurement based on these points is  $\pm 0.9\%$  of reading. This appears as a bias error in  $W$  when equation (I.18) is used.

### I.3.2 Temperatures

Temperatures are measured using thermistors, which are temperature sensitive resistors with a negative temperature coefficient. These thermistors have a nominal resistance of 50,000 ohms at 25 C and are highly sensitive to small temperature changes (about 1-2 K $\Omega$ /C). They are guaranteed, by the manufacturer, to have  $\pm 0.2$  C interchangeability over a range of temperatures from 0 C to 70 C. The resistances of the thermistors are measured by the ADACS. These thermistors are used to determine the freestream air temperature, the test plate temperatures, and the metal support rail temperatures.

The calibration of the thermistors was done in a Blue M Model MR-3210A-1 constant temperature bath. The bath temperature was monitored by a Hewlett Packard Model 2804A quartz thermometer

instrumented with a Model 18111A quartz probe. The absolute accuracy of this thermometer/probe combination is specified by the manufacturer as  $\pm 0.040$  C over a range of  $-50$  C to  $150$  C. The thermistors were placed individually inside glass test tubes to protect them and avoid their contamination. To ensure effective conduction of heat from the water bath to each thermistor, each test tube was filled with Megatherm 201 (by Omega Engineering, Inc.), which is a high thermal conductivity, filled silicone paste. The spatial variation in the temperature of the bath was found to be about  $\pm 0.4$  C. This variation was minimized to  $\pm 0.02$  C by centering the test tubes containing thermistors around the quartz probe in groups of fourteen. Since the reliability of measured thermistor resistances depends on the accuracy of measurements made by the ADACS, the proper use of the ADACS during the measurement process was carefully examined.

The thermistor calibrations were performed for the range of temperatures  $22$  C -  $50$  C using six evenly spaced points over this range. The thermistors are extremely nonlinear but their behavior can be very closely approximated by the Steinhart-Hart equation as

$$T[K] = 1/[A + B \ln R + C(\ln R)^3] \quad (I.20)$$

where  $R$  is resistance in ohms. The curvefit constants  $A$ ,  $B$  and  $C$  were calculated using the thermistor manufacturer's data as  $A = 9.6401 \times 10^{-4}$ ,  $B = 2.1095 \times 10^{-4}$  and  $C = 8.48 \times 10^{-8}$ .

Uncertainties: The temperatures obtained using the measured thermistor resistances in the Steinhart-Hart relation (equation (I.20)) were compared with the temperatures from the quartz ther-

mometer. The difference between the temperatures measured by the quartz thermometer and the temperatures calculated from the measured thermistor resistances using the curvefit equation was determined for a total of 360 calibration points. Figure I.3 shows the cumulative probability curve of the absolute values of the differences. As shown, 95% are less than about 0.09 C. This is taken as a bias limit since precision errors were observed to be negligible.

The bias limits for the elemental error sources which affect the various thermistors are estimated as

<u>Elemental error source</u>	<u>Bias limit</u>
Calibration: Quartz probe	$\pm 0.04$ C
Calibration: Bath nonuniformity & curvefit	$\pm 0.09$ C
Installation in test plates	$\pm 0.1$ C
Nonuniformity in side rail temperatures	$\pm 0.4$ C

The installation error for the test plate thermistors was estimated based on the temperature variations predicted within a test plate during the design calculations by Norton (1983). Since the temperature indicated by the plate thermistors is used as the plate surface temperature,  $T_w$ , in equation (I.8), such variations are the source of a bias error. The overall bias limit for each plate temperature measurement is found from the root-sum-square of the three appropriate elemental error sources as

$$B_{T_w} = [(0.04)^2 + (0.09)^2 + (0.1)^2]^{1/2} = 0.14 \text{ C}$$

For measurements of the side rail temperature,  $T_{rail}$ , at a given axial location, the overall bias limit is found from the root-sum-square of the three appropriate elemental error sources as

$$B_{T_{rail}} = [(0.04)^2 + (0.09)^2 + (0.4)^2]^{1/2} = 0.4 \text{ C}$$

For measurements of the freestream air recovery temperature,  $T_r$ , no installation bias appears and so

$$B_{T_r} = [(0.04)^2 + (0.09)^2]^{1/2} = 0.1 \text{ C}$$

Since the same calibration standard (quartz probe) was used for all thermistors, the standard's bias limit is a correlated bias error source that has to be accounted for in the data reduction uncertainty analysis. Thus,  $B'_{T_w} = B'_{T_r} = B'_{T_{rail}} = 0.04 \text{ C}$  in equation (I.16).

### I.3.3 Effective Conductance

The effective conductance  $(UA)_{eff}$  was determined from

$$(UA)_{eff} = \frac{q_c}{(T_w - T_{rail})} \quad (I.21)$$

where

$(UA)_{eff}$  is the effective conductance between a test plate and the support rails

$q_c$  is the input power to a plate heater under conductance calibration conditions

In order to estimate the effective conductance, an experimental approach was taken. Insulation was placed over the top of the test plates, which then were heated by power input to the plate heaters.

Since there were no radiative or convective heat losses from the covered plates, the total input power to the heater plates was equal to the conductive heat transfer loss from the plates, which was modeled with equation (I.21).

The support rails were heated by two 150 watt tape heaters installed on each side rail. When the plate temperatures and the rail temperatures reached a prespecified temperature, the powers to the plate heaters were reduced to 0.6 watts and the rail heaters were turned off. The test plate temperatures and the rail temperatures at  $x = 1.2$  m were monitored until the temperature differences between each test plate and the rail temperature approached a steady state condition.

For each plate, from each temperature difference and the corresponding input power, an effective conductance was determined. A single value of effective conductance (0.42 watt/C) was determined for use with all test plates. This value was obtained by averaging the effective conductances of test plates 6 through 18. The precision index  $S$  of this sample of effective conductances was 0.08 watt/C.

Uncertainties: The uncertainties were determined by using the uncertainty analysis equations (I.11) - (I.14) and equation (I.21) which models the conductive heat loss. Since

$$(UA)_{\text{eff}} = \frac{q_c}{T_w - T_{\text{rail}}}$$

then

$$\left[\frac{B_{(UA)_{eff}}}{(UA)_{eff}}\right]^2 = \left[\frac{B_{q_c}}{q_c}\right]^2 + \left[\frac{-B_{T_w}}{(T_w - T_{rail})}\right]^2 + \left[\frac{B_{T_{rail}}}{(T_w - T_{rail})}\right]^2 \\ + 2 B'_{T_w} B'_{T_{rail}} \left[\frac{-1}{T_w - T_{rail}}\right] \left[\frac{1}{T_w - T_{rail}}\right]$$

From previous discussion we have

$$B_{T_w} = 0.14 \text{ C}$$

$$B'_{T_w} = B'_{T_{rail}} = 0.04 \text{ C}$$

and

$$\frac{B_{q_c}}{q_c} = 0.009$$

The bias limit for  $T_{rail}$  does not include the 0.4 C nonuniformity contribution since only the middle 13 plates were used in the calibration test to avoid the larger variations in  $T_{rail}$  at the beginning and end of the test section. For this case, then,

$$B_{T_{rail}} = 0.1 \text{ C}$$

Using a nominal value for  $(T_w - T_{rail})$  of 1.3 C from the calibration test, the bias limit in the effective conductance becomes

$$\left[\frac{B_{(UA)_{eff}}}{(UA)_{eff}}\right]^2 = (0.009)^2 + \left[\frac{0.14}{1.3}\right]^2 + \left[\frac{0.1}{1.3}\right]^2 - 2(0.04)(0.04)\left[\frac{1}{1.3}\right]\left[\frac{1}{1.3}\right]$$

$$\left[\frac{B_{(UA)_{eff}}}{(UA)_{eff}}\right] = 0.13$$

Using the precision limit ( $P = tS = 0.174 \text{ watt/C}$ ) at a 95% confidence level calculated from the t-distribution ( $n=13$ ,  $t=2.179$ ) and the precision index  $S$ , the overall uncertainty for the effective conductance becomes

$$\left[\frac{U(UA)_{eff}}{(UA)_{eff}}\right]^2 = \left[\frac{B(UA)_{eff}}{(UA)_{eff}}\right]^2 + \left[\frac{P(UA)_{eff}}{(UA)_{eff}}\right]^2$$

$$\left[\frac{U(UA)_{eff}}{(UA)_{eff}}\right]^2 = (0.13)^2 + \left[\frac{0.174}{0.42}\right]^2 = (0.13)^2 + (0.42)^2$$

$$\left[\frac{U(UA)_{eff}}{(UA)_{eff}}\right] = 45\%$$

Since the constant value of 0.42 watt/C is always used for  $(UA)_{eff}$ , this uncertainty is fossilized (Coleman and Steele, 1989) into a bias limit when  $(UA)_{eff}$  is used in the calculation of Stanton numbers. Therefore,

$$B(UA)_{eff} = 45\%.$$

#### I.3.4 Area

The surface area of the plates is determined from the lengths of the sides (10.16 cm by 45.72 cm)

$$A = (S_1)(S_2)$$

The plates were manufactured with length and width tolerances of  $\pm 0.0025$  cm.

Uncertainties: The uncertainty in the plate area is assumed to be all bias and may be expressed as

$$\left[\frac{B_A}{A}\right]^2 = \left[\frac{B_{S_1}}{S_1}\right]^2 + \left[\frac{B_{S_2}}{S_2}\right]^2$$

Substitution of the plate dimensions and bias limits gives

$$\left[\frac{B_A}{A}\right]^2 = \left[\frac{0.0025}{10.16}\right]^2 + \left[\frac{0.0025}{45.72}\right]^2$$



$$\left\{\frac{B_A}{A}\right\} = 0.03\%$$

The possibility of thermal expansion of the test plates (which could introduce additional uncertainty into the area) was considered. It was found that this effect was negligible compared to the bias due to manufacturing tolerance.

### 1.3.5 Air Density and Specific Heat

The fluid in the test section is actually a mixture of dry air and water vapor. Therefore, fluid properties such as density and specific heat for the test air will depend on the ratio of dry air and water vapor in the mixture. The ratio of dry air and water vapor in air is reflected by the partial pressures of each. The density and specific heat of the mixture may be expressed in terms of the partial pressures of the dry air and water vapor. Once the partial pressures of the dry air and water vapor are known, they may be substituted into expressions for the density and specific heat of the mixture.

Psychrometrics: The partial pressure of the water vapor at saturation, evaluated at the dry bulb temperature  $T_{\infty}$ , is given by

$$P_{ws} = \exp[C8/T_{\infty} + C9 + (C10)T_{\infty} + (C11)T_{\infty}^2 + (C12)T_{\infty}^3 + (C13) \ln(T_{\infty})]$$

and the partial pressure of the water vapor at saturation, evaluated at the wet bulb temperature, is given by

$$P_{wswb} = \exp[C8/T_{wb} + C9 + (C10)T_{wb} + (C11)T_{wb}^2 + (C12)T_{wb}^3 + (C13) \ln(T_{wb})]$$

where the constants are

$$C8 = -10440.4$$

$$C9 = -11.2946669$$

$$C10 = -0.02700133$$

$$C11 = 1.289706 \times 10^{-5}$$

$$C12 = -2.478068 \times 10^{-9}$$

$$C13 = 6.5459673$$

the temperatures are in degrees R, and the partial pressures in psia [53].  $P_{wswb}$  can be used to determine the humidity ratio at wet bulb temperature from

$$W_{wb} = \frac{(0.62198) P_{wswb}}{(P_{bar} - P_{wswb})}$$

The humidity ratio is then obtained as

$$W = \frac{[1093 - (0.556)T_{wb}](W_{wb}) - 0.24(T_{\infty} - T_{wb})}{1093 + (0.44)T_{\infty} - T_{wb}}$$

and the humidity ratio at saturation as

$$W_s = \frac{(0.62198) P_{ws}}{P_{bar} - P_{ws}}$$

The degree of saturation is defined as

$$U_s = \frac{W}{W_s}$$

and the relative humidity is then calculated using

$$\phi = \frac{U_s}{1 - (1 - U_s)(P_{ws}/P_{bar})}$$

The partial pressure of the water vapor is determined from the relative humidity and the partial pressure of the water vapor at saturation, thus

$$P_w = P_{ws} \phi$$

Once the partial pressure of the water vapor and the ambient pressure are known, Dalton's law of partial pressure may be applied to determine the partial pressure of the dry air as

$$P_a = P_{bar} - P_w$$

Density: The density of the moist air flowing through the test section may be expressed as

$$\rho = \frac{m_a + m_w}{V_m} = \frac{m_a}{V_m} + \frac{m_w}{V_m}$$

The ideal gas law may be applied to the dry air and water vapor and written as

$$P_a V_m = n_a \bar{R} T$$

$$P_w V_m = n_w \bar{R} T$$

The number of moles of a gas is equal to the quotient of the mass of gas divided by the molecular weight of the gas. Therefore, the number of moles of dry air and water vapor may be expressed as

$$n_a = m_a / M_a$$

$$n_w = m_w / M_w$$

The specific gas constants of dry air and water vapor are defined as

$$R_a = \bar{R} / M_a$$

$$R_w = \bar{R} / M_w$$

Substitution into the ideal gas law relations gives

$$P_a V_m = m_a R_a T_m$$

$$P_w V_m = m_w R_w T_m$$

Solving for the dry air mass and the water vapor mass and substituting in the density equation yields

$$\rho = \frac{P_a}{R_a T_m} + \frac{P_w}{R_w T_m} \quad (I.22)$$

This equation states that the density of a mixture of gases is the sum of the densities of the component gases at their respective partial pressures.

Specific Heat: The specific heat of the test air may be determined by applying an energy balance to the dry air and water vapor system.

$$C_p m_m T_m = C_{p_a} m_a T_m + C_{p_w} m_w T_m$$

Solving for the specific heat of the mixture and substituting for the mass of mixture yields

$$C_p = \frac{C_{p_a} m_a + C_{p_w} m_w}{m_a + m_w}$$

Substituting for the mass of the dry air and the mass of water vapor and dividing by the total number of moles in the mixture gives

$$C_p = \frac{C_{p_a} M_a n_a / n}{M_a (n_a / n) + M_w (n_w / n)} + \frac{C_{p_w} M_w n_w / n}{M_a (n_a / n) + M_w (n_w / n)}$$

From the thermodynamic principles of the mixture of gases, we know that the ratio of each partial pressure to the total pressure is equal to the mole fraction of each component. Therefore, we have

$$\frac{P_a}{P} = \frac{n_a}{n}$$

$$\frac{P_w}{P} = \frac{n_w}{n}$$

Substitution for the number of moles in terms of partial pressures gives the final expression for the specific heat of the test air as

$$C_p = \frac{C_{p_a} M_a P_a + C_{p_w} M_w P_w}{M_a P_a + M_w P_w} \quad (I.23)$$

It should be noted that the following assumptions have been made in this section. The curvefit equations used to obtain partial pressures are assumed very accurate, and their uncertainties are negligible in comparison with the measurement uncertainties. The ideal gas thermodynamic relationships used to calculate the test air properties are applicable to the dry air and saturated water vapor, and the uncertainties introduced by their application to a non-ideal gas are negligible as compared with the measurement uncertainties and the uncertainties in the properties obtained from reference tables.

Uncertainties: A sling psychrometer is inserted through an access hole in the top of the test section and is used to find the wet bulb temperature of the test air. The bias limit in  $T_{wb}$  is taken as 1.0 C and precision error is assumed negligible. The static air temperature determined from the recovery temperature measured by the thermistor probe is used for the dry bulb temperature. A temperature compensated barometer with a resolution of 0.5

mm Hg is used to determine the ambient pressure. Since the pressure of the test air mixture (dry air + water vapor) in the test section is kept equal to the outside ambient pressure, using make-up air controls, the pressure read from the barometer is used as the air mixture pressure. A bias limit of 1.0 mm Hg and negligible precision error are assumed for  $P_{\text{bar}}$ .

The specific heats for dry air and for water vapor were obtained as (Tables of Thermal Properties of Gases, U. S. National Bureau of Standards Circular 564, 1955)  $C_{p\text{air}} = 1.006 \text{ kJ/kg C}$  and  $C_{p\text{water}} = 1.86 \text{ kJ/kg C}$  with with an uncertainty in each estimate as 0.5%. These uncertainty estimates are fossilized into bias limits when the specific heat values are used in calculations.

#### I.3.6 Air Velocity

A Pitot probe is used to determine the freestream velocity. The Pitot probe channels the stagnation pressure and static pressure exerted by the freestream into a differential pressure transducer so that the freestream dynamic pressure can be measured. Once the dynamic pressure ( $\Delta P$ ) is known, the freestream velocity may be determined from

$$U_{\infty} = \left( \frac{2\Delta P}{\rho} \right)^{1/2} \quad (\text{I.24})$$

where  $\rho$  is the density of the freestream air. The procedure for determination of the test air density has already been described. The dynamic pressure determination methodology is presented next.

Dynamic pressure measurement is performed using two differential pressure transducers with ranges of 0.55 and 3.45 KPa. These transducers cover the full range of dynamic pressures expected. Their accuracy, specified by the manufacturer, is  $\pm 0.5$  percent of full scale. Each transducer provides a voltage output of 0-5 Vdc proportional to the applied pressure difference. The voltage outputs of the pressure transducers are measured by the ADACS.

The calibration of each pressure transducer was accomplished by employing a very sensitive water micromanometer as the pressure source. The 25.4 cm range micromanometer is equipped with a magnifier which amplifies the fluid meniscus at the reference hairline and provides direct reading indication to 0.0025 cm of water.

Each pressure transducer was calibrated individually. Various pressures within the pressure transducer range were generated using the micromanometer and were applied to the transducer. The values of these generated pressures indicated by the micromanometer were recorded and the corresponding voltage outputs from the pressure transducer were measured using the ADACS in a manner corresponding to actual testing. The number of pressure calibration points obtained for the 0.55 and 3.45 KPa range transducers were 23 and 10, respectively. Both pressure transducers demonstrated small but stable voltage outputs at zero pressures (zero shift). The pressure calibration data collected from each transducer was corrected for the zero shift.

Subsequently, the data of each transducer was used to arrive at an appropriate curvefit equation for that transducer. A linear curvefit equation for the 3.45 KPa range pressure transducer was satisfactory, but a quadratic equation was necessary to fit the 0.55 KPa range pressure transducer calibration data satisfactorily.

Uncertainties: A comparison between the direct pressure measurement data (micromanometer readings) and the pressures calculated from the curvefit equation was made for each pressure transducer. The results indicated that the bias limits associated with using the calibration curvefits for the 0.55 and 3.45 KPa range transducers were 0.5 percent and 0.1 percent of reading, respectively. Precision errors were observed to be negligible during the calibration process, and the bias error inherent in the micromanometer (which was used as the calibration standard) was assumed negligible.

During the actual dynamic pressure measurement when a Pitot probe in the flow stream is the pressure source for the transducer, the elemental bias error sources are the Pitot probe and the measurement system calibration. Therefore, the calibration bias and the additional biases introduced by the Pitot probe must be combined using RSS to arrive at the overall bias limit for actual dynamic pressure measurements. Biases in the dynamic pressure due to errors caused by Pitot probe design, use, and misalignment have been estimated at 0.5 percent since the freestream flow is uniform and relatively free of perturbations and since the Pitot probe is very carefully aligned with the flow. The bias limit estimates are



for Pitot probe	0.5% of reading
for 0.55 KPa transducer (calibration)	0.5% of reading
for 3.45 KPa transducer (calibration)	0.1% of reading.

Therefore, bias limits for dynamic pressure measurements become

$$\left(\frac{B_{\Delta P}}{\Delta P}\right) = [(0.005)^2 + (0.005)^2]^{1/2} = 0.7\%$$

for the 0.55 KPa transducer, and

$$\left(\frac{B_{\Delta P}}{\Delta P}\right) = [(0.001)^2 + (0.005)^2]^{1/2} = 0.5\%$$

for the 3.45 KPa transducer.

The bias limit in the free stream velocity is dependent on the bias limit in the dynamic pressure and on the bias limit in the density. As discussed above, bias limits for the dynamic pressures measured using the 0.55 KPa and 3.45 KPa transducers are 0.5% and 0.7% of reading, respectively. For the bias limit of the air density, based on an analytical uncertainty analysis using nominal values of the related variables, an estimated value of 0.3% is used. This is a conservative value and does not change significantly with small changes in the environment and/or operating conditions of the tunnel.

Applying equation (I.14) to equation (I.24), the expression for the bias limit of the freestream velocity is

$$(B_{U_{\infty}})^2 = \left[\frac{\partial U_{\infty}}{\partial \Delta P} B_{\Delta P}\right]^2 + \left[\frac{\partial U_{\infty}}{\partial \rho} B_{\rho}\right]^2$$

which, after substitution of the appropriate partial derivatives and division by the velocity gives

$$\left(\frac{B_{U_{\infty}}}{U_{\infty}}\right)^2 = \left(\frac{1}{2}\right)^2 \left(\frac{B_{\Delta P}}{\Delta P}\right)^2 + \left(\frac{1}{2}\right)^2 \left(\frac{B_{\rho}}{\rho}\right)^2$$

The bias limit when the 0.55 KPa pressure transducer is used is

$$\left(\frac{B_{U_{\infty}}}{U_{\infty}}\right) = \left(\frac{1}{2}\right)^2 (0.007)^2 + \left(\frac{1}{2}\right)^2 (0.003)^2$$

$$\left(\frac{B_{U_{\infty}}}{U_{\infty}}\right) = 0.4\%$$

The bias limit when the 3.45 KPa pressure transducer is used is

$$\left(\frac{B_{U_{\infty}}}{U_{\infty}}\right)^2 = 0.3\%$$

Precision errors have been observed to be negligible in the determination of  $U_{\infty}$ , so the precision limit for  $U_{\infty}$  is assumed zero.

### I.3.7 Air Temperature Probe Recovery Factor

The temperature obtained from the air thermistor is the recovery temperature  $T_r$ . The freestream total temperature and static temperature are computed from  $T_r$  using equations (I.9) and (I.10), but a value for recovery factor  $r$  is necessary for the calculation. Based on the review of available data (Eckert and Goldstein, 1976), a value of  $r = 0.86$  was chosen with an uncertainty of 0.09. This uncertainty is fossilized into a bias limit when the recovery factor is used in calculations.

### I.3.8 Test Plate Emissivity

Radiation from the heated test plates primarily falls within the infrared range from 2 to 100 microns. Plexiglass has a high absorbtivity at these wavelengths and transmits only 2% of the incident infrared radiation. Since the test plates are enclosed by the plexiglass side and top walls, a gray body enclosure radiation model is used. Because plexiglass has a high emissivity of about 0.9 and because of the magnitude of the areas involved, the general gray body enclosure model simplifies to the special case of a small object in a large cavity.

As discussed previously with equation (I.6), the radiative heat losses from the test plates are modeled using

$$q_r = \sigma \epsilon A (T_w^4 - T_r^4)$$

The emissivity  $\epsilon$  of the test plates is very dependent on the state of oxidation and cleanliness of the plates. Typical values of the emissivity as quoted in various handbooks are -0.05 for a polished electroplated nickel surface at 23 C, -0.11 for an unpolished electroplated nickel surface at 20 C, and -0.37 for heavily oxidized nickel at 200 C. An emissivity typical of unpolished electroplated nickel (0.11) was assumed with a bias limit of  $\pm 0.05$ .

### I.4 UNCERTAINTY ANALYSIS RESULTS

A jitter program (Coleman and Steele, 1989) was used to determine an uncertainty estimate for each experimentally determined Stanton number. In the jitter program, the data reduction computer

program was treated as a subroutine and used to approximate the partial derivatives in equation (I.16) using finite differences. In this numerical uncertainty analysis scheme, the first step was to read the original experimental data from a data file and calculate the Stanton number for each of the 24 plates using the data reduction subroutine. Then the partial derivatives of the Stanton number with respect to each of the thirteen variables were determined numerically using finite difference approximations. The evaluation of a partial derivative was accomplished using a loop through which the original value of one variable was perturbed by a prespecified amount and calculating new Stanton numbers for all 24 plates using the data reduction subroutine. The difference between each new Stanton number and the original unperturbed Stanton number divided by the amount that the particular variable was perturbed resulted in a value for a partial derivative. Before calculation of the next partial derivative the perturbed value of the previous variable was reset to the original value and then the next variable was perturbed.

Upon completion of all partial derivatives, equation (I.16) was evaluated. Since precision limits in the measurements were assumed negligible, only the bias limits for the thirteen variables were required, and the bias limits used were

<u>Variable</u>	<u>Bias limit</u>	<u>Nominal Values</u>
Plate Temperature	0.14 C	45 C
Rail Temperature	0.4 C	45 C
Recovery Temperature	0.10 C	30 C
Wet-Bulb Temperature	1.0 C	27 C
Barometric Pressure	1.0 mm Hg	760 mm Hg
Recovery Factor	0.09	0.86
Power	0.9%	20-150 W
Area	0.03%	464.5 cm <sup>2</sup>
Air Velocity	0.4%	6-70 m/s
C <sub>P</sub> air	0.5%	1.006 kJ/kg C
C <sub>P</sub> water	0.5%	1.86 kJ/kg C
(UA) <sub>eff</sub>	45%	0.42 W/C
Emissivity	45%	0.11

In addition, some of the bias errors in temperatures were correlated since the same calibration standard was used. The correlated biases are

$$B'_{T_w} = B'_{T_r} = B'_{T_{rail}} = 0.04 \text{ C}$$

For the Stanton number data discussed in this report, the overall uncertainty (as computed using equation (I.11)) ranged from about 2 percent to 5 percent, depending on flow conditions. Uncertainty bars are indicated on representative data points when the St data are plotted. The uncertainties are also shown in the tabular listings in Appendix IV.

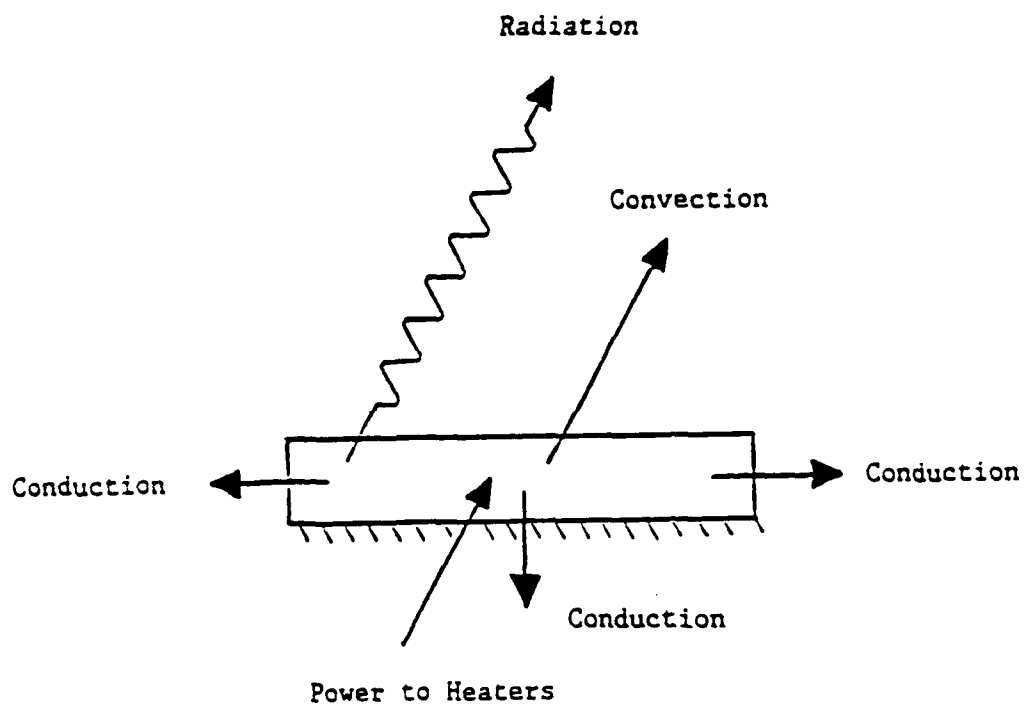


Figure I.1 Energy balance on a test plate.

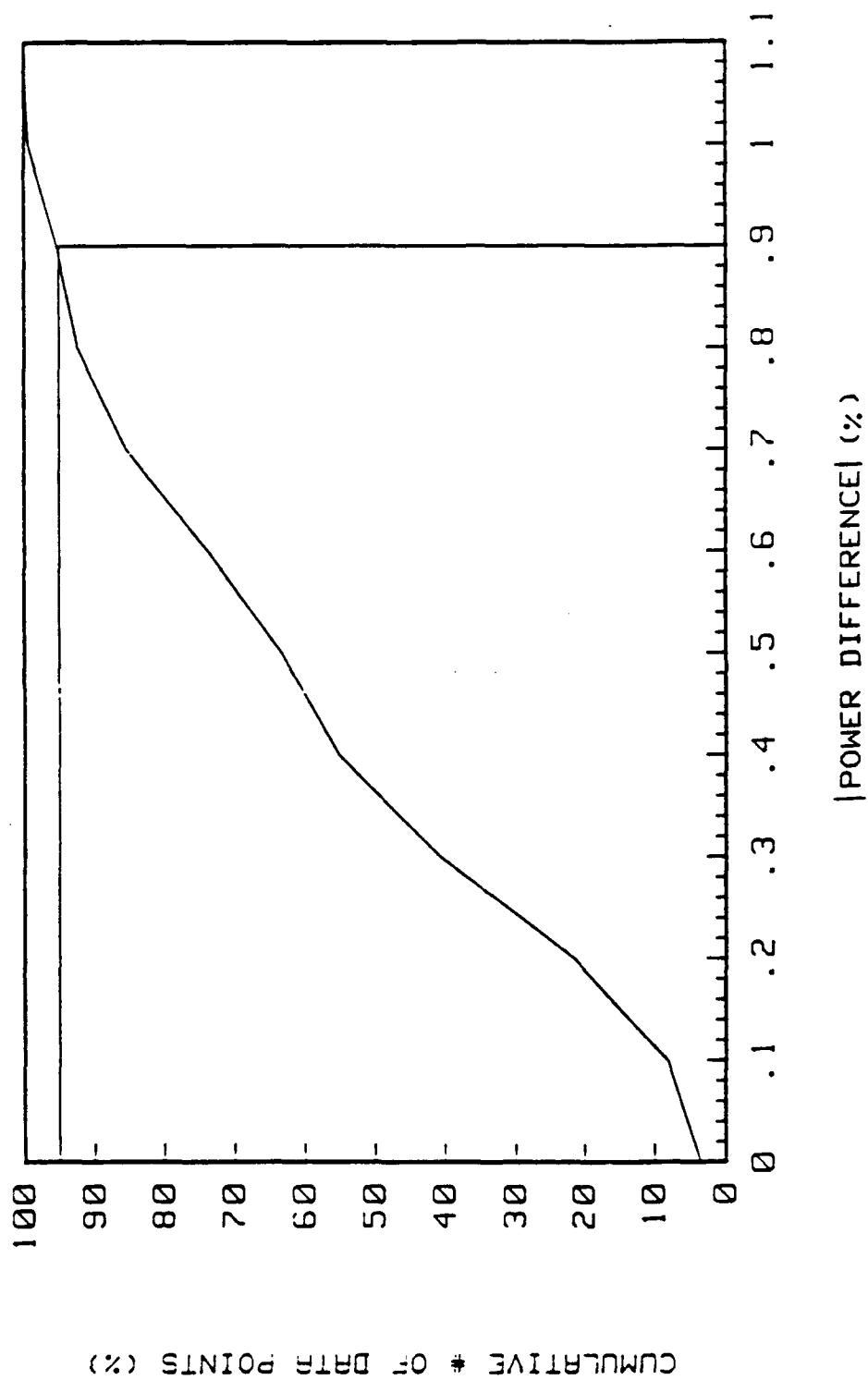


Figure 1.2 Power measurement calibration results.

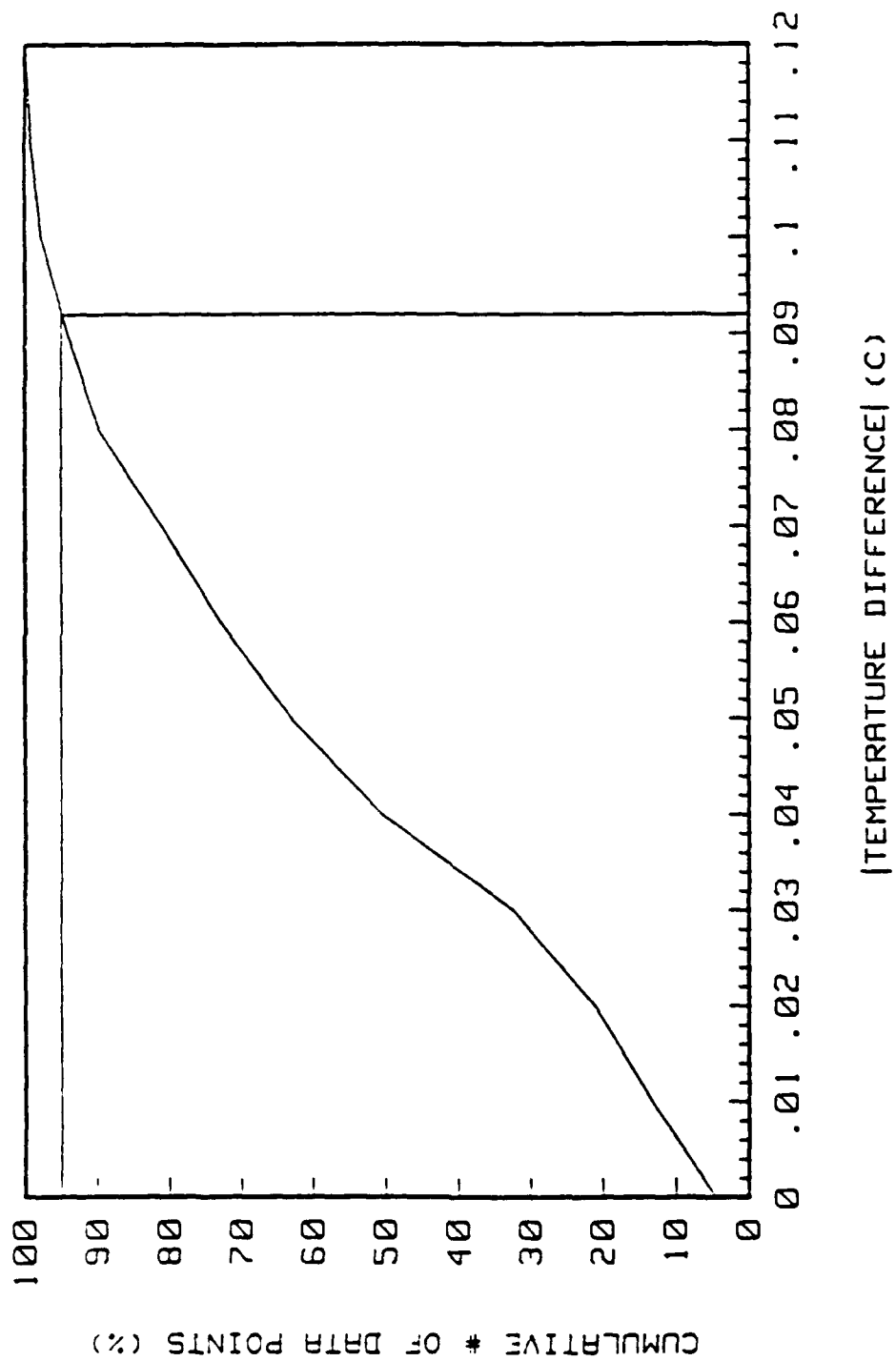


Figure 1.3 Thermistor calibration results.



## APPENDIX II

### BOUNDARY LAYER PROBE MEASUREMENTS

#### II.1 HOT-WIRE ANEMOMETRY

Profiles of boundary layer mean velocity and turbulence components were measured with hot-wire anemometry. The hot-wire instrumentation consisted of a TSI-IFA 100 Intelligent Flow Analyzer System with two constant temperature anemometer units and an HP-3437A high speed system voltmeter in the HP-3054A Automatic Data Acquisition and Control System (ADACS) which was linked to an HP-Series 9000 Model 220 microcomputer. Two hot-wire probes were used: a DANTEC 55P05 horizontal, boundary-layer type probe and a DANTEC 55P02 45° slant probe, both of 5 micron diameter platinum plated tungsten wire with gold plated ends. Each of the two anemometer units in the flow analyzer was dedicated to either the horizontal or slanted probe. Digital readings of the anemometer voltages were made with the HP-3437A high speed voltmeter connected directly to the signal conditioned anemometer output. These digital voltage readings were then relayed to the microcomputer.

The horizontal hot-wire probe and the slanted hot-wire probe are shown schematically with their supports in Figures II.1 and II.2, respectively. These probes are identical to those used by Pimenta (1975) and Coleman (1976). Each probe was mounted in a custom made holder with a vertical micrometer head traversing mechanism having a resolution of 0.025 mm. Both probe holders were

supported by an xz traverse attached to a special sled that spanned the tunnel and rested on the side walls. Locating pins held the xz traverse in place on the special sled. Four hold down screws fixed the sled to the side walls of the test section.

In use, both probes had to be lowered to the plate surface for a reference height above the plate to be established. To prevent the horizontal wire from hitting the wall, a keel or wall stop was epoxied to the probe stem of the horizontal wire. A collar on the spindle of the slant wire probe provided a wall stop for the slant wire. The probes were lowered until electrical continuity through the wall stop between the probe stem and the plate surface was established. Conductive ink was placed on the back of the horizontal wire keel to provide electrical continuity between the keel and probe stem. With the hot-wire/plate clearance provided by the wall stops known, any desired vertical probe height above the plate could be set to within 0.025 mm. When used with the rough surface, a cylindrical rod slightly longer than the roughness height was attached to the wall stops so that the smooth portion of the rough wall could be used as a reference position.

#### II.1.1 Horizontal Hot-Wire Probe Measurements

Measurements of the mean velocity and the fluctuating longitudinal velocity component ( $\overline{u'^2}$ ) were made with the horizontal hot-wire. The horizontal wire was aligned with the flow by matching etched marks on the holder and horizontal traversing mechanism. Once the probe was aligned with the flow and freestream measure-

ments had been taken, the boundary layer velocity profile measurements began with the probe keel starting just above the wall for the first measurement. Measurements were typically taken at every 1-2% of the normalized velocity ( $u/U_\infty$ ) in the inner region of the boundary layer and every 2-4% of the normalized velocity in the outer region. At each measurement position, 1000 instantaneous anemometer output voltage readings were taken 0.01 seconds apart and used to compute 1000 corresponding velocities. A fourth order least squares calibration equation was used to convert anemometer voltages into velocities. The mean of the 1000 computed velocities was used as the mean velocity at that location. The longitudinal velocity fluctuation ( $\overline{u'^2}$ ) was taken as the square of the standard deviation (the variance) of the 1000 computed velocities. Experience showed that stable averages were obtained using this number of readings over the 10 second time period.

#### II.1.2 Slant Hot-Wire Probe Measurements

The slant wire was used to determine the Reynolds shear stress factor ( $\overline{u'v'}$ ), the normal velocity fluctuation ( $\overline{v'^2}$ ), and the transverse velocity fluctuation ( $\overline{w'^2}$ ). The slant wire was mounted on the rotatable spindle of the probe holder with its prongs parallel to the mean flow direction at any angle of rotation. The spindle was rotated by a cable drive, which could be operated with the probe in the tunnel. A "lock-drum" system with eight radially drilled holes spaced 45° apart and a spring loaded pin with a lever

located at the top of the vertical traverse mechanism were used to lock the spindle into the desired orientation by fitting the pin into one of the drilled holes.

Alignment of the slant wire spindle with the mean flow was done in the freestream. A schematic of the slant wire geometry and coordinates is given in Figure II.3. The slant wire was placed in the horizontal plane ( $\theta=90^\circ, 270^\circ$ ) and the output of the anemometer was noted for these two probe orientations. Alignment of the probe spindle and slant wire with the mean flow was adjusted by rotating the probe stem around its y-axis. The alignment of the probe was adjusted back and forth in small increments across the flow direction in a iterative manner until the difference between the electrical signals at probe rotation angles of  $\theta=90^\circ$  and  $\theta=270^\circ$  was 3-5mV from a 3-5V signal. The corresponding error in the indicated mean velocity due to misalignment of the slant wire probe was less than 0.12 m/s for freestream velocities as high as 46 m/s.

To determine  $\overline{v'^2}$ ,  $\overline{w'^2}$ , and  $\overline{u'v'}$ , the slant wire was positioned approximately 3.3 mm above the surface of the smooth plate (or about 4 mm above the smooth surface of the rough plate) and measurements were made at three probe rotation angles  $\theta=45^\circ, 90^\circ$ , and  $135^\circ$ . At each probe rotation angle, 4000 instantaneous anemometer output voltage readings 0.025 seconds apart were taken and used to compute 4000 corresponding effective velocities ( $u_{eff}$ ). A fourth order least squares calibration correlation was used to convert anemometer voltages into effective velocities. The fluctuating component of the effective velocity ( $\overline{u'_{eff}^2}$ ) at each rotation angle

was taken as the square of the standard deviation (the variance) of the 4000 computed effective velocities. Experience showed that this many readings taken over the 100 second time period provided stable averages.

The values of  $\overline{u'_{eff}^2}$  at the three slant wire probe orientations were used in conjunction with the value of  $\overline{u'^2}$  from the horizontal wire measurements at the same y-position to solve a system of three linear equations for  $\overline{v'^2}$ ,  $\overline{w'^2}$ , and  $\overline{u'v'}$ . These linear equations were generated with equation (II.1) evaluated at the three probe rotation angles as discussed in detail by Coleman (1976).

$$\overline{u'_{eff}^2} = A \overline{u'^2} + \frac{D^2}{4A} \overline{v'^2} + \frac{F^2}{4A} \overline{w'^2} + D \overline{u'v'} + \frac{DF}{2A} \overline{v'w'} + F \overline{u'w'} \quad (II.1)$$

The coefficients in this equation depend on the orientation of the probe with respect to the flow coordinates,

$$\begin{aligned} A &= \cos^2\phi + k_1^2 \sin^2\phi \\ B &= (\sin^2\phi + k_1^2 \cos^2\phi) \cos^2\theta + k_2^2 \sin^2\theta \\ C &= (\sin^2\phi + k_1^2 \cos^2\phi) \sin^2\theta + k_2^2 \cos^2\theta \\ D &= (1 - k_1^2) \sin 2\phi \cos\theta \\ E &= (\sin^2\phi + k_1^2 \cos^2\theta - k_2^2) \sin 2\theta \\ F &= (1 - k_1^2) \sin 2\phi \sin\theta \end{aligned}$$

where

$\theta$  is the probe rotation angle (45°, 90°, 135°)

$\phi$  is the wire slant angle (45°)

The constants  $k_1$  and  $k_2$ , which are known for a DANTEC 55P02 probe, depend on the construction characteristics of the slant wire probe and were taken to have the values of

$$k_1 = 0.2$$

$$k_2 = 1.02$$

as previously done by others [Pimenta (1975) and Coleman (1976), for example].

### II.1.3 Hot-Wire Calibration

The hot-wires were calibrated in the test section in the uniform flow at the nozzle exit. A Pitot probe placed 2-3 cm to the side of the hot-wire and coupled to one of the differential pressure transducers discussed in Appendix I was used to determine the freestream velocity. The freestream air velocity in the tunnel was adjusted to different set points over the desired measurement range with the static temperature of the freestream held constant to within  $\pm 0.1^\circ\text{C}$ . At each velocity set point, 1000 anemometer voltage readings were taken and averaged. A least squares analysis was applied to the average voltages and the velocities determined from the Pitot tube to obtain a fourth order polynomial calibration equation for each wire.

In practice, the resistance of the heated wire during measurements (the operating resistance) is set above the resistance of the unheated wire (the cold probe resistance) to satisfy the desired overheat ratio requirements. The cold probe resistance is temperature dependent and must be remeasured and re-entered into the

anemometer unit if the freestream temperature of the test air changes more than about  $\pm 0.2^{\circ}\text{C}$  from the conditions of calibration. The required operating resistance used was always 3 ohms higher than the cold probe resistance at all operating conditions. A comparison of calibration equations from a calibration done at a freestream temperature of  $25.6^{\circ}\text{C}$  and a calibration done at a freestream temperature of  $29.9^{\circ}\text{C}$  showed that the velocities computed with the two equations differed by less than 1% over the entire calibration range. Since these calibrations had different cold probe resistances and the operating resistances were set by adding 3 ohms to the cold probe resistance, it was concluded that calibrations of the hot-wires at one freestream temperature would be valid over a small temperature range ( $\pm 3^{\circ}\text{C}$ ) as long as the difference in the probe resistances was held at 3 ohms and the freestream temperature of the test air was not allowed to vary more than about  $\pm 0.1^{\circ}\text{C}$  while data were taken for a profile at a particular x-location.

#### II.1.4 Uncertainties

Uncertainties in the hot-wire measurements were estimated by considering the uncertainties in the Pitot-determined velocity, in curvefitting of the calibration data, in anemometer adjustments, and in probe alignment; the observed scatter in the data; and the suggested uncertainties given in the literature [Kline, et al.

(1981), Yavuzkurt (1982)]. The order of the overall uncertainties (bias and precision) associated with the hot-wire measurements are:  $u$ , 2%;  $\overline{u'^2}$ , 5%;  $\overline{v'^2}$ , 15%;  $\overline{w'^2}$ , 10%; and  $\overline{u'v'}$ , 10%.

## II.2 THERMOCOUPLE PROBE

Time mean temperatures in the boundary layer were measured using a Type E (chromel-constantan) butt-welded thermocouple probe similar in design to that of Blackwell (1972). The output of the thermocouple is in the millivolt range and is measured by the ADACS.

The thermocouple probe holder, which is almost identical to the horizontal wire holder, was mounted on the same support sled used with the hot-wires. A schematic of the thermocouple probe and its support is shown in Figure II.4.

The thermocouple calibration was done in a Blue M Model MR-3210A-1 constant temperature bath, and the Hewlett-Packard quartz thermometer described in Appendix I was utilized to measure the bath temperature. The calibration water bath was in continuous movement due to an automatic stirrer, and the risk of breaking the fine thermocouple wire was large if the probe was placed directly into it. Besides, water could deposit some residue on the wire surface and the prongs, which could influence the thermocouple temperature response. Moreover, the water temperature close to the thermocouple could not be accurately monitored by the quartz thermometer. To alleviate those difficulties it was decided to insert the wire into a jar filled with alcohol, which was placed in the



water bath. The quartz thermometer was also positioned in the jar next to the thermocouple probe so that it would encounter the same conditions. To prevent any air current from convecting heat to or from the alcohol surface, the opening of the jar was sealed. The time constant of the jar was also accounted for by waiting an hour after the water bath temperature had reached the steady state condition before proceeding with the temperature measurement.

Calibration was performed for temperatures between 23°C-39°C using four points over this range. The thermocouple probe voltage outputs, as measured by the ADACS, were converted to temperatures using the HP system software package. The temperature of the reference junction (the isothermal terminal block) required for software compensation is established by the ADACS via a temperature transducer which provides a 100 mV/°C output voltage. This software performs the voltage-temperature conversion by dividing the thermocouple characteristic curve into eight sectors and approximating each sector by a third order nested polynomial. The temperatures measured by the thermocouple were compared with the temperatures from the quartz thermometer over the above mentioned calibration range. The departure of thermocouple temperatures, using the software package for conversion, from the corresponding temperatures obtained by the quartz thermometer was less than  $\pm 0.08^{\circ}\text{C}$ .

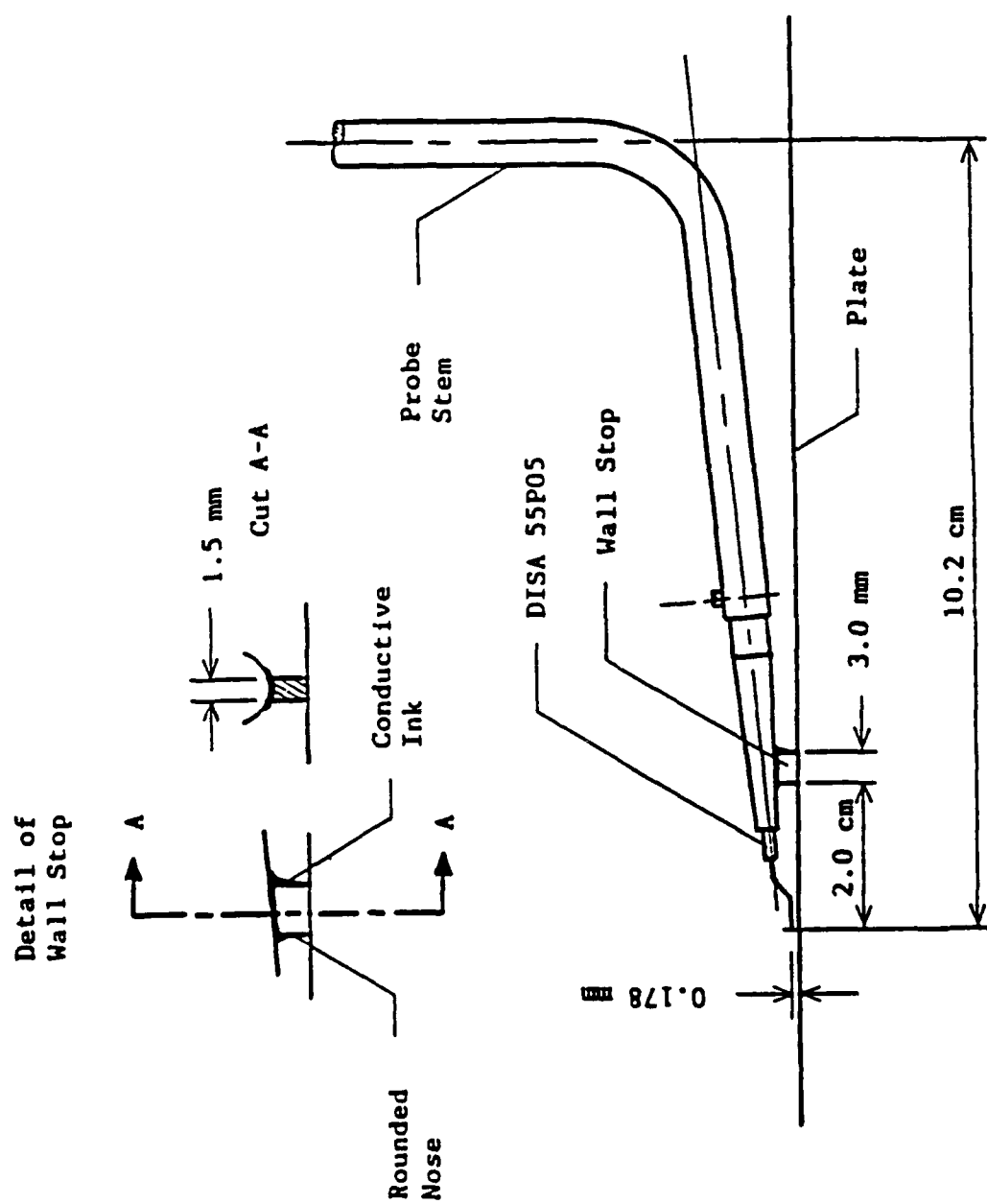


Figure II.1 Schematic of horizontal hot-wire probe.

# Detail of Wall Stop

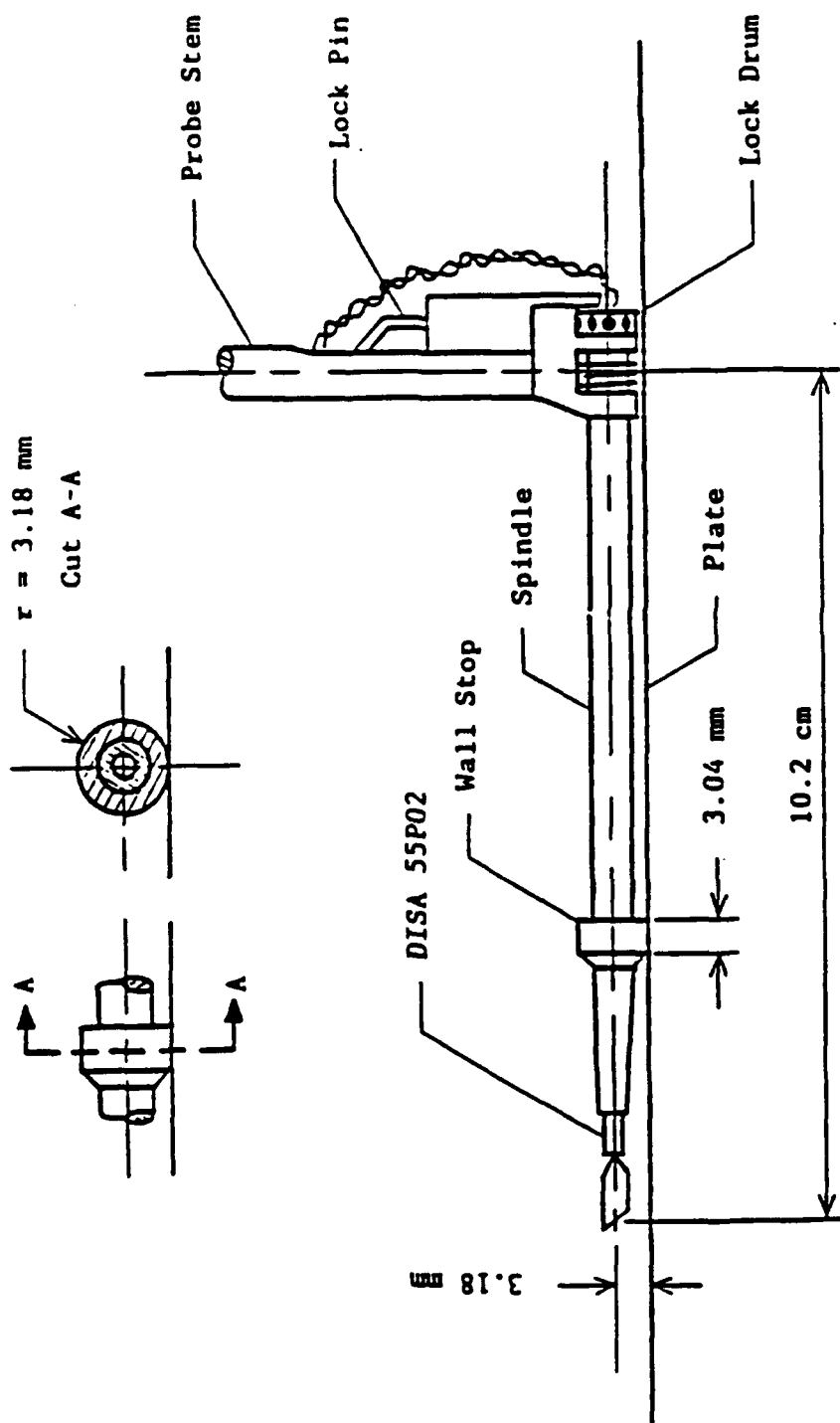


Figure 11.2 Schematic of slant hot-wire probe.

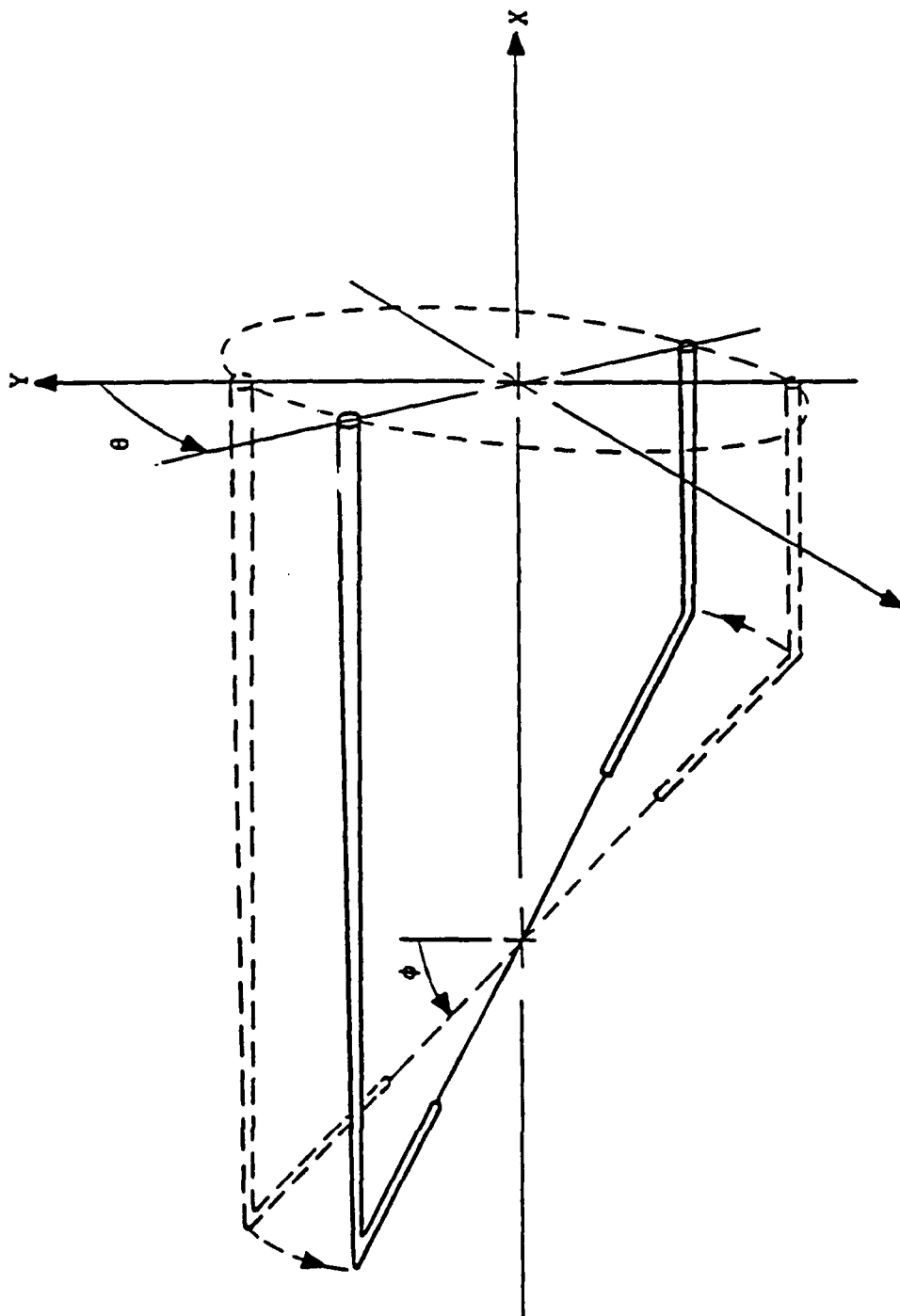


Figure II.3 Slant wire: Geometry and coordinates.

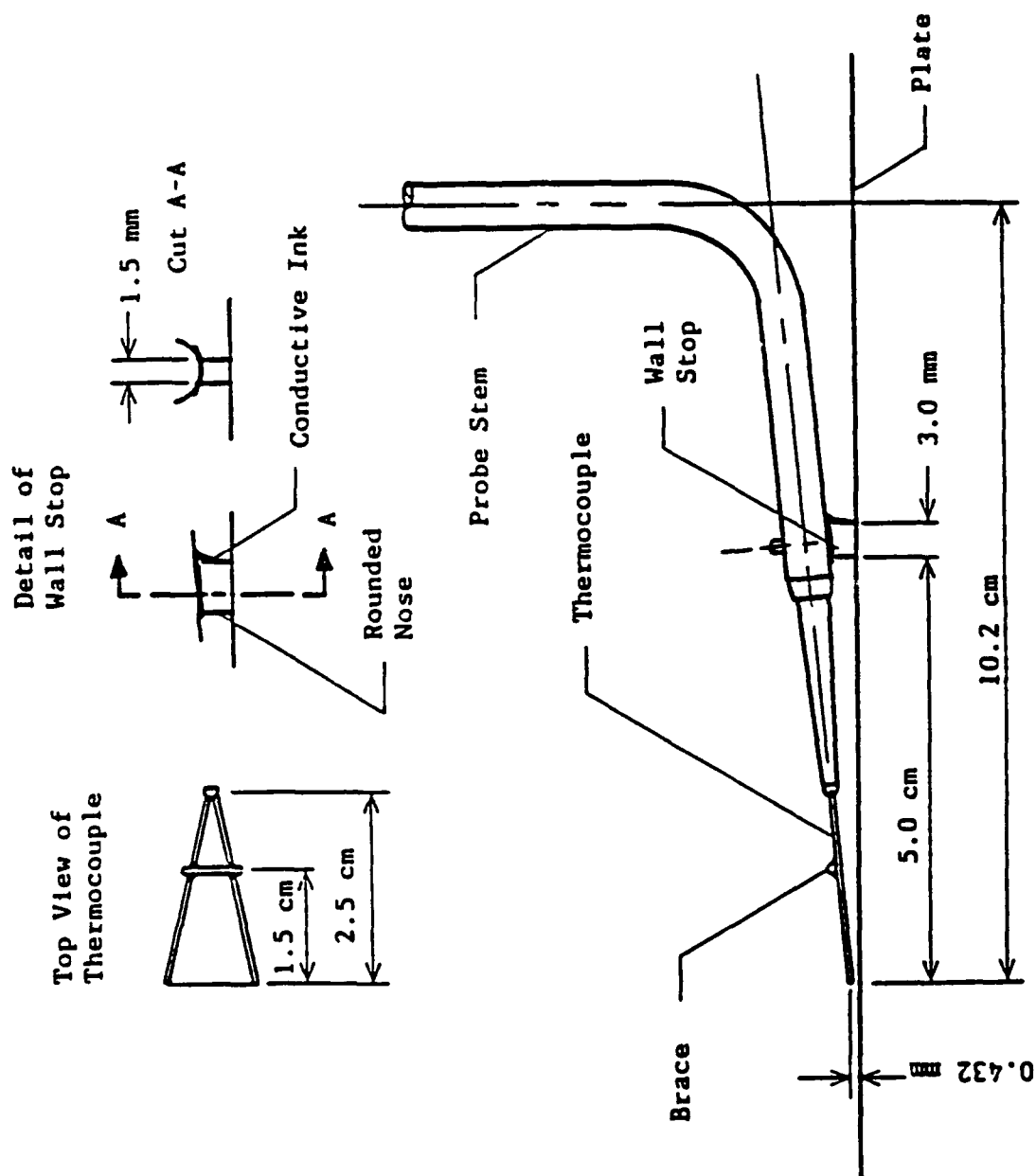


Figure II.4 Schematic of the thermocouple probe.

# APPENDIX III

## SKIN FRICTION COEFFICIENT DETERMINATION

Skin friction coefficients in this study were determined in two ways: (1) from hot-wire measurements of Reynolds shear stress and mean velocity profiles, and (2) from Preston tube measurements. These skin friction determination methods are discussed briefly below with detailed references given for further information.

### III.1 HOT-WIRE METHOD

The first means of determining the skin friction coefficients in this study was the hot-wire data method. (This procedure is the only method used for skin friction determination in the rough wall boundary layers.) Skin friction coefficients were determined using

$$\begin{aligned} \frac{C_f}{2} = & \frac{\nu}{U_\infty^2} \left. \frac{\partial u}{\partial y} \right|_{Y_1} - \frac{\overline{u'v'}}{U_\infty^2} \bigg|_{Y_1} - \frac{d}{dx} \left[ \int_0^{Y_1} \left( \frac{u}{U_\infty} \right)^2 dy \right] \\ & + \frac{u_{Y_1}}{U_\infty} \frac{d}{dx} \left[ \int_0^{Y_1} \left( \frac{u}{U_\infty} \right) dy \right] \end{aligned} \quad (III.1)$$

To derive equation (III.1), the Reynolds-averaged momentum equation (incorporating the usual boundary layer assumptions) and the continuity equation are integrated from the plate surface to a position  $Y_1$  in the boundary layer. Calculations of  $C_f$  are made using equation (III.1), mean velocity profiles measured over adja-

cent test plates ( $\Delta X = 10.2$  cm), and the measured value  $\overline{u'v'}$  at  $y=Y_1$ . The position  $Y_1$  was about 3.3 mm for smooth wall studies and 4 mm for rough wall studies. Further details of hot-wire data determinations of the skin friction coefficient are given by Andersen (1972), Pimenta (1975), and Coleman (1976).

The estimated uncertainty in the hot-wire determined skin friction coefficients in this study is about  $\pm 10$ -12%. This estimate is based on smooth wall comparisons of the hot-wire determined values of  $C_f$  with accepted  $C_f$  correlations and with the values determined using the Preston tube.

### III.2 PRESTON TUBE METHOD

The method of Preston (1954) for determining the skin friction in turbulent boundary layer flows uses a simple Pitot tube (Preston tube) resting on the surface and depends upon the assumption of a universal inner law (law of the wall) common to smooth wall boundary layer flows. The difference between the total pressure at the Preston tube of 1.6 mm (1/16 in) inside diameter and the undisturbed static pressure at a pressure tap in the test section sidewall at the same x-location was measured with the pressure transducers described in Appendix I. This difference in pressure was then used in conjunction with the calibration equations as given by Patel (1965) to solve for the local skin friction coefficient.

The Preston tube method of determining skin friction coefficients is only of use for the smooth plate case because calibrations have only been made for smooth walls. However, skin friction coefficient determinations made by Preston's method are quick and easy to make. The relatively low uncertainty (less than about 6%) in the skin friction coefficients determined with Preston's method made this method very important in establishing the qualification of the test facility and the correctness of the hot-wire based skin friction determination method.



## REFERENCES

- (1985), ASHRAE Handbook 1985 Fundamentals, ASHRAE, Atlanta, GA.
- (1986), Measurement Uncertainty, ANSI/ASME PTC 19.1-1985 Part 1.
- (1955), Tables of Thermal Properties of Gases, U. S. National Bureau of Standards Circular 564.
- Adams, J. C. and Hodge, B. K. (1977), "The Calculation of Compressible Transitional Turbulent and Relaminarizational Boundary Layers over Smooth and Rough Surfaces Using an Extended Mixing-Length Hypothesis," AIAA Paper 77-682.
- Andersen, P. S. (1972), "The Turbulent Boundary Layer on a Porous Plate: "An Experimental Study of the Fluid Mechanics for Adverse Free-Stream Pressure Gradients," Ph.D. Dissertation, Mech. Eng. Dept., Stanford Univ. (Also Report HMT-15).
- Blackwell, B. F. (1972), "The Turbulent Boundary Layer on a Porous Plate: An Experimental Study of the Heat Transfer Behavior with Adverse Pressure Gradients," Ph.D. Dissertation, Mech. Eng. Dept., Stanford Univ. (Also Report HMT-16).
- Cebeci, T. and Chang, K. C. (1978), "Calculation of Incompressible Rough-Wall Boundary-Layer Flows," AIAA Journal, Vol. 16, pp. 730-735.
- Chen, C. K. (1971), "Characteristics of Turbulent Flow Resistance in Pipes Roughened with Hemispheres," Ph.D. Dissertation, Washington State Univ.
- Christoph, G. A. (1982), "Law of the Wall Analysis for Turbulent Heating on Rough Surfaces," AIAA Paper 82-0197.
- Christoph, G. H., and Pletcher, R. H. (1983), "Prediction of Rough-Wall Skin Friction and Heat Transfer," AIAA Journal, Vol. 21, No. 4, pp. 509-515.
- Coleman, H. W. (1976), "Momentum and Energy Transport in the Accelerated Fully Rough Turbulent Boundary Layer," Ph.D. Dissertation, Mech. Eng. Dept., Stanford Univ. (Also Report HMT-24).
- Coleman, H. W., Hodge, B. K. and Taylor, R. P. (1983), "Generalized Roughness Effects on Turbulent Boundary Layer Heat Transfer," AFATL-TR-83-90.

Coleman, H. W., Hodge, B. K. and Taylor, R. P. (1984), "A Reevaluation of Schlichting's Surface Roughness Experiment," Journal of Fluids Engineering, Vol. 106, pp. 60-65.

Coleman, H. W., Hosni, M. H., Taylor, R. P., and Brown, G. B., "Smooth Wall Qualification of a Turbulent Heat Transfer Test Facility," TFD-88-2, Mechanical and Nuclear Engineering Department, Mississippi State University.

Coleman, H. W. and Steele, W. G. (1989), Experimentation and Uncertainty Analysis for Engineers, John Wiley, New York, NY.

Corrsin, S. and Kistler, A. L. (1954), "The Free Stream Boundaries of Turbulent Flows," NACA Tech. Note 3133.

Dipprey, D. F. and Sabersky, R. H. (1963), "Heat and Momentum Transfer in Smooth and Rough Tubes at Various Prandtl Numbers," International Journal of Heat and Mass Trans., Vol. 6, pp. 329-353.

Dvorak, F. A. (1969), "Calculation of Turbulent Boundary Layers on Rough Surfaces in Pressure Gradients," AIAA Journal, Vol. 7, pp. 1752-1759.

Eckert, R. G. and Goldstein, R. J. (1976), Measurements in Heat Transfer, 2nd edition, McGraw-Hill, New York, NY.

Finson, M. L. (1975), "A Reynolds Stress Model for Boundary Layer Transition with Applications to Rough Surfaces," AFOSR-TR-76-0322.

Finson, M. L. and Wu, P. K. S. (1979), "Analysis of Rough Wall Turbulent Heating with Applications to Blunted Flight Vehicles," AIAA Paper 79-008.

Finson, M. L. and Clark, A. S. (1980), "The Effects of Surface Roughness Character on Turbulent Reentry Heating," AIAA Paper 80-1459.

Finson, M. L. (1982), "A Model for Rough Wall Turbulent Heating and Skin Friction," AIAA Paper 82-0199.

Grass, A. J. (1971), "Structural Features of Turbulent Flow Over Smooth and Rough boundaries," Journal of Fluid Mechanics, Vol. 50, pp. 233-255.

Hama, F. R. (1954), "Boundary Layer Characteristics for Smooth and Rough Surfaces," Trans. SNAME, Vol. 62, pp. 333-354.

Healzer, J. M. (1974), "The Turbulent Boundary Layer on a Rough, Porous Plate: Experimental Heat Transfer with Uniform Blowing," Ph.D. Dissertation, Mech. Eng. Dept., Stanford Univ. (Also Report HMT-18).

Hinze, J. O. (1959), "Turbulence--An Introduction to its Mechanism and Theory," McGraw-Hill Book Co.

Hodge, B. K., Taylor, R. P. and Coleman, H. W. (1986), "An Investigation of Surface Roughness Effects on Adiabatic Wall Temperature," AIAA J., Vol. 24, pp. 1560-1561.

Holden, M. S. (1983), "Studies of Surface Roughness Effects in Hypersonic Flow," Calspan Report No. 7018-A-2, Advanced Technology Center, Buffalo, NY.

Hosni, M. H., Coleman, H. W., and Taylor, R. P. (1989), "Measurement and Calculation of Surface Roughness Effects on Turbulent Flow and Heat Transfer," TFD-89-1, Mechanical and Nuclear Engineering Department, Mississippi State University.

Kays, W. M. and Crawford, M. E. (1980), Convective Heat and Mass Transfer, 2nd edition, McGraw-Hill, New York, NY.

Klebanoff, P. S. (1955), "Characteristics of Turbulence in a Boundary Layer with Zero Pressure Gradient," NACA TR 1247, Washington, DC.

Kline, S. J., Cantwell, B. J. and Lilley, G. M. (1980), "Report of the Working Group on Hot-wire Anemometry at Low Mach Numbers," The 1980-81 AFOSR-HTTM-Stanford Conference on Complex Turbulent Flows: Comparison of Computation and Experiment, Stanford Univ., Vol. 1, pp. 583-585.

Laufer, J. (1954), "The Structure of Turbulence in Fully Developed Pipe Flow," NACA TR 1174, Washington, DC.

Lewis, M. J. (1975), "An Elementary Analysis for Predicting the Momentum and Heat Transfer Characteristics of a Hydraulically Rough Surface," Journal of Heat Transfer, Vol. 97, pp. 249-254.

Liepmann, H. W. and Goddard, F. E. (1957), "Note on the Mach Number Effect Upon the Skin Friction of Rough Surfaces," Journal of Aeronautical Sciences, Vol. 24, p. 784.

Ligrani, P. M. (1979), "The Thermal and Hydrodynamic Behavior of Thick, Rough-Wall, Turbulent Boundary Layers," Ph.D. Dissertation, Mech. Eng. Dept., Stanford Univ. (Also Report HMT-29).

- Ligrani, P. M. and Bradshaw, P. (1987), "Spatial Resolution and Measurement of Turbulence in the Viscous Sublayer Using Subminiature Hot-Wire Probes," Experiments in Fluids, Vol. 5, pp. 407-417.
- Lin, T. C. and Bywater, R. J. (1980), "The Evaluation of Selected Turbulence Models for High-Speed Rough Wall Boundary Layer Calculations," AIAA Paper 80-0132.
- Moffat, R. J. (1988), "Describing the Uncertainties in Experimental Results," Experimental Thermal and Fluid Science, Vol. 1, pp. 3-17.
- Nestler, D. E. (1970), "Compressible Turbulent Boundary Layer Heat Transfer to Rough Surfaces," ASME Paper 70-742.
- Nikuradse, J. (1933), "Stromungsgesetze in Rauhen Rohren," VDI-Forschungsheft 361. (Also Laws of Flow in Rough Pipes, NACA TM 1292.)
- Norris, R. H. (1971), "Some Simple approximate Heat Transfer Correlations for Turbulent Flow in Ducts with Surface Roughness," Augmentation of Convective Heat and Mass Transfer, published by the ASME.
- Norton, B. A. (1983), "Preliminary Analysis and Design of a Turbulent Heat Transfer Test Apparatus," M.S. Thesis, Mechanical and Nuclear Engineering Department, Mississippi State University.
- Nunner, W. (1958), "Heat Transfer and Pressure Drop in Rough Tubes," VDI Forschungsheft, No. 455, Series B, Vol. 22, pp. 5-39, 1956, English Translation, A.E.R.E. Library/Transactions 786.
- Patel, V. C. (1965), "Calibration of the Preston Tube and Limitations on its Use in Pressure Gradients," Journal of Fluid Mechanics, Vol. 23, Part 1, pp. 185-208.
- Perry, A. E. and Joubert, P. N. (1963), "Rough-Wall Boundary Layers in Adverse Pressure Gradients," Journal of Fluid Mechanics, Vol. 17, pp. 193-211.
- Perry, A. E., Schofield, W. H. and Joubert, P. H. (1969), "Rough Wall Turbulent Boundary Layers," Journal of Fluid Mechanics, Vol. 27, pp. 383-413.
- Pimenta, M. M. (1975), "The Turbulent Boundary Layer: An Experimental Study of the Transport of Momentum and Heat with the Effect of Roughness," Ph.D. Dissertation, Mech. Eng. Dept., Stanford Univ. (Also Report HMT-21).
- Preston, J. H. (1954), "The Determination of Turbulent Skin Friction by Means of Pitot Tubes," J. Roy. Aero. Soc., 58, 109.

Reynolds, W. C., Kays, W. M. and Kline, S. J. (1958), "Heat Transfer in the Turbulent Incompressible Boundary Layer, Parts I, II, and III," NASA MEMO 12-1-58W, 12-2-58W, and 12-3-58W.

Rohsenow, W. M. and Hartnett, J. P. (1973), Handbook of Heat Transfer, McGraw-Hill, New York, NY.

Scaggs, W. F., Taylor, R. P. and Coleman, H. W. (1988a), "Measurement and Prediction of Rough Wall Effects on Friction Factors in Turbulent Pipe Flow," Report TFD-88-1, Mech. and Nuc. Eng. Dept., Miss. State Univ.

Scaggs, W. F., Taylor, R. P. and Coleman, H. W. (1988b), "Investigations of Rough Surface Effects on Friction Factors in Turbulent Pipe Flow," Final Technical Report to USAF Wright Aeronautical Laboratories, AFWAL-TR-87-3101.

Scaggs, W. F., Taylor, R. P. and Coleman, H. W. (1988c), "Measurement and Prediction of Rough Wall Effects on Friction Factor - Uniform Roughness Results," Journal of Fluids Engineering, Vol. 110, pp. 385-391.

Schlichting, H. (1936), "Experimentelle Untersuchungen Zum Rauigkeits-Problem," Ingenieur-Archiv., Vol. VII, No. 1, pp. 1-34. (Also Experimental Investigation of the Problem of Surface Roughness, NACA TM 832).

Schultz-Grunow, F. (1941), "New Frictional Resistance Law for Smooth Plates," NACA TM 986, Washington, DC.

Seidman, M. H. (1978), "Rough Wall Heat Transfer in Compressible Turbulent Boundary Layer," AIAA Paper 78-163.

Sood, N. S. and Jonsson, V. K. (1969), "Some Correlations for Resistances to Heat and Momentum Transfer in the Viscous Sublayer at Rough Walls," Journal of Heat Transfer, Trans. ASME, pp. 488-494.

Suryanarayana, P. V. R. (1986), "Remote Data Acquisition and Control Techniques for Wind and Water Tunnel Experiments," M.S. Thesis, Mechanical and Nuclear Engineering Department, Mississippi State University.

Taylor, R. P., Coleman, H. W. and Hodge, B. K. (1984), "A Discrete Element Prediction Approach for Turbulent Flow Over Rough Surfaces," Mechanical and Nuclear Engineering Department, Mississippi State University, Report TFD-84-1.

Taylor, R. P., Coleman, H. W. and Hodge, B. K. (1985), "Prediction of Turbulent Rough-Wall Skin Friction Using a Discrete Element Approach," Journal of Fluids Engineering, Vol. 107, pp. 251-257.

Taylor, R. P., Scaggs, W. F. and Coleman, H. W. (1988), "Measurement and Prediction of the Effects of Nonuniform Surface Roughness on Turbulent Flow Friction Coefficients," Journal of Fluids Engineering, Vol. 110, pp. 380-384.

Townes, H. W., Cow, J. L., Powe, R. E. and Weber, N. (1972), "Turbulent Flow in Smooth and Rough Pipes," Journal of Basic Engineering, Trans. ASME, Series D., Vol. 94, No. 2, pp. 353-362.

Townes, H. W. and Powe, R. E. (1973), "Turbulence Structure for Fully Developed Flow in Rough Pipes," Journal of Fluid Engineering, Trans. ASME, Series I, Vol. 95, No. 2, pp. 255-261.

Wu, J., "Flow in Turbulent Wall Layer Over Uniform Roughness," ASME paper 73-APM-U, to be published in Journal of Applied Mechanics, Trans. ASME.

Yaglom, A. M. and Kader, B. A. (1974), "Heat and Mass Transfer between a Rough Wall and Turbulent Fluid Flow at High Reynolds and Peclet Number," Journal of Fluid Mechanics, Vol. 62, Part 3, 11, pp. 601-623.

Yavuzkurt, S. (1984), "A Guide to Uncertainty Analysis of Hot-Wire Data," Journal of Fluids Engineering, Vol. 106, pp. 181-186.

Zukauskas, A. (1972), "Heat Transfer from Tubes in Crossflow," Advances in Heat Transfer, Academic Press, New York, NY.